Sapienza Università di Roma
Dottorato di Ricerca in Fisica
Scuola di dottorato "Vito Volterra"

MEG, search for $\mu^+ \to e^+ + \gamma$ decay. A study of the Timing Counter Detector.

by

Dott. Alessandro Barchiesi

Program Coordinator

Prof. Enzo Marinari

Thesis Advisors

Dott. Dino Zanello

Dott. Giancarlo Piredda

Contents

III   The Timing Counter   51

3   The Timing Counter: studies and development.   53

. . . Faccio sempre ciò che non so fare,
per imparare come va fatto. . .

("Vincent Van Gogh")

Part I

Theory and phenomenology

Chapter 1

The Standard Model and SUSY extensions

In the following chapter we will give a short introduction to the main features of one of the most successful achievements in modern physics: the Standard Model (SM), It provides a very elegant theoretical framework, which is able to describe the known experimental facts in particle physics with high precision. [1, 3, 2, 4, 5, 6]. In the SM lepton flavor violation (LFV) is forbidden by a so called "accidental" symmetry and the recent evidence for neutrino oscillations implies that it no longer holds. This implies the existence of other LFV processes, such as $\mu^{\pm} \to e^{\pm}\gamma$ decay, nonetheless the branching ratios of the LFV processes in the SM are non detectable. We will focus on Lepton Flavor Violation (LFV) and we will discuss some of the possible extensions of the SM and how they reflect on the LFV.

1.1   The Standard Model

The SM is a gauge theory based on the symmetry group $SU(3)_C \times SU(2)_L \times U(1)_Y$ of color, weak isospin and hypercharge invariance, spontaneously broken to $SU(3)_C \times U(1)_{e.m.}$ at the Fermi scale $M_{\mathrm{F}}(\sim 100 \text{ GeV})$. It describes strong, weak and electromagnetic interactions through the exchange of the corresponding spin-1 gauge fields: 8 massless gluons and 1 massless photon for the strong and electromagnetic interactions, respectively, and 3 massive bosons, W^+,W^-,Z, for the weak interaction. The fermionic matter content is given by the known leptons and quarks, which

are organized in a 3-fold family structure:

$$\left[\begin{array}{cc} \nu_e & u \\ e^- & d' \end{array} \right], \left[\begin{array}{cc} \nu_\mu & c \\ \mu^- & s' \end{array} \right], \left[\begin{array}{cc} \nu_\tau & t \\ \tau^- & b' \end{array} \right] \tag{1.1}$$

where (each quark appears in 3 different *colours*)

$$\left[\begin{array}{cc} \nu_l & q_u \\ l^- & q_d \end{array} \right] \equiv \left[\left(\begin{array}{c} \nu_l \\ l^- \end{array} \right)_L, \quad \left(\begin{array}{c} q_u \\ q_d \end{array} \right)_L, \quad l_R^-, \quad q_{uR}, \quad q_{dR}, \right] \tag{1.2}$$

plus the corresponding antiparticles.

Thus, the left-handed fields are $SU(2)_L$ doublets, while their righthanded partners transform as $SU(2)_L$ singlets. The 3 fermionic families in Eq. (1.1) appear to have identical properties (gauge interactions); they only differ by their mass and their flavour quantum number.

The gauge symmetry is broken by the vacuum, which triggers the Spontaneous Symmetry Breaking (SSB) of the electroweak group to the electromagnetic subgroup:

$$SU(3)_C \otimes SU(2)_L \otimes U(1)_Y \longrightarrow SU(3)_C \otimes U(1)_{QED} \tag{1.3}$$

The SSB mechanism generates the masses of the weak gauge bosons, and gives rise to the appearance of a physical scalar particle in the model, the so-called Higgs. The fermion masses and mixings are also generated through the SSB.

1.1.1   The Lagrangian

We can write the Lagrangian of a free fermion field

$$\mathcal{L}_F = \bar{\psi} i \partial\!\!\!/ \psi - \bar{\psi} m \psi \tag{1.4}$$

whith ψ and $\bar{\psi}$ Weyl spinors [1], the first is the kinetic term and the second is the mass term. The Lagrangian is symmetric under a gauge group $\mathcal{G}$ if it is invariant with respect to a local phase transformation of the fields

$$\psi \quad \rightarrow \quad e^{i\theta^a(x)T^a}\psi = U(x)\psi \tag{1.5}$$

$$\bar{\psi} \quad \rightarrow \quad \bar{\psi} e^{-i\theta^a(x)T^{*a}} = \bar{\psi} U^\dagger(x) \tag{1.6}$$

where T^a $(a = 1, \ldots, N)$ are the N generators of the group, $\mathcal{G}$ and $\theta^a(x)$ are the (x-dependent) parameters of the transformation. To make the (1.4) invariant under such a transformation it is necessary to introduce N vector fields A_μ^a (gauge fields) which transform in the following way

$$A_\mu \quad = \quad \sum_a A_\mu^a T^a \tag{1.7}$$

$$A_\mu \quad \rightarrow \quad U^\dagger A_\mu U - i U^\dagger \partial_\mu U. \tag{1.8}$$

---

[1](ψ can in general be a k-dimensional multiplet)

It is useful to introduce the notation of covariant derivative

$$D_\mu = \partial_\mu + ig A_\mu \tag{1.9}$$

where g is a scalar parameter (the coupling constant) from which follows that

$$\bar\psi \slashed{D} \psi = \bar\psi \slashed\partial \psi + ig\bar\psi\gamma^\mu T^a \psi A_\mu^a \tag{1.10}$$

is invariant under gauge transformations. We need to add a kinetic term to allow the propagation of the gauge bosons.

$$\mathcal{L}_{\text{vb,kin}} = -\frac{1}{4}\text{Tr}_a F_{\mu\nu} F^{\mu\nu} \tag{1.11}$$

where $F^{\mu\nu}$ is the field tensor

$$F^{\mu\nu} = \partial^\mu A^\nu - \partial^\mu A^\nu + g[A^\mu, A^\nu]. \tag{1.12}$$

From Equation 1.10 it follows that the requirement of gauge invariance introduces couplings between the fermion current $J^\mu = \bar\psi\gamma^\mu T^a \psi$ and the vector bosons A_μ^a, all with the same strength g. The assignment of a fermionic field to some representation of the gauge group automatically determines its interactions with the gauge fields. It is well known that parity is maximally violated in weak interactions *i.e.* only left-handed (LH) fermions take part in weak phenomena. From this phenomenology it is natural to speak of LH and RH (right-handed) fields, and group the LH fermions in SU(2) doublets. All RH particles are $SU(2)_L$ singlets, there is no RH neutrino, and only quarks transform non-trivially under $SU(3)_C$. The gauge group possesses twelve gauge bosons which are usually indicated with λ_μ^i ($i = 1, \ldots, 8$; the gluons), W_μ^a ($a = 1, \ldots, 3$; the weak bosons) and B_μ. A mass term for the vector bosons, *e.g.* $\frac{1}{2}m^2 B_\mu B^\mu$, as well as for the fermion fields, $m\bar\psi_L\psi_R$, would spoil the gauge invariance, hence since this step all the particles in this model are massless.

1.2 SSB: the Higgs-Kibble mechanism

This Lagrangian has very little to do with reality. Our gauge bosons are massless particles; while this is fine for the photon field, the physical $W\pm$ and Z bosons should be heavy objects as comes from the experimental results. In order to generate masses, we need to break the gauge symmetry in some way; however, we also need a fully symmetric Lagrangian to preserve renormalizability. Particle masses are introduced via the so-called Higgs-Kibble mechanism to overcome the problem. A scalar field (the Higgs boson) is included in the Lagrangian, together with its interactions. The field is different from zero at the potential minimum, and it is said to develop a non-null vacuum expectation value (VEV). The effect is:

- generating particle masses and

- reducing the unobserved $SU(2)_L \times U(1)_Y$ symmetry down to the electromagnetic $U(1)_{e.m.}$ gauge symmetry.

The Higgs field is a scalar complex $SU(2)_L$ doublet with $Y = 1$

$$\phi = \begin{pmatrix} \phi^+ \\ \phi^0 \end{pmatrix}. \tag{1.13}$$

Its kinetic and potential term are added to the Lagrangian

$$\mathcal{L}_H = (D_\mu \phi)^\dagger (D^\mu \phi) - V(\phi) \tag{1.14}$$

where the most general, renormalizable form for the potential is

$$V(\phi) = -\mu^2 \phi^\dagger \phi + \lambda (\phi^\dagger \phi)^2, \quad \mu^2 > 0 \tag{1.15}$$

Together with the kinetic and potential part the Lagrangian can now include terms describing the interactions of the fermion fields with the scalar field (Yukawa couplings). All terms which are singlets under the gauge group can be written:

$$\mathcal{L}_Y = \sum_{\text{generations}} \bar{Q}_L^i \lambda_u^{ij} \phi^\dagger u_R^j + \bar{Q}_L^i \lambda_d^{ij} \phi d_R^j + \bar{L}_L^i \lambda_e^{ij} \phi e_R^j, \tag{1.16}$$

where $\lambda_{u,d,e}^{ij}$ are arbitrary 3×3 matrices. Two things are worth noticing:

- $\phi^\dagger$ is used in the first term in order to build a $Y = 0$ term.

- Due to the lack of a ν_R singlet we cannot write a term of the form $\bar{L}_L \phi^\dagger \nu_R$.

The potential (1.15) has infinite, degenerate minima for the Higgs field corresponding to a non-zero vacuum expectation value:

$$v = \sqrt{\frac{\mu^2}{2\lambda}}. \tag{1.17}$$

We can choose a gauge in which

$$\langle \phi \rangle = \begin{pmatrix} 0 \\ v \end{pmatrix}. \tag{1.18}$$

Notice that the vacuum state is now invariant under the $U(1)$ symmetry generated by $Q = T_3 + Y/2$ which is identified with the residual $U(1)_{e.m.}$ gauge symmetry. To see the effects of the spontaneous symmetry breaking we must replace ϕ with its vacuum expectation value in the SM Lagrangian.

1.2.1   Vector bosons masses

In the gauge (1.18) the kinetic term of the Higgs sector of the Lagrangian generates the following mass term for the gauge bosons

$$\mathcal{L} = \frac{v^2}{4} \left(g W_3^\mu - g' B^\mu \right)^2 + \frac{v^2}{2} g^2 W_\mu^- W^{+\,\mu} \tag{1.19}$$

where $W^{\pm \mu} = 1/\sqrt{2}(W_1^\mu \pm iW_2^\mu)$ are the fields mediating the weak charged current interactions. W_3^μ and B^μ can be rotated in the two mutually orthogonal fields

$$Z^\mu = \frac{1}{\sqrt{g^2 + g'^2}}(gW_3^\mu - g'B^\mu) = \cos\theta_w W_3^\mu - \sin\theta_w B^\mu \qquad (1.20)$$

$$A^\mu = \frac{1}{\sqrt{g^2 + g'^2}}(g'W_3^\mu + gB^\mu) = \sin\theta_w W_3^\mu + \cos\theta_w B^\mu \qquad (1.21)$$

where θ_w is the Weinberg angle. With the new notation the A^μ boson remains massless (photon) and the Z^μ acquires a mass term of the form

$$\frac{v^2}{4}\sqrt{g^2 + g'^2} Z_\mu Z^\mu, \qquad (1.22)$$

from which follows

$$m_W = gv \qquad m_Z = \sqrt{g^2 + g'^2}v \qquad m_\gamma = 0 \qquad \frac{m_W}{m_Z} = \cos\theta_W. \qquad (1.23)$$

1.2.2 Fermion masses

The replacement of ϕ with $\langle\phi\rangle = {}^t(0, v)$ generates the following form for the Yukawa couplings:

$$\mathcal{L}_Y = \sum_{\text{generations}} v\lambda_u^{ij}\bar{u}_L^i u_R^j + v\lambda_d^{ij}\bar{d}_L^i d_R^j + v\lambda_e^{ij}\bar{e}_L^i e_R^j + \text{h. c.} \qquad (1.24)$$

The interactions now mimic a mass term which can be diagonalized in the flavour space with biunitary transformations:

$$U_L^\dagger \lambda_{u,d,e} U_R = \lambda_{u,d,e}^{\text{DIAG}}, \qquad (1.25)$$

to make the masses for the three generations of quarks and leptons explicit. It is important to notice that these rotations affect also the kinetic term, which contains the fermion interactions with the vector bosons. The neutral and electro-magnetic currents remain flavor diagonal also in the mass eigenbasis. The charged current, instead, it is no longer diagonal and can be expressed as

$$J^\mu = \bar{d}_L' \gamma_\mu U_L^{d\,\dagger} U_L^u u_L' + \bar{e}_L' \gamma^\mu U_L^{e\,\dagger} \nu_L, \qquad (1.26)$$

where the primed fields are the rotated ones. Assuming neutrinos massless (and hence degenerate) we can rotate the ν_L field in such a way as to make the second term in Eq. (1.26) flavour diagonal. It is not possible however to perform such a rotation in the first term without changing the quark mass term. Therefore the 3×3 unitary matrix $U_L^{d\,\dagger} U_L^u$ retains a physical meaning, describing the inter-generation flavour transitions between quarks, and is known as the Cabibbo, Kobayashi and Maskawa matrix V_{CKM}.

Flavour transitions in the lepton sector, on the contrary, are exactly forbidden. For every global phase transformation of the fields $\psi \rightarrow \psi e^{iL\theta}$ a corresponding quantum number is conserved. The SM Lagrangian is invariant under four such global symmetries, which are not dictated by gauge invariance and are therefore called "accidental". They correspond to the conserved quantum numbers B, the barion number, and L_i, $i = e, \mu, \tau$, the lepton family number of each generation.

1.2.3   Neutrino masses and mixing

In the SM, lepton flavor is preserved because of the vanishing neutrino masses. It is possible to supplement the SM just inserting the field for the RH neutrino, ν_R, which could pair with the SM ν_L giving rise to the neutrino masses. In a way analogous to the quark sector we can now introduce in the Lagrangian the Yukawa coupling of the RH neutrino:

$$\mathcal{L}_Y^\nu = \bar{L}_L^i \lambda_n^{ij} \phi^\dagger \nu_R \qquad (1.27)$$

which becomes, after spontaneous symmetry breaking, the following mass term for the neutrino

$$\mathcal{L}_Y^m = v \bar{\nu}_L^i \lambda_n^{ij} \phi^\dagger \nu_R. \qquad (1.28)$$

This can be diagonalized to give the neutrino mass eigenstates. Consequently, for the leptons, the mass basis is different from the flavour basis, which gives rise to flavour violation also in the lepton sector.

The introduction of the right handed neutrino however does not account for the lightness of neutrinos with respect to all the other fermions. The see-saw model gives one possible explanation including a new field for the RH neutrino. The neutrinos being electrically neutral does not exclude the possibility for them to be their own anti-particle: neutrinos and anti-neutrinos are just opposite chiral states of the same particle and we can write in the Lagrangian additional mass terms of the form

$$m_L \nu_L \nu_L^c + M_R \nu_R \nu_R^c. \qquad (1.29)$$

The RH neutrinos are completely neutral under the SM gauge group. Consequently they can acquire Majorana masses M_R which are unrelated to the electro-weak symmetry breaking scale.

For one generation case, the complete mass term for the neutrino is written as

$$
\begin{aligned}
\mathcal{L}_m^\nu &= m_D \bar{\nu}_L \nu_R + M_R \bar{\nu}_R^c \nu_R + \text{h.c.} \\
&= (\bar{\nu}_L \bar{\nu}_R^c) \begin{pmatrix} 0 & m_D \\ m_D & M_R \end{pmatrix} \begin{pmatrix} \nu_L \\ \nu_R \end{pmatrix}.
\end{aligned}
\qquad (1.30)
$$

It is natural to have m_D comparable with the other lepton masses. If $M_R \gg M_Z$ the eigenvalues of the matrix, *i.e.* the neutrino physical masses, are

$$m_1 \sim M_R \qquad m_2 \sim \frac{m_D^2}{M_R}. \qquad (1.31)$$

One neutrino remains super-heavy while the other gets a tiny mass.

If neutrinos are not massless the mass basis is in general different from the flavour basis. Recent experimental results [7, 8, 9, 10, 11, 12, 13, 14] confirmed the existence of oscillations in solar, atmospheric and reactor neutrinos, proving that neutrinos have masses different from zero.

Atmospheric neutrino experiments prove a $\nu_\mu \leftrightarrow \nu_\tau$ oscillation with a $\Delta m^2 \approx 3 \times 10^{-3}$ eV^2 and an almost maximal mixing ($\sin^2 2\theta_{\text{Atm}} > 0.92$). Solar neutrino experiment suggests a ν_e disappearance in a $\nu_\mu \div \nu_\tau$ mixed state with a $\Delta m^2 \approx 7 \times 10^{-5}$ eV^2 and a nearly maximal mixing here [15].
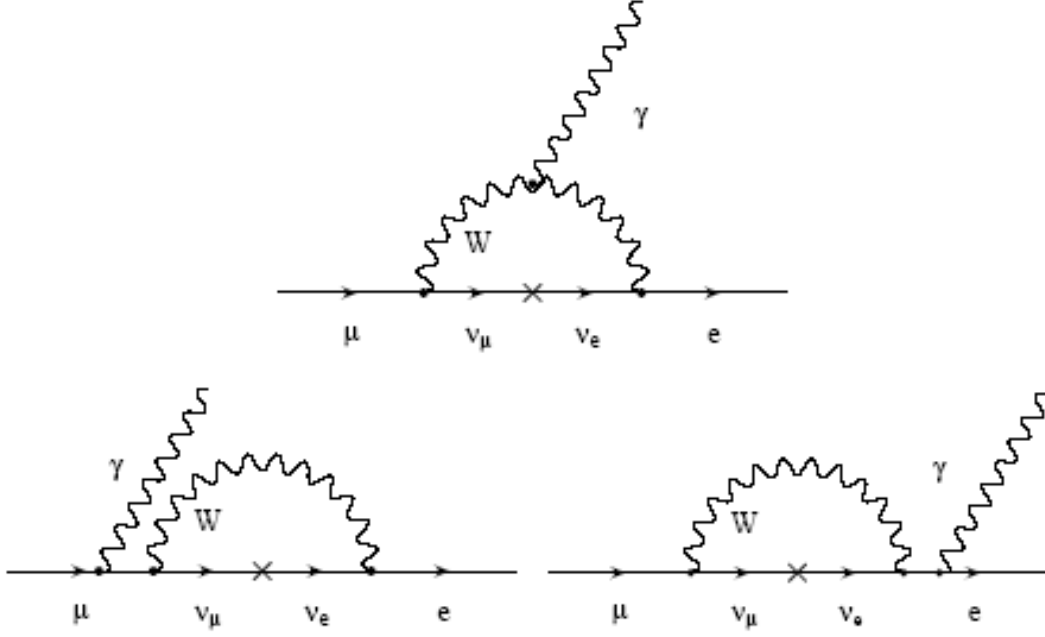
Figure 1.1: Diagrams describing the $\mu^{\pm} \to e^{\pm}\gamma$ decay in the Standard Model.

Neutrino oscillations show that lepton flavour is not conserved in the phenomenology of particle physics. This implies the existence of other LFV processes, such as $\mu^{\pm} \to e^{\pm}\gamma$ decay, due to the diagrams shown in Figure 1.1. The calculation of this amplitude is clear applying the usual Feynman diagram calculations, anyway a crude estimation of the transition rate is easily done observing that the oscillation (θ is the mixing angle between neutrinos) $\nu_{\mu} \to \nu_{e}$ should take place over a distance $L \sim 1/M_W$, the energy flowing in the loop is of order M_W and, otherwise, the diagram is the same as the muon Michel decay with one more photon leg.

$$\Gamma(\mu \to e\gamma) \approx \underbrace{\frac{G_F^2 m_\mu^2}{192\pi^3}}_{\mu - \text{decay}} \quad \underbrace{\left(\frac{\alpha}{2\pi}\right)}_{\gamma - \text{vertex}} \quad \underbrace{\sin^2 2\theta \sin^2\left(\frac{1.27\Delta m^2}{M_W^2}\right)}_{\nu - \text{oscillation}} \tag{1.32}$$

$$\approx \frac{G_F^2 m_\mu^2}{192\pi^3}\left(\frac{\alpha}{2\pi}\right)\sin^2 2\theta_{\odot}\left(\frac{\Delta m^2}{M_W^2}\right)^2, \tag{1.33}$$

normalized to the normal muon decay

$$\frac{\Gamma(\mu \to e\gamma)}{\Gamma(\mu \to e\nu\bar{\nu})} \approx \left(\frac{\alpha}{2\pi}\right)\sin^2 2\theta_{\odot}\left(\frac{\Delta m^2}{M_W^2}\right)^2$$

$$\approx \frac{1}{2 \times 137 \times \pi}\left(\frac{7 \times 10^{-5} \text{ eV}^2}{80 \text{ GeV}^2}\right)^2$$

$$\approx \quad 10^{-55}, \tag{1.34}$$

which is a very small branching ratio (the correct evaluation differs by a factor of 3/64).

1.3   Beyond the Standard Model

The SM is unsatisfactory from many points of view, most of them of theoretical nature because it does not account for the existence of three generations of quarks and leptons, nor for the quark and lepton masses and mixing pattern. Moreover it is appealing to think a unification of the strong and electro-weak forces with gravitation. In this way a new energy scale, $M_{\mathrm{Pl}} \approx 10^{19}$ GeV, the scale at which the three forces become comparable, is required.

In the SM the parameters of the Higgs potential are arbitrary and unrelated to other energy scales, yet quantum corrections to the Higgs mass m_{H} ,induced by loop diagrams, give contributions of order

$$\delta m_{\mathrm{H}}^2 \sim \Lambda^2 \tag{1.35}$$

where Λ is the cut-off energy of the theory ($\Lambda \sim M_{\mathrm{Pl}}$) making Λ as the natural scale for the Higgs boson mass.

This poses the problem of *naturalness* and stability of the Fermi scale because an extreme fine-tuning of the parameters to every order in perturbation theory is necessary to keep m_{H} at the Fermi scale.

1.3.1   Supersymmetry and the Grand-Unified Theory

Supersymmetry (SUSY) solve the naturalness problem of the Higgs mass keeping the scalar mass under control.

Supersymmetry is a symmetry which commutes with the gauge and the other internal symmetries and relates bosons and fermions with the same quantum numbers (apart from spin, which is a "Poincarè" quantum number). It predicts, along with every particle, its super-symmetric counterpart with, in the limit of non-broken SUSY, the same mass. The two particles are said to belong to the same super-multiplet. In this way the Higgs mass is kept under control by the following mechanism: for each fermion there is a contribution from its scalar partner, of the opposite sign due to the difference in Fermi-Bose statistics. The one-loop contribution to the Higgs mass is given by

$$\delta m_H^2 \sim \sum_i g_i^2 \left(m_{B_i}^2 - m_{F_i}^2 \right) \tag{1.36}$$

where B_i and F_i are the Bosons and Fermion belonging to the same super-multiplet and g_i is their (common) coupling to the Higgs scalar.

Supersymmetry is clearly broken, since we do not observe any partner of the known fermions. Furthermore, equation (1.36) establishes that the scale at which we expect to find SUSY particles is the same as the Higgs boson mass, *i.e.* the Fermi scale.

The non-kinetic part of the Lagrangian is expressed by means of a super-potential that is an analytic function of the super-multiplets. The Yukawa coupling between the matter fields and the Higgs is written as

$$W = y_u H_1 QU + y_d H_2 QD + y_e H_2 LE \tag{1.37}$$

where the contractions which render all the terms singlets are understood.

Being the super-potential an analytic function of the super-fields it is not possible to give mass to all fermions via Yukawa interactions with one Higgs doublet only ($\phi^\dagger$ cannot be included). Two doublets with opposite hypercharge are introduced which develop two different VEVs. The ratio of the two VEVs is called

$$\frac{v_1}{v_2} = \tan \beta$$

where it is assumed $\tan \beta > 1$.

There are other problems in the SM which SUSY does not address: the existence of three gauge groups with independent coupling constants is not theoretically appealing. Furthermore the hypercharge assignment to the particles is completely arbitrary, and adjusted to reproduce the measured particle charges.

There is no theoretical motivation (yet an astonishing experimental piece of evidence for something deeper) for the quark charges being related to the lepton charges, or for the charge being quantized at all.

In fact the values of the other quantum numbers (weak isospin, etc.) are dictated by the commutation relations of the gauge group generators. Charge quantization would occur if Q were a generator of the gauge group.

$SU(3) \times SU(2) \times U(1)$ possesses four independent commuting generators: Y, T_3, λ_3 and λ_8 (λ_3 and λ_8 are the diagonal generators of SU(3)).

The number of mutually commuting generators of a group is called the *rank* of the group. It is normal to try to embed $SU(3) \times SU(2) \times U(1)$ in a rank= 4 group $\mathcal{G}$ which is broken at some energy to $SU(3) \times SU(2) \times U(1)$.

The only rank= 4 group is $SU(5)$, whose fundamental representation is five-dimensional. It possesses 24 generators (gauge bosons). There is an obvious embedding of the eleven $SU(3) \times SU(2)$ generators in $SU(5)$ which is

$$(\lambda_i)_{3\times 3} \rightarrow \left(\begin{array}{c|c} \lambda_i & 0 \\ \hline 0 & 0 \end{array} \right)_{5\times 5} \qquad (\sigma_i)_{2\times 2} \rightarrow \left(\begin{array}{c|c} 0 & 0 \\ \hline 0 & \sigma_i \end{array} \right)_{5\times 5} \tag{1.38}$$

with the last diagonal generator being

$$
Y = y \begin{pmatrix} 1 & & & & \\ & 1 & & & \\ & & 1 & & \\ & & & -{}^3/_2 & \\ & & & & -{}^3/_2 \end{pmatrix}.
\tag{1.39}
$$

There are twelve generators left, which are of the form

$$
\left(\begin{array}{ccc|cc} & & & 1 & 0 \\ & & & 0 & 0 \\ & & & 0 & 0 \\ \hline 1 & 0 & 0 & & \\ 0 & 0 & 0 & & \end{array} \right) , \qquad
\left(\begin{array}{ccc|cc} & & & i & 0 \\ & & & 0 & 0 \\ & & & 0 & 0 \\ \hline -i & 0 & 0 & & \\ 0 & 0 & 0 & & \end{array} \right) , \quad \text{etc.}
\tag{1.40}
$$

The SM particles of each generation are placed in a $\bar{5} \oplus 10$ representation in the following way

$$
\bar{5} = \bar{F} = \begin{pmatrix} \bar{d}^r \\ \bar{d}^y \\ \bar{d}^b \\ e^- \\ \nu_e \end{pmatrix}_L
\qquad
10 = T = \left(\begin{array}{ccc|cc} 0 & u^b & u^y & -u^r & -d^r \\ & 0 & u^r & -u^y & -d^y \\ & & 0 & -u^b & -d^b \\ \hline & & & 0 & -e^+ \\ & & & e^+ & 0 \end{array} \right).
\tag{1.41}
$$

The representations are also called $\bar{F} = \bar{5}$ (from "five") and $T = 10$ (from "ten").

The gauge bosons of the SM are associated with block diagonal generators, thus act in the same way as before. Conversely the twelve new gauge bosons are associated to generators[2] connecting leptons and quarks, mediating quark-lepton transitions, giving rise to processes such as proton decay.

Their masses must be very large in order to make proton instability acceptably small, hence $SU(5)$ must be broken at a very high energy. The spontaneous symmetry breaking of SU(5) is accomplished by a 24-dimensional Higgs multiplet.

$SU(5)$ unification has two remarkable properties: it predicts charge quantization (and the correct relation between quark and lepton electric charge) and the unification of all coupling constants at an energy $M_{\mathrm{GUT}} \sim 10^{15}$ GeV (as well as a prediction of $\sin \theta_W$ consistent with measurements).

It removes all the SM accidental symmetries but preserves $B - L$, $(L = L_e + L_\mu + L_\tau)$. Unfortunately the prediction of the proton decay rate in the minimal SU(5) model is in conflict with the experiment.

The possibility of $SO(10)$ as a grand-unification group for the Standard Model was first noted by Georgi [16] and Fritsch & Minkowski [17]. Unlike $SU(5)$, $SO(10)$ is a rank= 5 group with

---

[2]Note that these new bosons are color triplets and SU(2) doublets; they are conventionally called $X^\pm$ and $Y^\pm$, whose charge are 4/3 and 1/3.

the extra diagonal generator being $B - L$. It is worth noticing that $SO(10) = SU(5) \otimes U(1)$ and that it possesses a 16-dimensional representation which decomposes, under $SU(5) \otimes U(1)$ as $16 = 10 \oplus 5 \oplus 1$. This is theoretically appealing because it can be regarded as a natural explanation of the fact that in the framework of $SU(5)$ the fermions belong to a reducible representation. In fact it is possible to accommodate all the fermions of one generation within a single 16-dimensional chiral multiplet with the extra singlet field easily associated with a right handed neutrino.

1.4 Phenomenology

In Grand Unified Theories the problem of naturalness is still present, since it is not possible to explain the existence of two energy scales which differ by so many orders of magnitude (M_{GUT} and m_H). They retain all the bad divergence properties of the Higgs mass.

The natural solution is provided by the SUSY generalization of GUT theories, the so-called SUSY-GUTs, which are among the most appealing candidates for the extension of the SM to date. At a certain level the presence of a lepton-flavor violating signal, other than neutrino oscillation, could really indicate the existence of new physics beyond the Standard Model.

Among the various channels, those involving muon decays are the most appealing, due to the comparative ease to have high fluxes of low energy muons at dedicated beams. Recent theoretical developments calculate rates for some LFV processes involving muon decays that are just below the present experimental limit.

1.4.1 Main LFV processes and limits

In Table 1.1 the upper limits of various lepton-flavor violating processes are listed. They involve decays of muons and tau leptons in neutrinoless final states, as well as those of heavy bosons, π, K and Z^0, in pairs of leptons of different generations.

The processes involving muon decays can be grouped in three categories:

1. Direct muon decays ($\mu^+ \to e^+\gamma$ and $\mu \to eee$);

2. Muon conversion on heavy elements, as Titanium or Gold;

3. Muonium—anti-muonium conversion.

The best limits are obtained for $\mu \to eee$ and muon conversion on heavy elements. This is due to the clear signature of the processes which allows for a search in a background-clear environment. However the exclusion power on $\Delta L_i = \pm 1$ processes due to their limits $\mu \to eee$ and muon conversion on heavy elements is comparable to that of the $\mu^+ \to e^+\gamma$ decay, since , in most theoretical models, the two former processes are suppressed by one power of α, the fine structure constant, with respect to the latter. There are however theories in which $\mu \to eee$ and muon conversion are enhanced with respect to the $\mu^+ \to e^+\gamma$ decay. The existence of $\Delta L_i = \pm 2$ processes, on the other way, is constrained by limits on the muonium anti-muonium conversion.

Reaction	Present limit	Reference
$\mu^+ \to e^+\gamma$	$< 1.2 \times 10^{-11}$	[18, 19]
$\mu \to eee$	$< 1.0 \times 10^{-12}$	[20]
$\mu^- Ti \to e^- Ti$	$< 6.1 \times 10^{-13}$	[21]
$\mu^+ e^- \to \mu^- e^+$	$< 8.3 \times 10^{-11}$	[22]
$\tau \to e\gamma$	$< 2.7 \times 10^{-6}$	[23]
$\tau \to \mu\gamma$	$< 1.0 \times 10^{-6}$	[24]
$\tau \to \mu\mu\mu$	$< 1.9 \times 10^{-6}$	[25]
$\tau \to eee$	$< 2.9 \times 10^{-6}$	[25]
$\pi^0 \to \mu e$	$< 8.6 \times 10^{-9}$	[26]
$K_L^0 \to \mu e$	$< 4.7 \times 10^{-12}$	[27]
$K^+ \to \pi^+ \mu^+ e^-$	$< 2.1 \times 10^{-10}$	[28]
$K_L^0 \to \pi^0 \mu^+ e^-$	$< 4.4 \times 10^{-10}$	[29]
$Z^0 \to \mu e$	$< 1.7 \times 10^{-6}$	[30]
$Z^0 \to \tau e$	$< 9.8 \times 10^{-6}$	[30]
$Z^0 \to \tau\mu$	$< 1.2 \times 10^{-5}$	[31]

Table 1.1: Limits for the branching ratio of the lepton-flavor violating processes involving muons, taus, pions, kaons and Z bosons.

The search of lepton-flavor violating muon decays is important as it is able to test the validity of the Standard Model. However there has been a recent revival of the subject after the discovery of the top quark, and the realization of its heaviness, $m_t = (174.3 \pm 5.1)$ GeV. The presence in the model of such a huge parameter leads to an enhancement of LFV processes [32, 33, 34]. Furthermore the evidence for neutrino oscillations can be related to amplitude predictions for SM-forbidden muon decays.

1.5   The $\mu^+ \to e^+\gamma$ decay: predictions

It is known that the $\mu^+ \to e^+\gamma$ decay amplitude induced by non-zero neutrino masses is negligible in the SM. If we expect the SM to be valid up to some energy scale M, the effects of physics above this scale may be accounted for by shifts in the SM couplings and by a series of non-renormalizable terms suppressed by powers of M and the effective Lagrangian for the $\mu^+ \to e^+\gamma$ process is given by [35]

$$\mathcal{L}_{\mu^+ \to e^+\gamma} = \frac{g}{M^2} \left[m_\mu A_R \bar{\mu}_R \sigma^{\mu\nu} e_L F_{\mu\nu} + m_\mu A_L \bar{\mu}_L \sigma^{\mu\nu} e_R F_{\mu\nu} \right] + \text{h.c.} \qquad (1.42)$$

where A_L and A_R are the coupling constants that correspond to $\mu^+ \to e_R^+\gamma$ and $\mu^+ \to e_L^+\gamma$ respectively, $F^{\mu\nu}$ is the usual electro-magnetic field tensor and $\sigma^{\mu\nu} = -i/2[\gamma^\mu, \gamma^\nu]$.

The mechanism that generates a $\mu^+ \to e^+\gamma$ amplitude in the Standard Model extensions is the following: SM particles have heavy partners whose interactions are in general non flavor-diagonal.

Flavor transitions in the heavy sector of the theory induces flavor transitions in the sector of the SM particles, suppressed by powers of the energy scale at which the symmetry between the light and the heavy sector is restored.

The processes occurring at a energy scale M can be summarized in the low energy Lagrangian by effective couplings (*e.g.* A_R and A_L in Equation (1.42)) suppressed by powers of M.

We will briefly describe the predictions for three most popular models: SU(5) SUSY-GUTs, SO(10) SUSY GUTs, and SU(5) unification with heavy right-handed Majorana neutrinos.

1.5.1 SU(5) SUSY GUTs with R-parity

The SM accidental symmetries (B, L, L_i) which forbid processes such as proton decay, neutrino masses and $\mu^+ \to e^+\gamma$ decay respectively, are removed at the unification scale M_G. In the effective theory beneath M_G (the Standard Model) the three phenomena are suppressed by powers of M_G. If the effective theory is super-symmetric at a scale $M_F \sim 100$ GeV, the energy scale which plays a role in the effective Lagrangian is M_F, hence the processes are suppressed by powers of M_F. Such interactions induce proton decay at unacceptable rate unless a new symmetry, called R-parity or matter parity, is introduced.

R-parity forces all interactions to have an even number of quarks and leptons and their super-partners (a consequence of this is that the lightest SUSY particle, called neutralino, is stable, allowing for the existence of SUSY dark matter). Thus all B and L-violating processes are forbidden at a scale M_F and remain suppressed by powers of M_G, while processes which violate L_i are still suppressed only by powers of M_F. In the most general form of super-potential

$$W = \quad y_e H_d LE + y_d H_d QD + y_u H_u QU +$$
$$+ \quad \lambda LLE + \lambda' LQD + \lambda'' UDD \tag{1.43}$$

which include the couplings between the Higgs field and the matter fields, as in Equation (1.37) as well as the couplings between the matter fields alone, the interactions of the second line are forbidden by R-parity.

The large Yukawa coupling of the top quark further enhances the lepton flavor transitions. This results in a large transition rate between the scalar partners of the muon and the electron, $\tilde{\mu}$ and $\tilde{e}$, which enhances the $\mu^+ \to e^+\gamma$ process.

In Figure 1.2 predictions are given as a function of slepton masses. It has been calculated that, since up-type quarks and down-type quarks and leptons belong to different representations of SU(5), the left handed sleptons are not significantly mixed, and the branching ratio $\mu^+ \to e^+_R\gamma$ is negligible, therefore only $\mu^+ \to e^+_L\gamma$ occurs in SUSY GUT SU(5) [36].

1.5.2 SO(10) SUSY GUT

In SO(10) SUSY GUT models both left-handed and right-handed (s)leptons receive LFV contributions, The diagrams shown in Figure 1.3 [37] give a large contribution because they are proportional
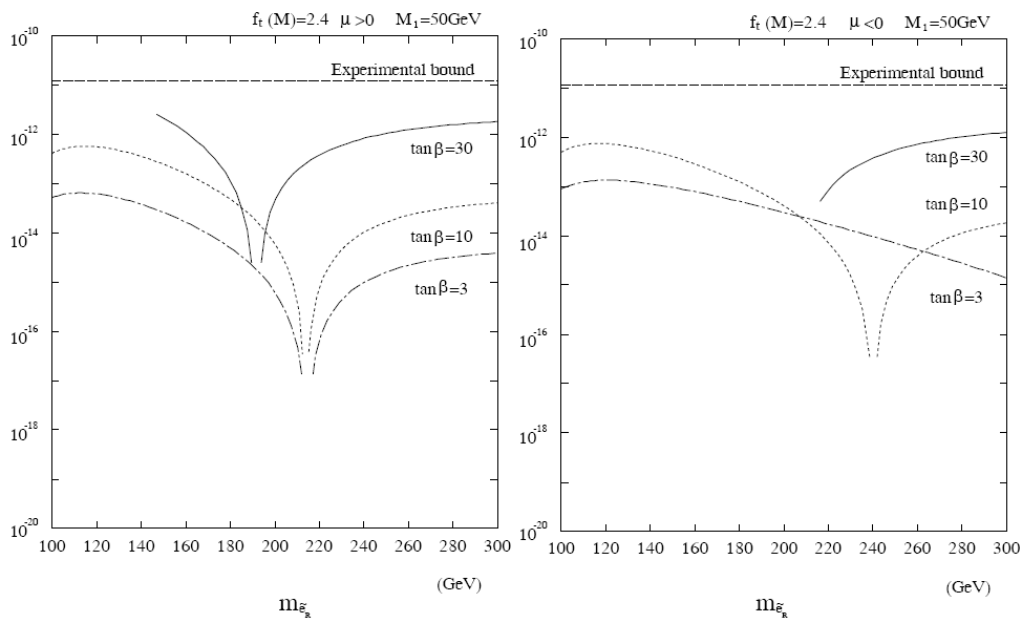
Figure 1.2: Branching ratio for the process $\mu^+ \to e^+\gamma$ as a function of the right-handed selectron mass $m_{\tilde{e}_R}$ for a reasonable choice of electro-weak breaking parameters (after [36]).

to m_τ, hence the $\mu^+ \to e^+\gamma$ branching ratio is enhanced by a factor $(m_\tau/m_\mu)^2$ compared to the minimal SU(5) SUSY GUT.

1.5.3   Super-symmetric models with right-handed neutrinos

Another source of LFV comes from SUSY models with right-handed neutrinos [38]. The smallness of neutrino masses can be explained by the see-saw mechanism induced by right-handed Majorana neutrinos. Rewriting Equation (1.30) taking all three generations into account a second Yukawa coupling matrix, which in general is not generation-diagonal, is introduced, inducing flavor mixing in the high energy sector of the theory between heavy Majorana neutrinos.

The expected magnitude of LFV processes depends on the Yukawa coupling constants but under the assumption that the observed neutrino mixing arises mostly from the Yukawa coupling constants [35] the information from atmospheric and solar neutrinos can be related to slepton mixing, which enhances the $\mu^+ \to e^+\gamma$ decay. Figure 1.4 shows the predicted BR($\mu^+ \to e^+\gamma$) for the Large Mixing Angle (LMA) solution of the solar neutrino mixing, as a function of the Majorana neutrino mass scale. A large fraction of the range for M_R is already excluded by the present experimental limit.
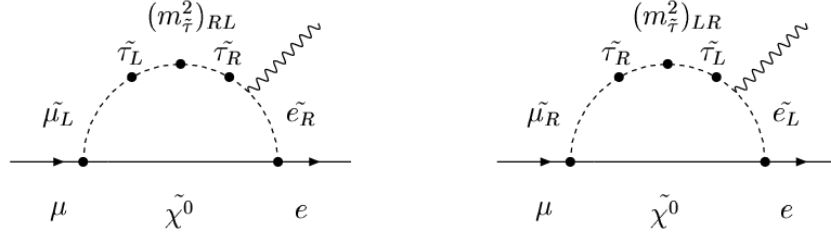
Figure 1.3: Feynman diagrams in SO(10) SUSY GUT which give dominant contributions to the $\mu^+ \to e^+\gamma$ process. The $\tilde{\chi}^0$ particle is a heavy neutralino mediating the flavor changing process.

1.5.4 Connections with $\tan\beta$ and a_μ

In all the predictions the $\mu^+ \to e^+\gamma$ decay rate increases with increasing $\tan\beta$, the ratio of the two SUSY Higgs boson VEVs as is shown, *e.g.* in Figure 1.4. It is worthwhile to notice that the non-discovery of super-symmetry at LEP and TeVatron excludes most of the small $\tan\beta$ region [39].

The branching ratio of the $\mu^+ \to e^+\gamma$ process is naturally linked to the value of the muon anomalous magnetic moment. In fact the general term of the Lagrangian (1.42) is written, taking the three generations into account, as

$$\mathcal{L} = g \frac{m_{l_j}}{M^2} \left(A_{ij}^R \bar{l}_i^R \sigma_{\mu\nu} F^{\mu\nu} l_j^L + A_{ij}^L \bar{l}_i^L \sigma_{\mu\nu} F^{\mu\nu} l_j^R \right) \tag{1.44}$$

The real diagonal parts of A_{ij}^L and A_{ij}^R, which are 3×3 matrices, contribute to the anomalous magnetic moment of the charged leptons,

$$a_{l_i} \equiv \frac{g-2}{2} = m_{l_i}^2 \left(A_{ii}^R + A_{ii}^L \right) \tag{1.45}$$

while the flavor transitions are produced by the off-diagonal terms, The latest result for the anomalous magnetic moment for the muon [40] is

$$a_\mu^{\text{exp}} = (116\,593\,023 \pm 151) \times 10^{-11} \tag{1.46}$$

while the SM prediction is

$$a_\mu^{\text{SM}} = (116\,592\,768 \pm 65) \times 10^{-11}. \tag{1.47}$$

The present measurement is 1.6σ away from the SM prediction.

Using Equation (1.44) non-SM contributions to a_μ can be related, in a model-dependent way, to the branching ratio of the $\mu^+ \to e^+\gamma$ decay.

1.6 Conclusion

The phenomenology of lepton flavor violation is very sensitive to the possible extensions of the Standard Model. The the muon sector research is promising because of the possibility to produce
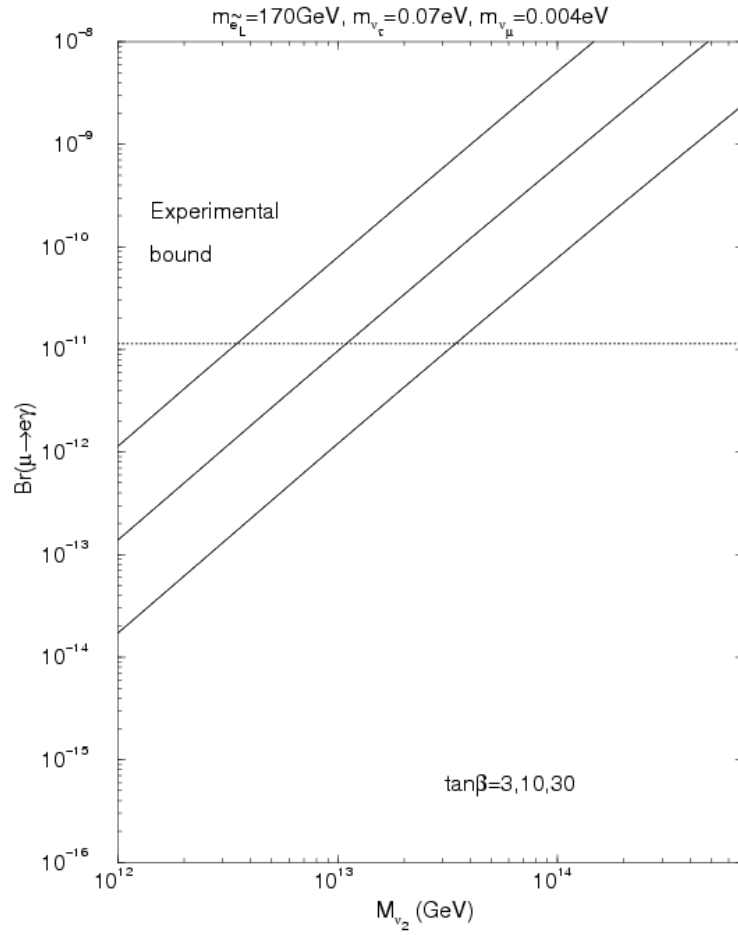
Figure 1.4: Predicted branching ratio of $\mu^+ \rightarrow e^+\gamma$ decay as a function of the Majorana mass of the second-generation right-handed neutrino in the MSSM model with right-handed neutrino, for the MSW large mixing angle solution. The three lines correspond to $\tan\beta = 30, 10, 3$ from top to bottom respectively.

large number of such particles at dedicated beams. We analyzed three popular models in which the predictions for the $\mu \to e\gamma$ decay branching ratio, due to different independent sources, is generally above $10-14$, almost independently from the model parameters: It is therefore worthwhile to try to push down the present limits toward this level.

Part II

The MEG experiment

Chapter 2

Search for the $\mu^+ \rightarrow e^+\gamma$ decay: the MEG experiment

In the following chapter we will describe the early experiments of LFV, emphasizing the key points to be addressed by future $\mu^+ \rightarrow e^+\gamma$ search experiments. We will focus on MEG experiment and on its sensitivity. We will analyze the expected sources of background and how MEG plans to deal with them. We will also focus on the experimental apparatus giving a description of the beam line, of detector and its sub detectors.

2.1 Experimental status of $\mu^+ \rightarrow e^+\gamma$ decay search

The $\mu^+ \rightarrow e^+\gamma$ decay was searched for soon after the muon discovery. Its absence was a key ingredient for the formulation of the Standard Model. The muon role in the spectrum of elementary particles has been a mystery since its discovery in cosmic radiation [42] (1937). For over a decade the muon was thought to be the quantum mediating the strong nuclear force, as predicted by Yukawa [43]. Yet the famous experiment by Conversi, Pancini and Piccioni [45] demonstrated that the muon did not interact through strong force, therefore it could not be the Yukawa meson. It was thought that if the muon were a heavy electron, it would also decay into an electron and a γ-ray. The first search for $\mu^+ \rightarrow e^+\gamma$ was made by Hincks and Pontecorvo in 1947 [46]. They stopped cosmic ray muons in a lead absorber (Figure 2.1) and measured the rate of the discharge coincidence of two Geiger-Müller tube trays. With an expected rate of 1.0 ± 0.3 counts/h they measured $0.01^{+0.06}_{-0.01}$ counts/h, setting an upper limit of less than 10% on the $\mu^+ \rightarrow e^+\gamma$ branching ratio.
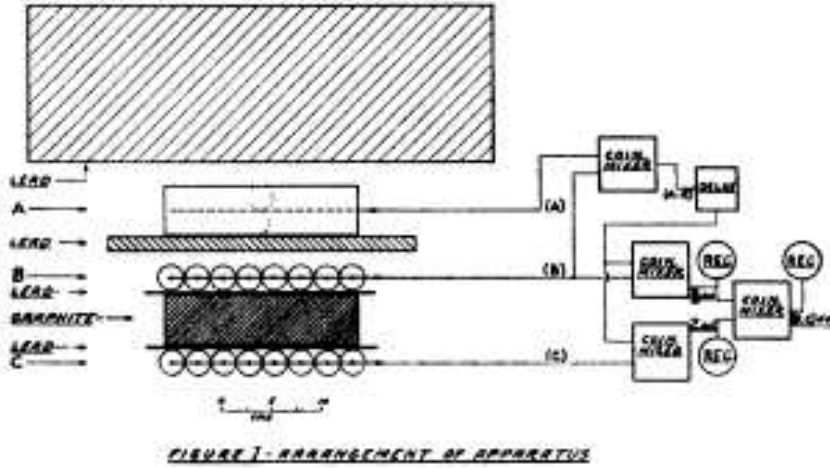
Figure 2.1: Drawing of the apparatus used by Hinks and Pontecorvo for the first search of the decay of cosmic ray mesons into an electron plus a photon.

The search was significantly improved when muons became artificially produced at accelerators, by using stopped pion beams, or directly with muon beams from the meson factories. In 1955, the upper limit of $B(\mu \to e\gamma) < 2 \times 10^{-5}$ [47] was set at the Columbia University Nevis cyclotron.

The discovery of parity violation suggested that the weak interaction takes place through the exchange of charged intermediate vector bosons. In 1958, Feinberg [48] pointed out that the intermediate vector boson, if it existed, would have led to $\mu^+ \to e^+\gamma$ at a branching ratio of 10^{-4}. In fact the process is described by the same diagrams as in Figure 1.1, but without neutrino oscillation, because at that time ν_e and ν_μ were thought to be the same particle.

The absence of any experimental observation of the $\mu^+ \to e^+\gamma$ process with $B(\mu \to e\gamma) < 2 \times 10^{-5}$ led directly to the two-neutrino hypothesis, in which the neutrino coupled to the muon is different than that coupled to the electron, and the $\mu^+ \to e^+\gamma$ process would be forbidden. The two-neutrino hypothesis was verified experimentally at Brookhaven National Laboratory (BNL) by confirming muon production, and no electron production, from the scattering of neutrinos coming from pion decays [49]. This introduced the concept of the separate conservation of lepton flavors, electron number (L_e) and muon number (L_μ).

Over the years, the search for the $\mu^+ \to e^+\gamma$ decay was performed at the intense muon beams available, e.g. at TRIUMF, PSI and Los Alamos National Laboratories. Limits on the $\mu^+ \to e^+\gamma$ branching fraction were constantly tightened by improving detector resolutions of the four relevant variables: positron and photon energy resolution, relative timing and direction. In Table 2.1 the historical progress of the $\mu^+ \to e^+\gamma$ search is summarized and in figure 2.2 a graphical view of the limit as a function of the year is given.

The groupings of points in the plot reflect innovation in muon source and instrumentation.
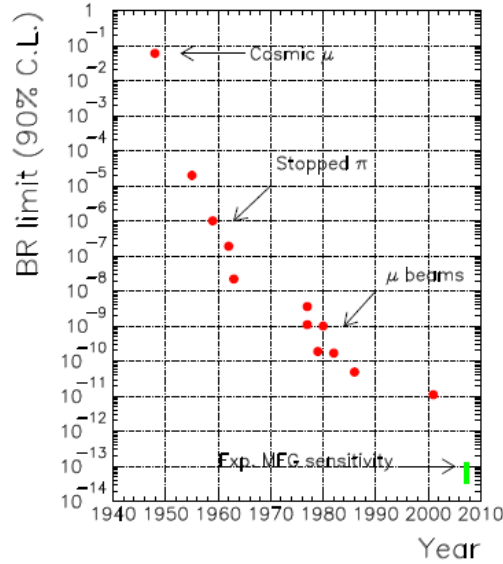
Figure 2.2: Improvement of the branching ratio along the years and the innovations in muon source and technological instrumentation

Place	Year	ΔE_e	ΔE_γ	$\Delta t_{e\gamma}$	$\Delta\theta_{e\gamma}$	Upper limit	References
TRIUMF	1977	10%	8.7%	6.7ns	−	$< 3.6 \times 10^{-9}$	[53]
SIN	1980	8.7%	9.3%	1.4ns	−	$< 1.0 \times 10^{-9}$	[54]
LANL	1982	8.8%	8%	1.9ns	37mrad	$< 1.7 \times 10^{-10}$	[55]
Crystal Box	1988	8%	8%	1.8ns	87mrad	$< 4.9 \times 10^{-11}$	[56]
MEGA	1999	1.2%	4.5%	1.6ns	15mrad	$< 1.2 \times 10^{-11}$	[18]

Table 2.1: Historical Progress of search for $\mu^+ \to e^+\gamma$ since the era of meson factories with 90 % C.L. upper limits. The resolutions quoted are given as a full width at half maximum (FWHM).

The largest steps towards an improvement in the $BR(\mu^+ \to e^+\gamma)$ determination were due to improvements in the muon source.

The limit improved essentially with the number of observed muons, and within each beam configuration improvements of the detectors were fundamental. The quality of a detector is judged by its capability of discriminating a signal event from the background. With the increased muon rate the number of background events was enormously increased, hence the design of new apparatus depend essentially on their background rejection capabilities.

The event signature of $\mu^+ \to e^+\gamma$ decay at rest is an e^+ and a photon in coincidence, moving collinearly back-to-back with their energies equal to half of the muon mass ($m_\mu/2 \cong 52.8$ MeV).

The searches are carried out by using positive muon decay, since a negative muon would be captured by a nucleus when it is stopped in the target, at rest to fully utilize its kinematic energy.

There are two major backgrounds in the $\mu^+ \to e^+\gamma$ experiment:

1. prompt or physics background; coming from radiative muon decay $\mu^+ \to e^+\nu_e\overline{\nu}_\mu\gamma$ when the positron and the photon are emitted back-to-back with a small energy of the two neutrinos;

2. accidental background; arising from the accidental coincidence of a positron in a $\mu^+ \to e^+\nu_e\overline{\nu}_\mu$ muon decay at an energy of 52.8 MeV, accompanied by a high energy photon. The photon sources might be either radiative decay, annihilation in flight or external bremsstrahlung of positrons from another $\mu^+ \to e^+\nu_e\overline{\nu}_\mu$ muon decay.

2.1.1   Physics background

The major physics backgrounds to the search for $\mu^+ \to e^+\gamma$ decay is the radiative muon decay, $\mu^+ \to e^+\nu_e\overline{\nu}_\mu\gamma$ (branching ratio = 1.4 % for $E_\gamma > 10$ MeV), when the e^+ and photon are emitted back-to-back with two neutrinos carrying off little energy. The differential decay width of this radiative muon decay was calculated as a function of the e^+ energy (E_e) and the photon energy (E_γ) normalized to their maximum energies, namely $x = 2E_e/m_\mu$ and $y = 2E_\gamma/m_\mu$ [57, 58]; therefore the kinematical ranges are $0 \leq x,y \leq 1$. As a background to $\mu^+ \to e^+\gamma$, only the kinematic region where $x \approx 1$ and $y \approx 1$ is important. In the approximation where the differential decay width of $\mu^+ \to e^+\nu_e\overline{\nu}_\mu\gamma$ has been computed as a function of x, y, and $z = \pi - \theta_{e\gamma}$, and expanded in the region $x \approx 1$, $y \approx 1$ and $z \approx 0$, the differential decay width of $\mu^+ \to e^+\nu_e\overline{\nu}_\mu\gamma$ decay is given by [59]:

$$dΓ(\mu^+ \to e^+\nu\overline{\nu}\gamma) \cong \frac{G_F^2 m_\mu^5 \alpha}{3 \times 2^8 \pi^4} \times$$
$$\left[(1-x)^2(1 - P_\mu\cos\theta_e) + \left(4(1-x)(1-y) - \frac{1}{2}z^2\right)(1 + P_\mu\cos\theta_e)\right]dxdydzd(\cos\theta_e), (2.1)$$

where G_F is the Fermi coupling constant, α is the fine-structure constant, $z = \pi - \theta_{e\gamma}$, and $\cos z$ is expanded in a polynomial of z, since z is small.

When $x = 1$ and $y = 1$, this differential decay width vanishes. However, in a real experiment, finite detector resolutions introduce background events which would ultimately limit the sensitivity of a search for $\mu^+ \to e^+\gamma$.

Given the detector resolution, the sensitivity limitation from this physics background can be estimated by integrating the differential decay width over the kinematic signal box. It is given by [35]:

$$dB(\mu^+ \to e^+\nu\overline{\nu}\gamma) \quad = \quad \frac{1}{Γ(\mu^+ \to e^+\nu\overline{\nu})}\int_{1-\delta x}^1 dx \int_{1-\delta y}^1 dy \int_0^{\min(\delta z, 2\sqrt{(1-x)(1-y)})} dz \ \frac{dΓ(\mu^+ \to e^+\nu\overline{\nu}\gamma)}{dxdydz},$$

$$= \quad \frac{\alpha}{16\pi} \Big[J_1(1 - P_\mu \cos\theta_e) + J_2(1 + P_\mu \cos\theta_e) \Big] d(\cos\theta_e), \tag{2.2}$$

where δx, δy and δz are a half width of the $\mu^+ \rightarrow e^+\gamma$ signal region for x, y and z, respectively, θ_e is the angle between the muon spin and the e^+ momentum direction, and $\Gamma(\mu^+ \rightarrow e^+\nu\overline{\nu})$ is the total muon decay width. J_1 and J_2 are given as the sixth power of a combination of δx and δy. For the case of $\delta z > 2\sqrt{\delta x \delta y}$, they are represented by

$$J_1 = (\delta x)^4 (\delta y)^2 \quad \text{and} \quad J_2 = \frac{8}{3}(\delta x)^3 (\delta y)^3. \tag{2.3}$$

While if $\delta z \leq 2\sqrt{\delta x \delta y}$, they are given by

$$J_1 = \frac{8}{3}(\delta x)^3 (\delta y)(\frac{\delta z}{2})^2 - 2(\delta x)^2 (\frac{\delta z}{2})^4 + \frac{1}{3}\frac{1}{(\delta y)^2}(\frac{\delta z}{2})^8, \tag{2.4}$$

$$J_2 = 8(\delta x)^2 (\delta y)^2 (\frac{\delta z}{2})^2 - 8(\delta x)(\delta y)(\frac{\delta z}{2})^4 + \frac{8}{3}(\frac{\delta z}{2})^6. \tag{2.5}$$

Experimentally, the resolution of the e^+ energy is better than that of the photon energy, *i.e.* $\delta x < \delta y$. Also, the angular resolution, δz, has been poor in past experiments. Thereby, J_2 is much larger than J_1 for most cases. Figure 2.3 shows the $\mu^+ \rightarrow e^+\nu_e\overline{\nu}_\mu\gamma$ decay fraction for the given δx and δy values with unpolarized muons in the case of $\delta z \geq 2\sqrt{\delta x \delta y}$. From Figure 2.3, it can be seen that both δx and δy of the order of 0.01 are needed to achieve a sensitivity limit at the level of 10^{-15} needed to achieve MEG's intended resolution, as will be showed further in this section.

2.1.2   Accidental background

The event rate of the accidental background (B_{acc}) normalized to the total decay rate can be estimated by

$$B_{\mathrm{acc}} = R_\mu \cdot f_e^0 \cdot f_\gamma^0 \cdot (\Delta t_{e\gamma}) \cdot (\frac{\Delta\Omega_{e\gamma}}{4\pi}), \tag{2.6}$$

where R_μ is the instantaneous muon intensity. f_e^0 and f_γ^0 are the integrated fractions of the spectrum of e^+ in the normal muon decay and that of photon (such as from $\mu^+ \rightarrow e^+\nu_e\overline{\nu}_\mu\gamma$ decay) within the signal region, respectively. $\Delta t_{e\gamma}$ and $\Delta\Omega_{e\gamma}$ are the full widths of the signal regions for time coincidence and angular constraint of the back-to-back kinematics respectively. The accidental background becomes more important than the physics background in presence of a high rate of incident muons. This is usually the case for the present and future experiments.

To estimate B_{acc} as given from eq. 2.6, given the width of the signal region we define: δx, δy, $\delta\theta_{e\gamma}$, and $\delta t_{e\gamma}$ as the half width of the signal region for e^+, photon energies, angle $\theta_{e\gamma}$ and relative timing between e^+ and photon, respectively.
f_e^0 can be estimated by integrating the Michel spectrum of the normal muon decay over $1 - \delta x \leq x \leq 1$, yielding $f_e^0 \sim 2(\delta x)$, since the Michel spectrum is constant at $x \sim 1$.
The back-to-back resolution $(\Delta\Omega_{e\gamma}/4\pi)$ is given by $(\Delta\Omega_{e\gamma}/4\pi) = (\delta\theta_{e\gamma})^2/4$, where $\delta\theta_{e\gamma}$ is the angular resolution.
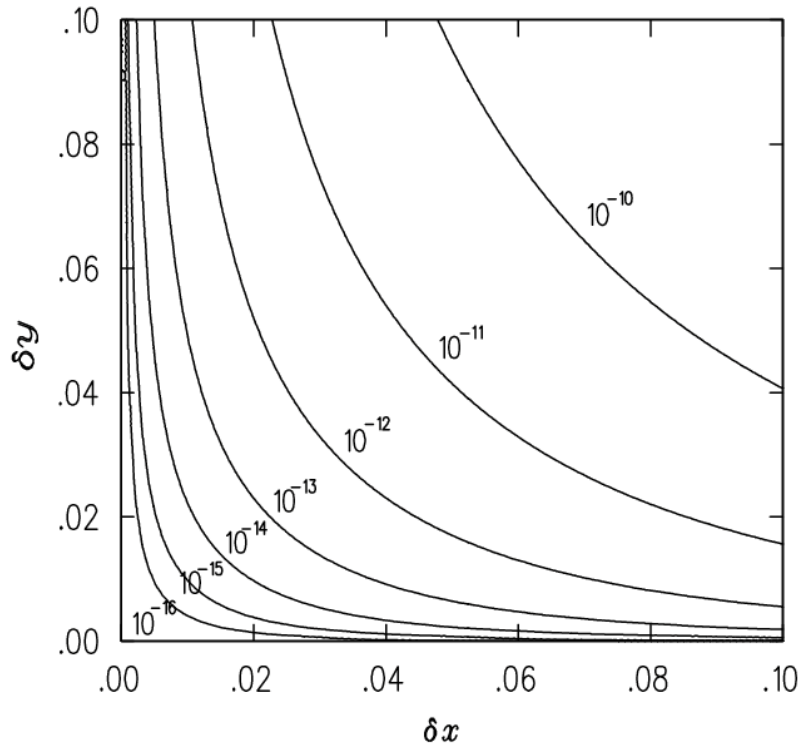
Figure 2.3: Branching ratio of the physics background from the muon radiative decay as a function of the e^+ energy resolution (δx) and photon energy resolution (δy). After [35]. For more details see also fig. 2.16.
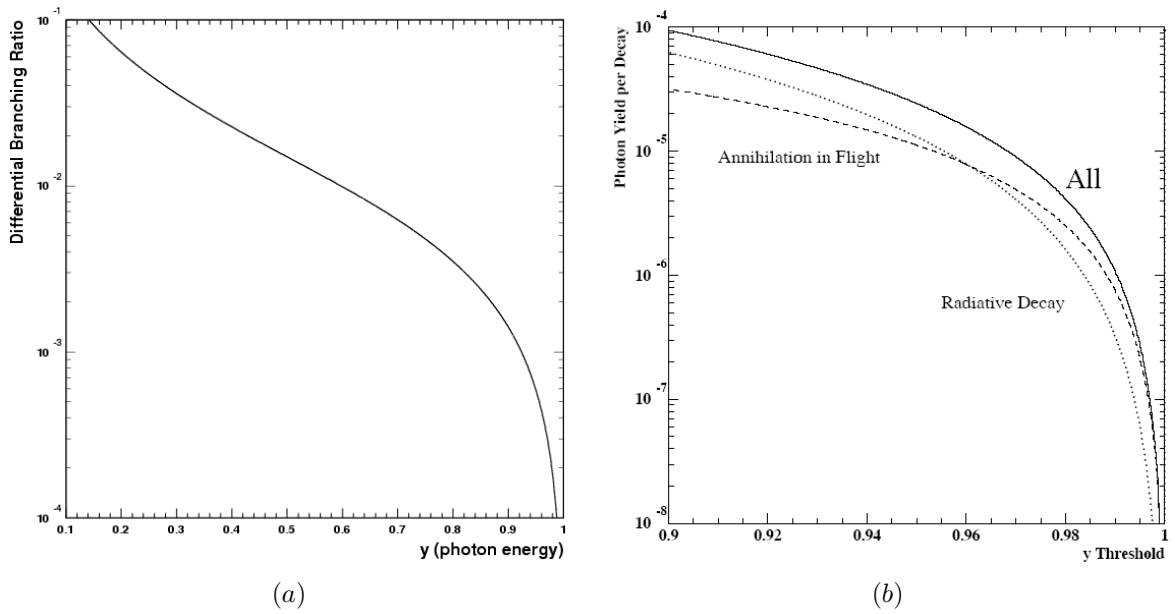
Figure 2.4: (*a*) Energy spectrum of the photon coming from the muon radiative decay ($y \equiv 2E_\gamma/m_\mu$). (*b*) Integrated rates of background from annihilation-in-flight (dotted line) and radiative muon decay (dashed line) as a function of the photon energy. The solid line shows the sum of the two. Both Figures are from [35].

If the radiative muon decay $\mu^+ \to e^+\nu_e\overline{\nu}_\mu\gamma$ is considered as a source of the 52.8 MeV photon, f_γ^0 is given by photon energy spectrum integration within the width of the signal region ($1 - \delta y \leq y \leq 1$). For unpolarized muons, it is given by [35]

$$f_\gamma^0 = \int_{1-\delta y}^{1} dy \int d(cos\theta_\gamma) \frac{dB(\mu^+ \to e^+\nu\overline{\nu}\gamma)}{dyd(cos\theta_\gamma)} \approx \left(\frac{\alpha}{2\pi}\right)(\delta y)^2\left[\ln(\delta y) + 7.33\right]. \tag{2.7}$$

From Equation (2.7), f_γ^0 for $\mu^+ \to e^+\nu_e\overline{\nu}_\mu\gamma$ decay is roughly proportional to $(\delta y)^2$.

The other sources of high-energy photons are annihilation in flight of e^+s in the normal muon decay and external bremsstrahlung. The contribution from annihilation of e^+ in flight depends on the materials along the material crossed from the e^+. Figure 2.4b shows the contribution of annihilation in flight for the case of e^+s passing through a Mylar muon-stopping target 150 μm thick. It indicates that the contribution from the target is smaller than the radiative muon decay, and only becomes important if the photon energy resolution becomes extremely good. However, it is dependent on the total amount of materials in an experimental setup.

From the above, the effective branching ratio of accidental background is given by

$$B_{acc} = R_\mu \cdot (2\delta x) \cdot \left[\frac{\alpha}{2\pi}(\delta y)^2(\ln(\delta y) + 7.33)\right] \times \left(\frac{\delta\theta^2}{4}\right) \cdot (2\delta t). \tag{2.8}$$

For instance, take some reference numbers such as the e^+ energy resolution of 1% (FWHM), the photon energy resolution of 6% (FWHM), $\Delta\Omega_{e\gamma} = 3 \times 10^{-4}$ steradian, $\Delta t_{e\gamma} = 1$ nsec, and $R_\mu = 3 \times 10^8$ μ^+/sec, B_{acc} is 3×10^{-13}. It is critical to make significant improvements in the detector resolution in order to reduce the accidental and physical background as we'll see in the next sections.

2.1.3   Background rejection

It's clear that the capability for an experiment to reject background events is related to its experimental resolutions on the photon and positron four momenta measurement.

The first experiments used spark chambers to detect the presence of both the positron and the photon [46, 60]; later on the configuration with two back-to-back large NaI crystals, became common [53, 54, 61, 62] allowing for a better energy and time determination. This technique was pushed to an extreme limit by the Crystal Box experiment where an almost 4π segmented NaI calorimeter surrounded the target region [56].

The number of produced pions and muons and their energy increases with the improving of producing tecniques. A larger particle flux requires a higher momentum for particles, which in turn, imply a thick target to bring stop them. An extremely good positron energy resolution was therefore not necessary because the target thickness usually contributed heavily to the positron energy loss. In the experiment at SIN [54] the energy loss in the target alone introduced a 4 MeV uncertainty in the positron momentum.

The introduction of "surface" muon beams [63, 64], originating from pions decaying on the

surface of a secondary target, brought low energy muon beams ($p = 28$ MeV) of high intensity, which could be stopped in thinner targets.

The use of a dipole spectrometer coupled to a hodoscope counter for the determination of positron momentum and timing was introduced in the $\mu^+ \rightarrow e^+\gamma$ search experiment at LAMPF [65]; in the MEGA experiment the photon was converted and measured with a pair spectrometer, and the positron with cylindrical tracking chambers in a solenoid magnetic field, hence the better energy resolutions shown in Table 2.1.

With a high intensity muon beam the capability of recognizing two coincident monochromatic photon and positron becomes essential. A thin target is the necessary choice for the precise measurement of the positron momentum with a magnetic spectrometer, while fast scintillators are able to provide extremely good timing for the positron.

The photon momentum and direction are well determined by a pair spectrometer, as in MEGA, but a thin converter is needed not to degrade the photon energy, therefore a low conversion efficiency is attained.

The time information provided by a NaI calorimeter is insufficient, because of its large decay time constant (470 ns). For this reason the MEG experiment proposes to use a liquid Xe (LXe) calorimeter, whose characteristics are comparable to NaI for luminosity, free from problems of non-uniformity and with far better timing capabilities (decay time of LXe is 4.2-22ns while NaI has a decay constant of 250-620ns).

2.2 $\mu^+ \rightarrow e^+\gamma$ experiment

The MEG experiment will operate on a low-energy muon beam line at the Paul Scherrer Institut located in Switzerland where the world most intense Direct Current (DC) muon beam (known as $\pi E5$ beam) is at present available. MEG has the aim to reach a sensitivity on the $\mu^+ \rightarrow e^+\gamma$ decay of 1.2×10^{-13} with an improvement of two orders of magnitude with respect to the actual limit, obtained by MEGA experiment in 1999 [66]. The coordinate system is such that the z-axis lies along the incoming beam direction. The plane perpendicular to this direction is called the $r - \phi$ plane, and we will use rectangular (x, y, z), cylindrical (r, z, ϕ) or spherical (ρ, θ, ϕ) coordinates to refer to the detector, depending on the convenience of the choice. In any case the origin of the reference system is in the center of the target, placed in the center of the detector ($x = y = z = 0$). The detector is designed to cover approximately 10% of the solid angle. Using the previously define reference system the photon acceptance is in the range $-60 < \phi < 60$ and $0.08 < \cos\theta < 0.35$.

As we saw before in a $\mu^+ \rightarrow e^+\gamma$ search experiment the accidental coincidence of a high energy photon and a high energy positron from two different muon decays represents the main source of background. Since each daughter particle comes from a different muon decay it increases quadratically with the *instantaneous* muon rate, The $\mu^+ \rightarrow e^+\gamma$ signal and the physics (prompt) background, conversely, increases only linearly because the two daughter particles have the same parent. For this reason the best choice for $\mu^+ \rightarrow e^+\gamma$ search is a continuous DC muon beam
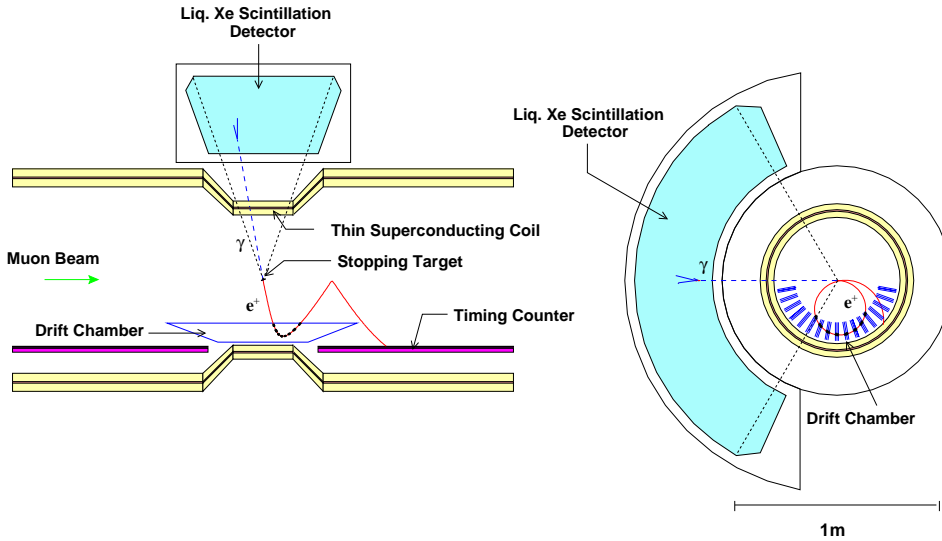
Figure 2.5: Layout of the MEG experiment

showing a lowest instantaneous rate rather than a pulsed beam.

This DC beam of $10^7 - 10^8 \mu/s$ is stopped in a thin polyethylene target. The MEG apparatus, covering ten percent of the solid angle, is optimized for the detection of a coincidence of a back-to-back, high energy positron and photon pair: the positron momentum is measured by a set of drift chambers placed in a inhomogeneous magnetic field and its timing is given by a scintillating bar timing counter.

The photon energy and time are measured by a ~ 0.8 m^3 liquid Xe scintillating calorimeter readout by 840 photo-multiplier tubes (PMTs). This calorimeter is located just outside a very thin-wall magnet called COnstant Bending RAdius (COBRA).

Positrons are tracked by drift chambers inside COBRA, which provides specially graded magnetic field. Their time is measured by plastic scintillation counters in the second turn of the helicoidal trajectories inside the COBRA.

A schematic view of the detector is shown in Figure 2.5.

2.3   Beam and target at PSI

The PSI cyclotron accelerator produces protons with an energy of 590 MeV. The proton beam, whose current maximum is 1.8mA, is transported to two meson production carbon targets in sequence, a thinner one called M-target (7 mm thick) and a thicker one called E-target ($40 - 60$ mm thick), before being stopped in a high power beam dump or refocused on the target of a high-flux spallation neutron source (SINQ) (figure 2.6 (a)).

The two targets are rotating truncated cones made of isotropic graphite (of semi-aperture α)

(a)

(b)

(c)
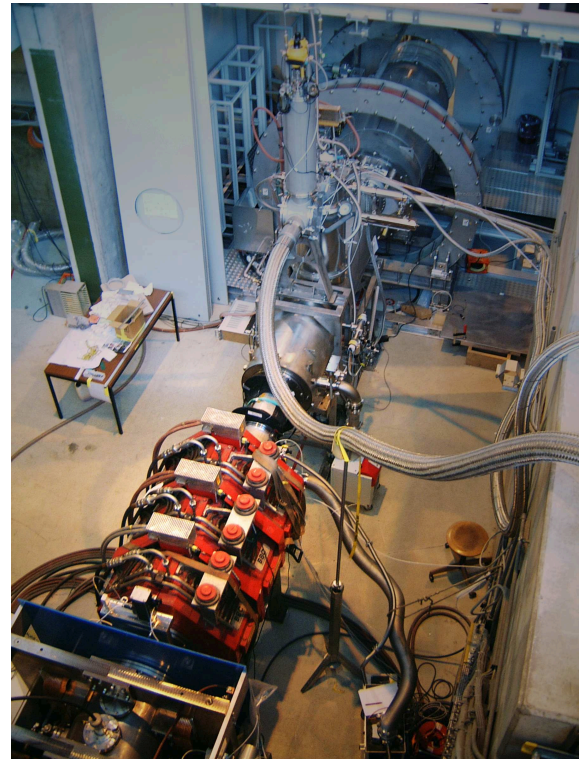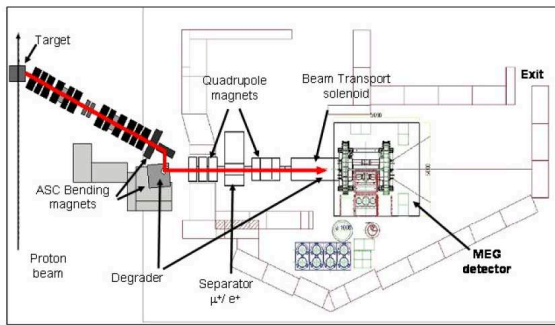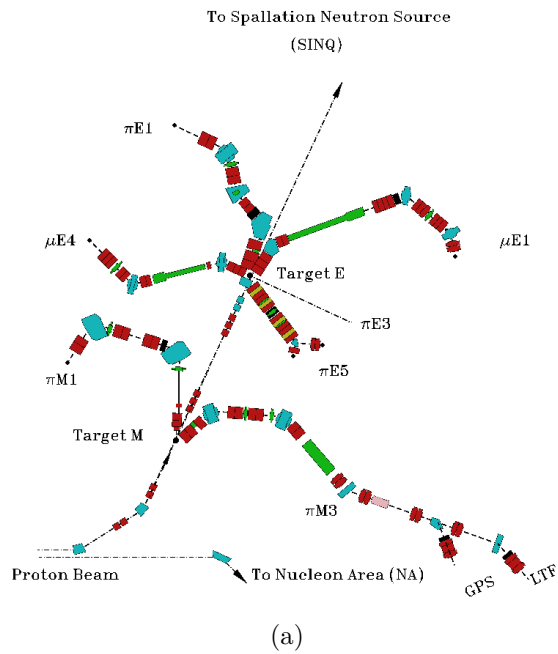
Figure 2.6: (a) The complete PSI beam line. (b)(c) The $\pi E5$ channel with the experimental area of MEG experiment.

solid angle acceptance	150 msr
momentum range	$20 \div 120$ MeV/c
length	10.4 m
momentum band (FWHM)	10%
momentum resolution (FWHM)	2%
horizontal emittance	15.3 cm·rad
vertical emittance	3.6 cm·rad
spot size	4×4 cm^2

Table 2.2: Main properties of the $\pi E5$ beam line

slanted at an angle α with respect to the beam axis in order to allow the incoming proton beam to uniformly hit the target surface, and the target surface to cool down by thermal radiation. Protons mainly produce charged pions which decay either in flight or in the target region, in turn generating muons and electrons of both charges. Seven beam lines branch out of the targets, and are named after the parent target (M, E). All secondary beam lines are available simultaneously.

The $\pi E5$ channel extracts low energy (10-120 MeV/c) positive charged pion and muon beams from the thick (E) production target at an angle of $175°$ with respect to the primary proton beam. The main characteristics of the beam are listed in Table 2.2. By tuning the $\pi E5$ beam line the so-called "surface" muons (coming from pion decay at rest of pions on the production target surface) are collected [63, 64]. Positive pions produced in the hadronic interactions may stop inside the proton target and decay to muons which may escape from the target with peak kinetic energy of 4 MeV (29 MeV/c momentum). These muons have a well determined momentum and polarization. However, the main drawback is the positron contamination which is high : $e^+/\mu^+ \sim 10$. These positrons arise from the decay of muons trapped in the E-target and from the conversion of photons from neutral pion decays. The positrons must be reduced to avoid their showing up in the positron spectrometer and to minimize the background of annihilation photons, if stopped in the experimental hall. So there are two objectives that must be reached: the reduction of positrons to a small fraction of muons flux and the reduction of the muon momentum in order to stop them in a thin target (150 μm). Consequently, the beam must be optimized as described below. The final setup of the $\pi E5$ beam line is shown in Fig.2.6 (b)(c).

There are two sets of quadrupole magnets and a solenoid magnet (inside this, there is a momentum degrader, that allows to reduce the μ^+ momentum) to couple the last quadrupole and the MEG magnet. An electrostatic separator is used as a velocity selector, to reject unwanted positrons in the beam. Indeed, the beam distribution intensity, after the separator, is split in two beams with Gaussian distribution of the intensity ($\sigma \sim$). The final separation between muons and positrons is $\sim 7.2\sigma$ [50]. Therefore, considering that the target size covers $\pm 2\sigma$ of the μ^+ distribution, the residual ratio e^+/μ^+ is given by the tail of the e+ distribution in the μ^+ beam. Being the $\pi E5$ e^+/μ^+ ratio ~ 10 with $N_e \sim 9.8 \times 10^8 e^+/s$ before the separator, the e^+ suppression factor introduced by the separator is 5.7×10^{-7}. In addition, the degrader inside the solenoid reduces

the positron contamination of the muon beam by a factor 9 [66]. Then we expect $\sim 60 e^+/s$ on the target with a residual ratio e^+/μ^+ of $\sim 6 \times 10^{-7}$. This way, the beam can be focused in ellipsoidal spot with horizontal and vertical profiles of $\sigma_x = 5.5$ mm and $\sigma_y = 6.5$ mm. In presence of helium gas, the profiles increase to a $\sigma_x = 10.0$ mm, $\sigma_y = 10.0$ mm. The introduction of surface muon beams allows to stop the muons in thinner targets. The target will be placed at a slant angle of $22°$, which corresponds to a slant ratio of $1/2.5$ in a He-gas atmosphere.

Several materials were considered, namely polyethylene $(CH_2)_n$, Mylar $(C_5H_4O_2)_n$ and Kapton $(C_{22}H_{10}N_2O_5)_n$, both for their stopping power and their short radiation length. Polyethylene was found to be the best material from both a background suppression and a beam quality point of view, mainly because of its larger radiation length [69].

Since the range of 29 MeV/c muons in polyethylene is about 1.1 mm, a 150 μm thick CH_2 target requires a ~ 700 μm thick polyethylene degrader to be placed along the beam line, in the last solenoid intermediate focus (the target is slanted, therefore the average muon path in a 150 μm target is of the order of 400 μm). The energy loss for positrons in a 150 μm polyethylene target is about 30 keV.

2.4   The photon detector

The precise measurement of the photon four-momentum is the key role of the MEG experiment photon detector, which is a ~ 0.8 m^3, C-shaped homogeneous scintillating liquid Xe calorimeter. Xe is a rare gas which is liquid at a comparatively high temperature (165 K), has a high atomic number, $Z = 54$, hence small radiation length $X_0 = 2.7$ cm, and its light yield is comparable to that of sodium iodide, but with a significantly lower emission time, of the order of tens of nanoseconds (compared to ~ 230 of NaI). Its scintillation peak is in the vacuum ultra violet (VUV) at 178 nm. The MEG calorimeter cryostat is placed just outside the COBRA magnet. It has a C-shape in order to minimize its volume and to have the photon impinging as perpendicularly as possible on its front face (see Figure 2.7). Its volume is read by 840 VUV-sensitive PMTs.

The photon parameters to be measured are its energy, direction and time. The energy is provided by the scintillation light collected by all PMTs. The photon is supposed to come from the same vertex of a companion positron on the target, and its direction is determined by looking at the interaction point on the calorimeter, extracted from the light distribution on the calorimeter front face. The light arrival time on all PMTs is used to extract the photon time.

The high light yield of Xe, comparable to that of NaI(Tl), and its uniformity are necessary ingredients for a good energy resolution. The scintillation pulse from Xe is very fast and has a short tail [51]. This allows to minimize the pile up problem of high rate γ-rays. The high atomic number and low radiation length X_0 of Xe, together with its high boiling temperature and the absence of radioactive isotopes make Xe the best choice for our scintillation detector.

The major limiting factor of this innovative detector is the absorption of the scintillation light inside Xe. Impurities in Xe, such as water and oxygen, reduce the light absorption length λ_{Abs}
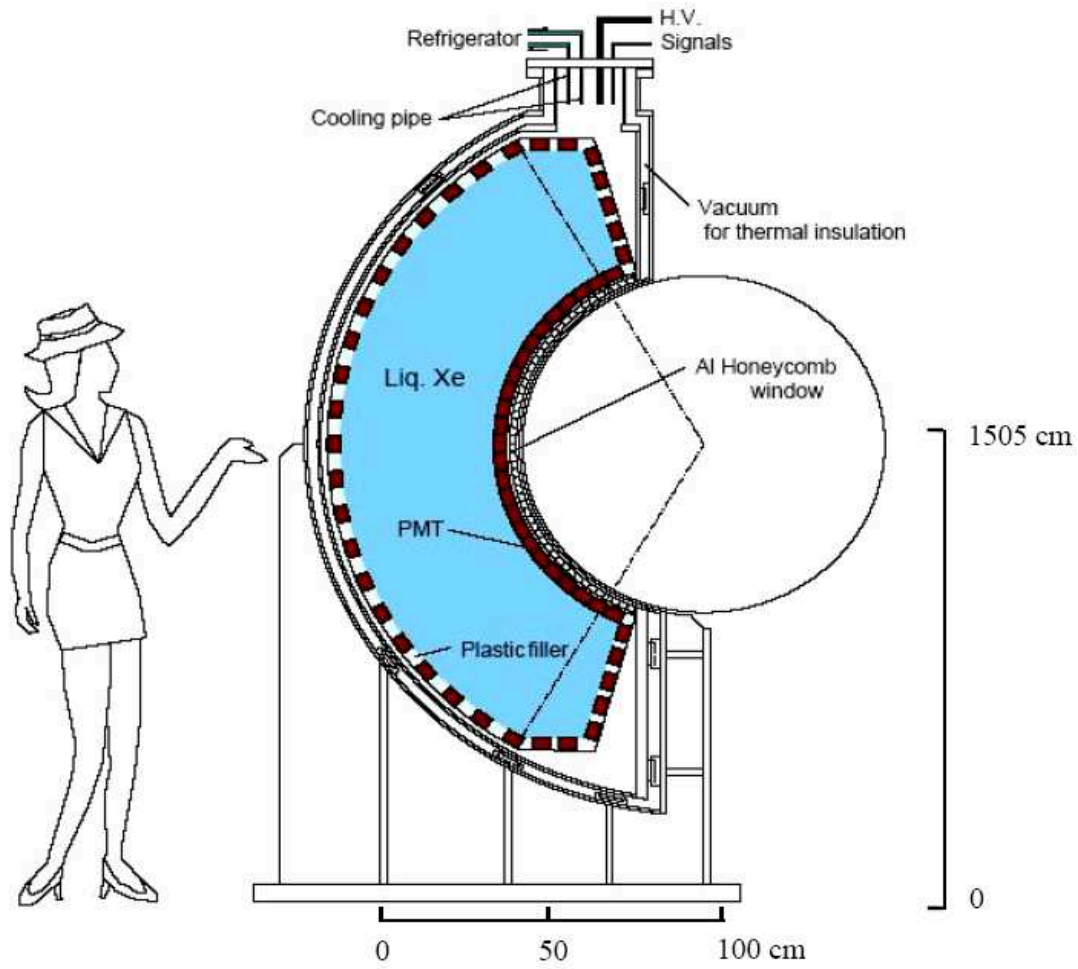
Figure 2.7: Schematic view of the liquid Xe photon detector

	Xe
ρ (g/cm^3)	2.98
Z	54
λ_{peak}	178 nm
boiling $T(K)$	167.1
dE/ dx (m.i.p.) (MeV/cm)	3.89
X_0 (cm)	2.77
Molière radius (cm)	4.1
τ_1 (ns)	4
τ_3 (ns)	22
τ_r (ns)	45
Light Yield	$\sim$ 42000 ph/MeV

Table 2.3: Main characteristics Xe. τ_1, τ_3 and τ_r are the singlet, triplet and recombination de-excitation time constants (see the text for details).

and degrade the detector performance. To study and to improve the energy and time resolution of this detector, a small prototype of 0.1 m^3, surrounded by more than 200 PMTs and called Large Prototype (LP), has been built and tested. PMTs, developed in cooperation with Hamamatsu Photonics, are sensitive to the UV scintillation light ($\lambda = 178$ nm) and can operate at the *Xe* temperature ($T \sim -100°C$). The first absorption length measurements indicated a length shorter than 10 cm. To remove the water contamination, an additional gas system was installed to circulate and purify *Xe*, with a gas getter purifier. The purification takes so long time because of large release of contaminants by the cable materials, PMTs and ancillaries. Light absorption was monitored by blue LEDs, cosmic-rays and alpha sources. After one month of circulation, light absorption length improved from 7 to more than 100 cm. Assuming a 100 cm absorption length, a Monte Carlo simulation predicts an average energy resolution of 5% for γ-rays uniformly entering the detector with an energy of 52.8 MeV. This value can be improved to 4% by exploiting the knowledge of the photon conversion point [115]. During the MEG experiment run, several methods will be used to calibrate and monitor the stability of the calorimeter, for example to study the time dependent attenuation length for the scintillation light or to monitor the quantum efficiencies of all PMTs; all these items are necessary to control the energy and time resolution [141]. Since the calorimeter has a big homogeneous volume we expect a high rate of low energy photons: it is therefore necessary to collect the waveform of every PMT to reject events in which pile-up between different γ-rays occur.

2.5 The positron detector

Positron tracks are measured by drift chambers inside an inhomogeneous magnetic field. The positrons eventually hit the scintillating bars of the timing counter.

(a)   (b)
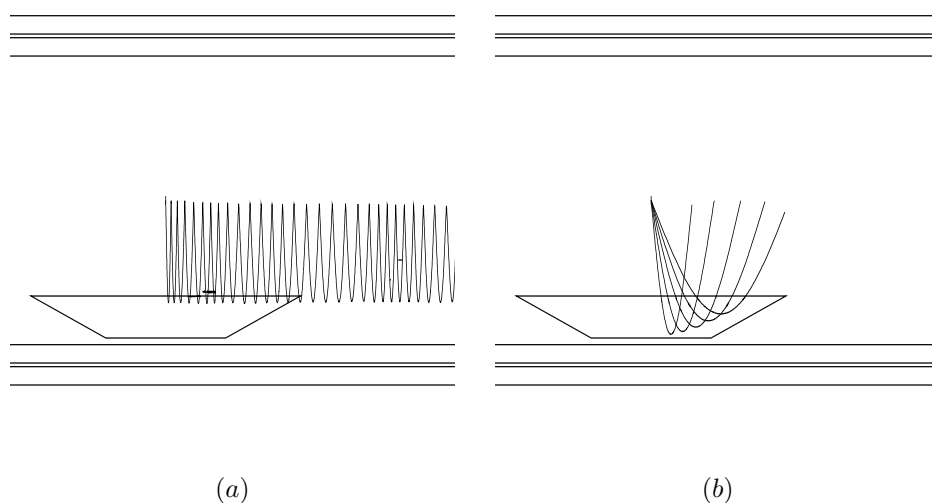
Figure 2.8: Particle trajectory in a uniform solenoidal magnetic field:
(a) $r - z$ view of the solenoid shown with the trajectory of a particle emitted at 88° making many turns inside the detector.
(b) Trajectories of monochromatic particles emitted at various angles. The bending radius depends on the emission angle.
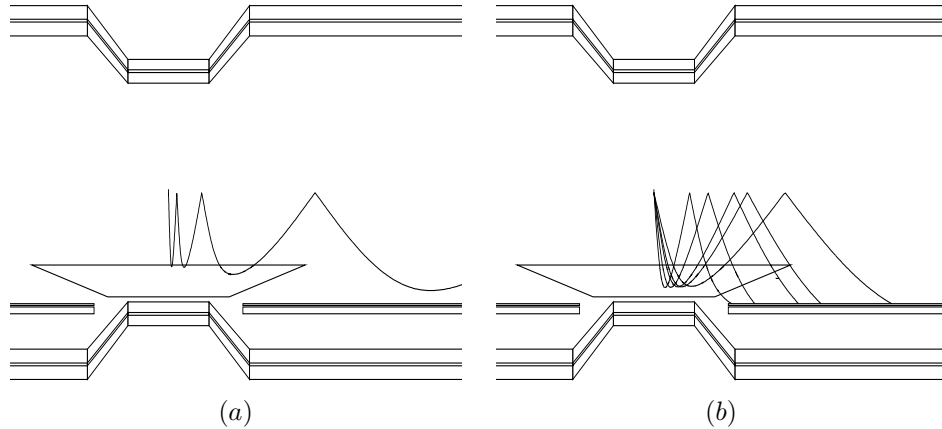
Figure 2.9: Advantages of a gradient magnetic field:
(a) $r-z$ view of the COBRA spectrometer shown with the trajectory of a particle emitted at 88°. The particle is swept away much more quickly than in Fig. 2.8.
(b) Trajectories of monochromatic particles emitted at various angles. The bending radius is independent of the emission angle.

As shown in Figure 2.8 and 2.9, in a conventional solenoid, positrons with high transverse momentum (p_t), emitted close to 90° with respect to the solenoid axis, make many turns in the drift chambers. The bending radius of positrons with a given absolute momentum is determined by its p_t, which makes difficult to select the positron by momentum reconstruction. This was the choice on the MEGA experiment, which suffered of the trapping of positrons emitted at large angles.

In a decreasing magnetic field high-p_t positrons are quickly swept away from the detector center, after one or two turns in the drift chamber zone. The field can be shaped so as to make the projected radius depend on the *absolute* value of the momentum, p, and not on its transverse component only, over a wide angular range as shown in Fig. 2.8(b). This way low momentum tracks are confined inside a cylindrical shell and the reconstruction of higher momentum tracks is greatly simplified by this feature, since the spread in the projected radius for particles with the same momentum depends almost exclusively on the beam spot on the thin target giving a different starting point for the trajectory.

2.5.1   The COBRA magnet

The inhomogeneous field is generated by a thin superconducting magnet called COBRA (COnstant Bending RAdius). The field, as stated before, is designed to achieve the good features of the positron spectrometer such as the constant bending radius of the positrons and the quick sweep of them. In addition the magnet is mechanically designed to be as transparent as possible to 52.8 MeV γ-rays directed towards the photon calorimeter.

Coil	Central	Gradient	Inner end	Outer end	Compensation
Conductivity	Super	Super	Super	Super	Resistive
Inner dia. (mm)	700	810	920	920	2210
Outer dia. (mm)	712.4	820.6	929.5	929.5	2590
Length (mm)	240.3	110.4	189.9	749.2	265
Layers	4	4	3	3	14
Turns per layer	267	123 (1st) 92 (2nd-4th)	80	624 (1st-2nd) 92 (3rd)	20
Turns (total)	1068	399	240	1548	280
Winding	edge-wise	edge-wise (1st) flat-wise (2nd-4th)	flat-wise	flat-wise	double pancake
Inductance(H)	1.64	0.62	0.35	2.29	0.54
I_{op}(A)	360	360	360	360	360
Energy E (kJ)	106	40	23	148	35
Weight M (kg)	9	4	7	28	1620
E/M (kJ/kg)	11.8	10.0	3.3	5.3	0.02

Table 2.4: Parameters of the COBRA magnet

The COBRA magnet is composed of five coils of three different radii: a central coil, two gradient coils and two end coils.

The parameters of the super-conducting cable and of the three types of coils are summarized in Table 2.4.

The cable consists of a Niobium-Titanium multi-filament wire embedded in a copper matrix, extruded in a rectangular, 1.2×0.9 mm^2, aluminum support cable. The current density variation in the coils is obtained by varying the winding pitch, the number of winding layers and the orientation of the super-conducting wire [52].The superconductivity windings are cooled by means of mechanical cryocoolers.

To reduce the stray field in the calorimeter zone to a level tolerable by the photo-multipliers, two resistive (*i.e.* non super-conducting) compensation coils are used. These are two large (120 cm radius) coils placed at both extremities of the COBRA magnet to reduce the field in the calorimeter zone to less than 50 Gauss.

The total equivalent thickness of the central part of the magnet is 3.83 g/cm^2 which corresponds to 0.197 radiation lengths. Therefore the conversion probability on the magnet for a 52.8 MeV photon is 18%. The COBRA magnet is already placed in the experiment area and has been successfully tested.

Figure 2.10: The COBRA magnet. Two large coils around the main magnet are to compensate and suppress the magnetic field at the L*Xe* detector.
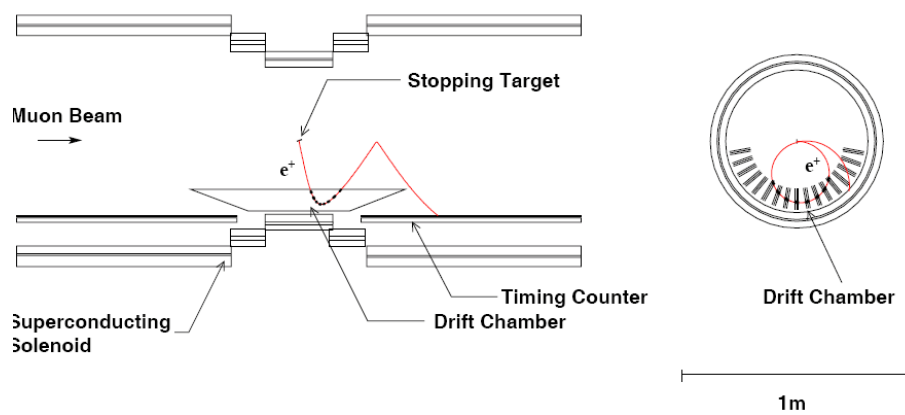
Figure 2.11: Schematic view of the positron spectrometer
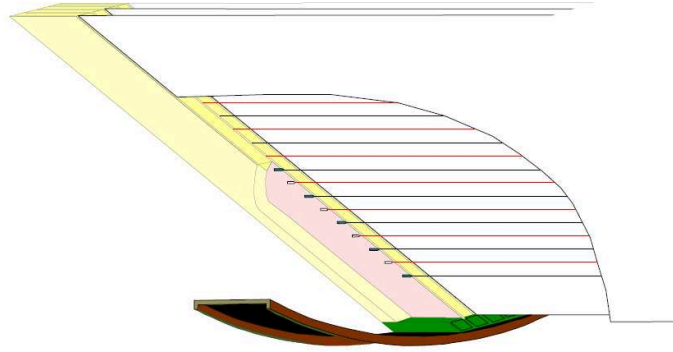
Figure 2.12: Schematic view of single array of DC.

2.5.2   The Drift Chambers

Positron tracks are measured with 16 trapezoidal drift chamber (DC) sectors aligned radially at
10.5° intervals in azimuthal angle. Each DC module consists of two layers of axial sense wires and
potential wires stretched with 4.5 mm pitch on a carbon-fibre frame. Each layer is isolated by
a ultra-thin cathode foil and shifted by one-half cell to resolve left-right ambiguity. A schematic
cross-sectional view of a part of single chamber module is shown in Figure 2.13(b), while Figure 2.12
shows a logitudinal section (along the z axis). The chamber wall is made of an extremely thin,
12.5 μm thick, plastic foil with aluminum deposition (2500 10^{-10}m). The frame of drift chamber
is shaped without any structure (Fig. 2.12), to have the minimum possible amount of material;
the average material in the volume amounts to 0.002 X0 for the signal positron (52.8MeV/c)
trajectory. The staggered-cell configuration allows for the measurement of the radial coordinate
and the absolute time of the track simultaneously. The difference between the drift times $(t_1 - t_2)$
in two adjacent cells gives the r-coordinate of the track with a ~ 150 μm accuracy, while the mean
time $(t_1 + t_2)/2$ gives the absolute time of the track with ~ 5 ns accuracy. This excellent time
resolution is important for the pattern recognition. The ratio of the charges observed at both ends
of a sense wire gives the z-coordinate with a ~ 1 cm accuracy. The pads have a *Zig-Zag* Vernier
shape [44], so that the ratio of the charges on the Vernier pads allows to define the z-coordinate
with an accuracy of about 300 μm [70] (Figure 2.13 (c)). A comparison between the induced
charges on different pads considerably improves the resolution in the longitudinal (z) direction.
The sensitive area of the chamber extends from a radius of 19.3 cm to 27.0 cm. In the z-direction
the active region extends up to $z = \pm 50$ cm at the innermost radius and $z = \pm 21.9$ cm at the
outermost. The chambers are filled with a 50% Helium, 50% Ethane mixture at 1Atm, chosen to
have sufficient ionization loss in the gas minimizing the multiple Coulomb scattering of tracks. In
fact as long as the position resolutions are at the 300 μm level, momentum and angular resolutions
are primarily limited by multiple scattering in the gas and also by chamber material.

The expected resolutions of the spectrometer have been studied with GEANT simulations
by incorporating detailed material distribution. 52.8 MeV positrons were generated and their
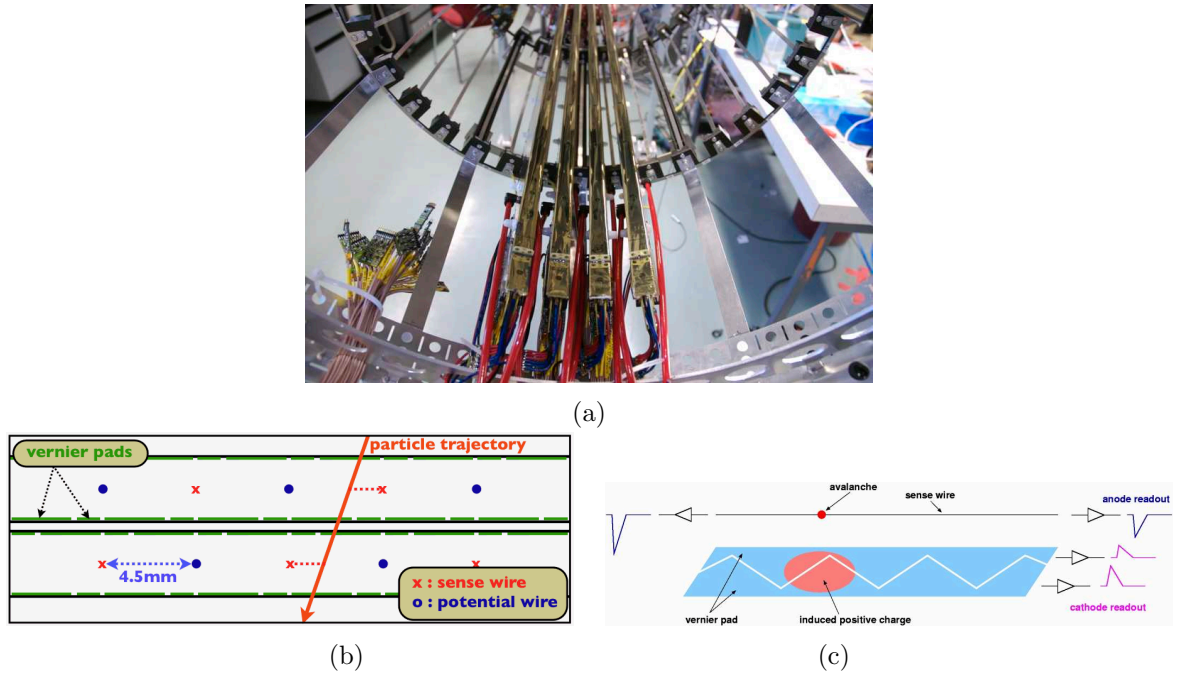
Figure 2.13: Drift Chambers view: (a)Installation, (b)cell section with wire scheme and (c) scheme of Vernier pad method.

trajectories reconstructed using several methods. The fractional momentum resolution turns out to be $\Delta E/E = 0.9\%$ FWHM and the angular one 12 mrad. The positron origin on the target can be reconstructed with a 2.5 mm resolution.

2.5.3 The Timing Counter

After leaving the drift chambers the positrons hit the Timing Counter detector that provides a fast signal from positrons in order to obtain both a very precise (Δt=100 ps FWHM) determination of the istant in which the particle emerges from the target and a reliable detection of positron-photon coincidence for triggering purposes. There are two identical Timing Counter modules, placed in symmetrical position with respect to the axis origin. They are placed on the inner surface of the two outermost coils of the COBRA in a position that allows for the detection of positrons emitted within the γ acceptance of the calorimeter. Each Timing Counter module consists in a longitudinal detector (Fig. 2.14) which is optimized for timing purposes, and a transverse one that is intended to provide the triggering signal for the DAQ system. The latter is located in the inner zone at a radius r =280 mm while the "average" radius of the longitudinal detector is 315 mm. Each longitudinal detector is an assembly of 15 scintillator bars whose light output is read by two photomultiplier tubes (PMTs), one at each end. For the transvers detector the PMT readout was found not to be possible due to the strong magnetic field in the zone of the detectors, so we developed a structure

(a)   (b)
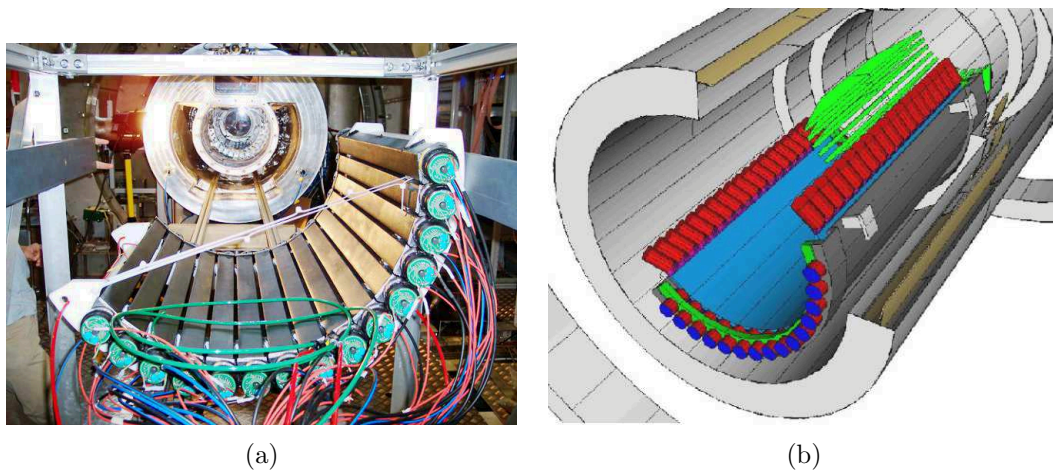
Figure 2.14: Timing Counter bars (a) during a PSI test, just in front of Cobra Magnet waiting for insertion, (b) preliminary CAD view.

made of scintillating fibers with an APD (avalanche photodiode) readout. The Timing Counter will be reviewed in deeper detail in Chapter 3.

2.6   Trigger and data acquisition system

The signature of a $\mu^+ \to e^+\gamma$ decay is a back-to-back photon-positron pair coincident in time, each of energy equal to half of the muon mass (52.8 MeV energy particles with opposite momenta). The information available at trigger level comes from the liquid Xe detector and from the timing counter. The signal from the drift chambers is avalaible with some delay ~ 100 ns, due to the electron drift time in the cells and therefore the drift chambers cannot be used for a fast first level trigger.

All the trigger system is based on VME boards equipped with Field Programmable Gate Arrays (FPGAs), which digitize the output of both the photon detector and the timing counter photo-multipliers and perform basic event reconstruction. The trigger boards perform PMT equalization and a 100 MHz waveform digitization, necessary in particular for the signal from the calorimeter in order to have an on-line subtraction of the pedestal and rejection of the common noise.

The photon energy is determined by the sum of the light collected by all PMTs, while its direction is determined by the position of the PMT with the largest signal, which is sufficient for trigger purposes. By setting a threshold level of at least 45 MeV of energy release in the LXe calorimeter, the estimated γ rate is given by:

$$R_\gamma = R_\mu \, f_\gamma \, \frac{\Omega}{4\pi} = 2.4 \text{ kHz} \tag{2.9}$$

where $R_\mu = 10^8 \; \mu^+/$s is the muon stopping rate, the solid angle fraction $\Omega \setminus 4\pi$ is 12%   and

$f_\gamma \sim 2 \cdot 10^{-4}$ is the fraction of background photons per stopped muon that satisfies this selection criterion.

The presence of a time-coincident positron is provided by the timing counter: its radial position already excludes most of low momentum positrons. The overall rate on each of the two timing counters due to Michel positrons is estimated to be $R_{TC} = 2 \times 10^6$ Hz for a muon stopping rate of $R_\mu = 10^8$ μ^+/sec (4% of the Michel positrons hit either timing counter). The azimuthal segmentation of the timing counter allows for a correlation of the positron direction with that of the photon, with a rejection factor of $f_\phi \simeq 5$.

If we define a coincidence window of $\Delta t = 10$ ns the trigger rate for the uncorrelated background is

$$R_{\text{trig}} = 2\Delta t\, R_\gamma\, \frac{R_{TC}}{f_\phi} \left(\frac{R_\mu}{10^8}\right)^2 \simeq 20 \text{ Hz} \left(\frac{R_\mu}{10^8}\right)^2 \tag{2.10}$$

The estimated trigger rate provides some margin in the case of other possible contributions to the background not taken into account The trigger system is based on a fast logic processor built with Field Programmable Gate Arrays (FPGAs) on Virtual Machine Environment (VME) boards. The trigger inputs are the digitized signals of the LXe and timing counter PMTs. This allows complex trigger solutions and improvements during the course of life of the experiment. The clock frequency of the trigger system is 100 MHz.

Being MEG a high rate experiment, the pile-up discrimination efficiency is a crucial parameter. In order to maximize it, it was proposed to digitize each signal for a carefully off-line analysis. Accordingly, the signals from all PMTs and from the drift chambers will be individually digitized by a custom chip, called Domino Sampling Chip (DSC). A "domino" wave runs circularly along a loop of 1024 capacitors which are sequentially cleared and opened to sample the incoming signal. When a trigger occurs, the domino wave is stopped and the charges collected on all capacitors are sequentially read out and digitized. This digitization method constitutes a sort of analog pipeline which minimizes the use of delay cables.

The signals will be digitized at 2 GHz (500 ps bin width) in order to be able to obtain a time resolution of 50 ps by bin interpolation [66], necessary for the positron timing counter and for the LXe calorimeter.

Wave-form digitizing on all channels gives an excellent handle on event pile-up and noise suppression, although the amount of data is large (~ 1.6 Mb per event). Studies are under way to reduce or compress the raw data.

For the $\mu^+ \to e^+\gamma$ experiment, the Data Acquisition (DAQ) is based onto the software framework, called MIDAS DAQ system [125]. Besides all the necessary means of data readout, transport and storage, MIDAS contains a full slow control system, an integrated data analysis functionality and a Web interface for remote control. The slow control system includes the measurement and control of environment variables such as temperature, pressure and humidity, as well as the control of high voltage channels (more than 900) for PMTs, wire chambers, superconducting solenoid and Xe calorimeter.

Quantity	resolution	value	uses MC	uses data
Photon detector energy resolution	δy	0.035		$\checkmark$
Positron energy resolution	δx	0.006	$\checkmark$	
Relative time resolution	$\delta t_{e\gamma}$	105 ps	$\checkmark$	$\checkmark$
Relative angle resolution	$\delta\theta_{e\gamma}$	23 mrad	$\checkmark$	$\checkmark$
"	δz	0.012	$\checkmark$	

Table 2.5: The resolutions on the various kinematical quantities of the positron-photon pair used to compute the expected sensitivity of the MEG experiment to the $\mu^+ \rightarrow e^+\gamma$ branching ratio. See the text for details.

2.7   Sensitivity in MEG experiment

2.7.1   Experiment resolution

The detector acceptance defined by the positron spectrometer and the liquid Xenon detector is $0.08 <| \cos\theta |< 0.35$ and $-60° < \phi < 60°$, amounting to $\Omega/4\pi = 0.09$.

For a given signal branching ratio B_{sig}, the number of observed events can be written as

$$N_e = R_\mu T \frac{\Omega}{4\pi}\epsilon_e\epsilon_\gamma\epsilon_{\text{cut}} B_{sig} \tag{2.11}$$

where R_μ is the muon stopping rate, T is the measuring time, Ω is the detector solid angle (we assume identical values for the photon and positron detectors), ϵ_e and ϵ_γ are the positron and photon detection efficiencies (we assume $\epsilon_e \approx 0.9$, $\epsilon_\gamma \approx 0.65$ due to the probability of gamma conversion in the materials before the liquid Xe volume, whose thickness amounts to 0.44 X_0) and ϵ_{cut} is the efficiency of the selection cuts. Those cuts can be applied on the reconstructed positron energy (E_e) photon energy (E_γ) opening angle ($\theta_{e\gamma}$) and relative time ($t_{e\gamma}$), and define the signal region.

The selection cuts must be chosen so as to keep the background within this region at a negligible level, and are therefore dependent on the detector resolutions. If we apply 90% efficient cuts on the four quantities (corresponding to 1.4 FWHM for Gaussian-distributed variables) $\epsilon_{\text{cut}} = (0.9)^4 = 0.66$.

As we stated in Chapter 2.1.2 the background is dominated by accidental coincidences of Michel positrons, close to the spectrum endpoint, with high energy photons from muon radiative decay or positron annihilation-in-flight.

The detector resolutions are summarized in Table 2.5, where δ means the half-width of a 90% efficient region.

- The photon energy resolution $\delta y = 0.035$ arises from a 90% efficient cut on a photon distribution with a 5% FWHM, which is the result obtained at the charge exchange test [115];

- The e^+ energy resolution value, $\delta x = 0.006$ is taken from MC simulation;
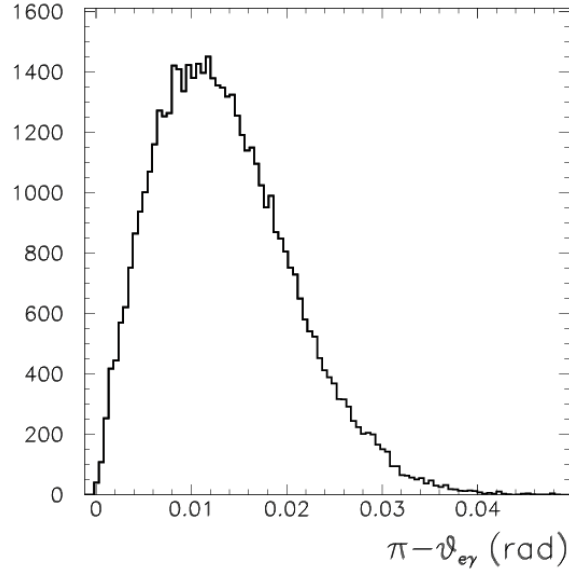
Figure 2.15: 90% efficient cut on the distribution of the positron-photon relative angle $\pi - \theta_{e\gamma}$.

- The relative time resolution, $\delta t_{e\gamma} = 150$ ps, is the average of the range quoted in [115], and is given by the convolution of the measured time resolution of the LXe and timing counter (including the contribution of the position resolution);

- The relative direction resolution is computed by folding the drift chamber resolution (12 mrad) with the curved calorimeter expected resolutions ($\sigma_\phi = 7$ mrad, $\sigma_\theta = 6.5$ mrad confirmed by the measurement at TERAS): two collinear but opposite vectors have been randomly displaced according to those resolutions, and their relative angle $\theta_{e\gamma}$ has been computed. The 90% efficient cut on the $\pi - \theta_{e\gamma}$ distribution is given by $\delta\theta_{e\gamma} = 0.023$ mrad (see Figure 2.15);

Now we can compute the expected background, and then state the required muon flux and running time to perform a sensitive search for the $\mu^+ \to e^+\gamma$ decay.

2.7.2 Background evaluation

The physics background branching ratio can be computed from the $\mu \to e\gamma\bar{\nu}\nu$ decay width. Two forms exist (ref.2.1.3), depending on whether the angular resolution is better or worse than the energy ones ($\delta z \lessgtr 2\sqrt{\delta x \delta y}$). In either case the contribution to the background is negligible, as clear observing Figure 2.16a and b. In our situation $\delta z = 0.012 < 2\sqrt{\delta x \delta y} = 0.028$, hence we must refer to Figure b. The contribution of the physics background to the branching ratio is $< 3 \times 10^{-15}$.

(a)   (b)
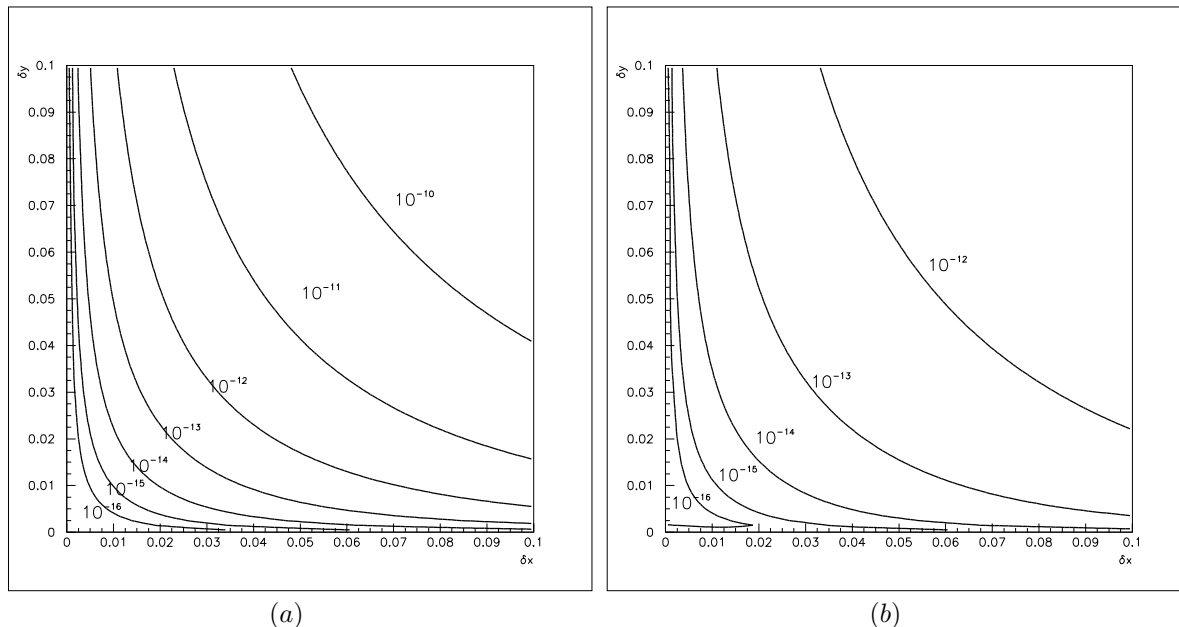
Figure 2.16: Computation of the dependence of the physics background branching ratio on the positron and photon energy resolutions in the case $\delta z > 2\sqrt{\delta x \delta y}$ (a) and $\delta z < 2\sqrt{\delta x \delta y}$ (b). To obtain this latter plot we assumed $\delta z = 0.012$.

The contribution of accidental coincidences is (as shown in 2.1.2)

$$B_{acc} = R_\mu \cdot (2\delta x) \cdot \left[\frac{\alpha}{2\pi} (\delta y)^2 (\ln(\delta y) + 7.33) \right] \times \left(\frac{\delta\theta^2}{4} \right) \cdot (2\delta t). \qquad (2.12)$$

For sake of convenience we define the branching ratio for which the observed number of events is exactly $N_e = 1$, all the other quantities being known, as the *single event sensitivity* (SES) of the experiment. We want to keep the number of expected accidental background events, given by B_{acc} divided by the single event sensitivity, [1] at the level of $N_{acc} \sim 0.5$ events. Fig. 2.17a shows B_{acc} as a function of the photon and positron energy resolution for a muon rate of 2.2×10^7 μ/sec, while Figure 2.17b shows the expected number of background events as a function of the muon stopping rate R_μ and measuring time T, for the resolutions quoted in Table 2.5.

2.7.3   Conclusions

The choice of the values of the muon stopping rate R_μ and the measuring time T is dictated by a compromise between the need to perform the experiment in a reasonable time and having a good single event sensitivity. The single event sensitivity [66] (which does not depend on the resolutions) is a function of the muon rate and of the running time. A reasonable choice, $R_\mu = 1.2 \times 10^7$ μ/sec, $T = 3.5 \times 10^7$ sec, yields a SES of 6×10^{-14}. It is clear that, due to the R_μ^2 dependence of the

---

[1] This number therefore scales with $(R_\mu)^2$.

(a) (b)
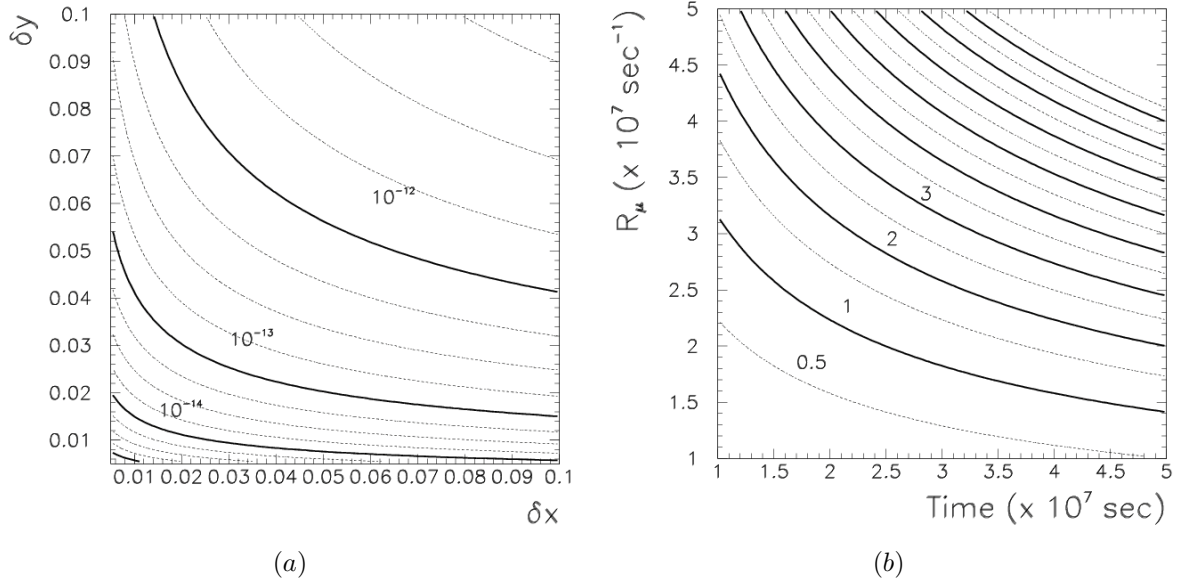
Figure 2.17: (a) B_{acc} as a function of the photon and positron energy resolution at $R_\mu = 2.2 \times 10^7 \text{ sec}^{-1}$; (b) Number of expected background events as a function of the muon stopping rate R_μ and measuring time T, for the resolutions quoted in Table 2.5.

(a) (b)
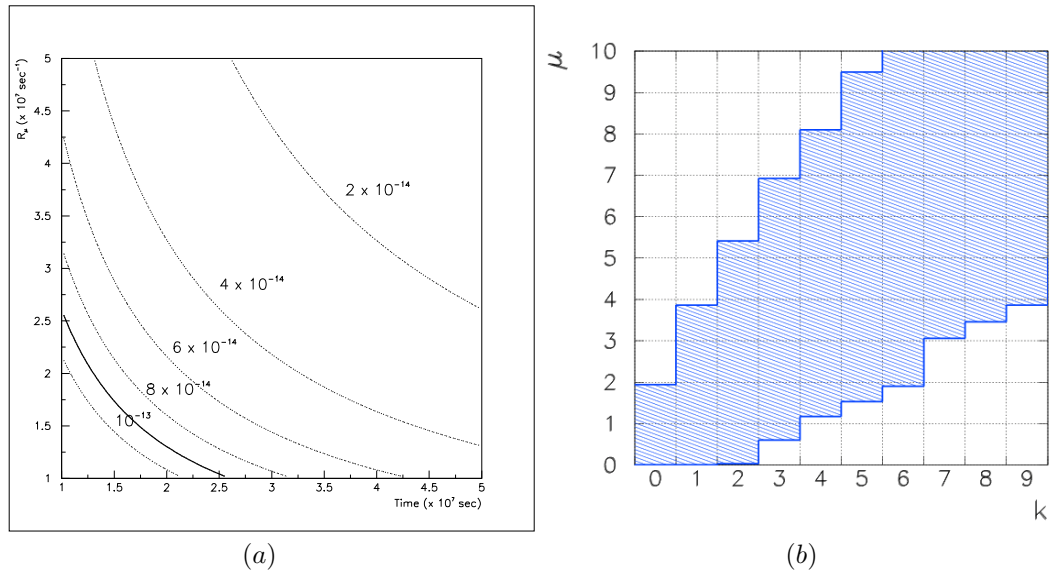
Figure 2.18: (a) Single event sensitivity as a function of the muon rate and of the running time; (b) the 90% frequentist confidence band for the average μ of a Poisson process when a number k of events is observed, in the presence of a background of 0.5 events calculated using the Feldman-Cousins ordering prescription [154],

accidental background, for a given number of accepted background events it is more convenient to run for a longer time at a lower beam intensity, because the SES increases.

We must emphasize that $= 6 \times 10^{-14}$ is *not* the sensitivity to the $\mu^+ \to e^+\gamma$ decay as defined previously (the 90% confidence level band and extract the limit on the $\mu^+ \to e^+\gamma$ decay in case of no candidate observed). In Figure 2.18*b* we show the confidence band calculated, in a frequentist framework using the Feldman-Cousins ordering prescription [154], for a Poisson-distributed signal over an expected background of 0.5 events. In case of no candidate observed ($k = 0$ on the $x-$axis) the 90% CL region yields $N_{\mu^+ \to e^+\gamma} < 1.98$ that, at a SES of 6×10^{-14} implies a limit on the $\mu^+ \to e^+\gamma$ branching ratio of [154]

$$BR(\mu^+ \to e^+\gamma) < 1.2 \times 10^{-13} \quad @90\% \text{ CL.} \tag{2.13}$$

A discovery can be claimed at this CL after an observation of at least three candidates, in which case the limit would be

$$4.2 \times 10^{-14} < BR(\mu^+ \to e^+\gamma) < 4.2 \times 10^{-13}.$$

A similar result may be obtained in a intuitive manner with the following reasoning: one is sensitive to $\mu^+ \to e^+\gamma$ branching ratios that yield a number of events in the signal region which is, say, 3σ higher than the expected background. Since the expected background is 0.5 events we ought to observe $0.5 + 3 \times \sqrt{0.5} \simeq 3$ events at least in order to make the statement of the 3σ discovery of the $\mu^+ \to e^+\gamma$ decay. And three events at the aforementioned SES imply that one is sensitive to branching ratios of the order of 1.8×10^{-13}.

It is clear that the number of background events entering the signal region can vary in case of time dependence of the detector resolutions, *e.g.* given by a time-dependent attenuation length for the scintillation light in xenon. It is therefore necessary to have a continuous and reliable monitoring system of all the experimental resolutions involved in the determination of the signal region .

Part III

The Timing Counter

Chapter 3

The Timing Counter: studies and development.

In the following chapter we will be present the details of the
MEG Timing Counter detector, the simulations which led to
the final design and the tests performed on both of the Timing
Counter sub-detectors. The tests started on different geome-
tries of the timing counter bars and on different types of PMTs
to define the best properties for timing and to proceed to the
design of the final detector. We will go through details of the
measurements executed on a single bar, on photomultiplier tubes
and eventually on a complete set of bars with PMTs in the final
configuration. We will also give details on the TC impact point
sub-detector, we will explain how scintillating fibers and APDs
play a key role in its operations. We will analyze the motivation
for the choice of the actual geometry and materials of both sub-
detectors. Eventually we will go through the resolutions and
efficiencies achieved during the test. Measurements were car-
ried out using the PSI site and the Beam Test Facility (BTF) of
Laboratori Nazionali di Frascati (LNF) and the simulation have
been developed on the Rome farm.

3.1   Introduction: scintillation Counters

In a scintillation counter the signals from each photomultiplier can be pulse height analyzed. The
arrival time is measured by first transforming it to a standard logic pulse into a discriminator and
then using this pulse to start and stop a fast digital clock (TDC). If t_1 and t_2 are the respective
signal arrival times from the discriminators connected to each end of the scintillator then the

location along the scintillator where the particle impinged the counter is given by (placing x=0 in the middle)

$$x = (\frac{t_1 - t_2}{2})v_{\text{eff.}} \tag{3.1}$$

$v_{\text{eff.}}$ is the effective propagation velocity of light in the scintillator and t_1 and t_2 are assumed to be corrected for additive constants arising from delay cables, or light guides (if present) delay time, etc. The time of penetration is

$$\tau = (\frac{t_1 + t_2}{2}) - \frac{L}{2v_{\text{eff.}}} \tag{3.2}$$

where L is the length of the scintillator. From Eq. (3.1) we see that x is independent of τ and similarly from Eq. (3.2) that τ is independent of x. Now let us consider what some of the sources for fluctuation in τ may be. The scintillator light results from energy lost by particles that penetrate it. Approximately one photon is produced for every 100 eV of energy deposited. For plastic scintillator a minimum of $2MeV$ of energy is deposited per cm traveled for particles with unit charge which results in about $20,000$ photons/cm being produced. The light is transmitted to the photomultiplier via the scintillator plastic and a light pipe may couple the round face of the photo tube onto the usually rectangular scintillator cross-section. The "straight shot" light produced in the middle of the counter will require a time,

$$t_{min} = \frac{L}{2} \times \frac{n}{c} \tag{3.3}$$

to reach the photomultiplier. In Eq. (3.3) n is the refraction index for the scintillator we can take a value of 1.58 which is the case of BC404: a common scintillation material. If the maximum angle away from the "straight shot" direction that light can make is given by the total internal reflection angle:

$$\theta_{\text{int}} = sin^{-1}(\frac{1}{n}) \tag{3.4}$$

then the maximum time for light transmission is:

$$t_{max} = (\frac{1}{cos(\theta_{\text{int}})})t_{min} \simeq 1.3t_{min} \tag{3.5}$$

Equations (3.3) and (3.5) show that the light emerges over a time interval approximately equal to $0.3\ t_{min}$. This time interval is proportional to the length of the scintillator, L. As such the density of photons per unit time decreases as $1/L$.

The effective transit time for light in scintillator TOF counters is measured by plotting the time difference ($\frac{(t_1 - t_2)}{2}$ from Eq. (3.1)) versus the measured impact positions of the particles. The data are then fit to a straight line and the slope measures the effective velocity of light in the scintillator: V_{eff}. From this value we can calculate the "straight shot" direction by

$$cos\theta_{eff} \simeq \frac{V_{eff}}{\frac{c}{n}} \tag{3.6}$$

The light pipe, if present, or the bar itself, transmits the light emerging from the scintillator onto the photo cathode. Usually the area of the photo cathode is smaller than the cross-section

of the scintillator. Some light will be lost in making this transition, but these losses must be minimized and uniformed over the cross-section of the scintillator and that the transit time from all points on the end of the scintillator to the photo cathode be approximately equal. Monte Carlo computer programs are useful in modeling and optimizing the design of this kind of detectors as we will show below. The photo tube produces the electrical signal that is measured by the electronics. Photons incident in the photo cathode cause the emission of *photo-electrons* which are collected on the first of many dynodes. Time jitter in photo tubes comes mainly from different transit times of photoelectrons from different locations on the photo cathode. These time differences have been measured (3.20). If a large number of photons N_p strike the photo cathode the spread due to the statistic of the jitter scales by a factor $\sqrt{(N_p)}$. The focusing elements between the photo cathode and the first dynode have a significant effect on the time jitter. The signals coming from the photo tubes are processed by fast electronics producing a time of arrival and a measurement of the integrated charge in the pulse.It has been observed that the time of arrival is correlated with the pulse height. The principal correlation is sometimes modeled to be [148]

$$\tau = t - W\left(\frac{1}{\sqrt{a_o}} - \frac{1}{\sqrt{a}}\right) - \frac{x}{v_{eff}} \tag{3.7}$$

where τ is the corrected time, t is the measured time minus any constant effects, W is a fitted parameter, a_o is a reference pulse height, a is the measured pulse height and $\frac{x}{v_{eff}}$ is the position correction due to the delay time for light to travel down the scintillator. Regarding the light that emerges from the scintillator the density of photo-electrons per unit time would be proportional to (N_e/L) where N_e is the average number of photo-electrons and L is the counter's length, while the time resolution shall be proportional to $\left(\frac{1}{\sqrt{N_e/L}}\right)$ if the contribution from the photo tube and electronics is negligible.

3.2 MEG Timing Counter

In MEG experiment the time resolution plays a crucial role. A precise definition of the positron timing is essential to have the $e^+\gamma$ coincidence window as narrow as possible, in order to have the highest power in rejecting accidental coincidences. The total time coincidence window is determined by the quadratic sum of the three contributions coming respectively from the Timing Counter resolution ($\sim$100 ps), the uncertainty coming from the track reconstruction and the timing resolution of the LXe calorimeter . The whole experimental apparatus has been designed to keep the overall timing uncertainty as low as 150 ps FWHM [69], which is required to keep the accidental background BR below 10^{-14}. Extensive discussion can be found in section 2.7 An important role is played by the Timing Counter (TC).

The layout of the detector consists of two (upstream and downstream) identical sections symmetrically located inside the COBRA magnet.

Each section consists of two layers (longitudinal and transverse) of orthogonally placed plastic scintillator hodoscopes (fig. 3.1), which are designed to measure the positron arrival time and to provide a first level trigger.

(a)   (b)
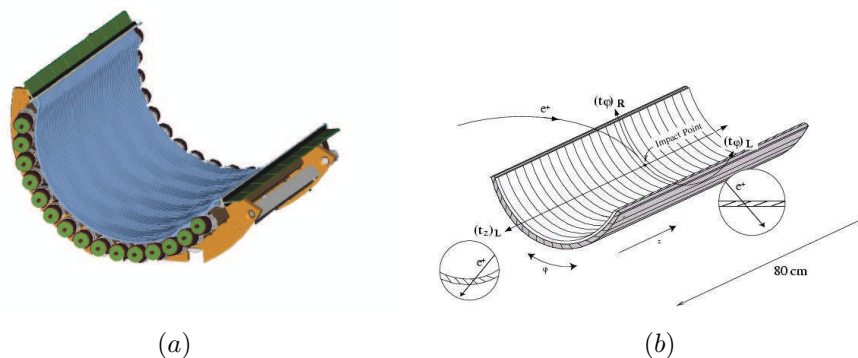
Figure 3.1: Final layout of the Timing Counter (a) CAD (b) working principle: the positron hits on the Transverse detector which gives its position at trigger level and crosses the scintillator bars of the longitudinal detector which gives the time of impact through the reconstruction of PMT signals.

The longitudinal layer is designed to obtain an accurate timing measure of the incident particle, as well as a fast estimation of the emission angle ϕ. This sub detector stands at radius of 320 mm and consists of 15 scintillating bars $78{\times}4{\times}4$ cm^3, placed inside the COBRA magnet separated from one another by $10.5°$, covering a total angle $\phi \sim 160°$. Each bar has two readout photomultiplier tubes one closer to the COBRA center where B=1.2 T and the other placed on the opposite side of the bar where the field decreases. PMTs are not aligned with the field lines, but are slanted by $11°$ as to reduce the performance decrease caused by the field (see 3.3.3).

The transverse detector is made of two layer of 128 scintillating fibers (BCF20) with square cross-section (5×5 mm^2) readout at both ends by Avalanche Photo diodes (APDs) with a low-noise front-end electronics. It stands on the inner surface of the longitudinal one with a radius of 292.4 mm. The transverse module will provide the impact point z on the TC, that will be used for a first raw determination of the positron trajectory, allowing for the fast rejection of events with unmatched kinematic parameters: the trigger rate goes from 200Hz to 20Hz thanks to the informations coming from this sub detector.
Moreover the z point increases the constraints for the track reconstruction and can be used for analysis.

The position of the Timing Counter is such to cover the same solid angle covered by the drift chambers, which is the same acceptance angle of the LXe calorimeter, given the positron trajectories inside the COBRA magnet: the required position extends in the region $25 < |z| < 105$ cm along the cobra axis and $220° < \phi < 380°$ in the azimuthal direction.

The definition of the final geometry required a careful optimization of all the parameters concerning the timing resolution combining a detailed simulation and experimental effort that gave a

good result as shown below.

Because of the key role of the longitudinal sub detector a bigger effort have been put in its R&D and it will be described in details in section 3.3.

At the same time also the transverse sub detector have been built and tested with care and will be discussed extensively in section 3.5.

3.3 The longitudinal Timing Counter sub-detector.

3.3.1 Analysis of Time Resolution.

Preliminary time resolution tests were executed by the Pisa group [149] with 1×5 cm^2 thick BC404 scintillator and light guides to match it with the $2''$ PMTs PHILIPS XP2020-UR, which has a TTS of 250 ps.

The obtained resolution was $\sigma \sim 60$ ps $\cong 142$ps FWHM.

In order to obtain a comparable result with a PMT like hamamatsu R5924 (which can be used in magnetic field and has a TTS of 440ps see below for a more accurate description), not changing all the other parameters (*i.e.* electronic timing resolution, impact point spread) the number of photoelectrons, and so of primary photons produced by the energy release of the particle crossing the scintillator, should be scaled by a factor $(TTS_H/TTS_{XP})^2 \sim 3$.

This brought to the choice of 4 cm thickness for the scintillating slabs. We will discuss below the other optimization needed.

A first consequence of the use of such a thick scintillator was the choice for $2''$ PMTs in order to have the best matching without usage of light guides which decrease the timing resolution due to some inefficiency in coupling with bars (see for example [150] or [148]).

The actual plastic scintillator bars composing each TC element measure $40 \times 40 \times 780$ mm^3.

At each end of the bar is directly coupled a $2''$ diameter Hamamatsu fine-mesh PMT (R5924). Its diameter is 52 mm and its photo cathode diameter is 39 mm, thus optimally fitting the bar cross-section and eliminating the need of a light guide giving an effective coupling efficiency of$\sim$74%.

As we saw in section 3.1, we could think to measure the time of a positron hitting a single element of the counter checking with a discriminator when the signal crosses a threshold value.

During the experiment will be measured $(t_1 + t_2)$, to obtain the impact time, which have the same statistical error of $t_1 - t_2$, for sake of a simpler electronic setup the latter was the quantity measured at the BTF as we will see below.

We can break into several contributes the sources of errors we will face during the measure of $t = t_1 - t_2$ so to study them and try to keep them as small as possible.

$$\sigma_T^2 = \sigma_{El}^2 + \sigma_{ip}^2 + \frac{\sigma_{PMT}^2 + \sigma_{scin}^2}{N_{pe}} \qquad (3.8)$$

where σ_{El}^2 refers to the jitter of the readout system and to *Time Walk* errors (details in 3.3.4),

σ_{ip}^2 is strictly related to the determination of the impact point along the bar, σ_{PMT}^2 contains the terms related to PMT intrinsic jitter (details in 3.3.3), σ_{scin}^2 depends on the characteristics of the scintillating material namely rise and fall time and light yield; N_{pe} is the number of photoelectrons generated at the photo cathode.

We can analyze the σ considering the sources of different terms:

- σ_{El}^2 depends on the electronics used and has been measured during LNF tests and has been estimated $\sim 38ps$ FWHM as an indication value, more precise determination will be available when the final electronics will be ready [143].

- σ_{ip} is caused by the impact point position error. In the BTF single bar test setup (fig. 3.9) the spread of the beam hitting the bar under test was kept as low as 5mm by using a small scintillator placed upstream of the bar which gave the trigger signal to the measurements, acting *de facto* as a beam collimator. This contribution is $o(10ps)$ and could be estimated as

$$\sigma_{pl} \sim \frac{\sigma_x}{v_{eff}} \sim \frac{2.5mm}{1.5 \cdot 10^{-1}mm/ps} \sim 17ps \; FWHM \qquad (3.9)$$

however in the final setup will be measured the impact time from $(\frac{t_a+t_b}{2} = \frac{L}{2v_{eff}} + t_0)$ which results position independent (as explained in 3.1).

- σ_{PMT}^2 is due to the PMT anode pulse time response and is related to Transit time spread (TTS)(fig. 3.20): the fluctuation in transit time between individual pulses, defined as the FWHM of the frequency distribution of electron transit times. The TTS spread is statistically reduced by a factor $\sqrt{N_{pe}}$ emitted by the photo cathode as show below and so it gives a contribute which is negligible. The value given by the producer (440 ps FWHM for a single photo-electron) resulted lower than the one coming from measurements $\sim 650ps$ FWHM. This value is used from us to be conservative.

- σ_{scin} has been analyzed using MC simulations and can be broken down in 3 different contributions:

  - the most important is the time spread induced by the *photon generation* inside the bar which is a stochastic process, the absorption and emission band are partially overlapped and this causes photons to be re-absorbed and re-emitted determining the scintillator rise-time (0.7 ns),

  - the spread caused by the *light propagation* through reflections inside the scintillator acting as a wave guide,

  - the *different path length* of the particle crossing the bar due to different impact angles.

The first step in building the sub detector was the choice of scintillators and PMTs, through the help of simulation followed by the definition and optimization of their geometry.

Table 3.1: Properties of plastic scintillators from BICRON [144]

parameter	BC404	BC408
Light Yield (% Anthracene)	68	64
Rise time (ns)	0.7	0.9
Fall time (ns)	1.8	2.1
FWHM pulse width (ns)	2.2	2.5
Attenuation length (cm)	140	210
emission peak λ (nm)	408	425

3.3.2 Scintillator choice.

BC408 or BC404 ?

The leading idea during the Research and Development (R&D) phase of the Timing Counter design was to trigger on the first photons produced inside the scintillator bars. The scintillator BC404 and BC408 produced by Bicron were both good candidates. Table 3.1 summarize their properties. BC404 has more light output, faster rise and decay times, but shorter attenuation length, which means a bigger *rms*.

Simulation.

Monte Carlo simulation for the above scintillation counters was performed to be able to predict the transport efficiency and transmission time of photons for the different materials. This purpose lead us to monitor the attenuation and flight distance of each photon.
We developed our own Monte Carlo simulation program for the two different candidate counters used in our test.
We assumed that charged particles hit the scintillator in a fixed position, with an average angle that was calculated through the GEANT321 simulation described below, with the correct spread. It's also accounted the contribution of the different impact angles of the positron on the slab resulting in different path lengths. We can estimate this latter from the maximum and minimum path length resulting in $\Delta L = L \cdot (1/cos(\theta) - 1) \sim 1cm$. At most the time difference introduced from this contribute is ~ 30ps which is negligible compared to the resulted light generation spread ~ 700ps.

The simulation allows to select different impact position.
At each impact point a statistical number of scintillation photons (with 54400 as a mean and a Gaussian distribution with a 10% sigma) is emitted with random directions and distributed uniformly along the charged particles track and is studied.
The mean number of photon distribution is estimated from the properties of the *BC404* and the geometry of the bar as follows:

$$N_{phot} = \frac{2MeV}{cm} \cdot 4cm \frac{1}{100eV} \cdot 68\% = 54400 \tag{3.10}$$

each positron of ~50MeV is considered as a minimum ionizing particle. It releases about 2MeV per cm crossing the scintillator (~4cm) and the generation of a photon requires about 100eV. These data with a 68% of light yield as a percentage of antracene (Tab.3.1) corresponds to the number of photons expected from a minimum ionizing track. The simulation takes into account the contribution of the different light time emission inside the scintillator caused by the particle finite crossing time (Fig. 3.3).

Each photon is tracked by extrapolating its direction vector to intersect all surfaces and choosing the closest intersection point.At the intersection tests are made to see if the photon is reflected and, in case, with what efficiency. At each reflection the new photon direction is determined and the process is repeated until the photon hits the PMT or is lost.

The Monte Carlo simulations predicts a light collection efficiency for photons originating from the center of the bar of 4%.

The PMT QE can be taken into consideration from the simulation to have as a output the distribution of photoelectrons at the photo-cathode of the PMT reading the bar.

The time distribution was built in order to reproduce the properties of the scintillator bar (summarized in table 3.1) and can be written as:

$$t_{dist} = A(exp(\frac{-t}{\tau_{decay}}) - exp(\frac{-t}{\tau_2})) \qquad (3.11)$$

where τ_{decay} is 1.8ns, given by Bicron; τ_2 has been calculated to match the exact rise time (0.7 ns) given by the scintillator manufacturer.

The results from the MC simulations are shown in figure 3.2 and are obtained simulating 10000 positrons, each one producing ~54000 scintillation photons.

From the simulation is clear that the main contribution to the time spread is due to the photo statistic (fig.3.3).

More in details: we call t_o the instant when the positron crosses the bar. The observed signal is the statistical superposition of photons correlated to the particle arriving with a delay $\Delta t_i = t_i - t_o$, where t_i is the i-th photon arrival time. This delay should follow a time distribution given by the probability density function (*pdf*) of time emission (figure 3.2).

If we take a single photon emission, the delay Δt_1 can assume all values within the *pdf* of the scintillator response. This will give the occurrence time t_1 with an uncertainty given by the *r.m.s.* of the scintillator response. When a number N of photons are emitted we can define the minimum of all the delays $\Delta t = min((\Delta t_i))$. It can be shown that this quantity has smaller fluctuations. These are determined by Poisson statistics of Δt_i convolved by the scintillator *pdf*. Its mean value scale as $\sim \sqrt{N}$. This discussion gives the possibility to evaluate the time resolution limit achievable. For a scintillator with:

  − high light Yield, which means high N produced,

  − large attenuation length,
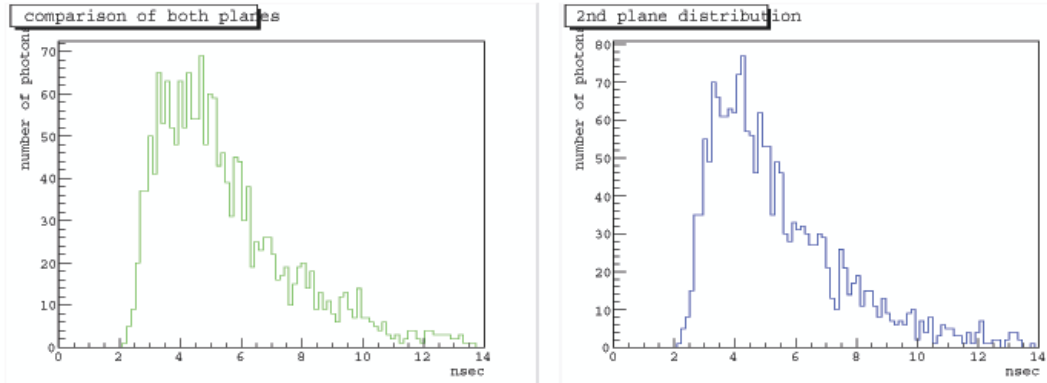
Figure 3.2: Distribution of photon generation for a MEG scintillator bar: inner and outer PMT separately.
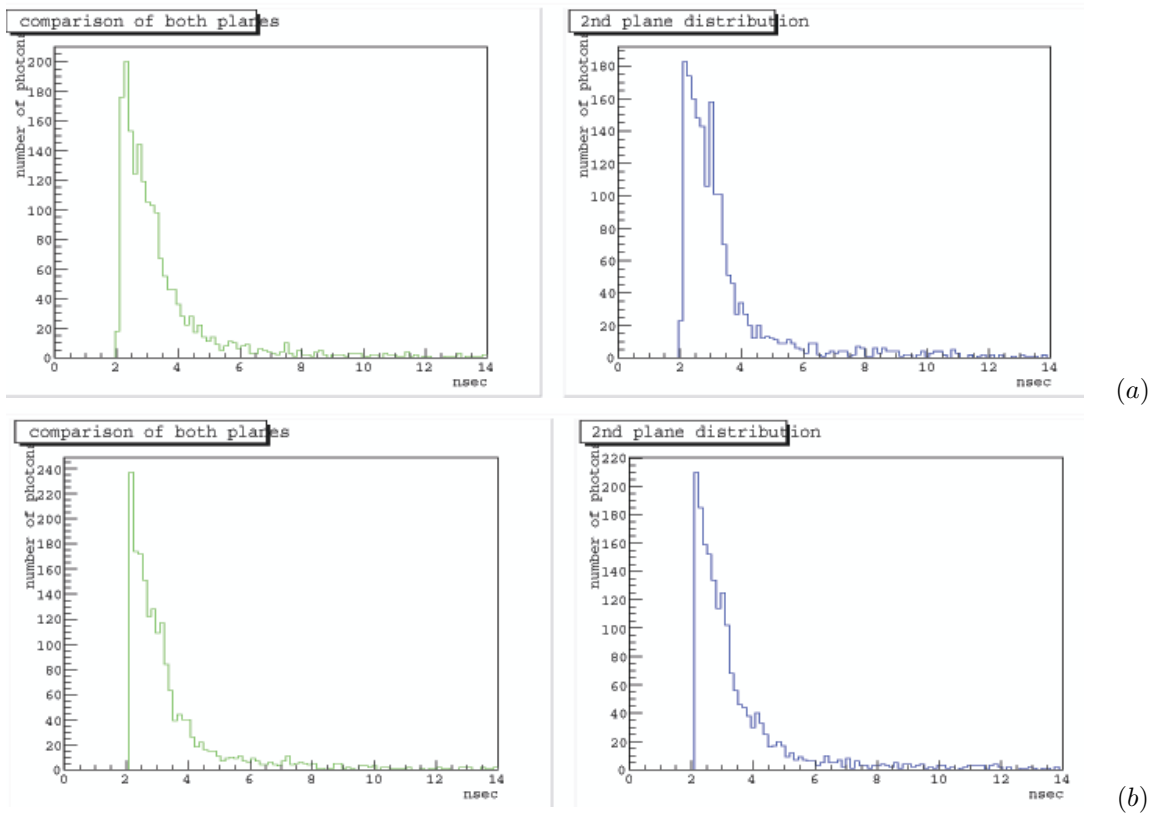
Figure 3.3: Distribution of photon generation for a MEG scintillator bar (a) neglecting the photon spread due to the production along the track and not in a single point (b) neglecting also the spacial spread.

– fast rise time τ_{rise} which means high photons density at the leading edge;

the value of ΔT can have small fluctuations, allowing to obtain the timing resolution needed for the TC.

For BC404 in our final configuration we have: $N \sim 5, 4 \times 10^4, t_{FWHM} = 2.2\,\text{ns}, \tau_{rise} = 700\,\text{ps}$. It should be noted that the factor $\sqrt{N}$ takes into account only the fraction of photons emitted with a direction close to the bar axis, which have smaller time-of-flight inside the scintillator. Assuming a fraction of about 3% of the total, corresponding to photons emitted within 15° from the axis, this yields a rough estimate for $\Delta t \sim \frac{2.2\text{ns}}{\sqrt{10^3}} \sim 75\,\text{ps}$ FWHM.

More accurate results have been obtained with Monte-Carlo simulations of light generation shown in figure 3.5. The number of photoelectrons involved in the process can be evaluated considering the threshold as follow:

$$V_{th} = \frac{n_{phe} \times G \times e \times 50\Omega}{t_{rise}} \qquad (3.12)$$

where e is the electron charge which multiplied by the number of photoelectrons (N_{phe}) and by the gain of the PMT G gives the charge at the anode which is collected during the constant ($t_{rise} \sim 2,5\,\text{ns}$) raise time of the photo tube by *discharging* the current on a 50 Ω resistance. For a gain $\sim 10^6 - 10^7$ and a threshold of $\sim 300mV$ the correspondent number of photoelectrons is ~ 100 which means a time spread of $\sim 65ps$ FWHM which is pretty near to the estimated value and fits the BTF experimental results properly.

In Fig.3.4 are reported the arrival times and the relative spread for the photons detected on the photo cathode. The time spread has very low fluctuations for the very first photons.

Assuming an effective light speed inside the scintillator of $15cm/ns$, as measured at the BTF (see figure 3.6 and below for details), we can also calculate the effective transmission angle, θ_{eff}

$$\theta_{eff} = sin^{-1}(t_{acc} \times v_{eff}) \sim 37,5cm \qquad (3.13)$$

Taking a particle hitting at the center of the bar we have that the effective path length range goes from $x_{min} =40\text{cm}$ to $x_{max} =77,5\text{cm}$. This gives a $cos(\alpha) = x_{min}/x_{max} = 0,52$ which means $\alpha = 58,9°$ (and less for positions different from center). From here we can evaluate the number of reflections in $N_{ref} = \frac{x_{max} sin(\alpha)}{L/2} \sim 17$ with $L/2 = 40\text{cm}$ distance of the center from the PMT.
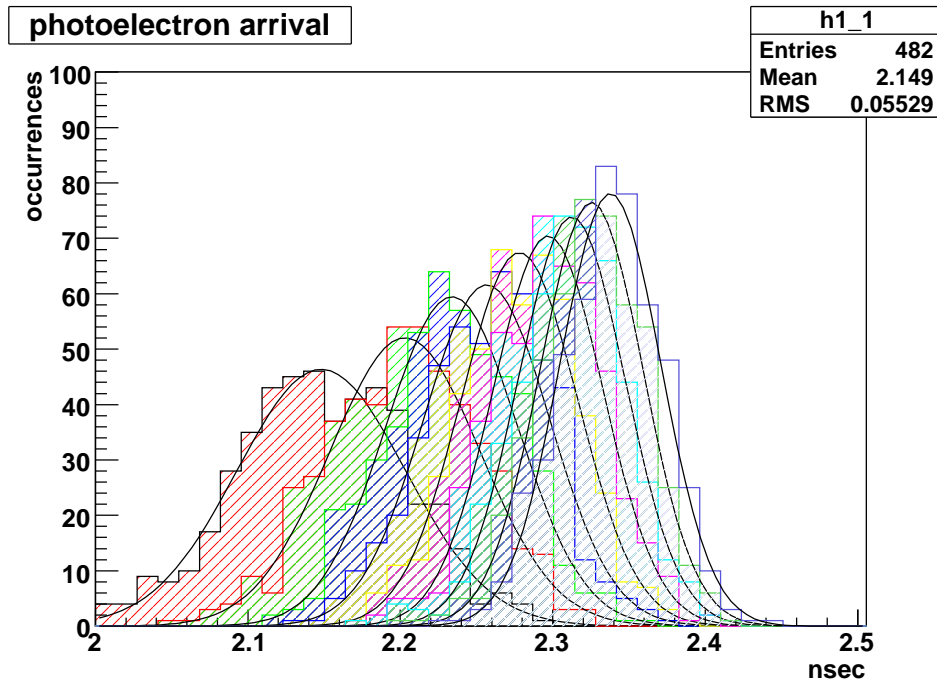
(a)
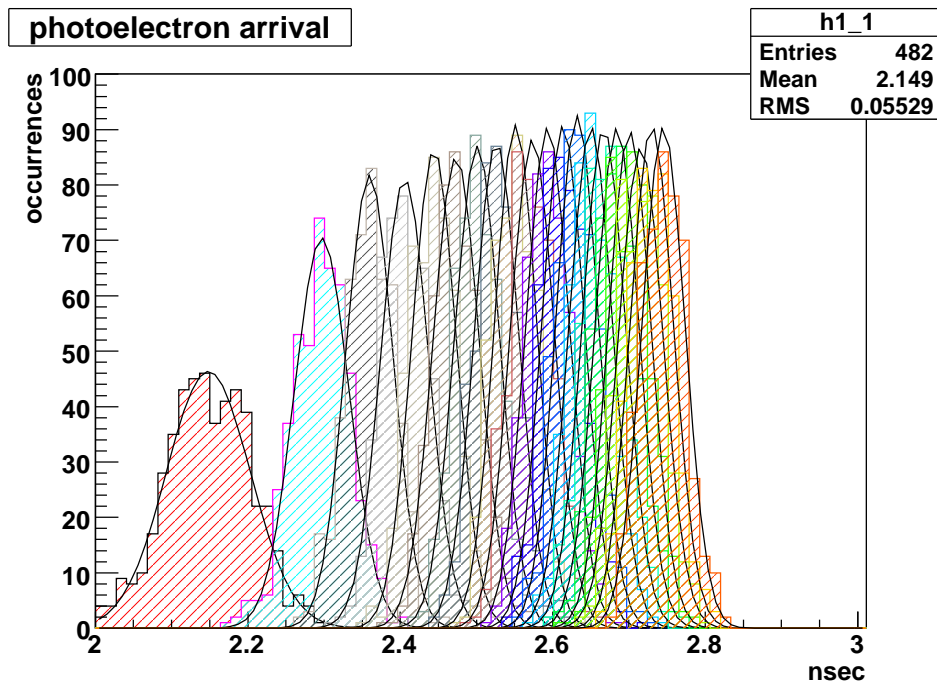
(b)

Figure 3.4: Distribution of the arrival time of photoelectrons at the photo cathode. Generated from a simulation of a 52,8MeV positron hitting the scintillator bar in the middle. The time spread of single arriving photon slightly decreases on the leading edge of the scintillator *pdf*, increasing during the fall. Plots show the distribution of 1000 hitting positrons; the scintillating photoelectrons (QE is taken into account) are ordered with photo-cathode arrival time. (a) First 10 photons plot one by one, (b) first 100 photons plot 1 each 5.
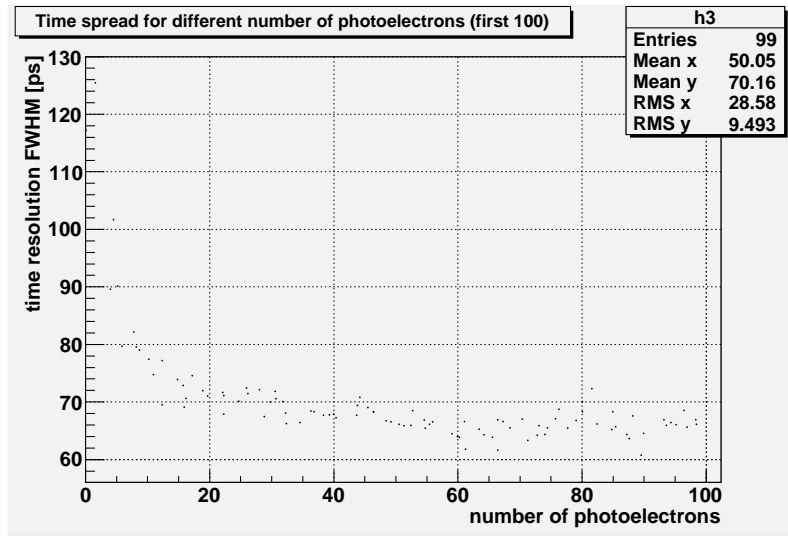
Figure 3.5: The time spread for arriving photoelectrons versus the number of photoelectrons themselves. It's clear that to achieve a good resolution it's enough to collect more than 10 photoelectrons.
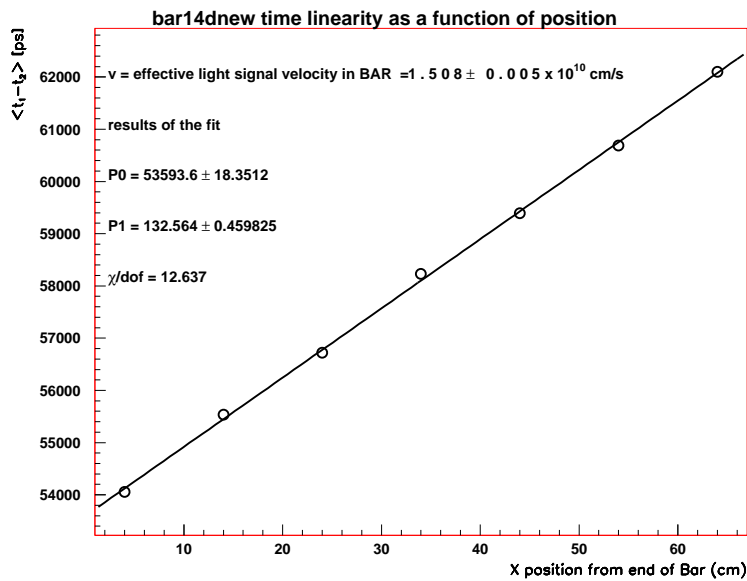
Figure 3.6: Time difference versus position for a plastic scintillation counter BC404 as measured in the BTF with one of the MEG scintillator bars. The fit gives 15 cm/ns

.
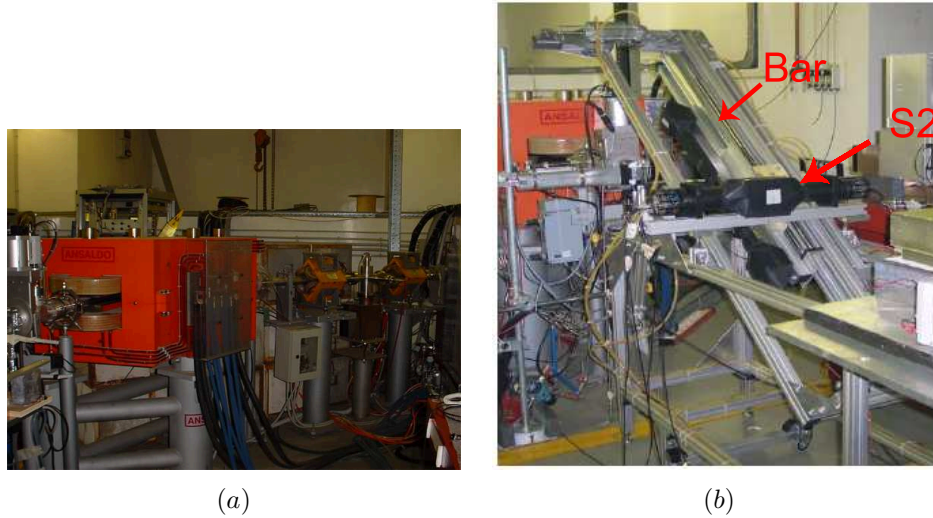
Figure 3.7: Beam Test Facility (*a*) the beam line, (*b*) experimental setup for the single bar measurements .

BTF: tests on single bar

Both scintillators are made by polyvinyl toluene plastic with density $\rho = 1.032 g/cm^3$ so that the mean energy loss for 50 MeV positrons is approximately 2 MeV/cm. The refractive index of both is 1.58 which results in a limit angle of 39.3° for internal reflection.

Given the properties of these two materials, it is clear that while BC404 has a shorter time response with less spread in time emission and a more efficient light production, BC 408 provides a slightly longer attenuation length; however the value given in the data sheet is measured for a sheet with dimensions $1 \times 20 \times 200$cm, rather different from our configuration: so it was important to perform some tests with both scintillators in the final shape, in order to make the best choice.

The two candidate scintillating materials were tested at the Beam Test Facility of Laboratori Nazionali di Frascati.

The BTF (Fig.3.7 shows the beam line) provides e^-/e^+ beams in the energy range of 25-750 MeV, with an intensity that can range from a single particle per bunch with 1-10 ns pulse length, up to 10^{10} particles per pulse, with 50 Hz of cycling rate. The average number of electrons per bunch was in the range 0.5-1.5 during our tests.[1] Both the scintillators were provided by the Saint-Gobain Crystal company. The electronic setup for timing measurements has been tuned in order to reduce the *time walk* effect to a negligible value. Time walk effect (see Fig.3.23 (b)) causes different time measurements depending on amplitude of the signal (see below for more details).

Each TC element consisted of a scintillator bar with a PMT at each end, called PM1 and PM2. In this configuration, the PM1 signal provided the START ($t1$) signal to a Time to Amplitude

---

[1]The duty cycle is limited to about 50%: particles are not available to the BTF when DAFNE is filled, which usually happens every 40 minutes, for a time interval of 20 minutes.
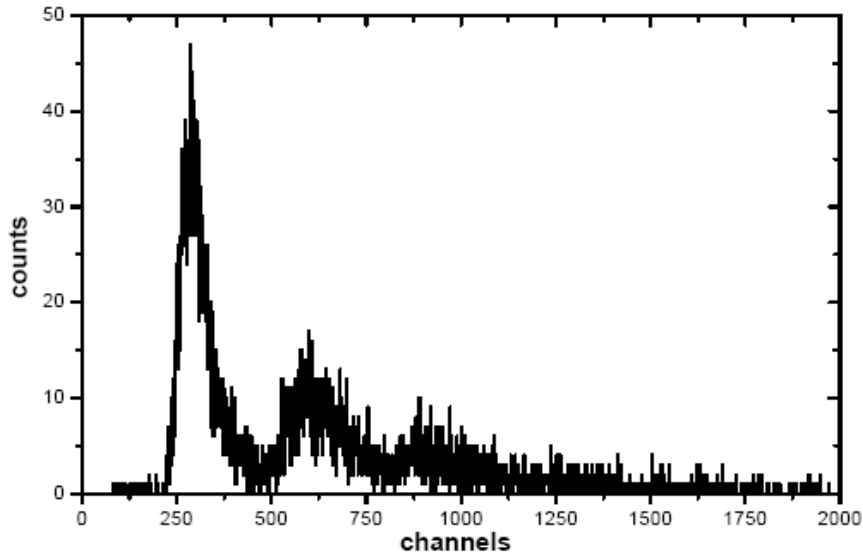
Figure 3.8: Energy spectrum obtained from tail scintillator in test apparatus. The channel number is directly correlated to particle energy. Well separated peaks indicating simultaneous hits of 1,2,3 positrons.

Converter stopped by the PM2 signal ($t2$). A time delay is included to insure that $t2$ is greater than $t1$. After the STOP signal, the Voltage outputting from the TAC, which is proportional to the time difference ($t2 - t1$), is sampled and converted with a Analog to Digital Convert (ADC) with $28ps$ least count. The overall resolution of this DAQ system was $6.33ps/ch$. Using a single threshold discriminator time fluctuations were observed due to the so called *time walk* effect caused by a large variation of PMT's pulse-height. To overcome the problem a double-threshold technique was used: a low-threshold discriminator sensitive to the early arriving photons, was used to introduce negligible *time walk* fluctuations. A high-threshold discriminator was used to validate the low-threshold signal in order to suppress events produced by dark current noise The setup for the test at the BFT is sketched in figure 3.9. The positron beam had 420MeV energy. The possibility to have a average value of single particle per pulse gives a energy well separated spectrum. A threshold in energy was used to select the single-hit events (Fig.3.8). Extensive time resolution studies took place during period 2004-2005 at the BTF. During the tests we measured $t_1 - t_2$ for sake of convenience, since $t_1 + t_2$ has the same statistical error. The measures took place at different positions along the bar and different impact angles, the whole of the test was supported by accurate MC simulations. The bar under test was placed between two BC422 scintillators (S1, S2 in Fig.3.9). The S1 is a slab of 23x12x5 mm^3 coupled with a $1''$ PMT (Hamamatsu R 647-01), and S2 is a slab of 50x50x20 mm^3, measured by two PMTs (Philips XP2020). Two fine mesh PMTs (Hamamatsu R5924) were coupled with the bars; The small S1 was used to have a spot size well defined and small (from Gaussian fit 3×2.1 mm^2) so not to add fake time spread.
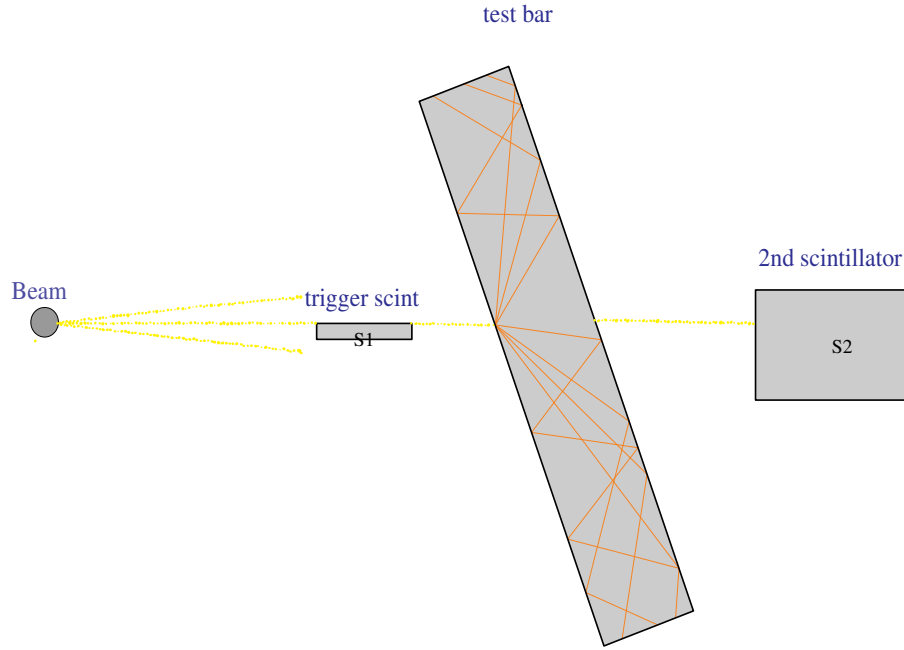
Figure 3.9: Layout of the test at the BTF LNF.

A raw estimation of the contribution of the spot size, from the size of S1, gives a time spread $\sim \frac{\sigma_x}{v_{eff}} \sim \frac{2.5mm}{1.5 \cdot 10^{-1} mm/ps} \sim 17ps FWHM$. A threshold on the energy deposited in the S2 scintillator makes it acting as a multi-hit event discriminator; when multi-events occur the Time to Amplitude Converter (used to measure just the time difference between PMTs) is cut off from the acquisition. After selection of single positron events through S2 and a threshold discriminator the test consisted of 3500 events taken at about 10 different positions along the bar at 4 different impact angles, for a total of 38 points with both materials. We can summarize the results obtained in the plot [2] (shown in fig.3.11) from which is clear that the required resolution is not only correctly achieved but better than the project one being $\sim 92ps\ FWHM$ at the positron impact point. It is useful to point out that it has not been taken into account the additional error due to the positron track reconstruction toward the target, so called *swim back*. Monte Carlo simulations helped in estimating the additional spread caused by the reconstruction of the track through the chambers in about 40 ps FWHM, giving 100.3 ps FWHM total spread, which is a order of magnitude better than the previous MEGA ([19]) experiment. Table 3.2 shows a comparison among different scintillating detectors and MEG TC.

---

[2]The error bars comes from the Gaussian fit in units of the $6.33ps/ch$ of electronic resolution
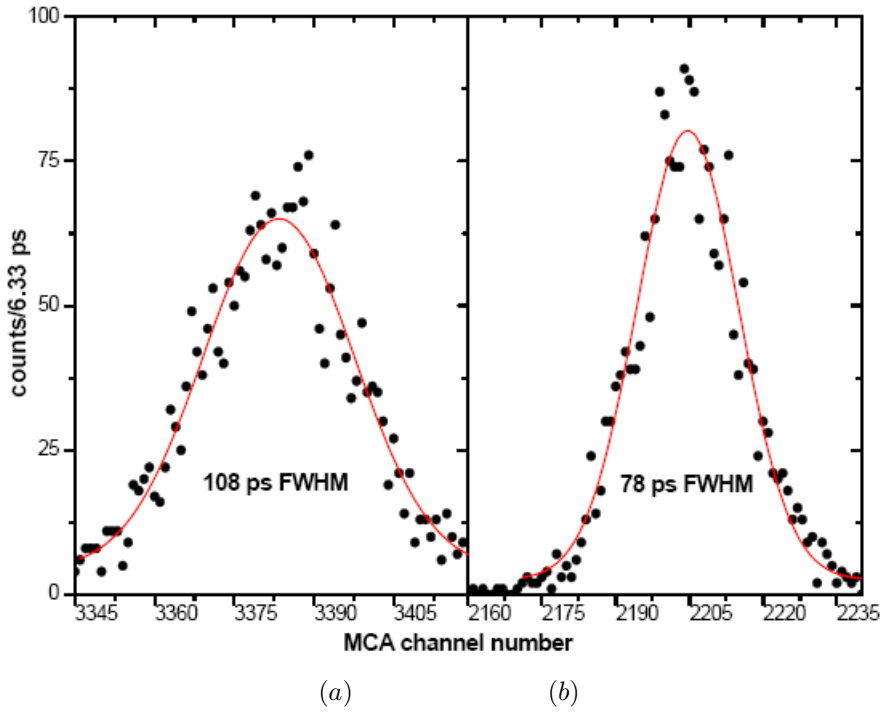
Figure 3.10: Time resolution for different scintillators (*a*) BC408 (*b*) BC404. The impact point is the bar center and the impact direction is 90° respect to the bar length.

Table 3.2: Comparison among different scintillating timing detectors. Last one is MEG (resolution is expressed as σ and not as usual in FWHM to allow a direct comparison with other results).

Scintillator Types	PMT	Dimension (*cm*)	$\sigma(ps)$	
BC420	R1828-01	40x7x2.2	123	[126]
BC408	R3478	12-48x1-1.25x1.5-2.4	85	[127]
BC408	H1949	200x8.5x5	110	[128]
BC408	XP2020	180-250x21x2.5	160	[129]
BC408	XP2020	280x10x5	139	[130]
NE110	XP2020	210-300x21x2	300	[131]
NE110	XP2020	300x9.3x4	170	[132]
BC408	XP2020	305x10x5	110	[133]
NE Pilot F	XP2020	317.5x15.6x5.1	163	[134]
BC408	XP43132B/D1	32-450x15-22x5.1	163	[135]
BC404	R5924	80x4x4	40	MEG
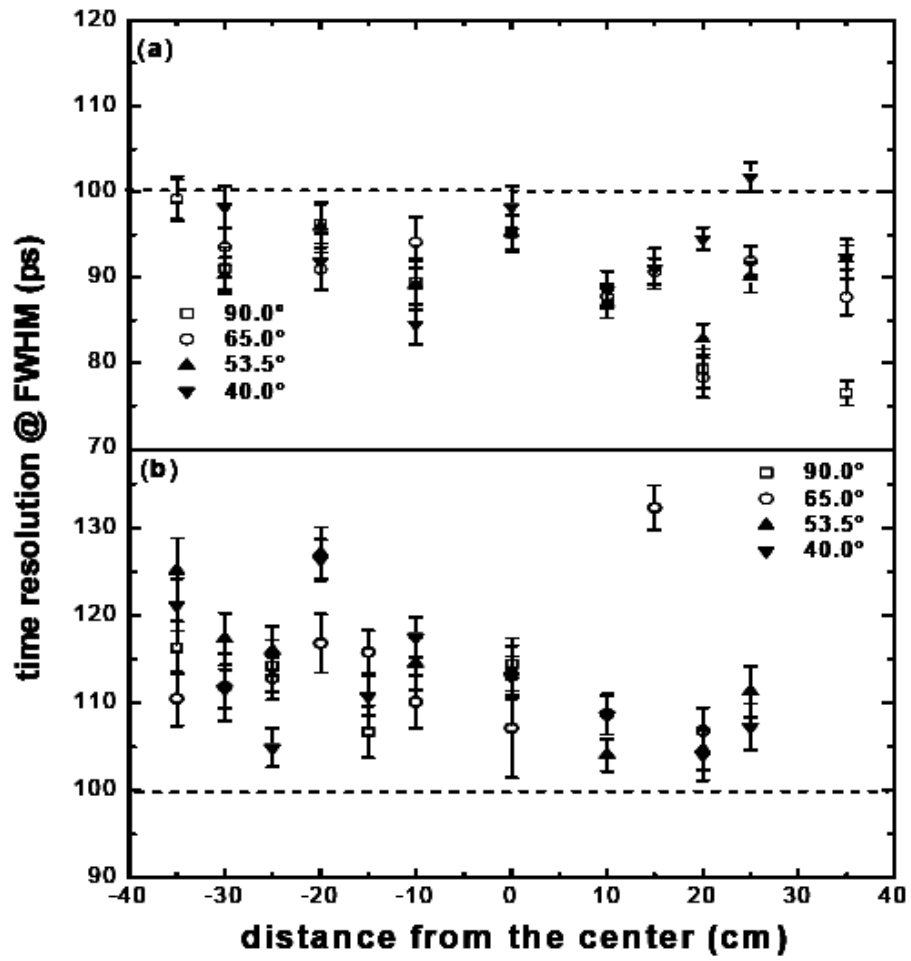
Figure 3.11: Time resolution for different scintillators (a): BC404 (b): BC408 and different impact positions along the bar, the dashed lines represent the required resolution.

Conclusions.

The properties of two candidate scintillators, BC408 and BC404, have been studied. The performances of the two materials (plot in fig. 3.10) resulted better for BC404 as expected from preliminary considerations and confirmed by simulations.
Scintillator with faster timing property seems to be essential in the timing resolution as well as maximizing the number of photoelectrons.
Various parameters of the counters, including the attenuation length, the time resolution and effective light velocity were measured.
A Monte Carlo simulation of photon transmission in the counters has been done; the measured results on the performance of the counters agree well with the predictions of simulation.

3.3.3   PMT choice.

PMT introduction.

Photomultiplier tubes are extremely sensitive detectors of light in the ultraviolet, visible and near infrared. These detectors multiply the signal produced by incident light by as much as $10^7 \div 10^8$, from which single photons can be resolved. They are constructed from a glass vacuum tube which houses a photo cathode, several electrodes (called dynodes), and an anode. Incident photons strike the photo cathode material which is present as a thin deposit on the entry window of the device, with electrons being produced as a consequence of the photoelectric effect. These electrons are directed by the focusing electrode towards the electron multiplier, where electrons are multiplied by the process of secondary emission. The electron multiplier consists of a number of dynodes. Each dynode is held at a more positive voltage than the previous one. The electrons leave the photo cathode, having the energy of the incoming photon (minus the work function of the photo cathode). As they move towards the first dynode they are accelerated by the electric field and arrive with much greater energy. On striking the first dynode, more low energy electrons are emitted and these, in turn, are accelerated toward the second dynode. The geometry of the dynode chain is such that a cascade occurs with an ever-increasing number of electrons being produced at each stage. Finally the anode is reached where the accumulation of charge results in a sharp current pulse indicating the arrival of a photon at the photo cathode (working principle is showed in fig. 3.12).

Preliminary considerations

To choose a suitable PMT, attention should be paid to all the parameters namely rise and transit time spread, effective area, gain loss in magnetic field, cathode quantum efficiency and spectral response. A shorter PMT is preferred because of the small space available inside the detector. The Hamamatsu R5924 fulfills most of these requirements:

- Its diameter is 51mm and its cathode diameter is 39mm (See Fig.3.12). For a scintillator
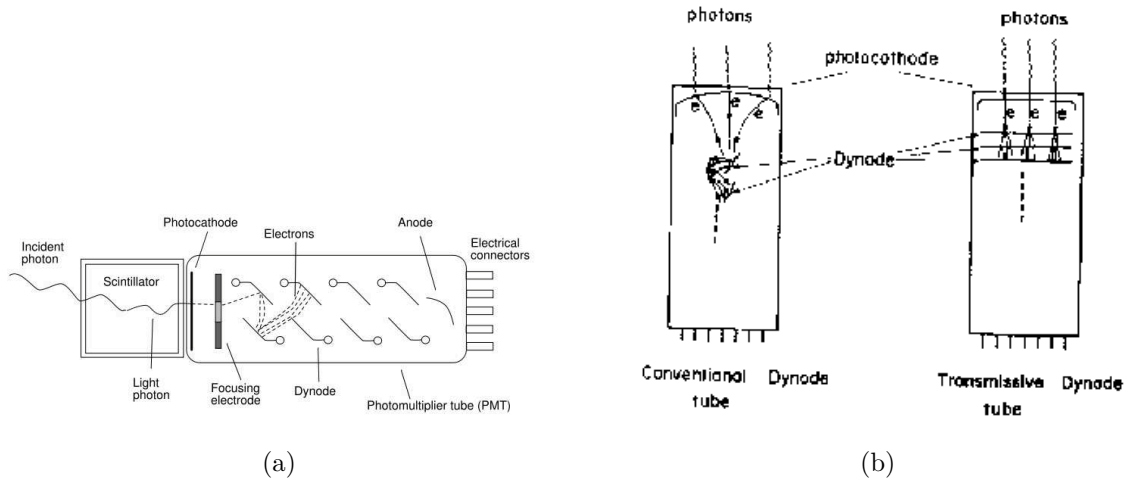
Figure 3.12: (a) Working principle of a Photomultiplier. (b) Different arrangement of dynodes inside conventional and fine mesh PMTs.

section of 40mm × 40mm, the effective area ratio is 75%.

- It has high quantum efficiency ($\sim$ 23% [3]) for the light with a wavelength from 300nm to 500nm.

- It has good timing performance: anode pulse rise time is 2.5 ns, transit time 9.5ns, and transit time spread (TTS) 0.44ns FWHM.

- Its length is 50mm.

Since the PMTs have to operate inside the 1.2 T magnetic field of COBRA, the choice was to use fine mesh PMT (Hamamatsu R5924), with a typical gain of $2.5 \cdot 10^5$ in a magnetic field of 1.0 T. Such a performance is due to the fine-mesh structure: since its very minute diameter and also the close-proximity spacing between dynodes, the electron trajectories of the secondary electrons emitted from the fine-mesh dynodes are resistant to external magnetic fields. The difference in the structure of the dynodes, compared to a conventional PMT, is shown in Fig.3.13 [137].

PMT tests.

Systematic studies [140] to investigate the linearity of voltage response took place to choose the proper PMT to be coupled to our scintillator bars (the PMT properties are summarized in table 3.3). Tests to investigate the behavior inside magnetic field took place both at INFN-LASA Facility in Milan and at PSI with COBRA field. The relative gain [4] for each PMT, in the magnet (and without magnetic field), was measured. A gain decrease associated with magnetic field increase and

---

[3]The QE is given by the manufacturer for a λ=408 nm.
[4]relative stands for referred to gain at zero B field.

(a)   (b)
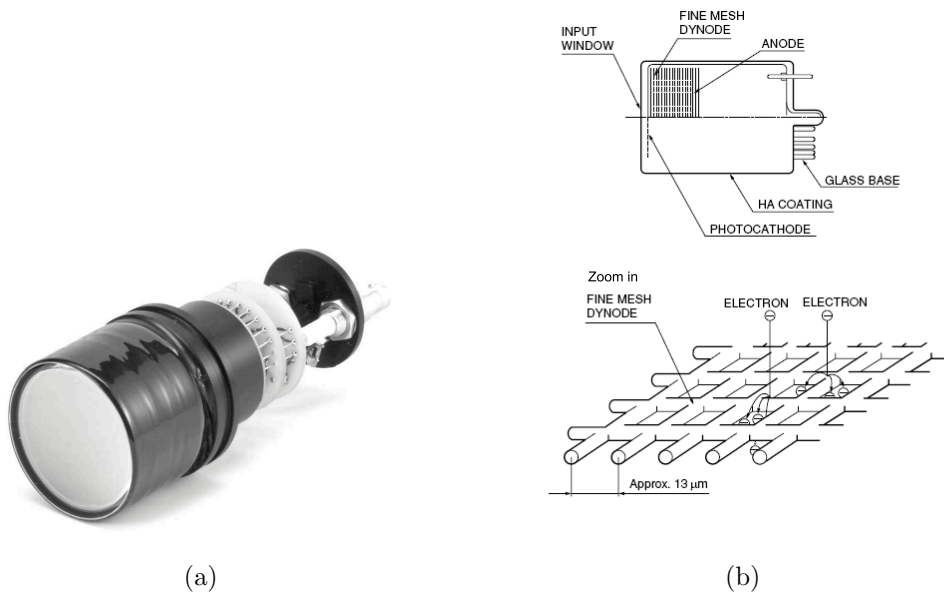
Figure 3.13: (a) A 2″ fine mesh PMT (b)Details of dynodes' structure of a fine mesh PMT.

Table 3.3: Characteristics of *fine-mesh* PMTs from HAMAMATSU [138]

parameter	1.5"diameter	2"diameter
Quantum efficiency ($\lambda = 408$ nm)	23%	23%
Typical gain (0 T)	10^6	10^7
Typical gain (1 T)	$2.9 \cdot 10^4$	$2.0 \cdot 10^5$
raise time ns	1.9	2.5
transit time ns	7.2	9.5
transit time spread ns	0.35	0.44
average anode current mA	0.01	0.1
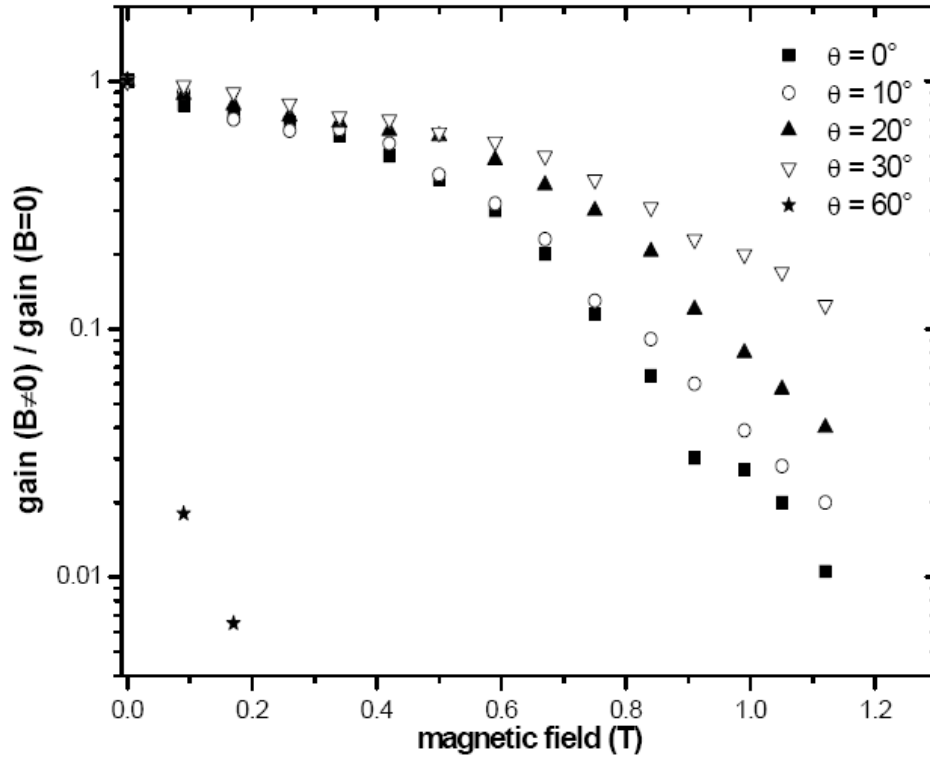
Figure 3.14: Study of PMT gain inside B field at several angles

a strong dependence on the orientation as expected from the producer data sheet was confirmed (see fig. 3.14). The timing properties of fine-mesh PMTs show a low dependence on field strength and direction (see fig.3.15) and only at an angle of 0° with the B field lines there is a sensitive decrease.

Another goal was to study the incident photon rate dependence of the gain which is mainly limited by the maximum allowable average anode current (0.1 mA for R5924 [138] versus 0.01 for other tested PMT namely R5505, R7761). During LASA test peak amplitude was measured, as a function of a light pulses emitted from a laser with different rates. Three different diameter PMTs and in different B field conditions with a standard High Voltage value of 2000V and R5924 confirmed the best behavior as expected from the producer data sheet. The results from these measurements are reported in Fig. 3.16.

This preliminary tests showed that the maximum PMT gain inside a magnetic field can be obtained tilting them of 30° respect to the field direction. Considering geometrical constraints namely the maximum allowable radius inside COBRA and interactions with the Drift Chambers the maximum possible angle was 27.5° (Fig. 3.17) which is enough to recover the gain adjusting also the applied Voltage.

The bars' geometry have been modified as showed in figure 3.18 (top) so to match the new
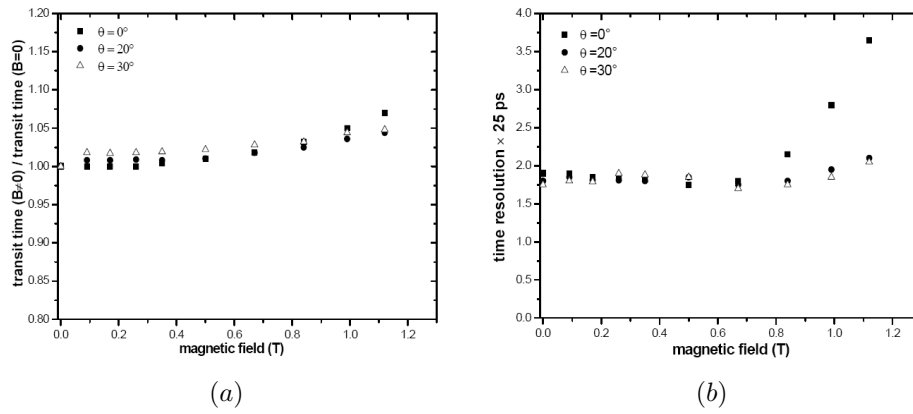
Figure 3.15: Study of PMT timing inside B: (*a*) Transit Time Spread as a function (*b*) timing as a function of magnetic field and angle.
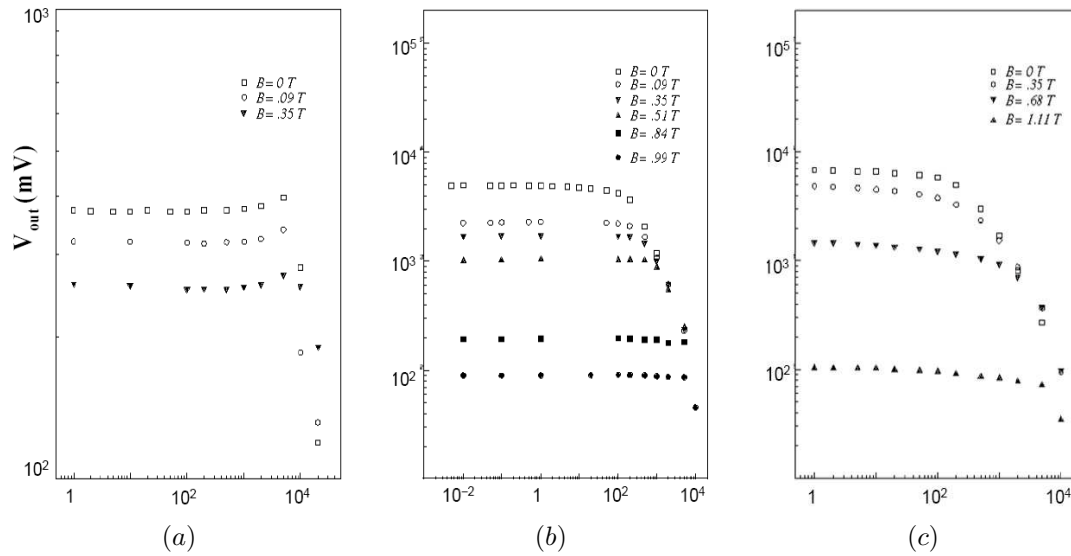
Figure 3.16: Study of rate response of PMT inside B: (*a*) results for 1″ diameter PMT (*b*) results for 1.5″ diameter PMT (*c*) results for 2″ diameter PMT.
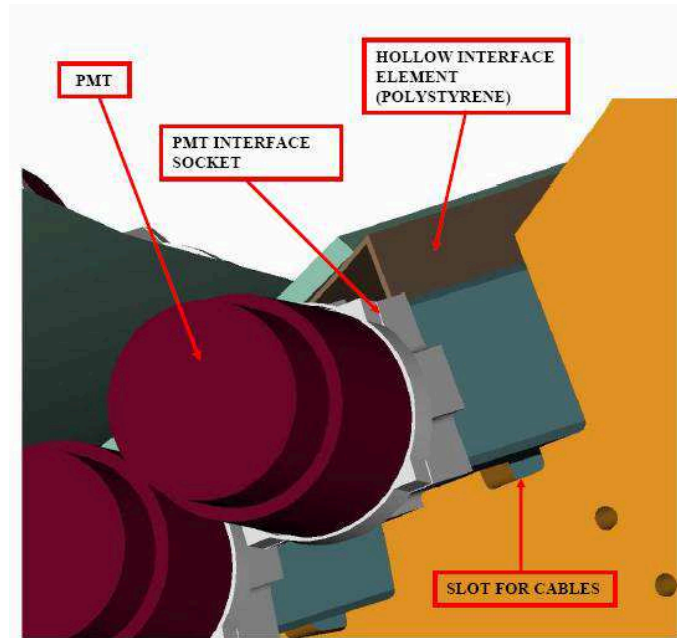
Figure 3.17: Final position of PMT inside COBRA.

PMT position and the longitudinal edges have been removed to match the geometry constraints inside the detector (figure 3.18 bottom).

This configuration has been tested inside the COBRA magnet for both the PMT in the inner part of the magnet where the field is maximum and for the one in the outer part. The results [140] indicates that for R5924 the decrease of performance due to the magnetic field can be fully recovered increasing the bias voltage supplied to PMTs by some 100 V. During BTF test the time resolution was measured also with the help of a laser diode with λ =408 nm, $width$ =250ps and $risetime$ =100ps coupled with a fast pulse generator. The same measurement took place inside COBRA to keep the same conditions and verify that we were able to achieve the same resolution in presence of magnetic field. The only change needed to the setup of BTF was the increasing of PMTs bias voltage to recover the gain:

- for inner PMTs from 1700V to 2300V

- for outer ones from 1600V to 1750V

In Fig. 3.19 Working at a low threshold the main contributing to time resolution is due to the PMT TTS which gives a spread of 440ps. This one scaled by the the number of photons emitted at the photo cathode when illuminated by a certain number of photons.

The number of photoelectrons is related to the properties of the PMT and is expressed through quantum efficiency (QE) which is the ratio of the number of photoelectrons emitted from the photo
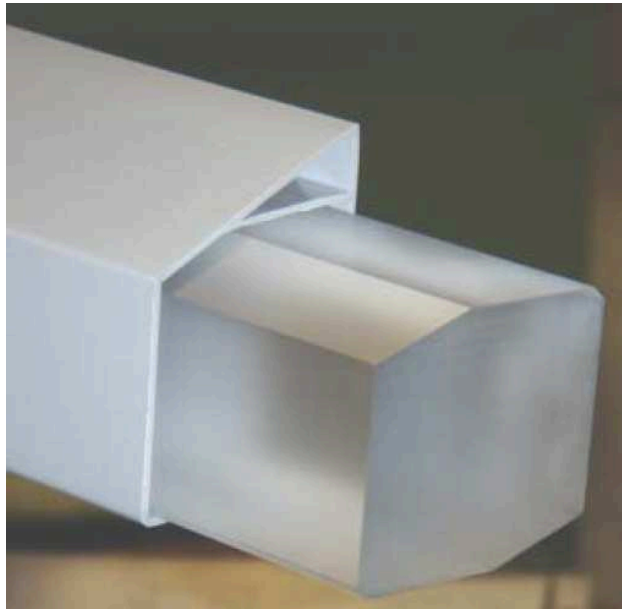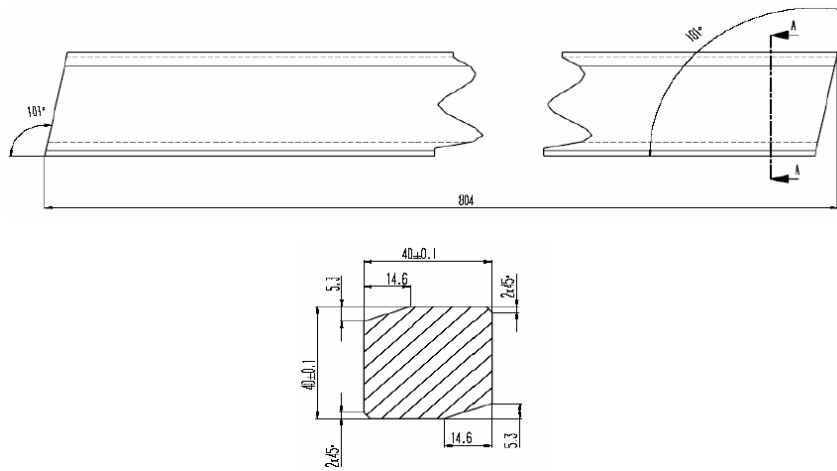
Figure 3.18: Final design of scintillator bar, side view (top) and front view (bottom).
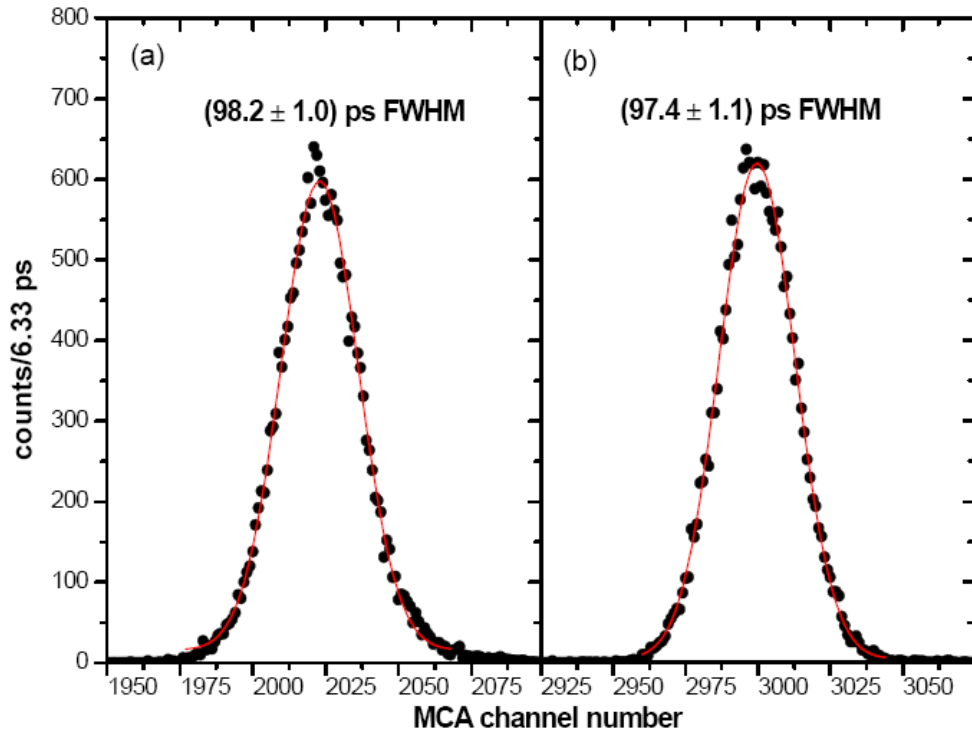
Figure 3.19: Experimental resolution for BC404 (*a*) inside the COBRA magnet (*b*) at BTF. For details see text.Plot are in MCA channels 6.33ps/ch

cathode to the number of incident photons [5] QE= $\frac{Number of Photoelectrons}{Number of photons} \times 100(\%) = 23\%$ for PMT used. The multiplication process is statistical and as such the Transit Time of a photo electron is subject to fluctuation namely to a transit time spread (Fig.3.20). The TTS has been measured (Fig. 3.20) and even if it resulted to be larger than the data sheet value (440ps), it verifies the law $1/\sqrt{N_{Pe}}$, so taking a reasonable value of 300 photoelectrons it gives a contribute which is negligible $\sim 25ps$ when scaled by the number of photoelectrons received by the photo cathode which will give the final pulse.

3.3.4   Electronics.

The spread in time of photo-electrons reaching the PMTs is directly related to the time distribution of photons produced inside the scintillator scaled by QE and as we saw before is dominated by the statistic of scintillating photons. The observed signal is the statistical superposition of almost uncorrelated photons each one generating an electron cascade inside the PMT; on their own any shower is delayed by its own (fluctuating) transit time before arriving at the anode where it is detected. In particular, the summed signal shows a time fluctuation which is inversely proportional to the square root of the number of photons in a given time interval, so the minimum fluctuations are achieved when the signal [6] has its maximum, which corresponds to the bulk concentration of incoming photons. This condition is verified during the leading edge of the light signal, hereafter the need for intercepting the very first photons in order to obtain a very good timing. Moreover it should be noted that late photons do not affect the timing resolution, Since in actual implementation we have to take into account the tube single electron response (SER) which worsen the time resolution for the arrival time of $n-th$ photon by a factor proportional to $\sqrt{n} \cdot \sigma_{SER}$; since our PMT has a SER following almost an exponential distribution (3.22) this would exceed the low intrinsic jitter; furthermore the time-walk effect would become dominant. By placing a threshold as low as the first photon we can overcome the time-walk effect. This has two main sources: the energy deposit spread and the gain distribution of the PMT, which is indeed very large in the case of fine-mesh PMTs.

The effect of time-walk is schematically shown in fig. 3.23 and can be parametrized as an additional time spread $\sigma T_{tw} = \frac{R \cdot T}{h} \cdot (\frac{\sigma_R}{R} + \frac{\sigma_T}{T} + \frac{\sigma_h}{h})$ where h is an average pulse amplitude, R is the rise time of PMT pulses and T is the threshold voltage. Taking typical values of the quantities: $h \sim 5$ V, $R \sim 3$ ns, $T \sim 10$ mV, and remembering that the main source of σ_h (3.3.1) is due to the photon emission distribution we can take a reasonable value for σ_h/h ranging between $0.1 \sim 0.2$, we find the contribution to the resolution is of $\mathcal{O}(\text{ps})$ and therefore negligible as showed in Fig.3.24.

Double threshold discriminator.

The implementation of the timing procedure described above, in which the detector timing depends on the first photon statistics, is in principle subject to error. Setting the threshold at such a

---

[5]It's usually given as a percentage.

[6]note that is intended as the *light signal* from the scintillator, not the electrical output of the PMT.

(a)

(b)

(c)
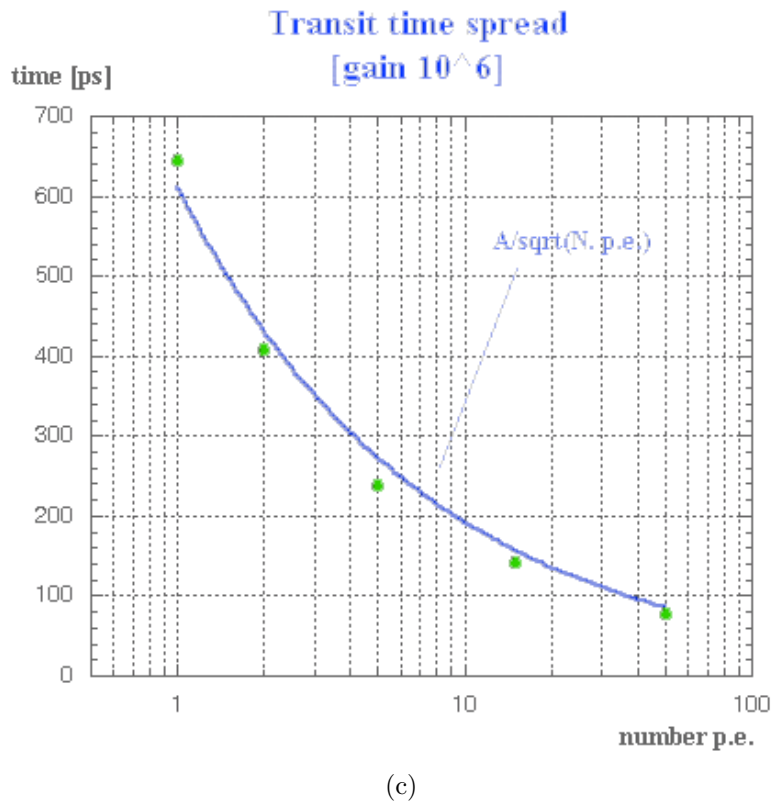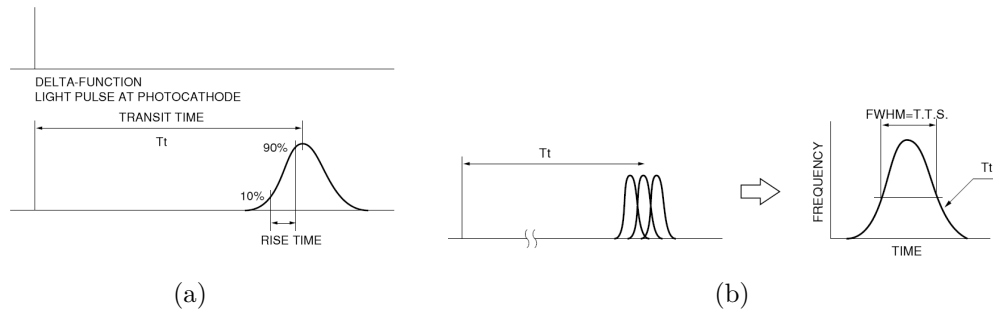
Figure 3.20: (a) Definition of PMT transit time and rise time. (b) Definition of PMT Transit time spread. [137] (c) Measure of TTS, it scales following the inverse square root of the number of photoelectrons produced at the cathode.
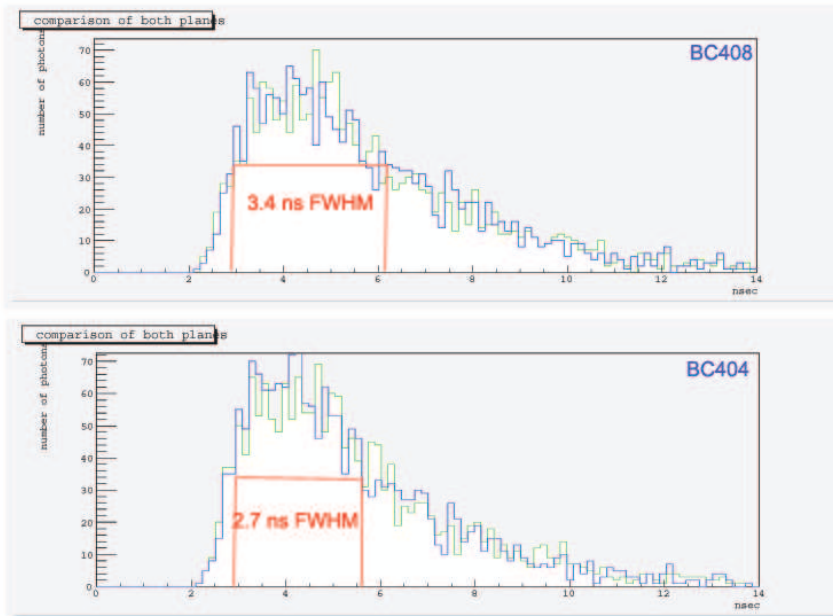
Figure 3.21: Simulation of time distribution for the photoelectrons arriving at PMTs from two different scintillator materials: (upper) even if it has a smaller attenuation lenght BC408 has a worse time spread of 3.4 ns FWHM due to a slower rise time, (lower) BC404 instead has a better timing with 2,7 ns FWHM spread. Both the plots are timing of two bar PMTs superimposed.
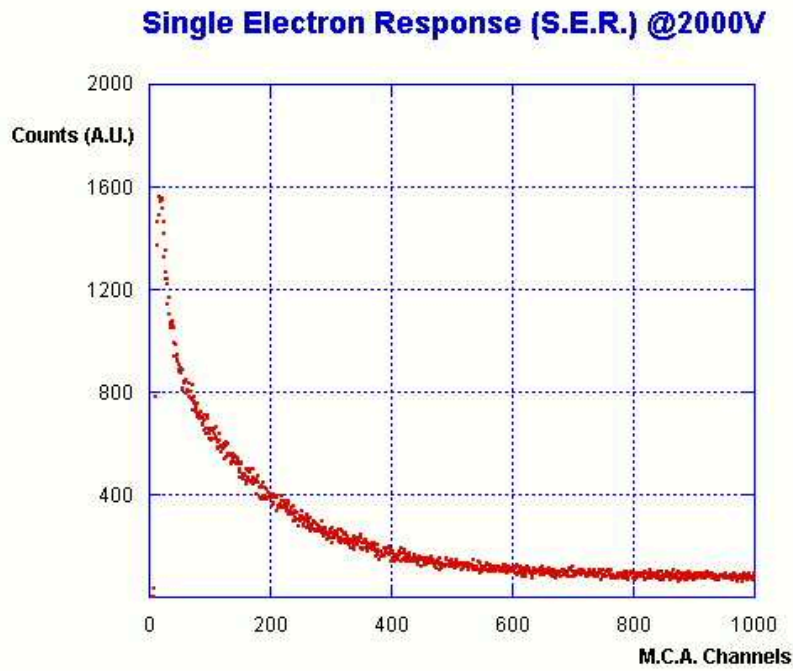
Figure 3.22: Single electron response as measures for hamamatsu R5924 in use by MEG Timing Counter .
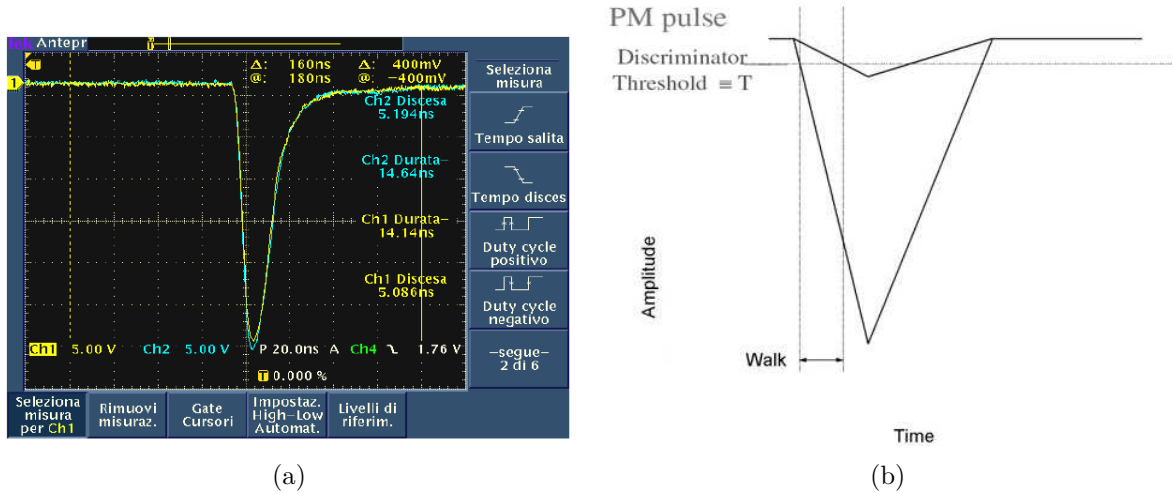
Figure 3.23: (a) A signal captured from a oscilloscope screen with two different amplitude signals coming from PMTs, (b)scheme of the so called Time Walk effect enhanced: for a fixed trigger level the time of threshold crossing depends on pulse amplitude.

theoretical time walk at fixed δh/h
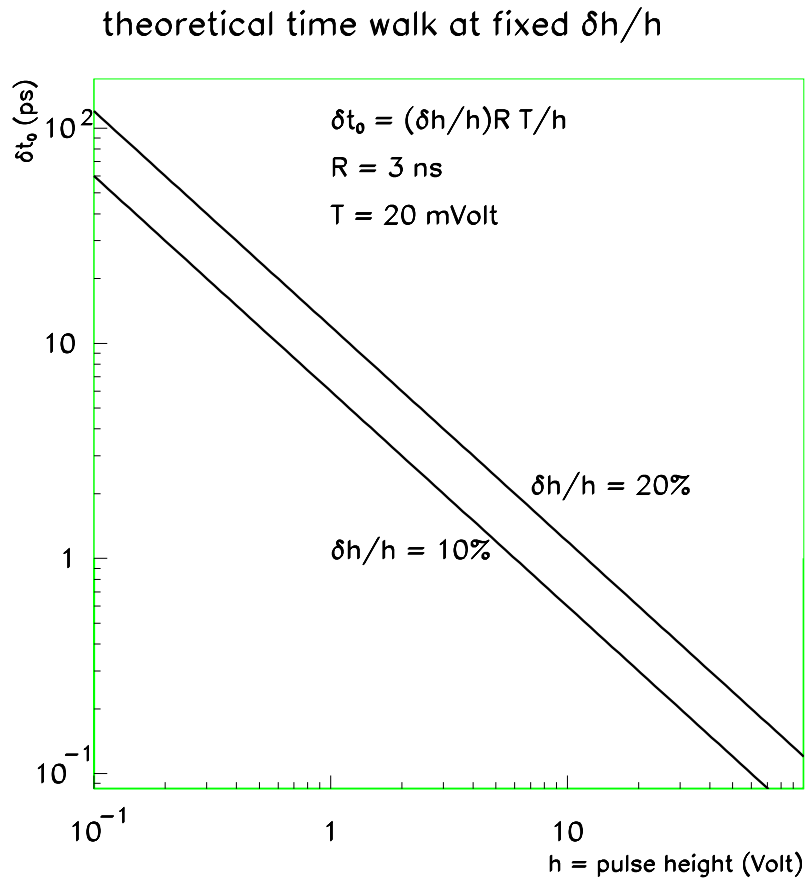
Figure 3.24: Estimation of Time Walk effect on time resolution.
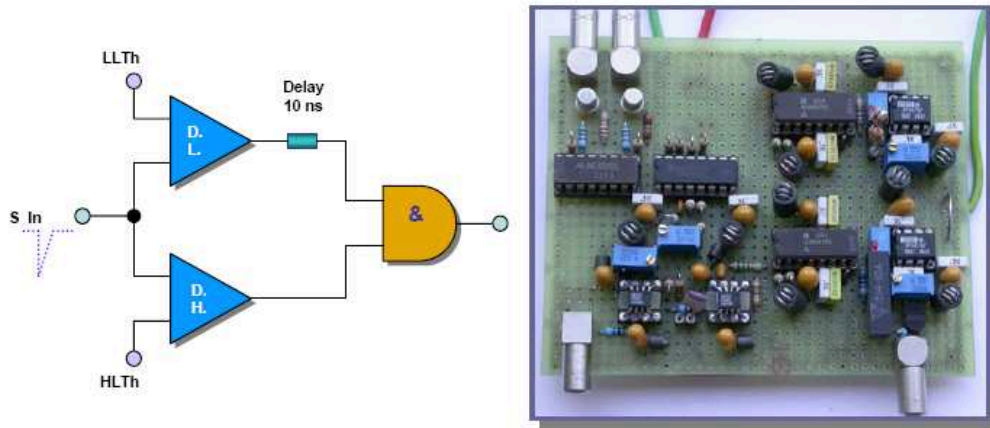
Figure 3.25: Layout of the dual threshold discriminator (left) and Bread Board prototype (right).

low value would certainly cause problems due to noise sources. To overcome the problem the discrimination is based on a double threshold mechanism (Fig.3.25) as already mentioned.

The signal from PMT is split through a passive splitter [7] (during our tests the signals were sufficiently high to allow us to use a passive splitter). Fig.3.26 shows a scheme of the front-end electronics for the PMTs of the timing counter. The signal reaching the passive splitter is addressed to different lines:

- Line 1: the analog signal sent to the trigger board is used to get a time coincidence between the calorimeter photon signal and the positron signal coming from the timing counter. Timing is obtained by a linear interpolation on the rise front, with a resolution between 2.5 and 5 ns. The coincidence window TC-LXe of the trigger is $10 - 20$ ns.

- Line 2: the analog signal can be view before it is formed. This output can be used to estimate the charge accumulated by each PMT determining the real aging ($100\mathtt{mA}\times100\mathtt{h}$)[137].

- Line 3: the analog signal goes through the double threshold discriminator as shown in Fig.3.26 (left). The double threshold discriminator, through the use of trimmers, allows to set the low ($10 - 300$ mV) or high (10 mV-5 V) threshold level. Once the signal is generated, it is stretched with a ramp signal and then sent to DRS. The ramp generator is designed to produce both a ramp with rise time between 7 and 60 ns and a square wave with rise time of $\sim$ns and a variable amplitude up to 1.2 V, by using a shape selector. In this way, it should be possible to get rid of any problem related to the limited dynamic of DRS.

Once the signal has been split, each copy is sent to a channel of a fast discriminator. One of the copies is delayed of a time longer than the pulse rise-time and then discriminated with the low

---

[7]The splitter could also be an active one, but in this case the bandwidth must be checked to ensure to be wide enough to avoid adding more jitter.
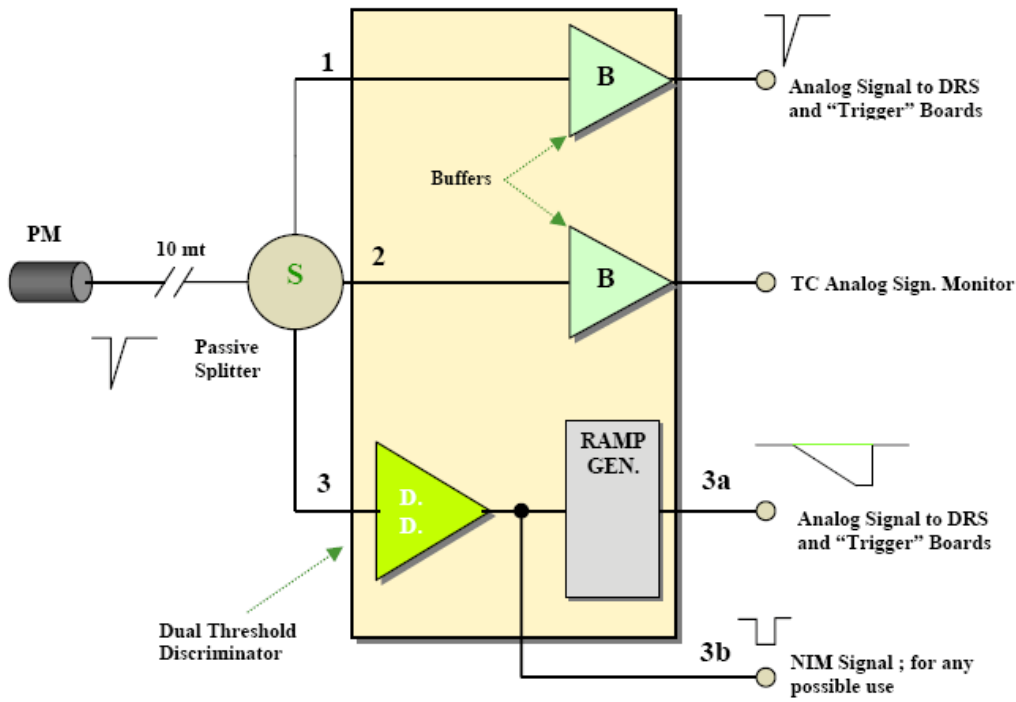
Figure 3.26: Layout of the front-end electronics.
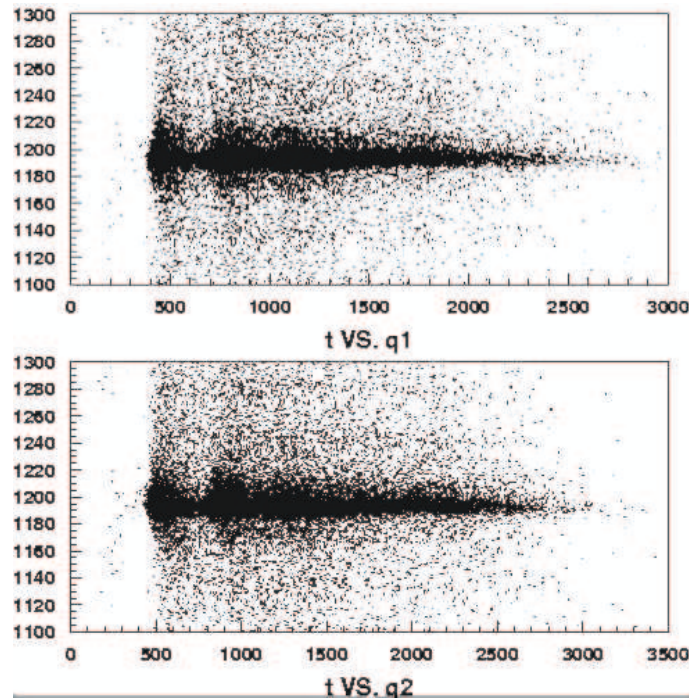
Figure 3.27: Time *vs.* Charge plot for a typical data sample taken during a PSI beam test, for both PMTs. There is no Time Walk effect.

threshold needed for timing; the other is sent directly to a discriminator with a high threshold value. Then both discriminated signals are fed into a coincidence module; since the lower threshold signal has been delayed, it arrives *always* after the higher threshold one, which works as an enabling. The coincidence output is high if both signals are present and its timing is determined by the lower threshold one, which is the most accurate. This method ensures that the discrimination happens with a signal and not with noise pulses, and allows for a better timing response in which the time-walk correction is negligible as showed in Fig.3.27, which shows the amplitude of pulse versus the time registered with no sensitive deviation from linearity (the thresholds have been set to 0.5% of the average pulse height: 3 V).

Because of the loss of gain due to the presence of B field explained we performed some tests with our prototype electronics lowering the PMT gain of 20dB and then recovering the signal amplitude through the splitter/amplifier stage before discriminating it. The resulting time resolution was comparable to the one obtained without the electronic splitter/amplifier[152]. Fig.3.28 shows a comparison between the time resolutions obtained with NIM electronics used in the tests described (Octal Discriminator Philips mod. 710, Delay Time Philips mod. 792 and Logic Unit LeCroy mod. 365 AL) and with the double threshold discriminator that will be in use during the experiment (with lower threshold set to $\sim 30mV$ and higher one set to $\sim 200mV$). The results obtained do not show significant differences.
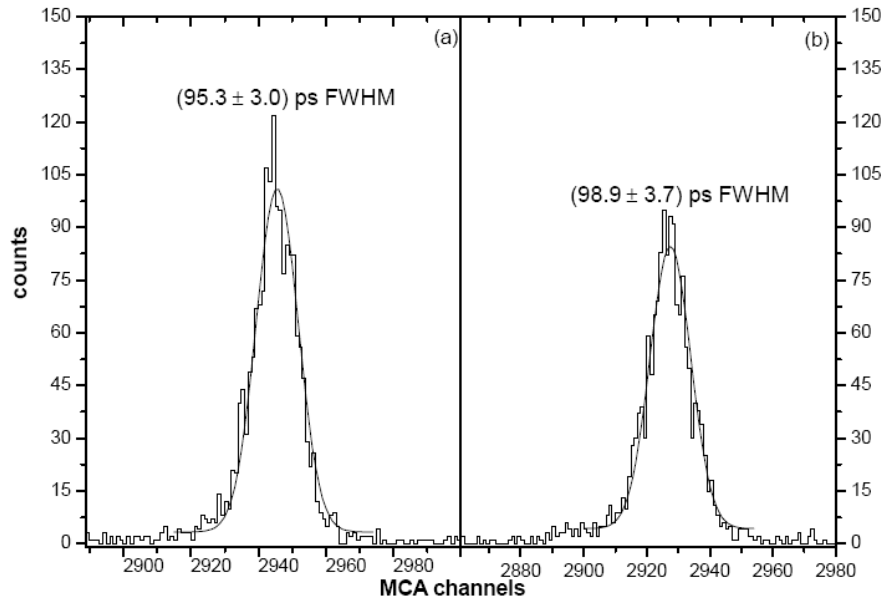
Figure 3.28: Experimental time resolution (see text for details) using (a) traditional electronics, (b) double threshold discriminator prototype.

Conclusions.

The performance of fine-mesh photo multipliers with a diameter of 2 inches R5924 has been measured in magnetic fields (up to 1.2 T) to determine gain and timing properties. Rate capabilities have also been studied.

A study of gain characteristics as voltage changes is also presented.

The PMTs gain dependence from B field have been investigated and the gain loss resulted to be recoverable with an increase of voltage supply.

Timing characteristics of two scintillator bars viewed from both end by R5924 PMTs have been studied.

Using leading edge discriminator with double threshold the time resolution for one bar was free of time walk corrections and was measured to be less than 100ps for a particle crossing 4 cm of scintillator, depending mainly from the photo-statistic of the scintillation process.

3.3.5   Geometry optimization.

Preliminary considerations

The timing resolution is mainly limited by the photo electron statistics, as we saw in previous section, nevertheless [148] the time resolution is proportional to the inverse square root of the path
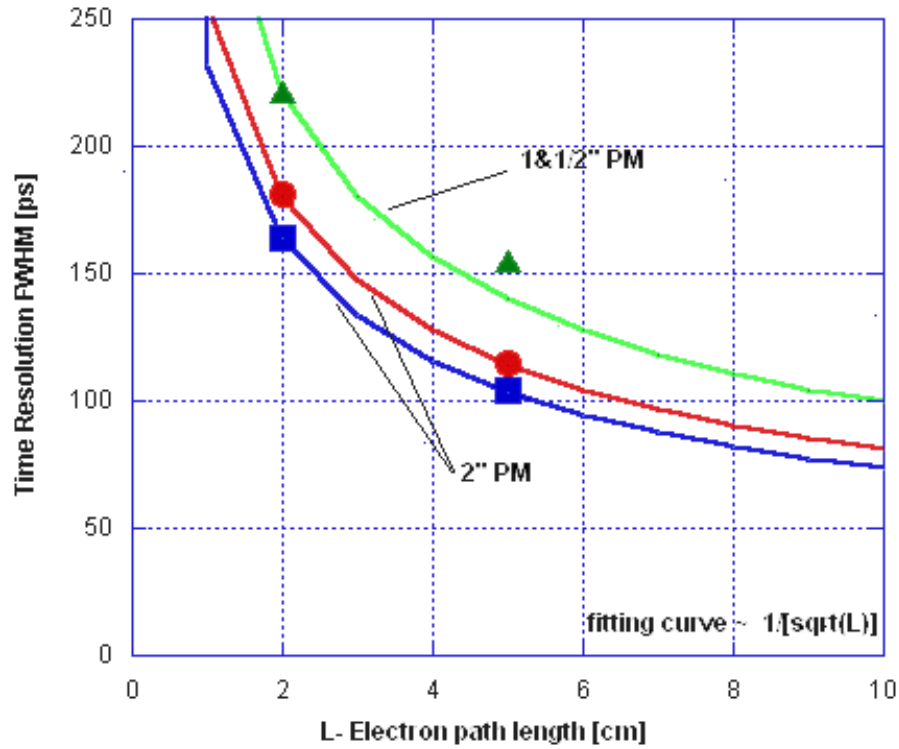
Figure 3.29: Timing resolution as a function of the path length. The curves show the $1/\sqrt{(PathLength)}$ trend.

length of the positrons crossing the plastic scintillators so it would be desirable to have the tracks crossing the maximum length of the scintillators. During tests with several materials and PMTs it was verified this dependence which is strictly related with geometrical optimization. The test took place at the BTF and at the $\Pi E1$ and $\Pi E5$ beam lines at the PSI. Fig. 3.29 shows the trend of the resolution with superimposed the theoretical curves.

3.4 Simulation

The geometry of Timing Counter has been deeply investigated with a detailed Monte Carlo simulation so to choose the proper parameters. In particular impact angles and energy losses have been estimated with great detail in order to optimize the geometry of the scintillator bars and their final position inside the COBRA (Fig. 3.17). In the following we make use of some angles namely:

1. θ is the overall impact angle, defined by

$$\cos\theta = \hat{P} \cdot \hat{n} \tag{3.14}$$

2. β is the angle between the particle trajectory and the bar axis, given by the relationship

$$\cos\beta = \frac{P_X}{\sqrt{P_X^2 + P_Z^2}} \tag{3.15}$$

3. α is the angle between the transverse momentum and the bar, given by

$$\cos\alpha = \hat{P}_T \cdot \hat{n} \tag{3.16}$$

4. γ is the rotation angle of the scintillator bar with respect to the radial versor of the Main Reference System.

In the previous definition $\hat{P}$ is the positron momentum direction, whose transverse component is $\hat{P}_T$; $\hat{n}$ is the normal versor to the scintillator impact side.

Path lengths inside the scintillator, as well as its spreading, are fully determined by the impact angles and the rotation angle of the bar. Since path length spread depends on $1/\cos(\alpha)$ it has a minimum for $\alpha=0$. To achieve this configuration the bar is rotated along its axis by an angle $\gamma = \langle\alpha\rangle$. The new impact angle α' has a narrow distribution with $\langle\alpha'\rangle = 0°, \sigma\alpha' = 8.9°$, as shown in fig. 3.30. The main contribution to the path spread arise from the sweep angle β; which is

$$\frac{\Delta L}{L} \propto \frac{\sin\langle\beta\rangle}{\cos\langle\beta\rangle}\Delta\beta \tag{3.17}$$

which yields, taking $\langle\beta\rangle = (37.0 \pm 7.8)°$, $\Delta L/L \sim 0.11$. The simulation gave as a optimized value for the rotation angle $\gamma = 20.3°$, this is important to achieve a narrow pulse height distribution so to have track lengths as uniform as possible which is the needed condition to optimize the double-threshold implementation to achieve the most reliable performance of the TC. Since the value for γ the support structure was designed to held the scintillating bars with such an angle (in Fig. 3.31).

With this geometry the track spread is given mainly by the equation 3.17 where the angle β distribution is reported in fig 3.32.

In fig. 3.33 is reported the simulated track length distribution for the first bar hit by a positron emitted within the acceptance angle of the TC, while in fig. 3.34 the corresponding energy deposit is plotted. The average values are $\langle L\rangle = 3.705$ cm and $\langle\Delta E\rangle = 7.747$ MeV, respectively. Events with small track length, that results in a small energy deposit, is due to events hitting the scintillator near its longitudinal edges. Due to mechanical constraints, the bar has not a squared cross-section, resulting in a somewhat higher amount of events with small path lengths. As sowed by Fig. 3.34(d) correlation between the energy deposit in the two scintillator bars gives a threshold on the signal from each bar, corresponding to an energy value $\mathcal{E}_o = 6$ MeV, the system will reject only those events with energy deposit less than $\mathcal{E}_o$ on both the bars. The cuts $\Delta E1$ or $\Delta E2 > \mathcal{E} = 6$ MeV discard less than 10% of events. That means the detector is optimized for a high detection efficiency.

The development with use of both (experimental and MC) information led to the actual TC geometry, which is summarized in tab. 3.4. Bars number was determined through accurate Monte
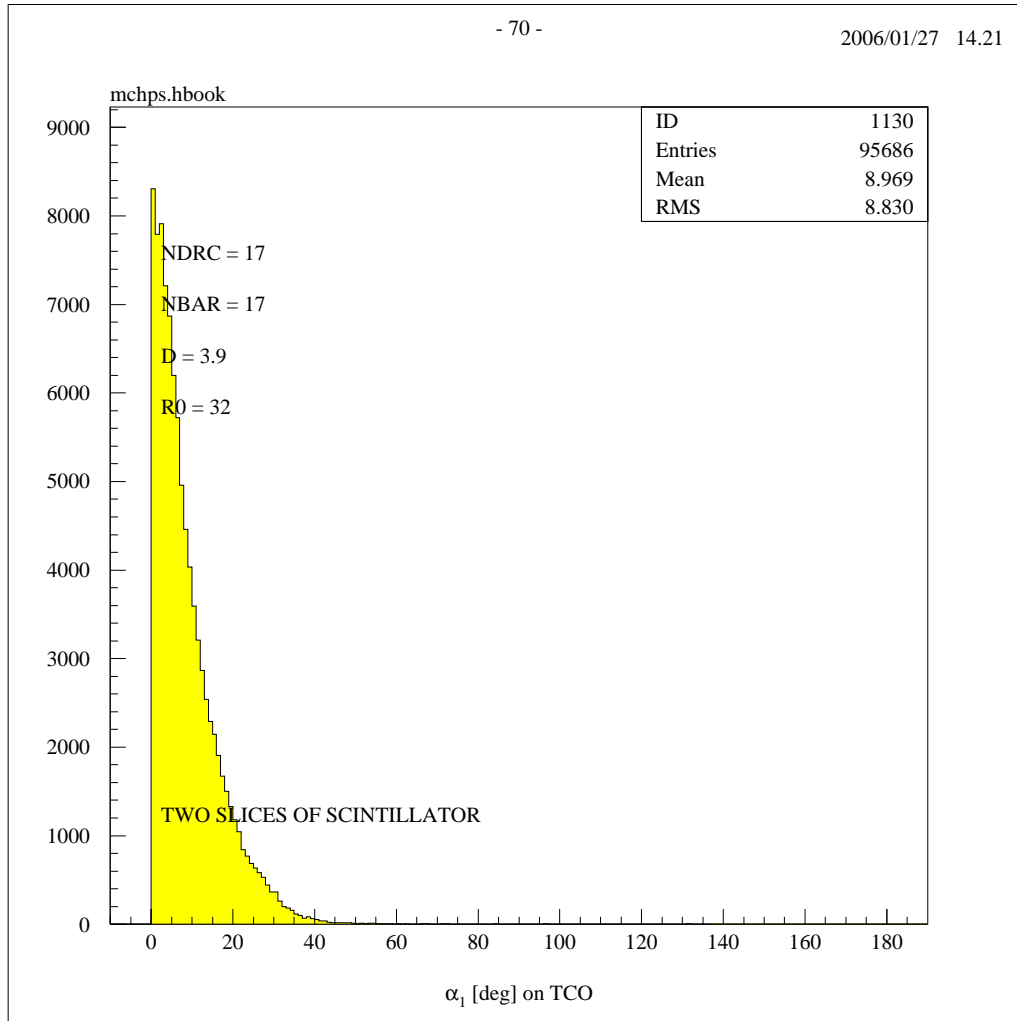
Figure 3.30: Angular distribution of the impact angle α with $20°$ rotated scintillator. Angular spread is small $\sigma\alpha' = 8.9°$.

Figure 3.31: The Timing Counter upstream waiting to be installed. The arrows indicates the support structure (detailed on the right) with not all the bars installed.

Parameter	Value	From
Scintillator dimensions (`cm`)	$78 \times 4 \times 4$	Exp.
Bar rotation angle γ	$20°$	MC
Number of bars	15	MC
Displacement between bars	$10°$	MC+Exp+Eng

Table 3.4: Final geometric configuration of the TC. The last column shows the source which brought to the choice of the value: Monte Carlo simulation, Experimental results, Engineering constraints.

Carlo simulation aimed to determine the best choice for total coverage required to match the LXe and DC acceptances. After angular displacement has been fixed by the simulation matched with scintillator-PMT geometry and the result from actual placement has been again checked with MC code to confirm that the detector geometry was the proper one. As a final result the "geometric" efficiency has been found as high as 95.7% for the final geometry. This last important result will contribute, together with electronic efficiencies, to the final efficiency of the longitudinal detector.

3.4.1   Experimental tests

After having established the geometrical constraints a complete set of 15 scintillating bars has been realized with the final shape and assembled into the final geometrical configuration. Timing resolution of all scintillators with the final configuration found through MC has been tested at the BTF. At the BTF each bar has been tested reproducing the average MC impact angle β, according to the value reported in fig. 3.32 which shows a peak centered at $36.95°$.

With the one-electron multiplicity of the beam we measured the timing resolution for each bar by measuring the time differences between the two opposite PMTs of each bar ($T_1 - T_2$). A
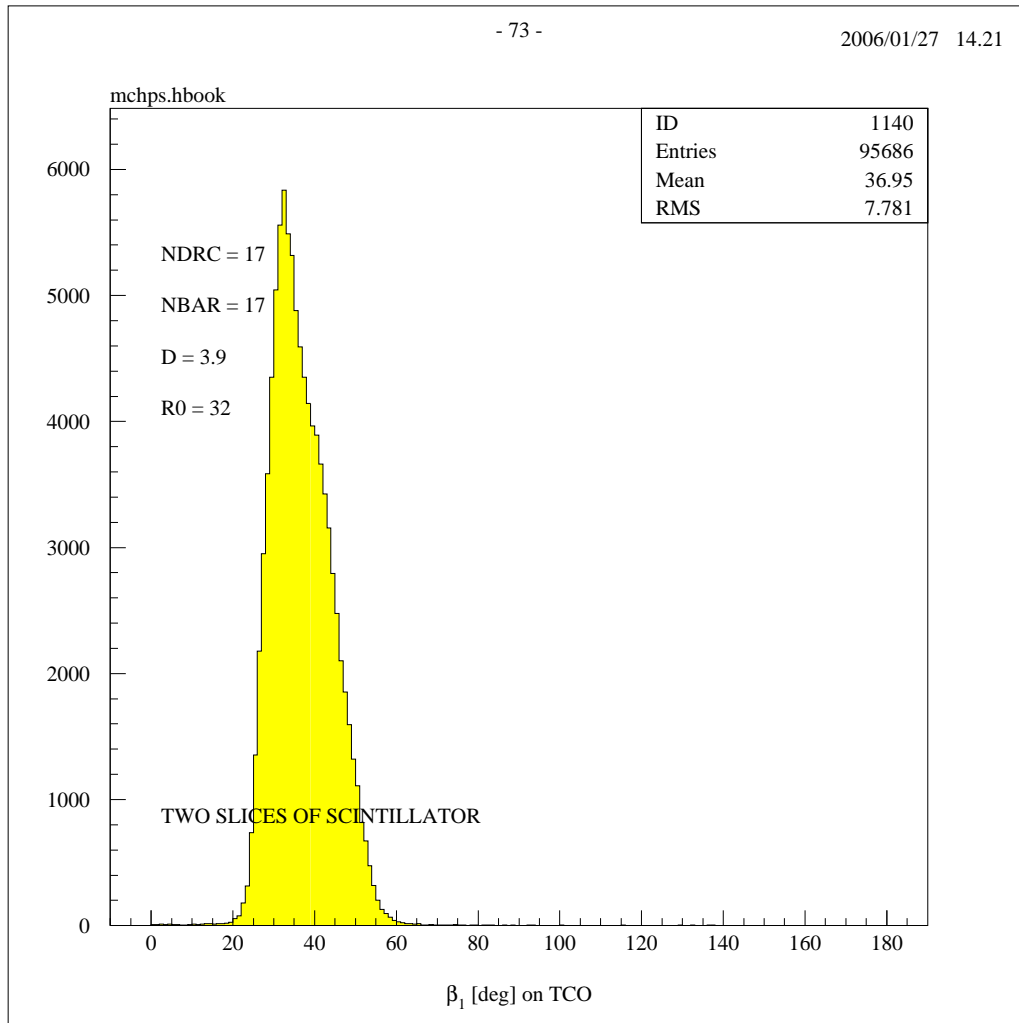
Figure 3.32: Impact angle β on the first bar hit, used for positrons track length optimization.The $\langle\beta\rangle = 37°$.
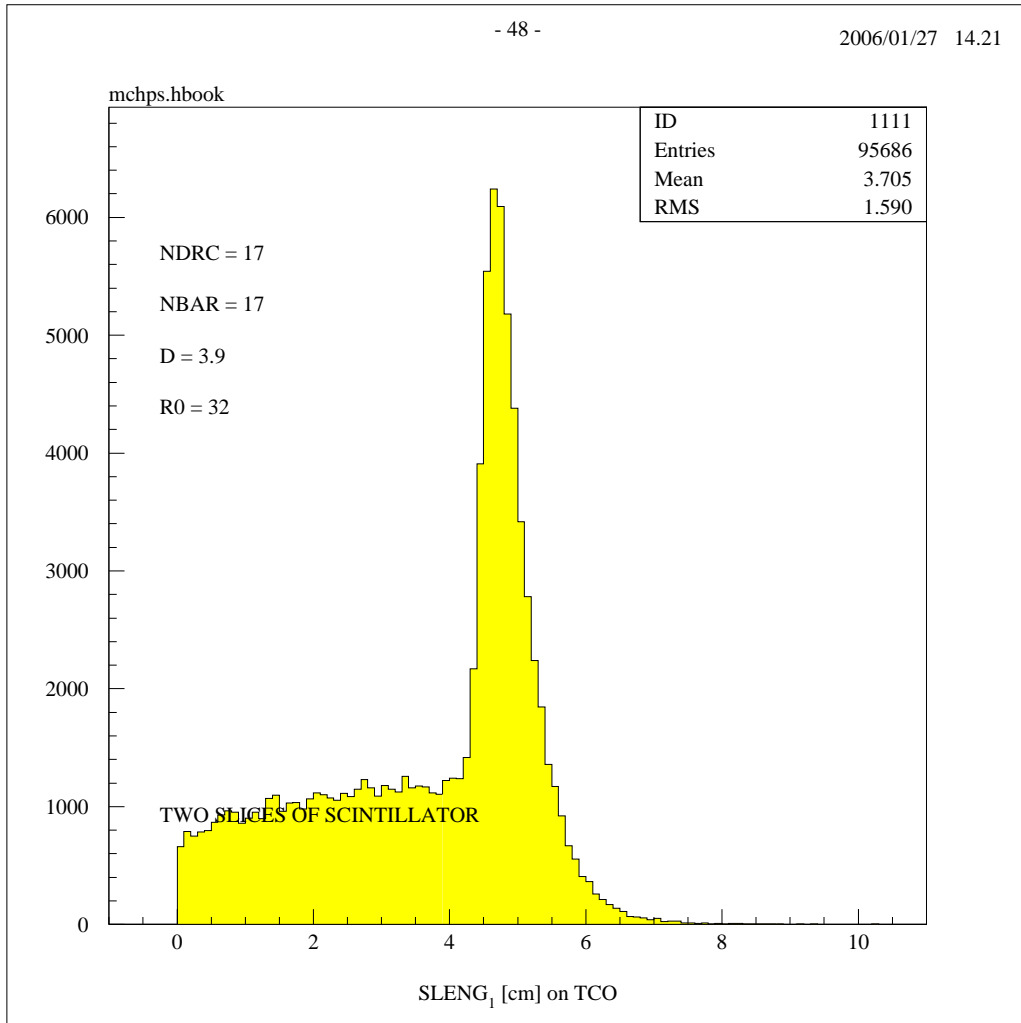
Figure 3.33: Track length distribution inside the first bar hit by positrons.
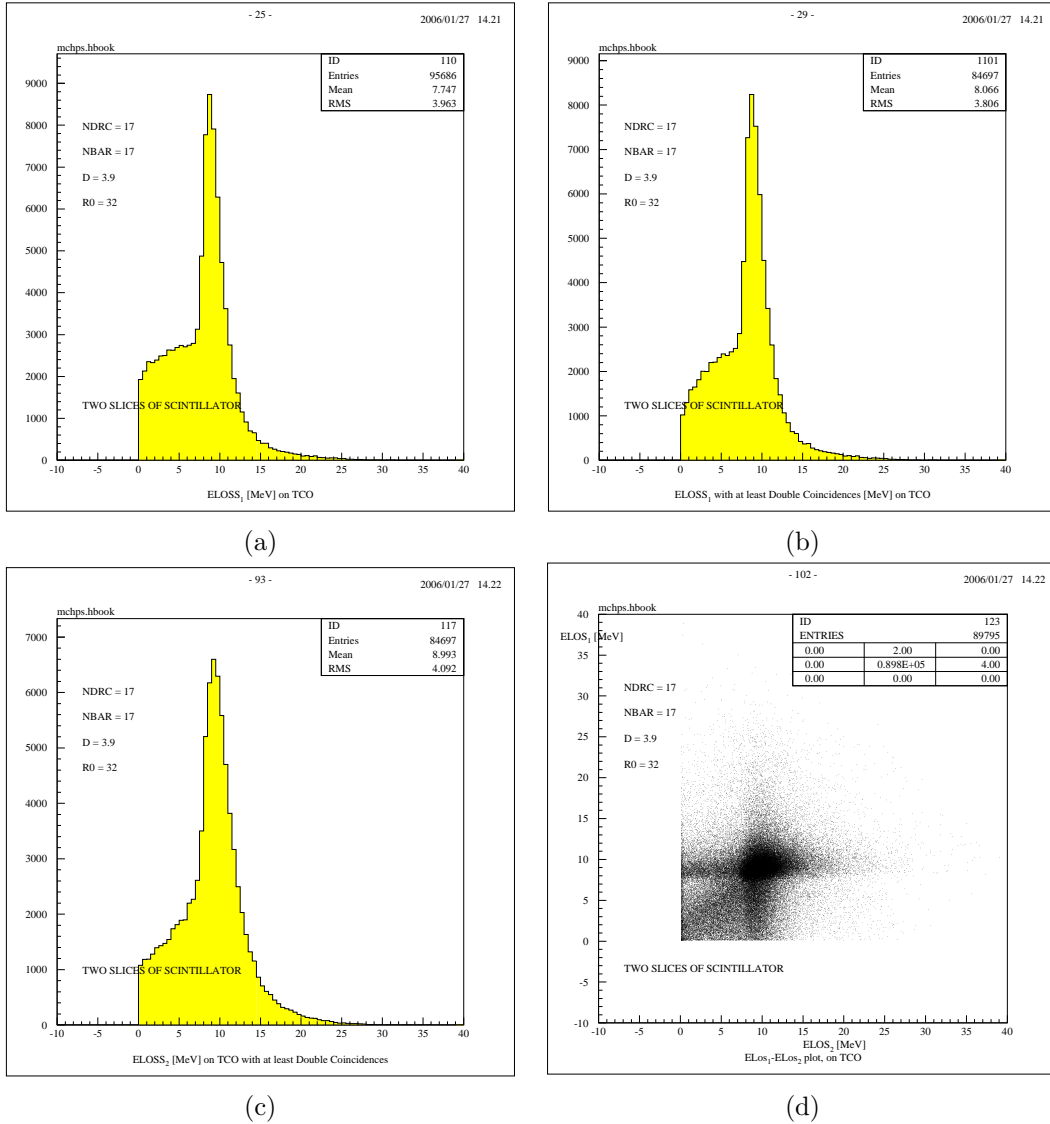
Figure 3.34: Energy deposit on TC bars. (a) energy deposit on the first bar hit, no selection applied; (b) energy deposit in the first bar, for two or more bars hit; (c)energy deposit on the second bar hit, as in previous case. Corresponding average energy deposit are: 7.747, 8.066 and 8.993 MeV (d)Scatter plot of energy deposit in the first two bars hit by a 52.8 MeV positron.

| BarID | z-position along the bar cm | | | | | | |
	+24.0	+14.0	+4.0	-6.0	-16.0	-26.0	-36.0
	time resolution $T_1 - T_2$ ps						
1	73	76	87	85	85	69	66
2	112	87	88	95	89	94	93
3	114	94	81	65	72	86	93
4	123	72	70	88	66	75	89
5	100	90	106	87	98	83	93
6	96	86	94	87	93	87	86
7	92	79	73	86	75	83	93
9	77	76	68	76	77	69	96
10	80	78	84	81	90	84	102
11	75	96	102	93	98	93	80
12	110	78	90	86	65	68	78
13	112	89	78	68	80	90	96
14	126	80	92	71	88	68	65
15	99	80	81	91	81	87	73

Table 3.5: Experimental resolution for a complete set of TC scintillator bars. The z-coordinate is measured from the center of the bar, along its longitudinal axis and is relative to the impact point of the positron on the front face. Quoted resolutions are in ps FWHM. Bar ID is for our reference and does not correspond to a precise positioning of the bars in the final TC.
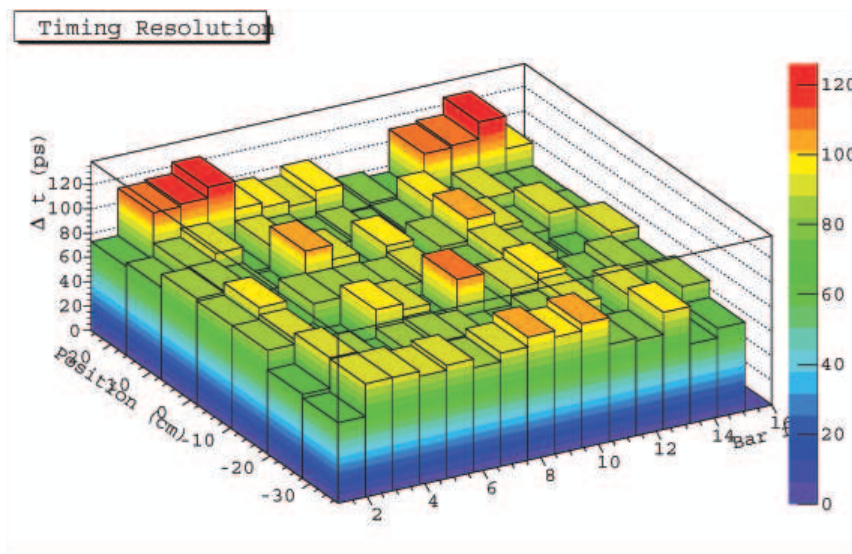
Figure 3.35: Timing resolution versus position along the bar. The resolution is in most cases well below the experimental requirement.

proper beam spot with size $\Delta z = 0.5$ `cm` on the bar has been defined by means of two coincidence counter that triggers the whole acquisition. Tab. 3.5 summarizes the time resolutions measured. Quoted resolutions, in `ps` FWHM, are estimated using a fitting algorithm implemented in the Multi-Channel Analyzer MAESTRO.

3.4.2   Conclusions.

The timing resolution of the single counters has been studied. The simulations helped in the choice of the proper materials and geometry as for the bars as for the PMTs. The gain loss due to magnetic fields has been proved to be recoverable with a voltage increase. The final resolution resulted mostly better than the required value, being worse than 100 `ps` only in few points. It could be useful to notice that using two bar coincidence, the timing resolution is improved by a factor $\sqrt{2}$, which should be a good way to improve performance in the final configuration.
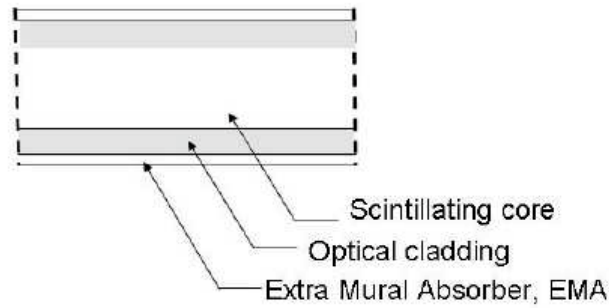
Figure 3.36: Elements of a scintillating fiber.

3.5   The transverse sub-detector

.

3.5.1   Scintillating fibers

APDs coupled scintillating fibers are recently used for impact point detection of charged particles,. Their small diameter allows to have a low occupancy rate; besides, a fluorescence time decay as short as a few nanoseconds makes a high rate operation possible, being able to be used as trigger pulses generator. Figure 3.36 shows the typical elements of a plastic scintillating fiber.

The scintillating core material is clad with a non-scintillating material of lower refractive index, which is at least several wavelengths thick. A thin opaque extra absorber, EMA, can be applied to the outer fiber surface, primarily to eliminate crosstalk among adjacent fibers. Even if this shall cause a small decrease of the signal intensity. There is also a special class of fibers named Multi-clad, which have a second layer of cladding with an even lower refractive index, permitting a total internal reflection at a second boundary. The additional photons guided by multi-clad fibers increase the output signal up to 60% over conventional single clad fibers.

The fiber used for the final detector is BCF 20 Multi-clad produced by Saint-Gobain Crystals Inc. It has an emission peak at 492 nm, a time decay of 2.7 ns and a nominal attenuation length greater than 3.5 m. It yields ~ 8000 photons per MeV for a minimum ionizing particle. The main characteristics are summarized in Table 3.5.2.

The reason to choose a square section scintillating fiber is because it is simpler to identify a positron fully crossing the fiber giving the possibility to set a threshold near to the maximum energy release so to improve the efficiency.

In a square section fiber the light (L) piped along the material is almost independent from the light emission position within the volume of the fiber. In a circular section fiber, instead, L is a function of the emission position and increases with the particle *impact parameter*, that is the normal distance from the fiber center in units of radius.

For the case of a square fiber the transport efficiency can be estimated using the Snell law as the

fraction of photons emitted inside the guiding solid angle $\Omega/2\pi$. This can be evaluated by

$$\Omega = \int_0^{2\pi} \mathrm{d}\phi \int_0^{\theta^*} \sin\theta \mathrm{d}\theta \qquad (3.18)$$

where the fiber axis is the $z-$axis, with its sides parallels to the x and $y-$axis respectively. So the incidence angle α is given by $\vec{r}\wedge\vec{n} = \sin\alpha_y = \sqrt{1 - \sin^2\theta\sin^2\phi}$ or $\vec{r}\wedge\vec{n} = \sin\alpha_x = \sqrt{1 - \sin^2\theta\cos^2\phi}$ for incidence respectively on the $y-$sides or on the $x-$sides. The limits of integration in Eq. 3.18 are given by $sin^2\alpha < (n_{clad}/n_{core})^2$, where n_{clad} is the cladding refraction index while n_{core} is the fiber's core one.

The resulting collection efficiency is so [145]

$$\mathcal{E} = \frac{1}{2\pi} \cdot 4 \int_{-\pi/4}^{\pi/4} (1 - \sqrt{\cos^2\phi - \frac{n_1^2 - n_2^2}{n_1^2}} \mathrm{d}\phi \qquad (3.19)$$

after the integration on θ and considering the total solid angle as the sum of four equal contributions from each side. The resulting transport efficiency is 7% for $n_1 = 1.60, n_2 = 1.42$.

3.5.2 APD

Photo detectors made of semiconductor materials received an increasing interest in recent years, being specially tailored for the needs of optical applications and being produced at a relatively low cost. Size, and geometry in general, spectral response and other parameters such as reduced power requirement, reduced sensitivity to temperature and insensitivity to magnetic fields, can be obtained easily by choosing the right device. The detectors can be produced with several kinds of semiconductor materials: Si, Ge, GaAs, InGaAs, but also of materials with wide-band gap like InI, AgI2, PbI2, TlBr for applications at high temperatures or for a particular spectral response requirement.

Since the number of photons captured at the end of the fiber depends on the geometry matching, it is very important to find a photon detector with high quantum efficiency and good geometrical matching to read out each fiber efficiently.

Hamamatsu Photonics developed avalanche photo diodes which are well-suited for these demanding applications. This APD is made by epitaxial growth on low resistivity N-type silicon and by ion implantation and diffusion.

The P-type material in front of the amplification region, which forms the P-N junction, is less than 7 μm thick, in order to reduce the sensitivity to ionizing radiation. Surface currents are suppressed by making a groove, which is $\sim$30 μm deep and wide as showed in Fig. 3.37.

In the MEG detector the S8664-55 APD type was used, which has an active surface of 5×5 mm^2 and matches perfectly the dimensions of scintillating fibers. Furthermore, as shown in Fig. 3.37, the quantum efficiency (Q.E.) of this device is more than 80% for wavelengths in the range 500-800 nm. In comparison with photomultiplier tubes, APDs have several advantages: the Q.E. is typically a factor of 3 higher than for a PMT (for a PMT the Q.E. does not exceed 20-30%) and since the thickness is less than 1mm and the weight is only few grams, they can be easily mounted

<center>(a)   (b)</center>
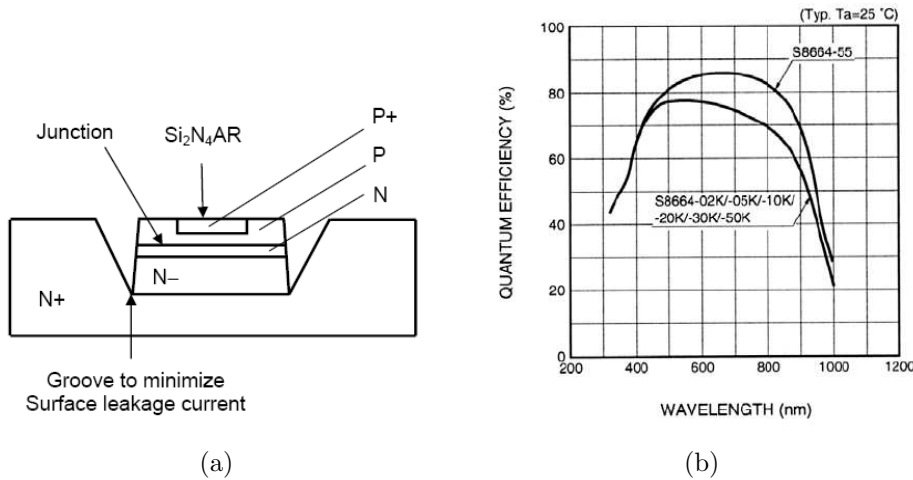
Figure 3.37: (a)Scheme of Hamamatsu Avalanche Photo Diode (AR stands for anti-reflecting) (b) quantum efficiency as a function of wavelength for an APD (type S8664) for different active areas.

in complex systems and can work in high magnetic fields. However, APDs have a relatively small gain (~ 100), and a charge amplifier is needed.

The charge amplifier is a reliable solution for read out of a charge signal from a capacitive detector[143]. Its working principle relies on the effective transfer of the charge generated inside the solid-state detector to a feedback capacitor C_f in a closed-loop amplifier: in this way the output voltage is related to the charge generated by energy release inside the detector by the simple relationship $V_{out} = Q/C_f$. The gain of the charge amplifier used for this sub detector is 1 `V/pC` ($1.6 \ 10^{-7} V/e$)[141].

The total output signal is $V_{out} = Q \cdot G_{charge} \cdot G_{shaper} = 2.5 \cdot 10^4 e/\texttt{mm} \cdot 1.6 10^{-7} V/e \cdot 15$ ($\sim$) 60 `mV` for each `mm` of fiber crossed by e^+.

Where G_{shaper} is the gain (24dB) of a shaper stage and with a value of 500 for the APD gain.

The APD readout ensures that the performances of this detector are quite independent from the magnetic field. PMT read out would be difficult due to the orthogonal placement of the fiber slices respect to the B field which causes a large gain loss with respect to normal operation. This is true even for the fine-mesh type which can be used successfully up to 1 `Tesla` of magnetic field intensity and with the axis rotated by a small angle with respect to magnetic field direction, as described previously for the longitudinal detector. PMTs could be used in such conditions by building a detector with suitable light-guides allowing for a better placing of PMT, *i.e.* with a maximum angle between tube axis and magnetic field lines of 30°.

3.5.3   Experimental tests: APD

To obtain the higher gain (order of 1000) the APD must operate near the breakdown region. Both the breakdown Voltage and the dark current (the current flowing when the APD does not receive

Table 3.6: Main characteristics of square fibers BCF-20 with double cladding

Property		value
Light Yield	(phs/MeV)	8000
density	$(g/cm3)$	1.05
core refractive index (r.i.)	n_{core}	1.60
1st cladding r.i.	n_{inter}	1.45
2nd cladding r.i.	n_{clad}	1.42
Trapping efficiency		7%
Numerical Aperture	NA	0.74
Attenuation length	cm	3

light) depend on the working temperature.

APD gain is proportional to its working temperature. The colder it is, the longer electrons mean free path between elastic collisions with the lattice. Consequently electrons will gain more kinetic energy for an equal electric field and ionization rate and gain increases.

As in every semiconductor thermal generation of electron-hole pairs decreases with decreasing temperature, since the probability for electrons to cross the band gap decreases exponentially with temperature. In an APD the dark current rises as the temperature falls, but there is no contradiction with what just stated. The dark current is $I_D = I_s + M \cdot I_b$ where surface leakage current, I_s flows through the interface between the PN junction and Si oxide layer, and bulk current, I_b, is generated inside the Si substrate. The surface leak current is not multiplied since it does not flow in the avalanche region, while the bulk current is multiplied and this explains the gain increase.

The first step in characterizing the devices was to set a condition as near as possible to he MEG final one.

Studies [140] of thermal dependence have been done. The setup for the test is the following: a pulsed laser (model NDHV310ACA with AVTECH pulsing system) with $\lambda = 408$ nm simulates the light coming from the scintillating fiber. The pulse from laser excites the APD (few nanoseconds) which is kept at different temperatures by a Peltier cell and a thermocouple PT 100 is used as a thermal sensor.

A photometer sensitive to wavelengths in the range 190-1100 nm (NEWPORT, Mod 2930C) and the photo multipliers as sketched in figure 3.38 are used to monitor the amplitude and the duration of the light pulse and to determine the number of incident photons.

In figure 3.39 the dark current as a function of the bias voltage for an APD of the MEG experiment at five different temperatures is shown. It indicates that for a given bias, the dark current is much larger at higher temperatures. On the contrary, observing the zoom in the figure near the breakdown voltage (right of figure 3.39) for a fixed bias voltage the dark current is larger for lower temperature due to the exponential increase of APD gain in the breakdown region and the decrease of the breakdown Voltage with temperature Fig.3.40.

It is important that the number of thermal electrons decrease with decreasing temperature and

(a)   (b)
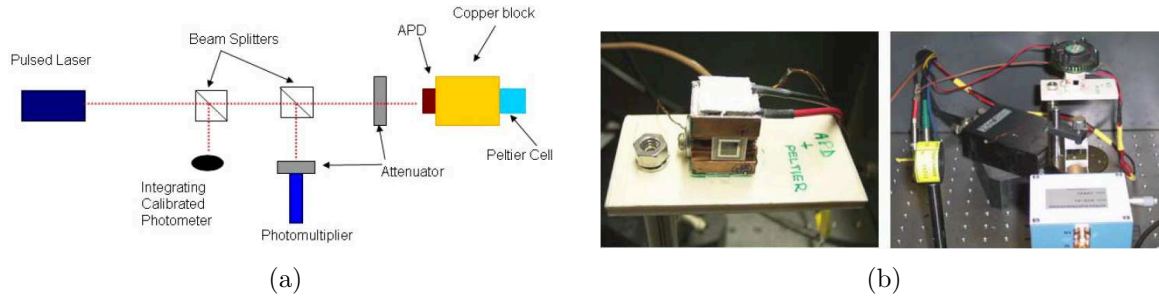
Figure 3.38: testing system for the APDs characterization:(a) Schematic view, (b) experimental setup; it's clearly visible the Peltier cell for thermalization.
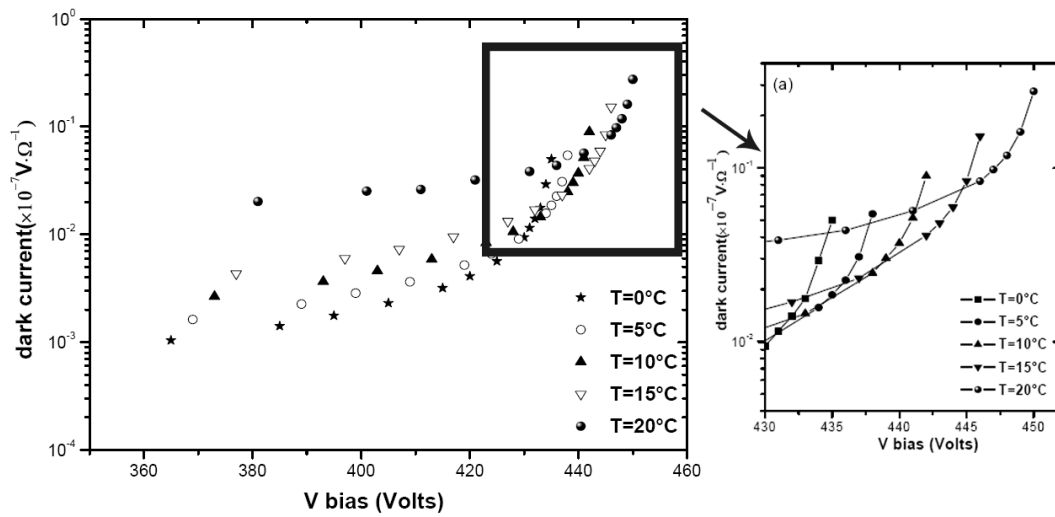
Figure 3.39: Dark current as a function of voltage bias at different temperatures. The current is measured across a 10 $M\Omega$ resistance in series with the APD.The zoom is the part where the
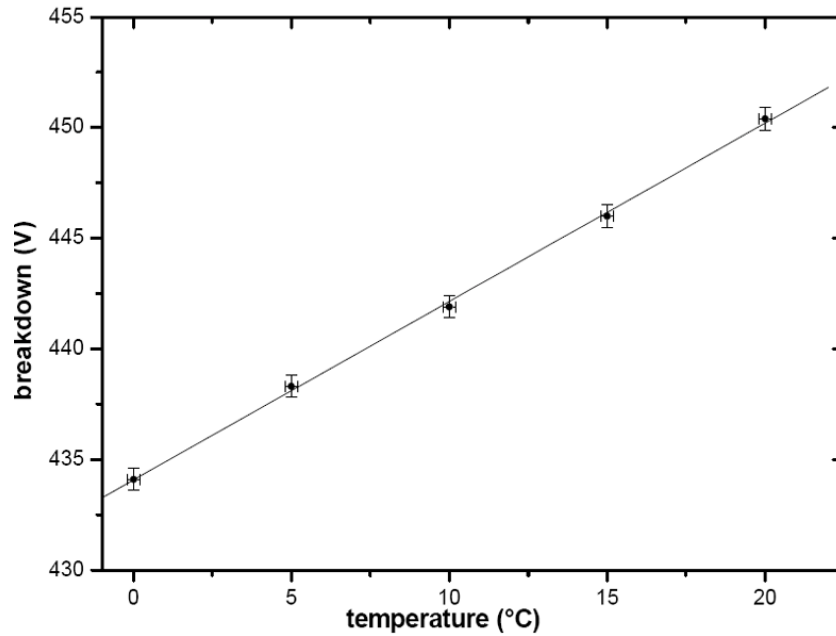
Figure 3.40: Breakdown voltages as a function of different temperatures (dots) and Linear fit (line).

so decrease the signal-thermal noise ratio which is proportional to the number of electron-hole pairs, independently from the gain. To keep the temperature as low as possible so to maximize performances a water cooling system made of 2 thermoelectric chillers (400w each) with water pipes has been used for the final detector design (figure 3.43).

From a fit of measures (Figure 3.40) the temperature coefficient, which indicates the change of the breakdown voltage as a function of the APD temperature, results 0.80 ± 0.03 $V/°C$ in agreement with the value reported by the manufacturer (see Table 3.5.2).

The measurement of the breakdown voltage are in agreement with those given by the manufacturer within 1%. From figure 3.41 we can see the dependence of gain from the break down voltage, obtained for two different wavelengths.

3.5.4 Experimental tests: fibers.

Scintillating fiber are shaped to follow the curvature of the magnet so they have an average radius of 288.9 mm (Figure 3.42). The APD needs 10.6×9.0 mm^2. For this reason the fibers differs at the end both in length, 22 cm, and in shape (Figure 3.43 shows the final part of the fibers) to allow the coupling with the APDs.

It is important that the light collected inside the fiber reaches the APDs with the minimum loss.

Monte Carlo simulations helped in estimating the amount of energy released and the average
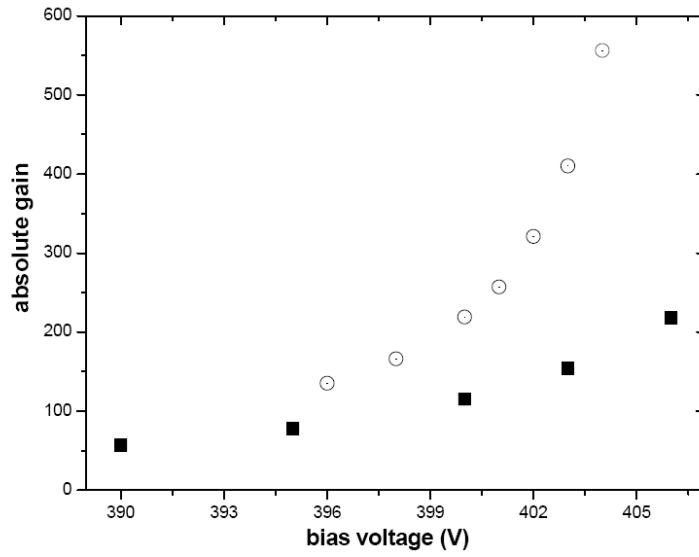
Figure 3.41: Wavelength dependence of APD gain at 408 nm (square) and 780 nm (circle).

(a)   (b)
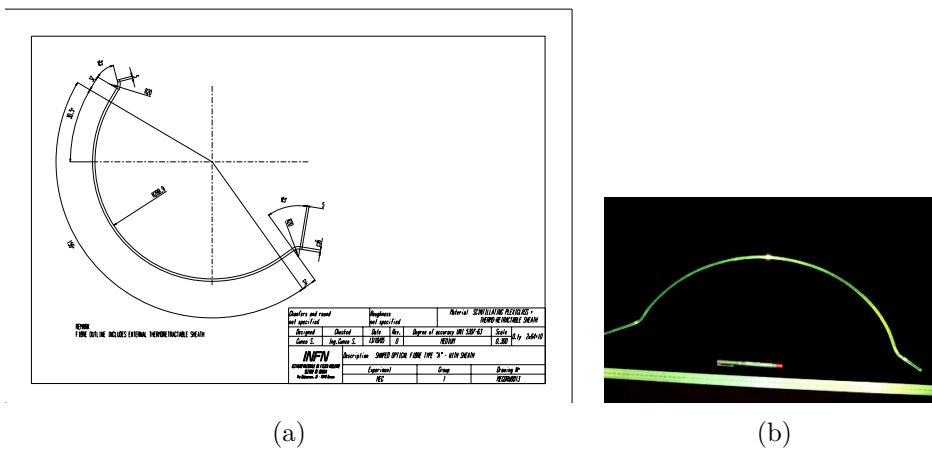
Figure 3.42: (a)Mechanical scheme of the shape of a fiber (b)A fiber as in its final shape.
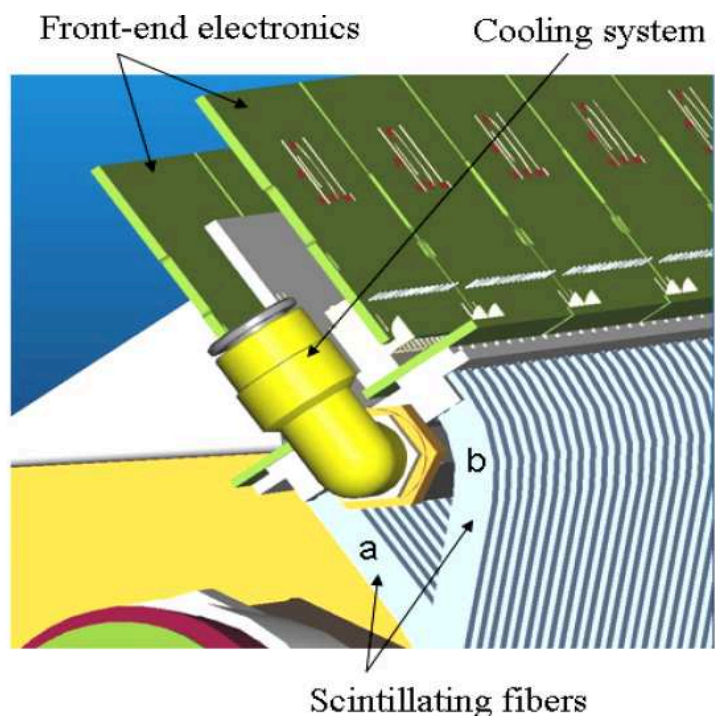
Figure 3.43: Layout of final part of scintillating fibers; notice the two ends shape with different lengths; electronics and cooling system for APDs are also visible.
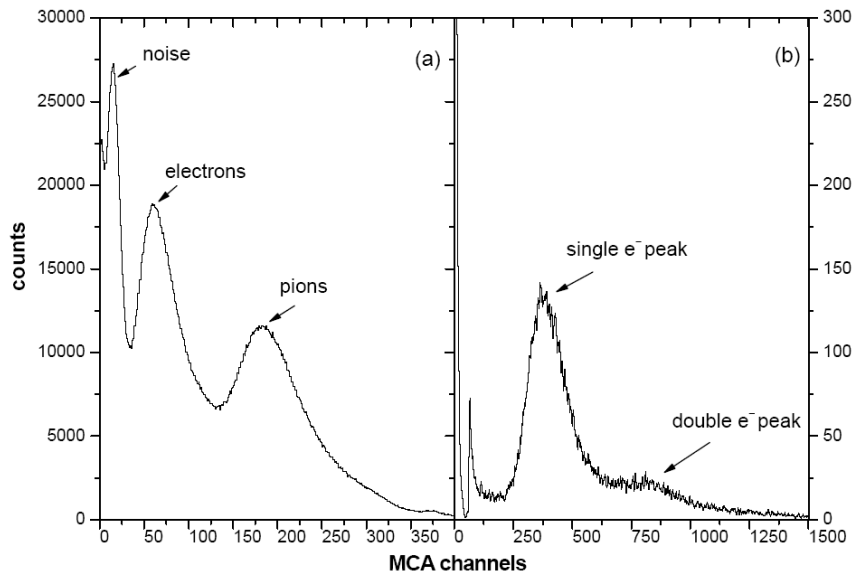
Figure 3.44: Spectrum obtained with e^- π beam at PSI (a) and with e^- at LNF (b).

number of crossed fibers per event. Figure 3.50 shows that the energy released by the positrons inside the fiber is less than 1 `MeV`, and that on average two fibers are hit.

To investigate the overall signal to noise properties of the fiber-APD measurement of attenuation length have been executed at PSI and BTF using pieces of fibers coupled to APDs. From this tests results:

- that photon yield at the fiber output is high enough for APD readout. In Figure 3.44 (a) the spectrum obtained from a 5 cm scintillator fiber coupled with an APD acquired during the PSI tests is reported. The two peaks referred to electrons and pions, coming from the πE1 beam line, are clearly visible. Figure 3.44 (b) shows the charge spectrum made at the BTF (LNF) beam test, where single and double electron peak are well separated.

- That signal to noise ratio is high enough to fire a discriminator acting as a 1-0 detector (fiber crossed-not crossed). It is worth noticing that the electronic readout is switched on only if both APDs reading a fiber receive enough photons to turn on the discriminators.

- Attenuation length measurements was done first at BTF. Figure 3.46 shows a exponential fit which gives a value of 65±4 `cm`. Then through the usage of a ^90Sr radioactive source (2.7· 10^6 Bq). The experimental setup is shown in figure 3.45. Sr shows a β^- decay in ^90Y which also decays β^- with an end point energy of 2.28 MeV [146]. In this condition the energy released inside the fiber is comparable to the one resulting from the MC simulation. The readout was both through a APD and a PMT and the results are in figure 3.47, from a double exponential fit can be extracted two different attenuation lengths one of the order of 2.5 `m` more in accordance with the value given by producer and the other one of about
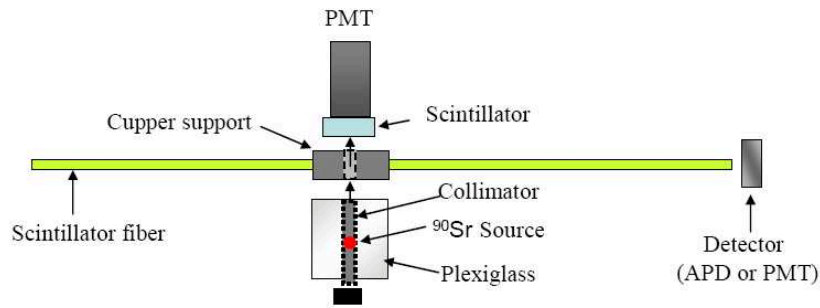
Figure 3.45: Experimental setup for the attenuation length measurements with ^{90}Sr source.
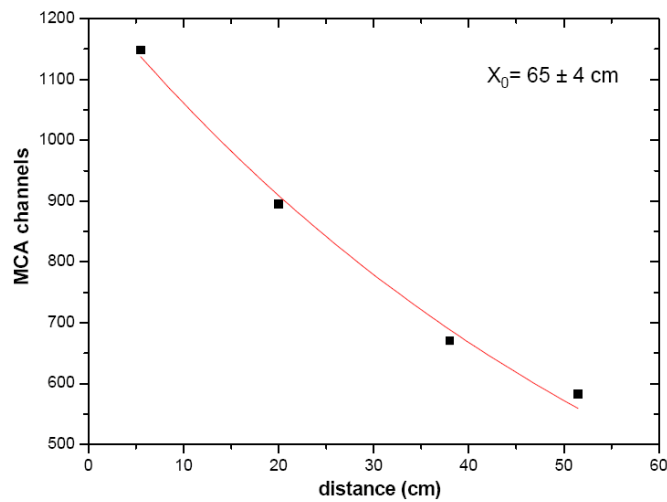
Figure 3.46: Measurement of the attenuation length using the data from the BTF tests (dots) and exponential fit (line).

20 cm. The producer values are reported in figure 3.48. The main differences between the measurements and data sheet can be addressed to double-cladding of fibers which make it possible to observe three different attenuation lengths (for fibers longer than 1m [140]). At distances of 40-50 cm, typical of the MEG experiment, the light is influenced by the shortest attenuation length, with a signal reduction of more than 50% because of losses at the outer cladding. To enhance the light collected inside the fibers a double layer of reflective material covers both the surfaces (inner and outer) of the actual sub detector.

• Emission spectrum resulted in good agreement with the one from the manufacturer and is shown in figure 3.49 [140].

Table 3.7 summarize the measurements comparing them with the producer values.
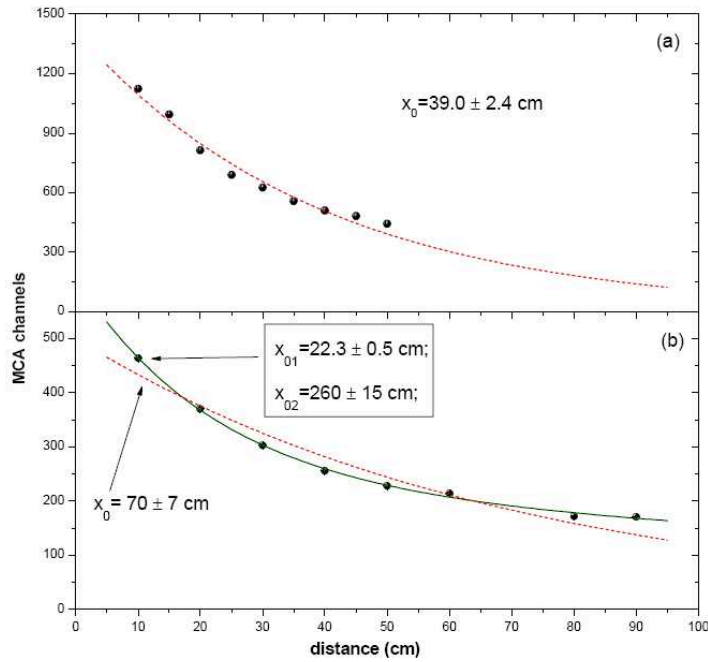
Figure 3.47: Measurements of the attenuation length using a APD (a) and an PMT (b) as detector. Points and dashed lines represent the experimental data and a single exponential fit respectively. Solid line represents a double exponential fit.
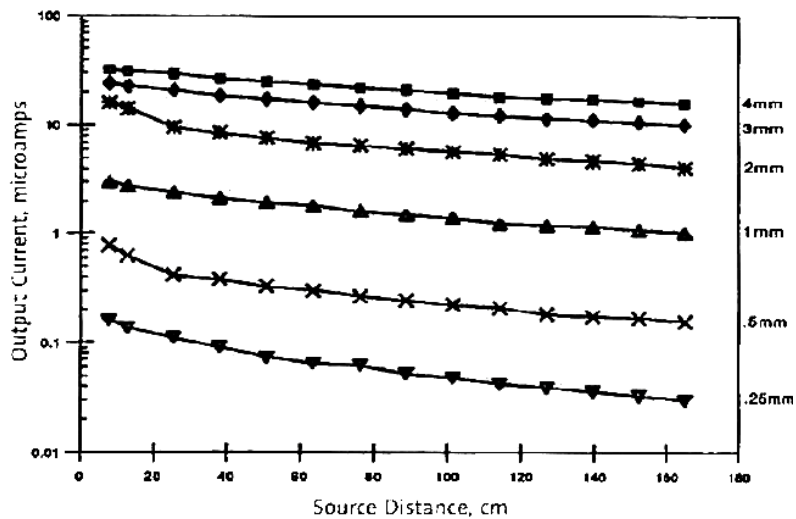
Figure 3.48: Attenuation length as given by the producer for different size section fibers measured with ^{90}Sr source.
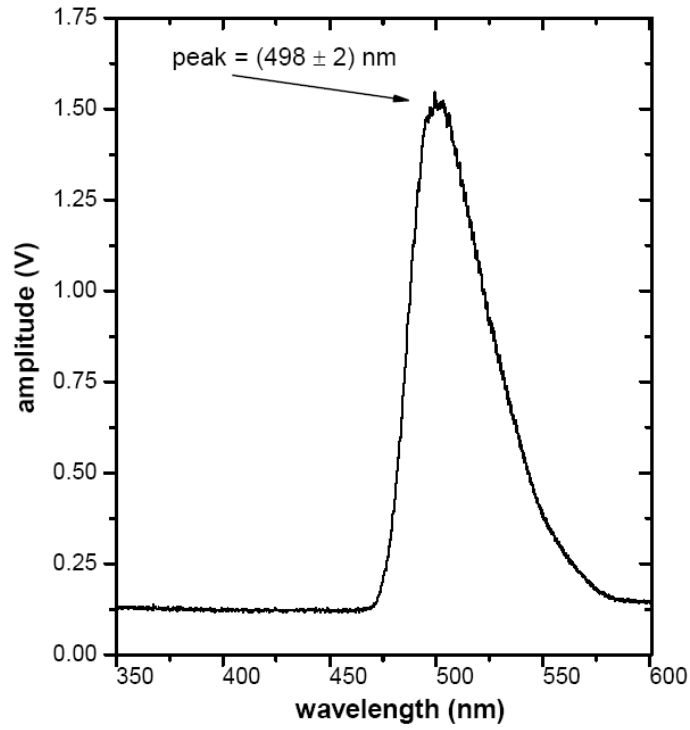
Figure 3.49: Measured spectral response for BCF20.

Table 3.7: Fiber parameters.

	Expected	Measured
Emission spectrum peak	492 nm	498.5 ± 2.0 nm
Attenuation length	≥ 3.5 m	X1= 22.3 ± 2.3 cm X2= 260 ± 15 cm
Cladding-core ratio	1.37	1.44 ± 0.18
Trapping efficiency	7.3%	6.6 ± 0.5 %
Light efficiency loss - final design	Not available	26 ± 2 %
Efficiency loss - annealing process 120°C	Not available	Below instruments sensitivity
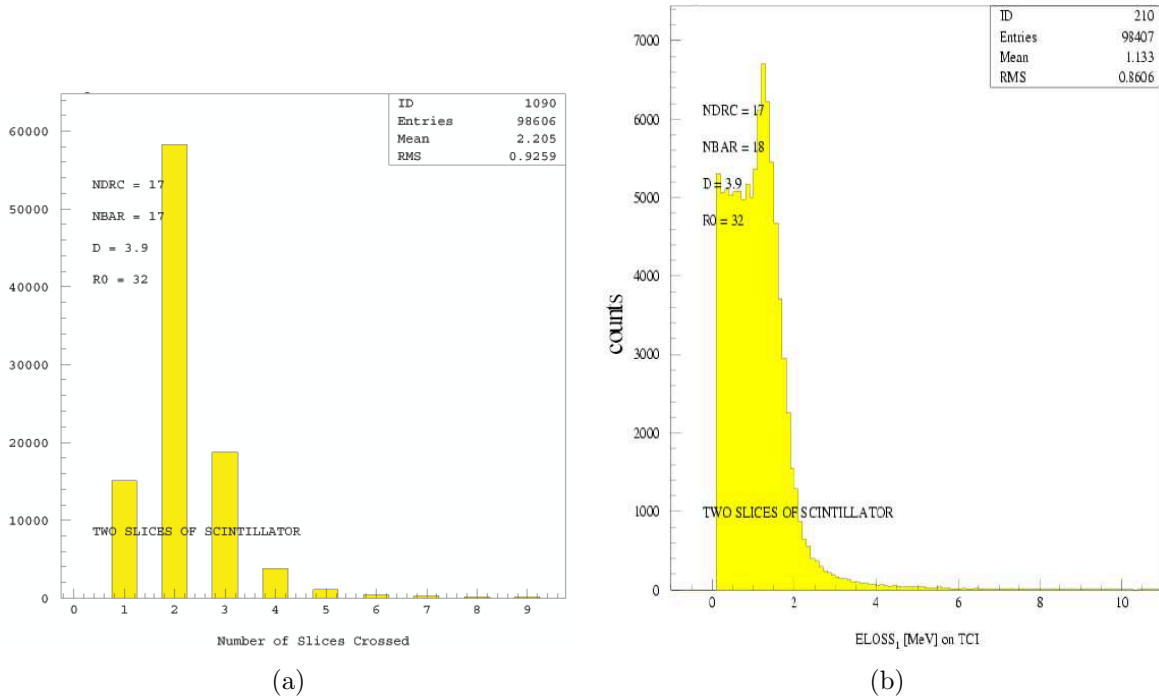
Figure 3.50: (a) Distribution of positron events in hit fibers, (b) energy loss inside fiber. Both obtained from MC simulations.

3.5.5   Signal estimation

From the properties of the scintillating fibers (table 3.1) we can estimate the signal produced by a particle crossing a single scintillating fiber. The energy loss for 52.8 `MeV` positrons is approximately 2 `MeV/cm` with a light yield (8000 ph/`MeV`), the fiber collection efficiency (7.3%) and the APDs quantum efficiency (QE $\approx$ 0.8), we have a signal at the fiber's end of about 100 ph/`mm` . We are not accounting the light which remains trapped at the outer interface; its contribution to the total light piped is not small due to the low reflectivity of the outer surface. This is caused by both geometrical and surface properties such as scratches, powder and fingerprints absorbing photons. The curvature of the fiber has a greater effect on this fraction of light. By means of MC simulation of positrons hitting the TC we obtained some noticeable results, which can be used for the efficiency estimation of the sub detector.

From fig 3.50 we see that almost 90% of events have positron hitting two consecutive fibers and most of the events are split between two or three consecutive fibers.

To achieve a good detector efficiency (η_{tot}) it's needed enough energy deposit at least in one fiber so to produce a detectable signal.

We are confident in detecting positrons with path length inside the fiber of at least 2 `mm` (giving a signal of the order of 100mV).

We can consider this as the minimum detectable signal. We checked through MC simulations the
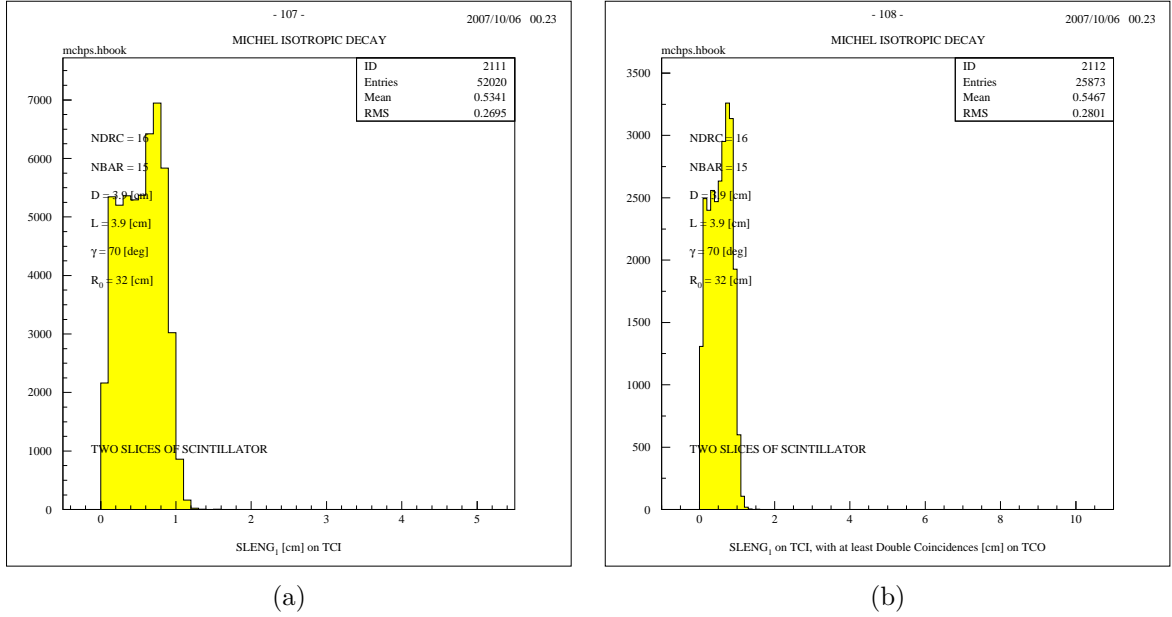
Figure 3.51: Track length of positrons inside fibers: the fraction of events with track length less than 2 mm is 13%.

expected efficiency. The simulation results, reported in figure 3.51(a), shows that only 13% of events have less than 2 mm path length. In Fig. 3.51(b) is reported the path length distribution for positrons hitting two fibers. These events are about 60 % of total.

Positrons with three or more fibers hit are about 25% of the total events. For these kind of events the hit has, from geometrical considerations, at least 5 mm of track length (in the second fiber) so we can consider for them an almost maximal detection efficiency of 99 %. Events with only one fiber hit have also track length forced by geometrical constraints to a minimum value of 5 mm. Thus for them also we can take a 99 % efficiency. From the MC (figure 3.50) we have the geometry efficiency for the detector of 98.6%. Combining these data, the overall efficiency for the inner TC can be estimated higher than ($\sim$90%):

$$\eta_{tot} = (\eta_1 \cdot \mathcal{P}_1 + \eta_2 \cdot \mathcal{P}_2 + \eta_{\geq 3} \cdot \mathcal{P}_{\geq 3})\eta_{geom} \approx (0.99 \cdot 25\% + 0.87 \cdot 60\% + 0.99 \cdot 15\%) \cdot 0.986 = 0.905 \quad (3.20)$$

where η_i are the efficiencies of positron with i fiber hit and P_i are the probability of that kind of event.

3.6 Conclusions.

The geometry and implementation of the impact point sub-detector has been presented, the motivations of the choices both for materials and electronics have been clearified. The performed tests

gave good results and have been shown. The efficiency from MC simulations is expected to be as high as 90% which will reduce of a factor 10 the trigger rate. The sub-detector is inserted recently into the final position inside COBRA magnet and there will be soon experimental results in the final setup.

Chapter 4

Test beam results.

In this chapter we will discuss the preliminary measurements done with the Timing Counter longitudinal detector during a test run of December 2006 at PSI. We will show how data are in good agreement with Monte Carlo simulations and how it has been possible to use the timing sub-detector to have a raw estimation of impact positions through analysis of charge depositions inside the bars.

4.1 Introduction

During the December 2006 test beam the detector was partially working without the LXe calorimeter, with only 8 drift chambers out of 16, without the Timing Counter transverse detector and with the bars of the longitudinal TC detector shifted by 13 cm along the Z axis due to a small geometry problem caused by the rails for the insertion (which were 5mm thicker than the design) preventing a deeper insertion inside the COBRA as shown in figure 4.1. In Figure 4.2 are sketched the connections of PMTs to data acquisition systems used during the test.

The acquisition occurred through three different acquisition system: the DRS (final DAQ) and two different systems (one for charges, the other for time acquisitions) used for the final tuning up of the Timing Counter: a CAMAC based one with a charge to digital converter (QDC) giving the charges registered from the PMT and a VME based one with a TDC and an ADC from which we obtained both time and charge measurements.

Figure 4.1: The red arrows indicate the inner PMTs touching the COBRA frame inner surface.
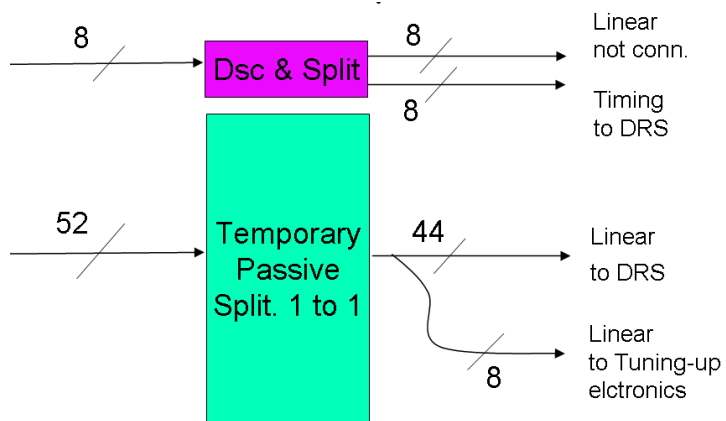
Figure 4.2: Configuration of the acquisition for December 2006 test beam: scheme of PMT signals connections to the different part of the system and to the Tuning electronics.

4.2 2006 test beam results

4.2.1 Charge data analysis (CAMAC).

Equalization of PMTs.

First of all PMTs have been equalized inside the COBRA magnetic field with cosmic rays. This means that the Voltages have been regulated so to have the same pulse height from both inner and outer COBRA PMTs (since the field is not constant this requires different Gains).

The charges collected at the PMTs for 4 bars during a cosmic run are summarized in figure 4.3 after pedestal and overflow channel suppression. As expected the charge distributions are almost equivalent from bar to bar for cosmic ray, influenced only by the different angular position which causes a different exposition surface and by different number of events acquired. This can be clearly observed from the plots showing energy deposit in figure 4.4 where the third bar which is the one with best statistics and also offering the best surface matching has a distribution showing the clear evidence of a peak in energy corresponding to about 4 cm bar crossed (8MeV).

The equalization of PMTs was previously done at BTF (without B field) and corrected at LASA (inside magnetic field) (see 3). From the Voltage-Gain table obtained during tests x has been calculated the correct values for the COBRA field for all PMTs, so that only a small refinement was needed.
The calibration was realized through the equalization of the height of cosmic signal pulses and the offline analysis of cosmic hits distribution along the bar can be used to verify the correct calibration as explained below.
The distribution of $log(Q_1/Q_2) \sim 2x/\lambda + log(A_1/A_2)$, where Q_i is the charge read at the anode of a PMT, A_i is the gain times a factor taking into account the number of photo-electrons and the gain loss caused by the not uniform B field (it is the quantity to be equalized to have the same pulse height at each PMT for a center bar hit) and x is the impact position taken with origin in corresponding to the center of the bar so to have a Gaussian distribution centered at zero. It has zero mean value when the two *gain-factors* A are equals, that means the term $log(A_1/A_2)$ is null. It can be seen also as a way to have the PMTs with the same gain when scaled with the loss factor coming from the value of the field (see 3 for details).
Figure 4.5 shows the distributions of the logarithm of charge ratios for 6 bars (3 belonging to TC upstream and the correspondent 3 of TC down stream) which has been used as a check of the correct calibration done with cosmic run.
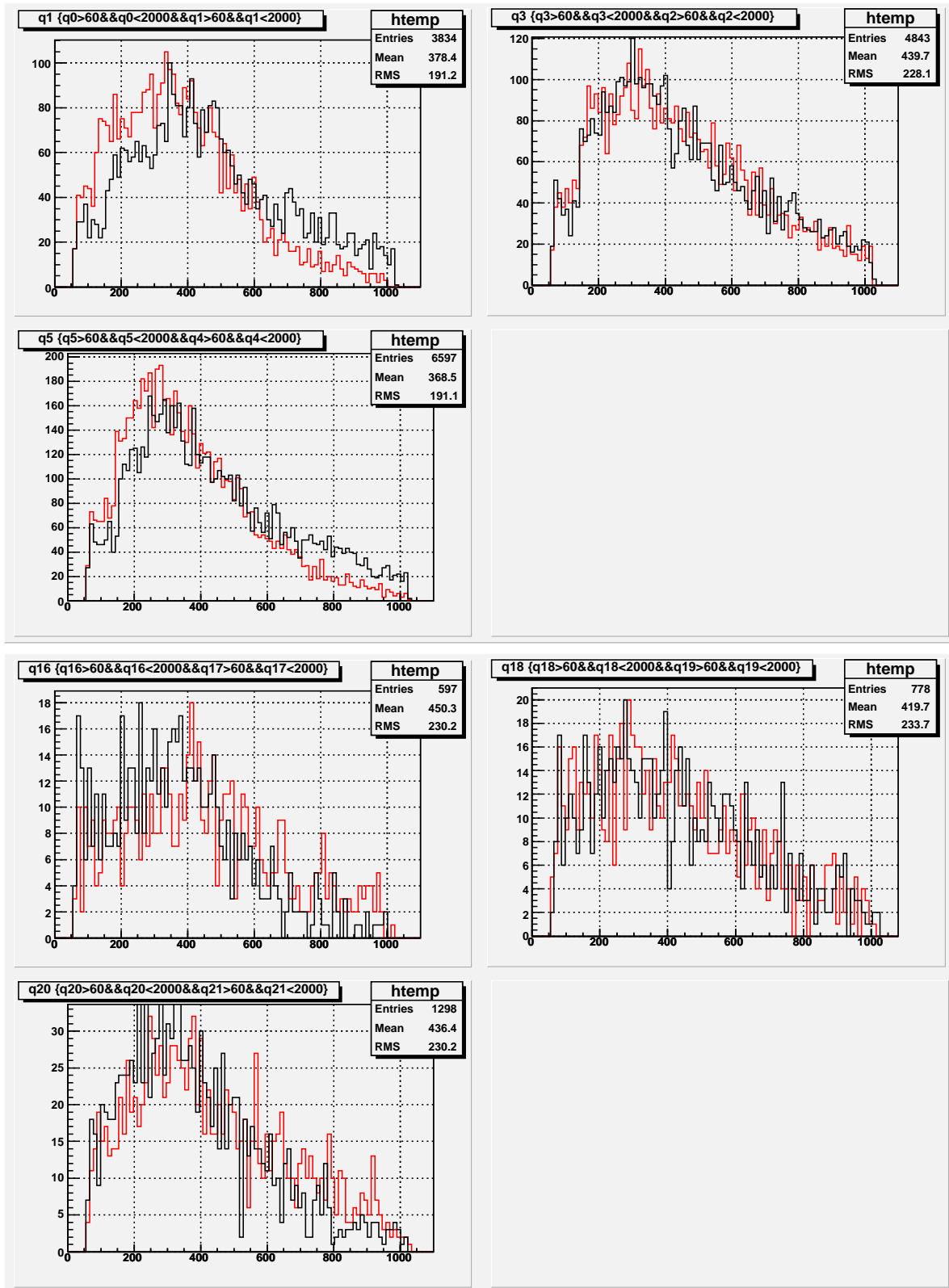
Figure 4.3: Charge distribution on a set of 6 down stream (upper 3 panel), 6 up stream (lower 3 panel) TC PMTs during cosmic runs. Black plots represent inner COBRA PMT, Red plots outer ones. From upper left (for each group) clockwise the first to third bar. The latter is the one offering a better surface matching. Acquisition time increases clockwise. (for each plot: Q on x axis in channels 0.25pC/ch and Counts on y; the scale is the same to allow easier comparison).
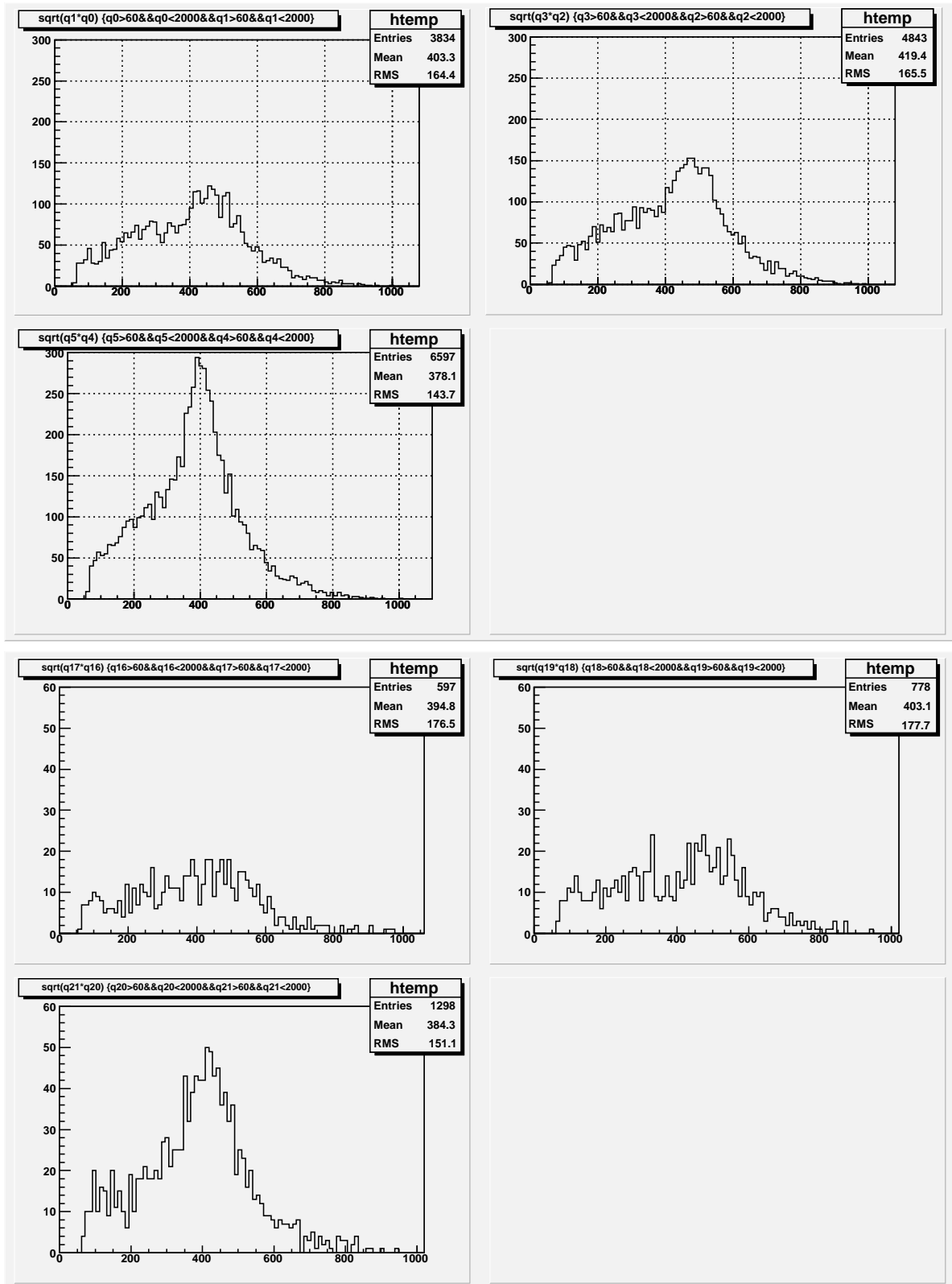
Figure 4.4: Energy distribution for a set of 3 bar down stream TC (upper 3 panels) and up stream TC (lower e panels) coming from cosmic runs. From upper left (for each group) clockwise the first to third bar. The latter is the one offering a better surface matching. Acquisition time increases clockwise. (for each plot: sqrt(Qin*Qout) on x axis in channels 0.25pC/ch and Counts on y).
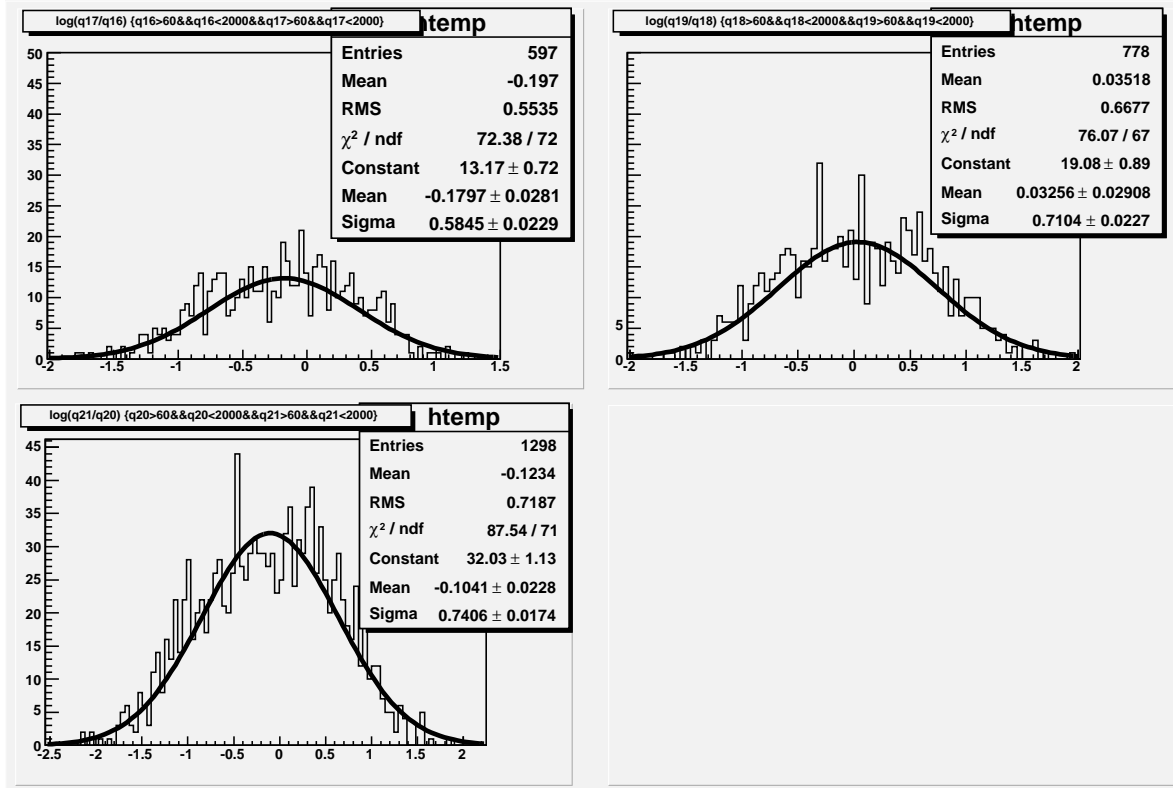
Figure 4.5: Calibration with cosmic rays: impact point distributions during cosmic run; the difference from a zero mean value shows differences in PMT equalization for the two PMTs belonging to the same bars.First 3 bars TC up stream.

4.2.2 Data - MC comparison

Beam data have been acquired with a CAMAC system 8 at the time PMT channels simultaneously (since the system had only 8 channels). We did studies of energy loss, energy and impact point distribution and events correlation on different bars coming from charge analysis.

We can compare the charge distributions obtained with beam with the ones coming from cosmic data. From figure 4.6 it's visible how the charge is not uniformly distributed. The inner PMT collects a greater amount of charge (the positron has a component of acceleration along the Z coordinate due to the disuniform magnetic field) and this is reflected from the impact point distributions in figure 4.7 from where it's clear the accumulation of impact position toward the target.

The distribution coming from data is in agreement with the simulations shown in figure 4.8, where the plot refers to the trigger bar.

Also the results obtained for energy distribution show agreement with the MC simulations. In figure 4.10 and 4.11 is shown a comparison between the Energy loss inside the bar as reconstructed from the data and as coming from the MC simulation superimposed.

The data acquisition have been done requiring the coincidence of the signals of two consecutive bars. The comparison between data and simulation gives not an exact agreement, even if the shape of MC data and measured ones is near, the energy distribution peak is wider in real data.

The same result can be deduced from DRS data analysis below in this section, where charge distributions show a bigger spread than the simulated ones giving as a result a higher energy spread.

From figure 4.12 it's clear the correlation between the energy released from the positron inside adjacent bars, as we expect from MC simulations. The left figure comes from data while the MC plot is on the right side.

The shape of energy distributions reflects the Timing Counter geometry which, has been designed and tuned with simulations and tests (see 3) to minimize the positron track spread so to make possible an efficient energy selection of events with large track lenght inside the bars. Small track lenght events give the low energy tail clearly shown also in figure 4.13. Large track lenght events give the clear Landau peak as shown from the fit in figure 4.13. The Landau peak is at about 8 MeV which is the value corresponding to a track lenght of 4 `cm` inside the scintillator. This value corresponds to a impact angle of $\theta = 90°$ realized through the geometry with slanted bars (figure 4.14) described in previous section.

In figure 4.15 is shown the distribution of Energy loss of an entire set of 4 bars during two different acquisitions with beam. The trigger required a single bar coincidence with 150mV threshold for each PMT on the same bar. The triggering bar is represented in the upper left plots and it's clear that adjacent bars from left to right had a smaller number of hits in agreement with MC simulations summarized in figure 4.9 which shows that only the 6,4% of events have three bar hit (with 70% of events having at least 2 bar hit).
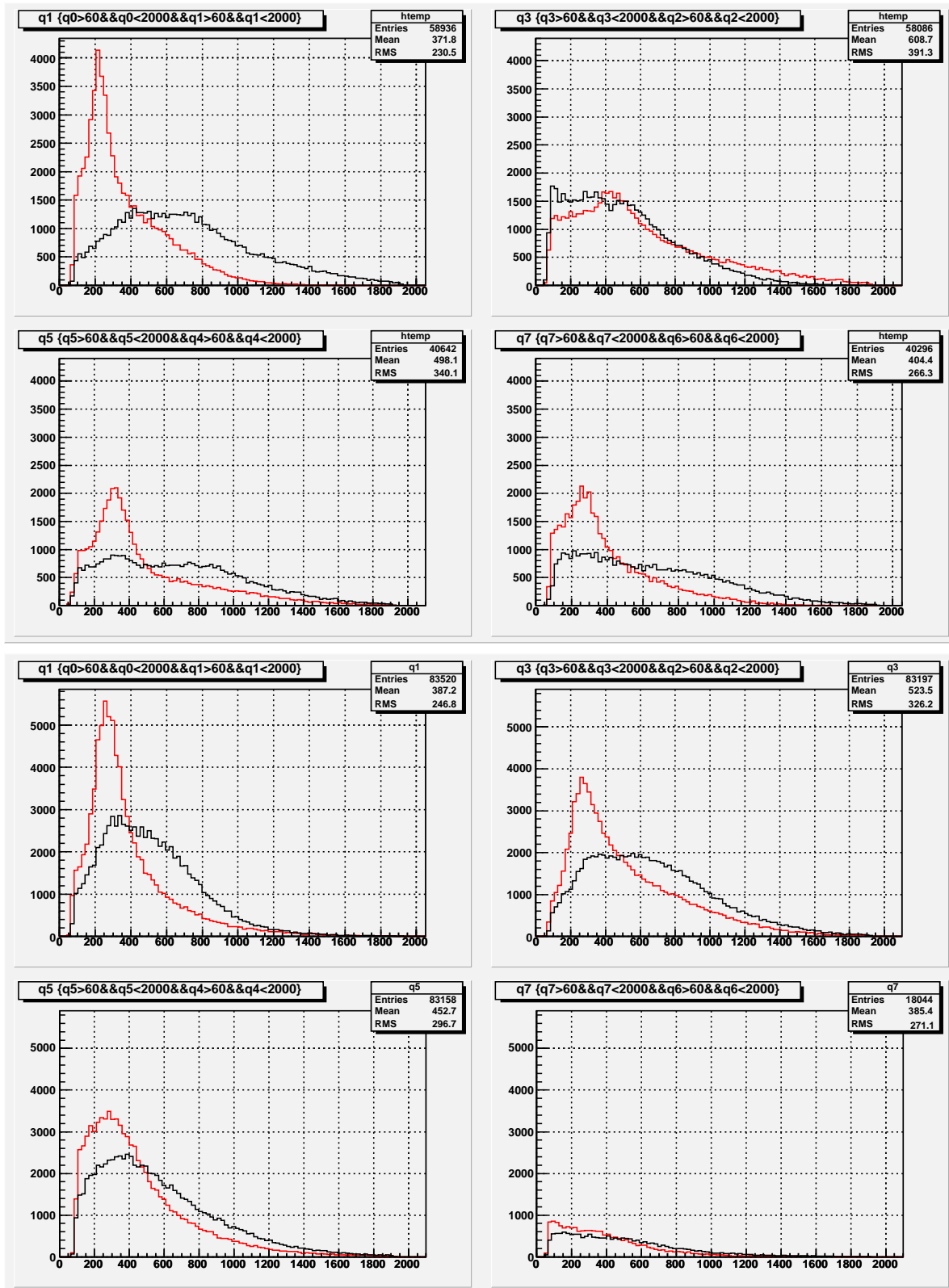
Figure 4.6: Charge distribution on a set of 8 down stream (upper 4 panel), 8 up stream (lower 4 panel) TC PMTs during a beam run. Black plots represent inner COBRA PMT, Red plots outer ones. From upper left (for each group) clockwise the first to fourth bar data. The triggering bar was the first. (for each plot: Q on x axis in channels 0.25pC/ch and Counts on y; the scale is the same to allow easier comparison).
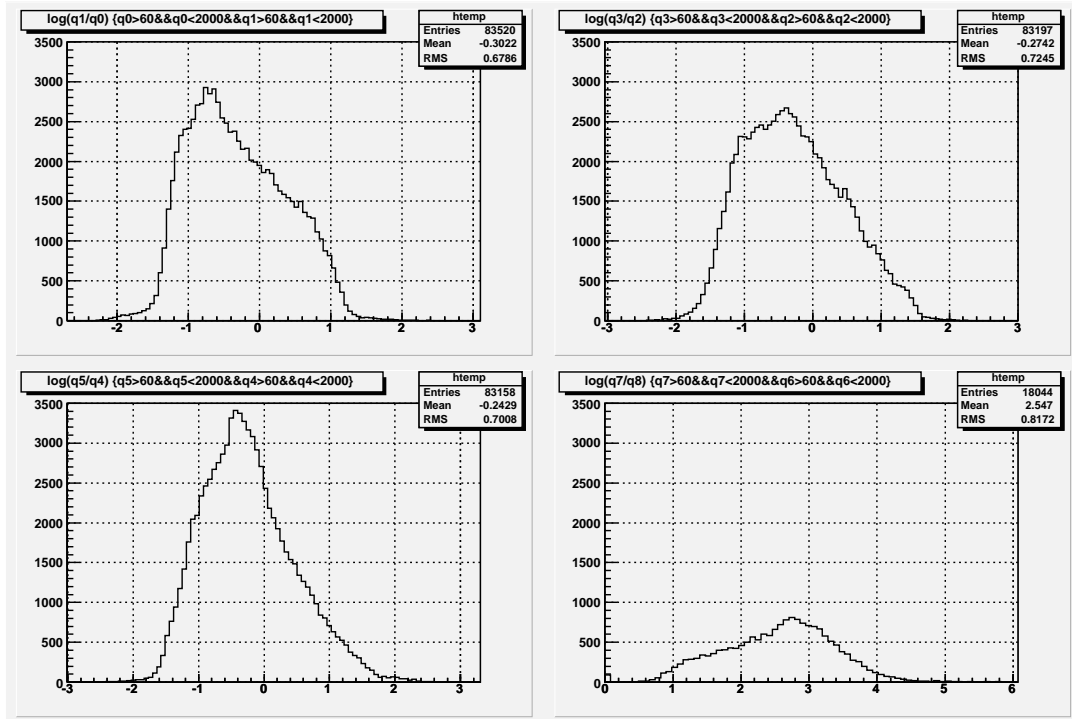
Figure 4.7: Impact point along the bar: distributions of a set of 4 up stream bars from test beam run. Trigger bar was the upper left, clockwise the other three bars (for each plot: log(Qout/Qin) on x axis and Counts on y; the scale is the same to allow easier comparison).
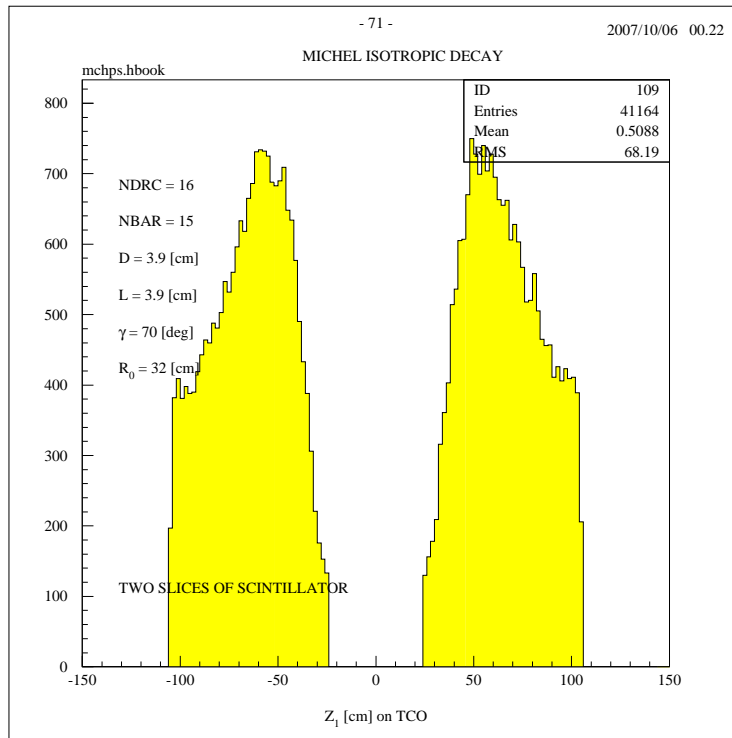
Figure 4.8: Impact point along the bar as obtained from a MC simulation of 10^6 isotropic generation of Michel positrons: distribution is for both up and down stream for the triggering bar and the same cutting on time of flight less than 6ns.
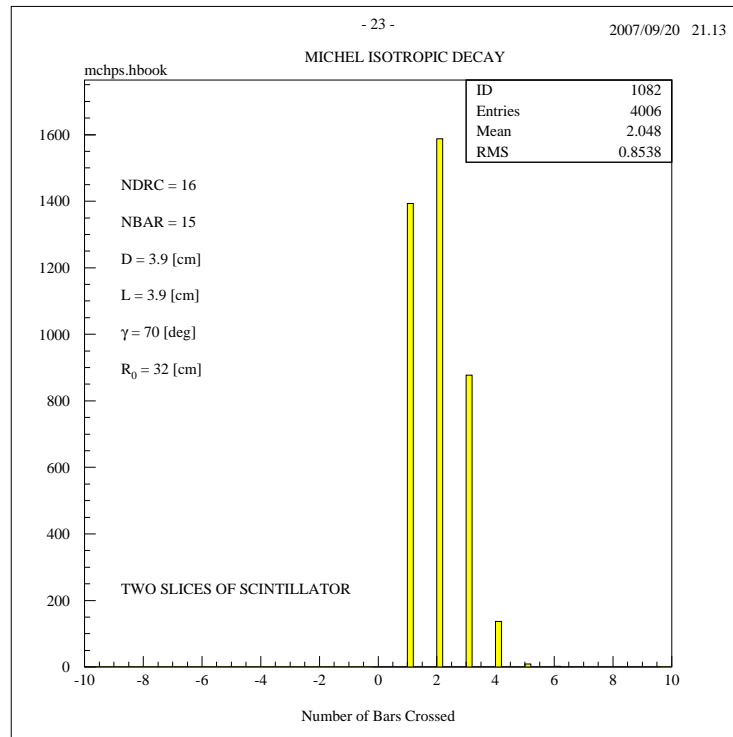
Figure 4.9: MC simulation: the total number of bar crossed. Notice how the number is pretty small for 4 bars as noticed from energy plot of beam data.
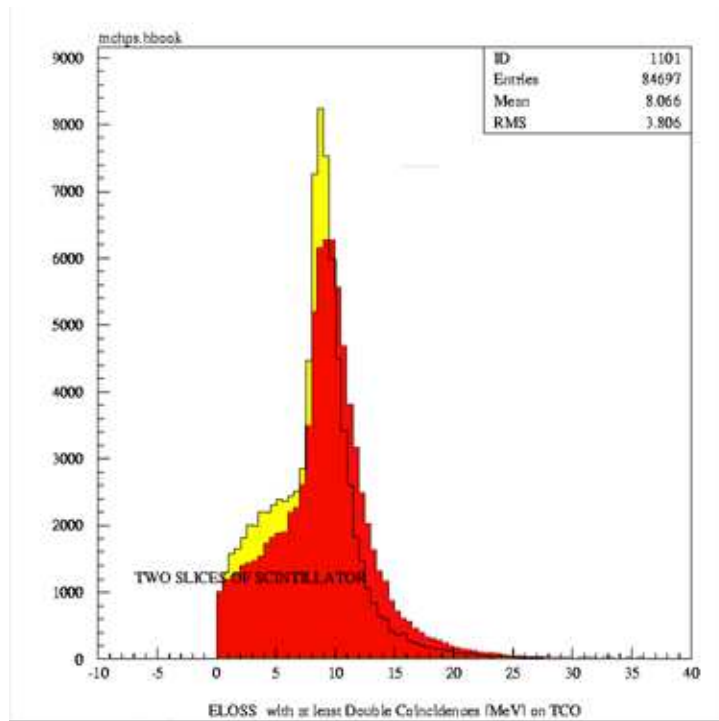
Figure 4.10: Energy loss requiring at least two coincidence bars signal : MC data for first (yellow) and second bar hit (red).
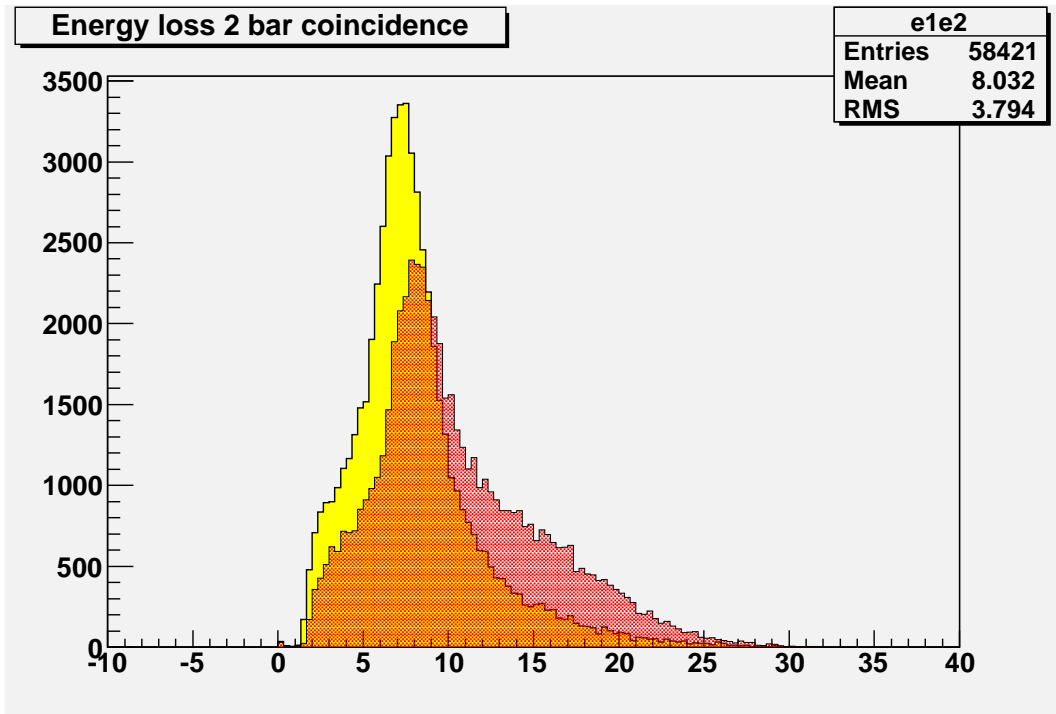
Figure 4.11: Energy loss requiring at least two coincidence bars signal : Beam data. The yellow plot is the triggering bar (first bar hit) the other one is the adjacent.
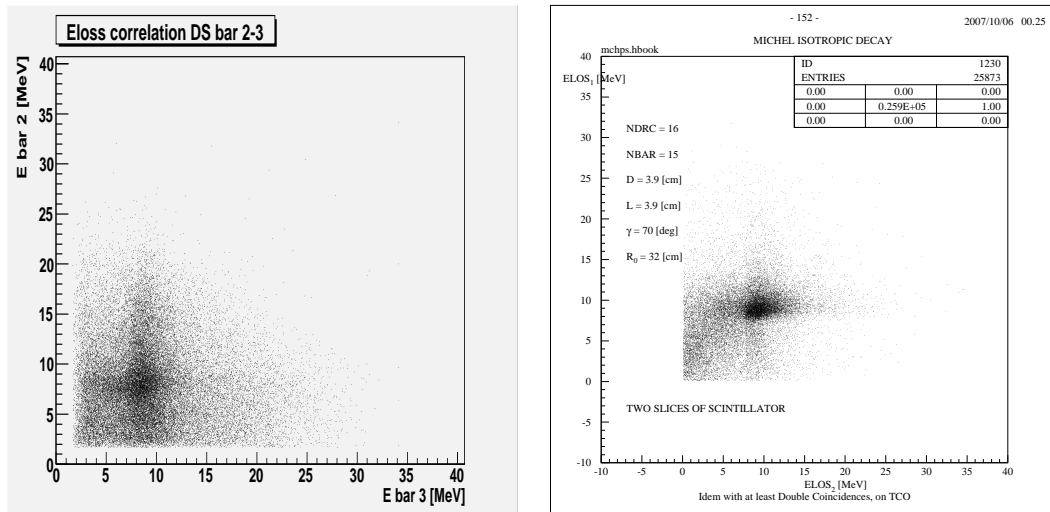
Figure 4.12: Comparison between Energy loss correlation between adjacent bars: MC data(right) and data from full intensity beam run (left).
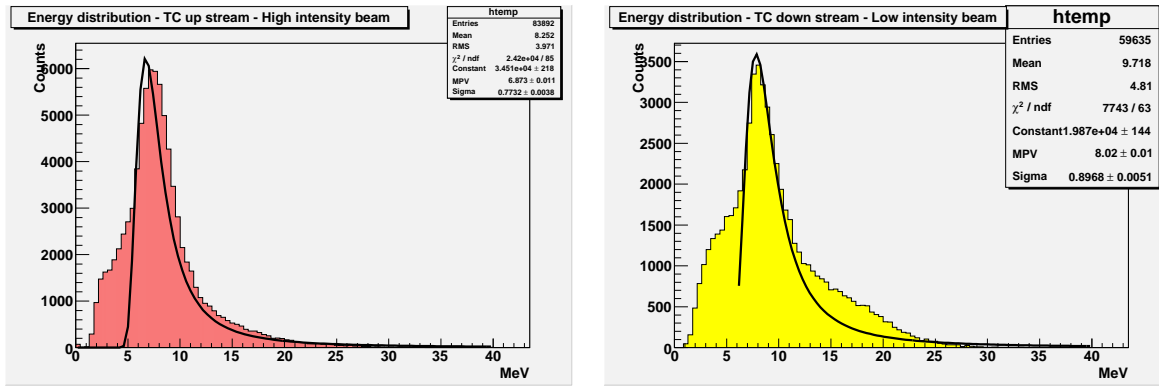
Figure 4.13: Landau fit of Energy loss inside a TC scintillating bar (left) first up stream TC bar during a high intensity run (right) first down stream TC bar. The geometry position of the bars is optimized to make the Energy loss as narrow as possible. With an energy selection it's possible to cut out the positron with small path length.
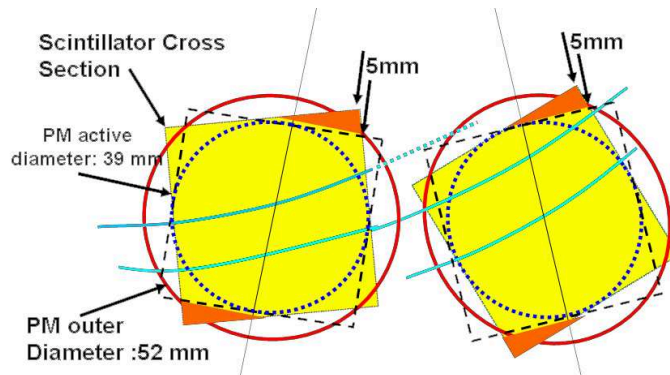
Figure 4.14: Tracks directions crossing the bars with the optimized geometry. The geometry is such that the positron hits at $\sim 90°$.

The energy released in the fourth bar (counting from the triggering one) is pretty small confirming the small number of events with 4 crossed bar of MC simulation (less than 1%).

Charge analysis and impact point reconstruction

It's worth noticing that through charge analysis it's possible to obtain an estimation of the impact point along the bar independently from the point given by the transverse detector. This tecnique gives a far worse resolution than the one achievable with the transverse detector, but can be useful as a monitor to check if the transverse detector is working properly.

In figure 4.16 is shown, through the plot of charge depositions, the clear correlation between positions along two adjacent bars.

The charge analysis began during the BTF tests. We collected data scanning along scintillator bars, 6 positions with 10 cm step.

The impact point was determined by means of a small telescope (0.7 cm of spot size) triggering the acquisition. Waveforms were digitized with sampling oscilloscope to have almost the same conditions of the DRS DAQ. Offline analysis of waveform allowed to select single electron events by cut on the energy distribution. In figure 4.17 it's clear the separation between charge distribution corresponding to different impact positions. In figure 4.18 the impact positions are reconstructed through charge analysis obtaining a *rms* of 2,8cm.

The BTF result is obtained from the equation:

$$log(Q_1/Q_2) = 2x/\lambda + log(G_1/G_2) \tag{4.1}$$

Figure 4.18 shows the Gaussian fit of these data. The results are in units of $log(Q_1/Q_2)$ for a clearer comparison, because of the differences in attenuation length (λ_{pos}) for each bar. The difference between first and last peak is $\Delta log(QL/QR) = 1.416$, corresponding to 50cm along the bar. We can estimate the real path length of light from $x = pos/sin(\theta_{lim})$, where *pos* is the distance between impact points and x is the real path of light inside the bar from total reflection. From here we can estimate $\lambda = 120cm$ for this bar (comparable with the value of 140 cm given by the producer). From fitting datasets for each bar the *rms* obtained results for each Gaussian $\sigma_{log} < 0.05$, which means $\sigma_{pos} < 2,8cm$. In figure 4.18 is shown a fit of position resolution of a BTF measure. Even if λ differs from bar to bar for some 10% the accuracy on the position reconstruction remains as good as $\sim$ 3cm.

From data taken during test beam at PSI with CAMAC system we can extract informations about the impact point using the adjacent bar correlations like we did in the BTF setup.
In figure 4.19 it's visible the separation between charge depositions corresponding to different impact positions well separated.

The previous analysis has been done taking the relative impact position with one bar as a reference since the attenuation length of the scintillators is not equal bar by bar, because the surfaces has been treated by hand and the reflection-absorption properties differ bar by bar. To provide an absolute estimation of impact points on subsequent bars, a better knowledge of bar
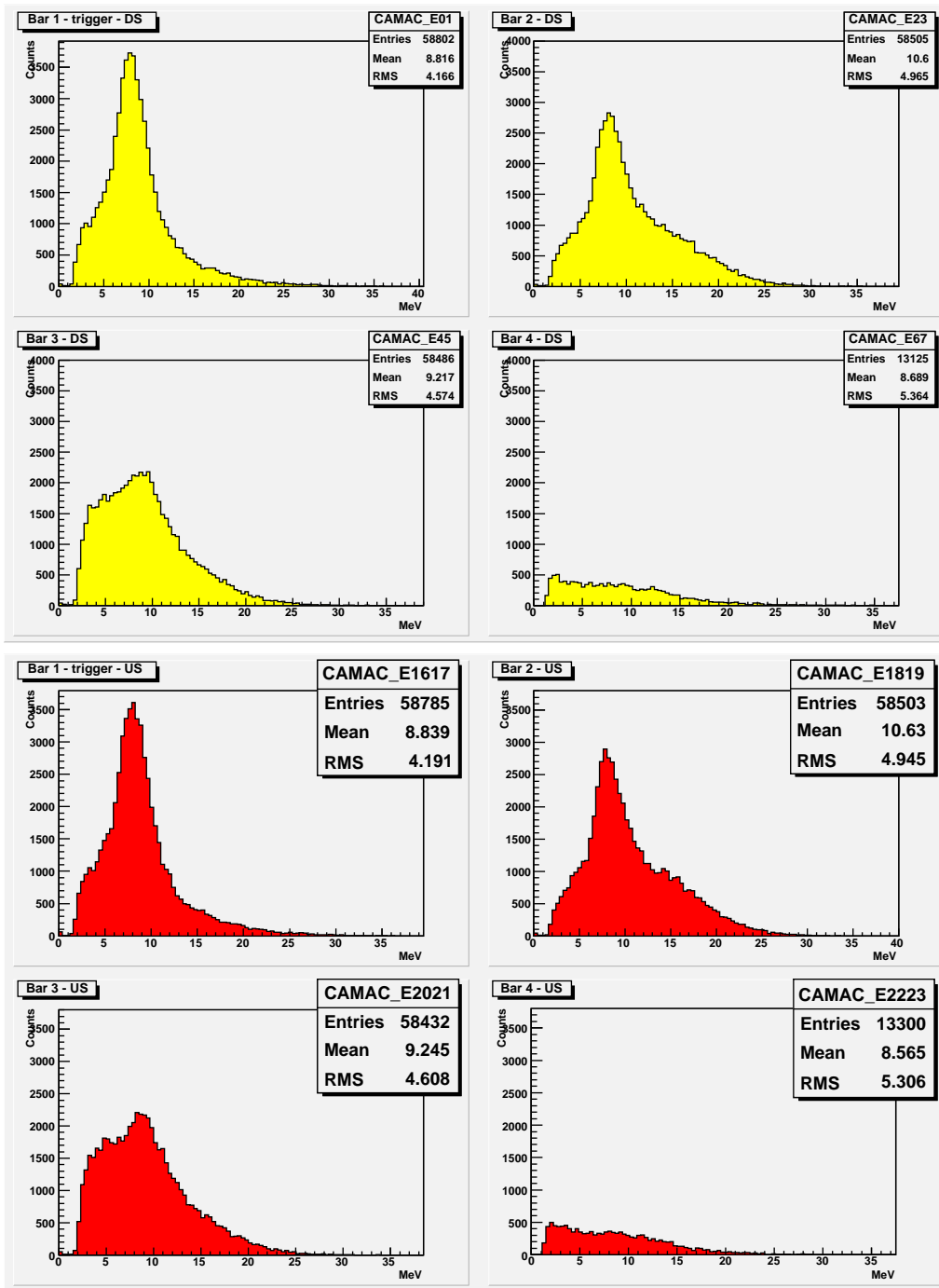
Figure 4.15: Summary of energy loss in Timing Counterbars acquired with CAMAC system (4 bars TC down stream: upper plot ; 4 bars TC up stream: lower plot) during a beam run acquisition. The triggering bar was the upper left in both cases. The plots reports the square root of the product of the charges from the PMTs' signal.
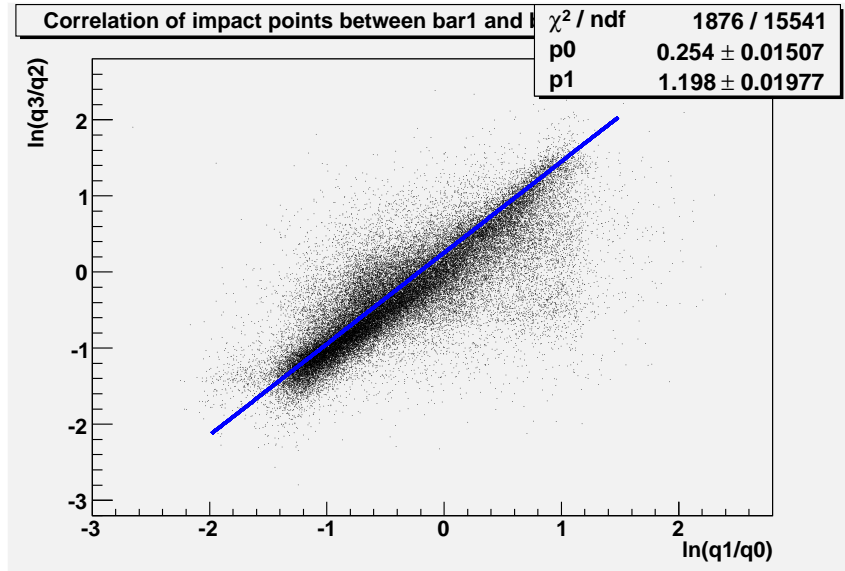
Figure 4.16: Correlation between charge deposition inside two adjacent bars given in units of charge ratio.
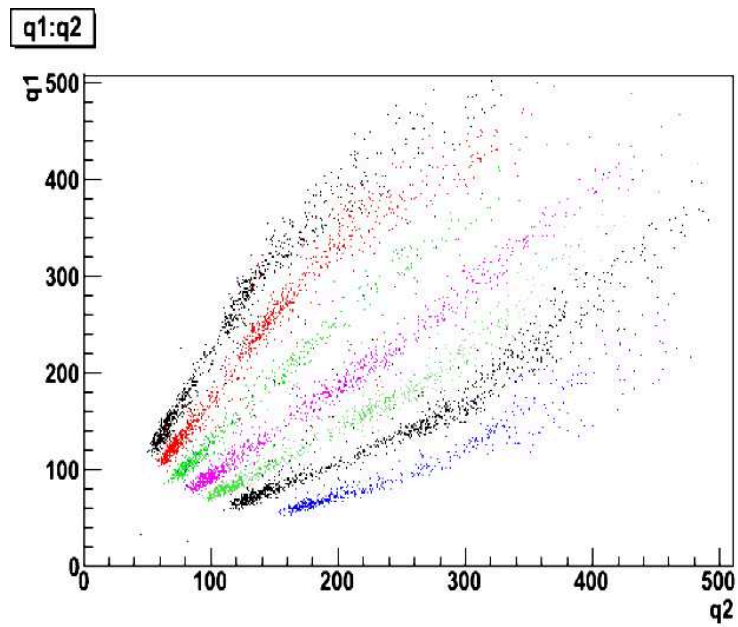
Figure 4.17: Scatter plot of the charges of two PMTs of the same bar corresponding to different impact positions.
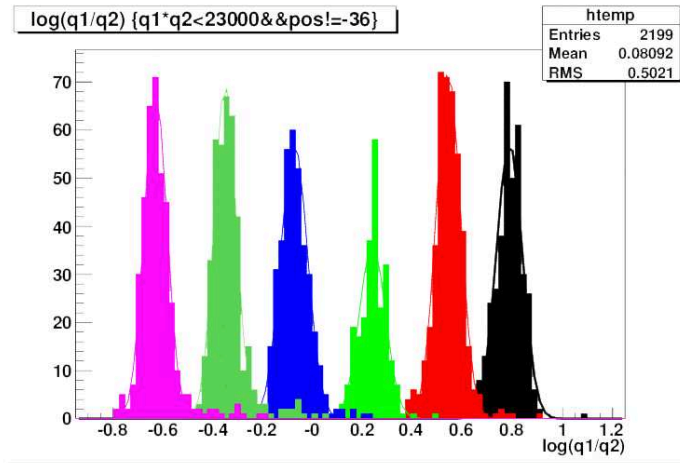
Figure 4.18: Gaussian fit of the position data collected from charge ratios corresponding to 7 different impact positions along the bar during BTF measurements.
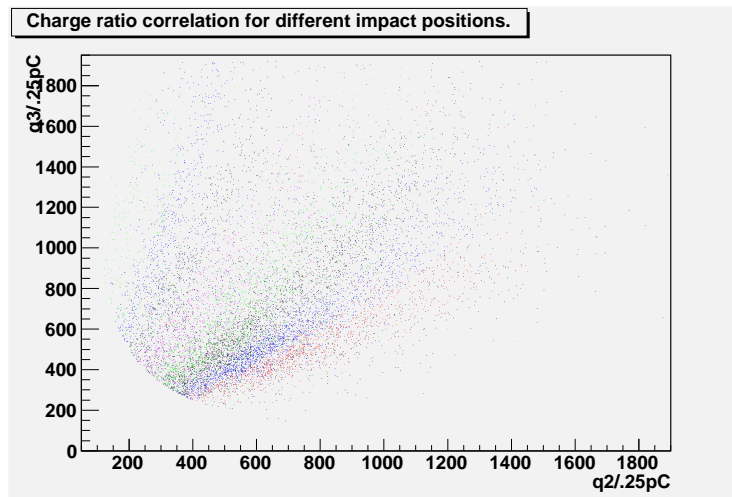
Figure 4.19: Scatter plot of correlation of the charges of the two first bars' PMTs for different positions. Different colors indicate different positions along the bar selected through the use of a charge cut on the adjacent one.
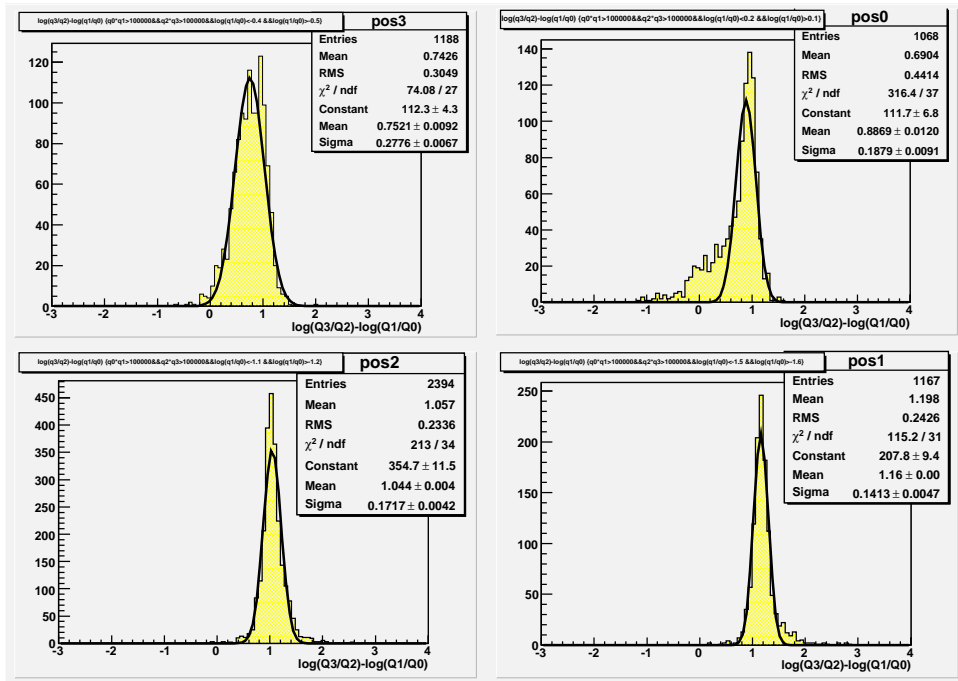
Figure 4.20: Distribution of charge inside bar 1 for different positions. With Gaussian fits for determination of impact point.
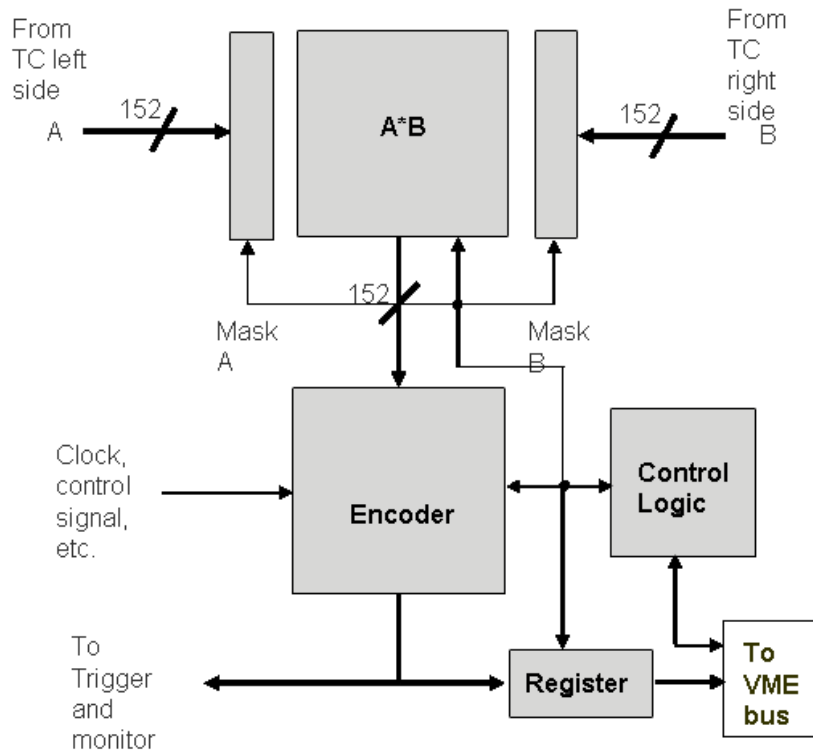
Figure 4.21: Scheme of VME DAQ.

parameters is needed (attenuation length).

4.2.3   Time data analysis (VME).

During the same data taking of December 2006 also a VME system has been used with the QDC and an ADC to acquire both Time and Charge in addition to the DRS acquisition system and the results are shown in the following section. A scheme of the DAQ is in figure 4.21.

4.2.4   Time results

With the VME system it was possible to take time data.

The main purpose of this data taking was to verify the correct time inter response of the detector, namely time-position correlation and time to time correlations between adjacent bars.

Taking into account two adjacent bars it's possible to analyze the correlation of the time differences registered from the PMTs of each bar. Taking for instance the first (PMT 0 and PMT 1
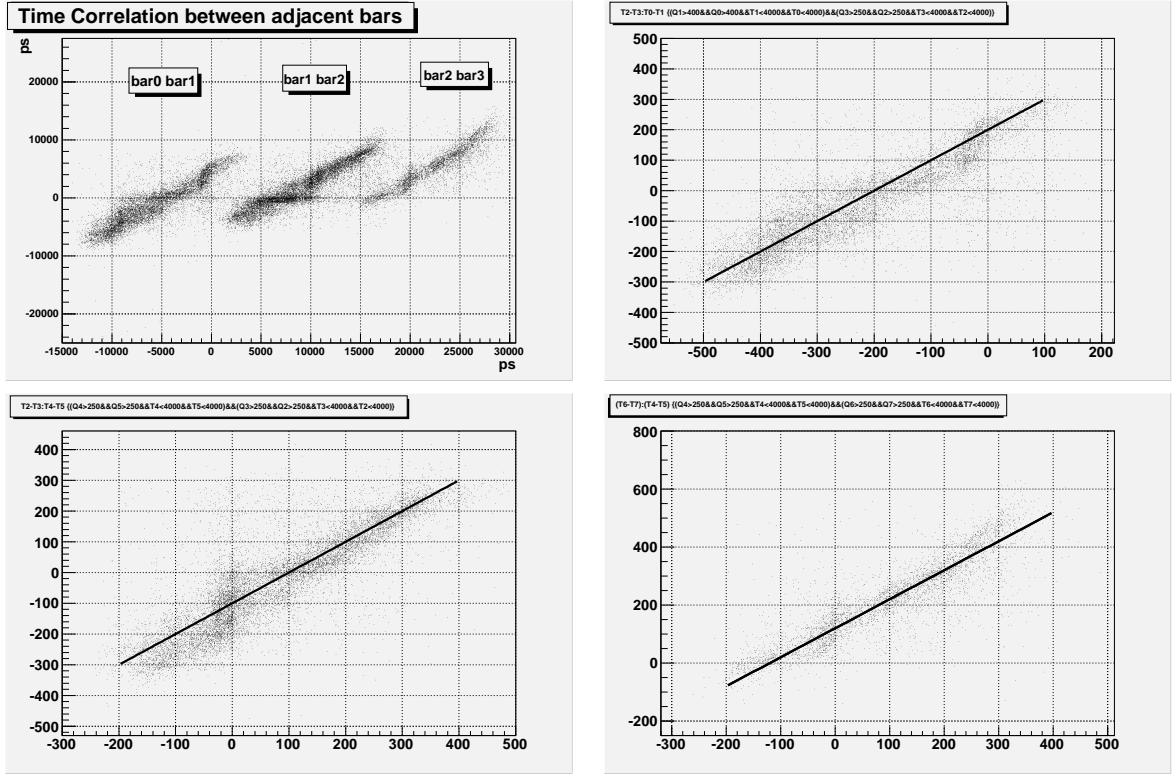
Figure 4.22: Correlation between time differences for adjacent bars.(Top left) summary plot of the correlations, the plots have been arbitrarily shifted on x axis to make view easier, (Top right) the results for the first two bars with fit, (bottom from left to right) the results for bar2 versus bar3 and bar3 versus bar4 both fitted. The plots are in channels (25ps/ch). The fits are with a slope-1 straight line and the matching is as expected.

)and the second (PMT 2 and PMT 3) bars we have the following equation:

$$t_2 - t_3 = (t_0 - t_1)(v_{effB0}/v_{effB1}) + K_{01} + \delta t_{01} \tag{4.2}$$

and the same for the other bars (see figure 4.22) where v_{effBi} is the effective light propagation velocity in Bar i (i=1,2,3,4), K_{01} is a constant depending only on the cable length and geometry of the TC bars, δ_{01} is the time difference due to different velocity of positron along the Z axis (this may be different from event to event). We can also have a measure of how different can v_{effBi} be by fitting the data with a slope 1 straight line, which means we assume the effective speed to be the same in the two bars under consideration. The time correlations between bars is showed in figure 4.23 and from the plots is clear the correlation between time and position which also mirrors the correct working point in the linearity plateau of the PMTs.

The correlation between time an charge data have been analyzed through DRS and in figures below (fig. 4.24 4.25 [74]) there is a comparison between the two systems. They are in a quite
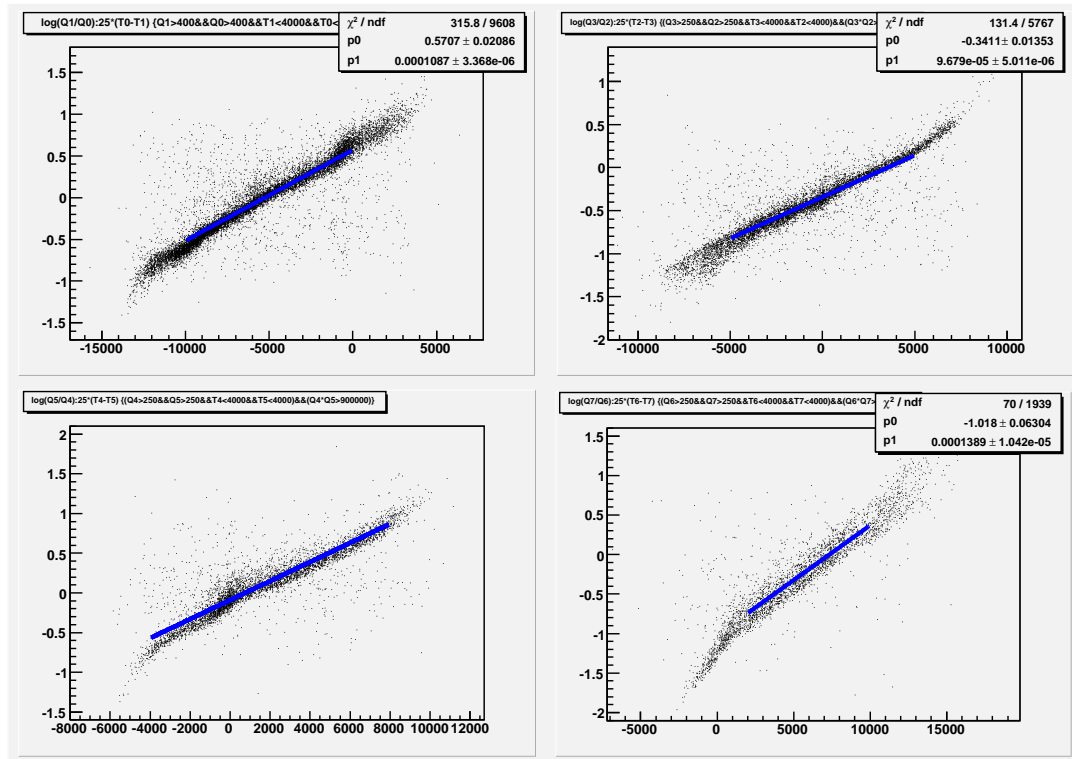
Figure 4.23: Time position correlation for a set of 4 bars coming from data acquisition with VME system with double bar coincidence trigger. The correlation is clearly visible after suppression of pedestal and overflow. The plots are in units of ps and logarithm of charge ratio (which is proportional to the impact position along the bar. In blue the fit with a straight line.).
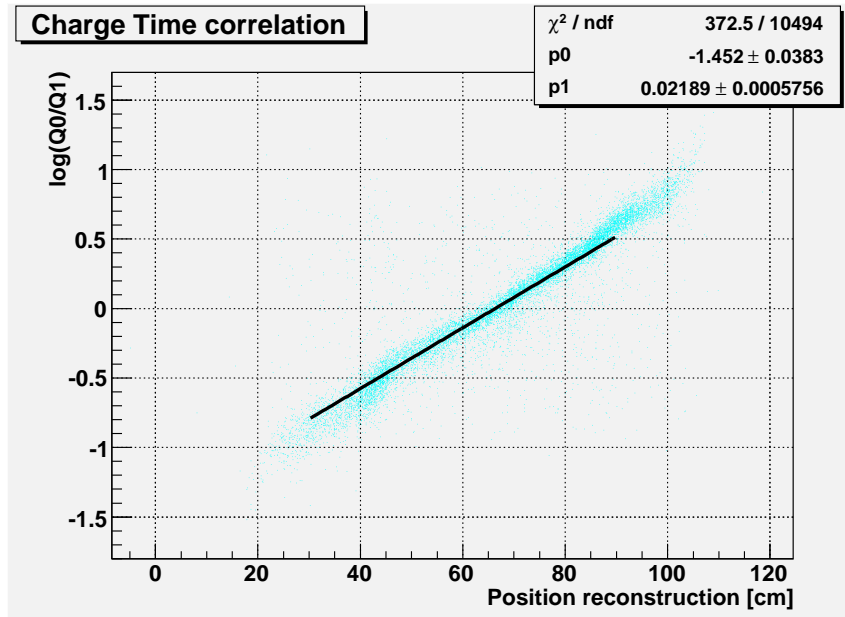
Figure 4.24: Charge time correlation obtained with data coming from CAMAC acquisition. The trend is in agreement with the DRS daq shown below.

good agreement considering the low statistic (the results from VME system have been rescaled with $\lambda = 140cm$ and $v_{eff} = 15cm/ns$ to match the DRS ones).

4.2.5 Energy results

Also with data coming from VME system Energy distributions have been reconstructed as a check of the consistency with the CAMAC system. A summary is shown in figure 4.26 for 2 bar coincidence trigger. In figure the two upper plot are the triggering bars. Again it's visible the effect of geometry on the number of bar hit, confirming the consistency with the results obtained with the CAMAC daq previously discussed.
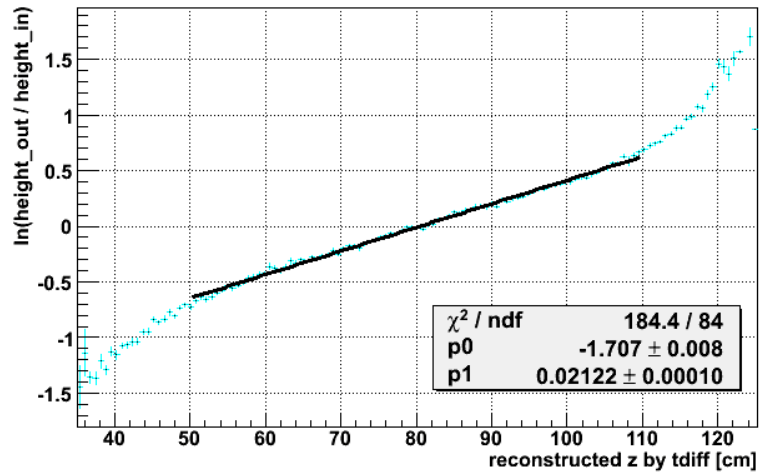
Figure 4.25: Charge time correlation obtained with data coming from DRS acquisition. The trend is in agreement with the CAMAC daq shown previously, even if the statistic is quite low.
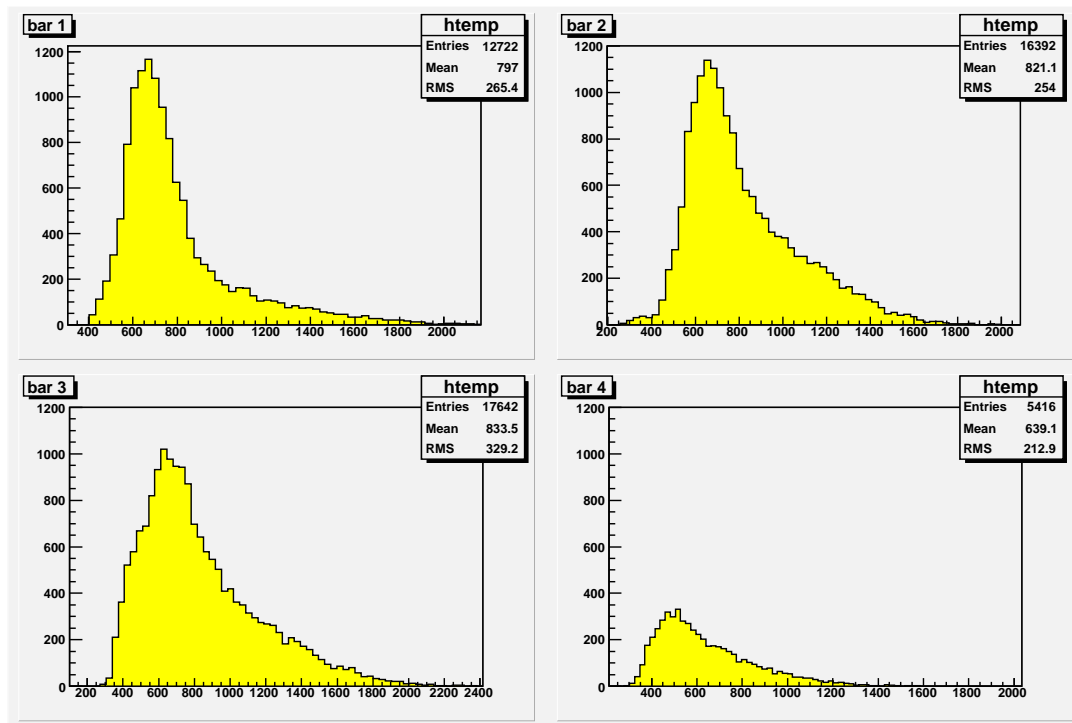
Figure 4.26: Energy loss in each of the acquired Timing Counterbars during test beam of December 2006 with VME acquisition system, two bars coincidence. On the X axis: the square root of the PMT charges product expressed in channels (0.25 ps/ch), on Y axis: Occurrences.
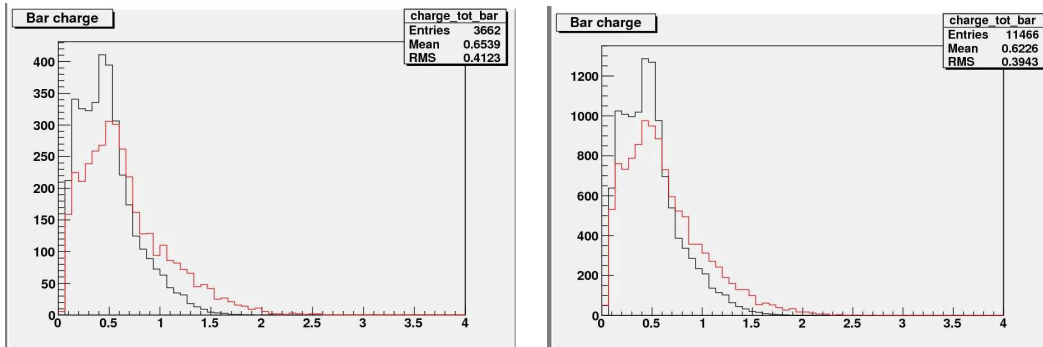
Figure 4.27: Comparison between expected (red) and measured (black) charge deposition inside two bars of the Timing Counter. During a low intensity (10% of nominal intensity) beam (left) and a high intensity (100% of nominal intensity) one. The MC results have been shifted to superimpose the peak position.
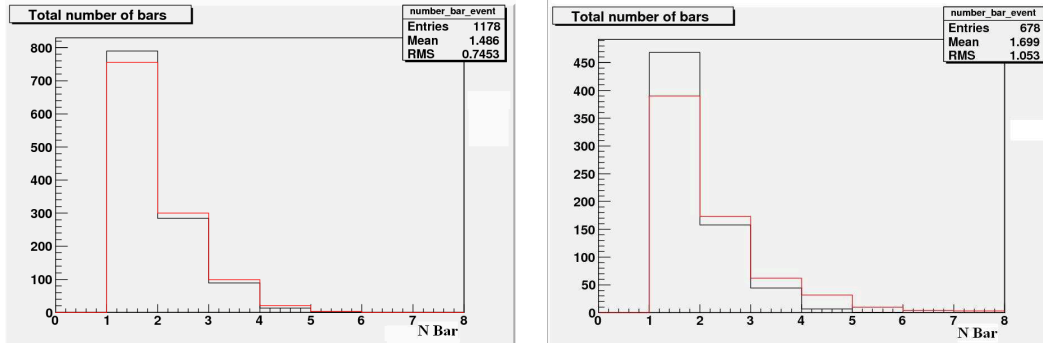
Figure 4.28: Comparison between expected and measured number of bars hit. During a low intensity (10% of nominal intensity) beam (left) and a high intensity (100% of nominal intensity) one.

4.2.6 First DRS data.

The official DRS acquisition system worked properly even if it had a smaller dynamical range than the projected one and the signals from Timing CounterPMTs needed to be attenuated by a factor 2 to fit it; results are reported in the following section. Analyzing the shape of the charge depositions for two bars against the MC simulated ones It's again possible to notice that the MC distributions are narrower than the real data, as we noticed with CAMAC system. In figure 4.27 [142] are reported superimposed the sum of charge distribution inside the bars. Red line is data while the black plot is MC events. The number of hits per bar has been checked (see figure 4.28) and it resulted to follow the expected distribution quite well. In figure in Red are plot the data for both low and high intensity run. Also the reconstructed hit distribution inside the bars follows the same shape distribution of the MC as can be seen in figure 4.29.
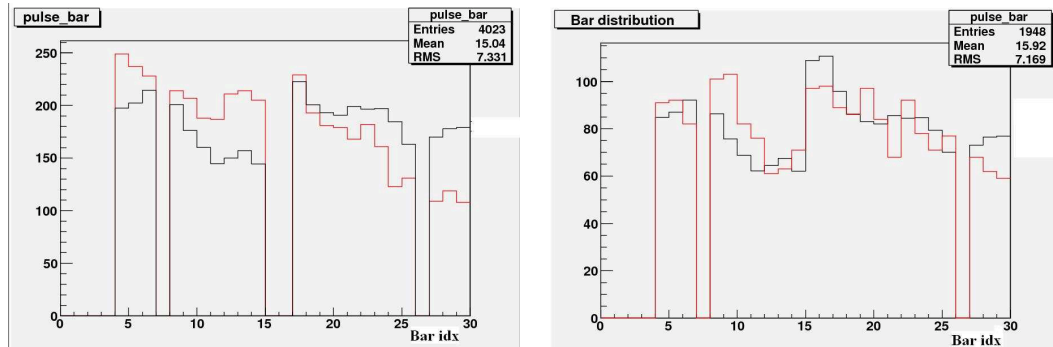
Figure 4.29: Comparison between expected and measured number of hits per bar. During a low intensity (10% of nominal intensity) beam (left) and a high intensity (100% of nominal intensity) one. The missing bars are the channels connected to the VME system.

4.3   2007 test beam results

A new test beam to improve the energy and timing measurements with almost all sub-detectors started in November 2007 and the preliminary results are presented in the following section. The transverse subdetector was switched off and the Drift Chambers were doing tuning up at time of writing. The runs were taken both with muons and a Cokcroft-Walton accelerator used to shoot 440 keV protons against a Lithium Fluoride target producing 7 MeV and 17.6 MeV photons [157] (details in 5). The spectra of the gamma emitted by the LiF are shown in figure 4.30.

4.3.1   Energy results with LiF

The data coming from the LiF target are supposed to be used for LXe calibration purpouse but a few runs were taken triggering on the timing counter. A LiF run consisting of 100K events with trigger on TC have been taken with a trigger threshold set to 20 mV for the coincidence of any couple of PMTs belonging to the same bar.

The isotropic distribution of Fluorine and Litium photons make this kind of data a good way to study the uniformity of the response of TC detector. In figure 4.31 the TC hit map for both upstream and downstream counters shows how the response is roughly uniform from bar to bar.

From these data it has been possible to confirm a problem on one bar (namely the 13th upstream), clearly visible in figure 4.31 (a), due to the active splitter which has been already fixed and another one related to a noisy trigger channel which gave a smaller signal than others likely because of a wrong DRS chip calibration.

From the hit map along the Z direction (figure 4.32) we can verify that the distribution goes like 1/*cos* of the emission angle respect to the Z direction. The difference between the Downstream counter and the Upstream one is due to the material of the insertion system of the CW itself. There is a bellow system which inserts the target in the right position inside the magnet from the
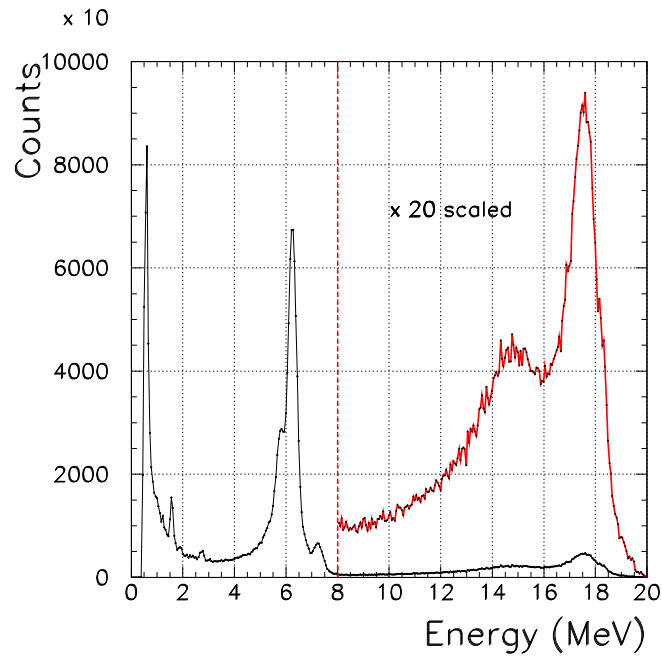
Figure 4.30: Measured spectra from gamma emitted by LiF thin target shoot with 440 `keV` protons.

(a)   (b)
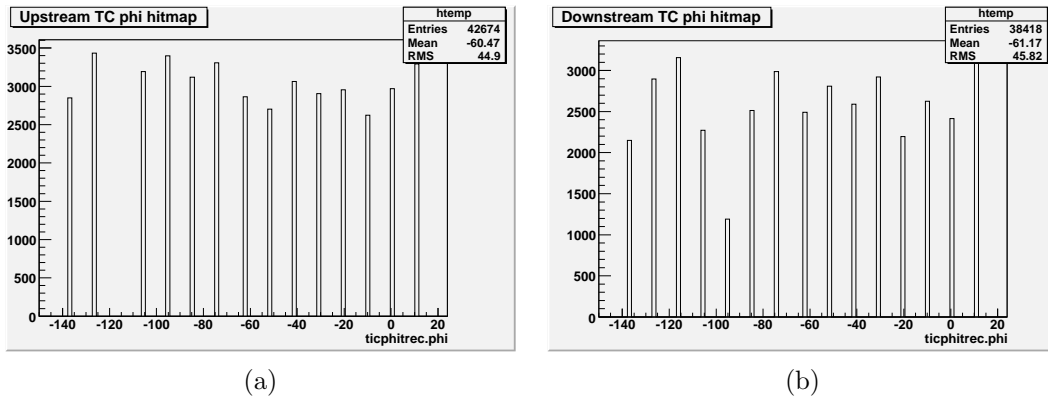
Figure 4.31: Hit map of LiF data for the phi coordinate. Upstream Stream timing counter (a) and Downstream Timing Counter (b)

(a)   (b)
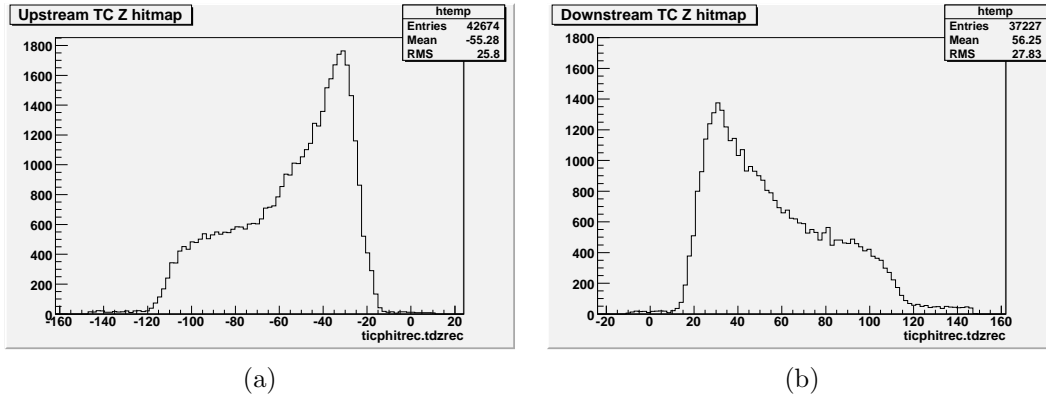
Figure 4.32: Hit map Z. Upstream Stream timing counter (a) and Downstream Timing Counter (b)

(a)   (b)
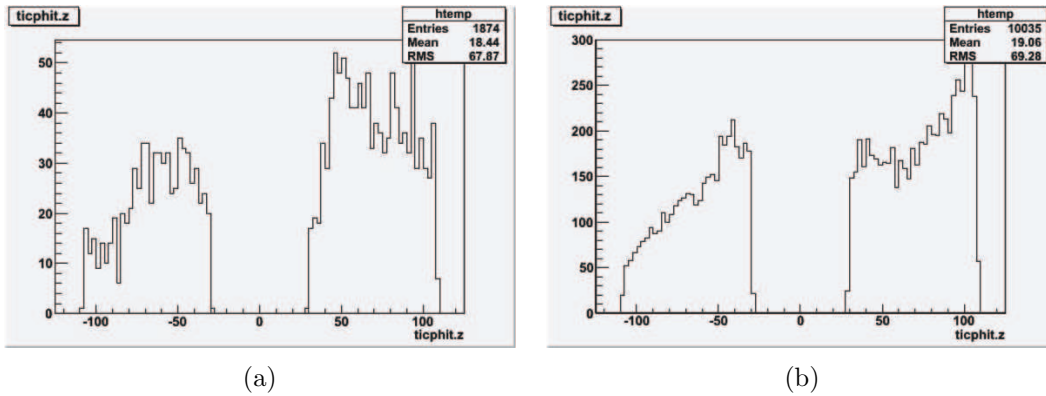
Figure 4.33: Hit map Z with Michel data. (a) Data and (b) Monte Carlo preliminary simulation.

down stream side, which acts as a target holder.

If we compare this hitmap with the same one coming from Michel positrons run it's clearly visible the different rate (figure 4.33 (a)) between Down stream (on the right side) and the Up stream part of the Timing Counter (on the left side) due to the muons which decay after the target. This has been included in the Monte Carlo which preliminary results are shown in figure 4.33 (b) A better simulation is still needed to improve the MC-data agreement. account this effect.

From the LiF data and cosmic data taken with the same trigger conditions we can extract the informations regarding the inter calibration of the bars. In figure 4.34 is shown a Landau fit of the energy release due to a cosmic ray crossing the bar. The energy release is 8 MeV as a average value since we consider the cosmic as a minimum ionizing particle and the path lenght inside the scintillator is 4 cm (2 MeV/cm is the energy loss inside the scintillator, as previously stated).

In figure 4.35 is shown the summary plot of the landau fits for all the available bars and
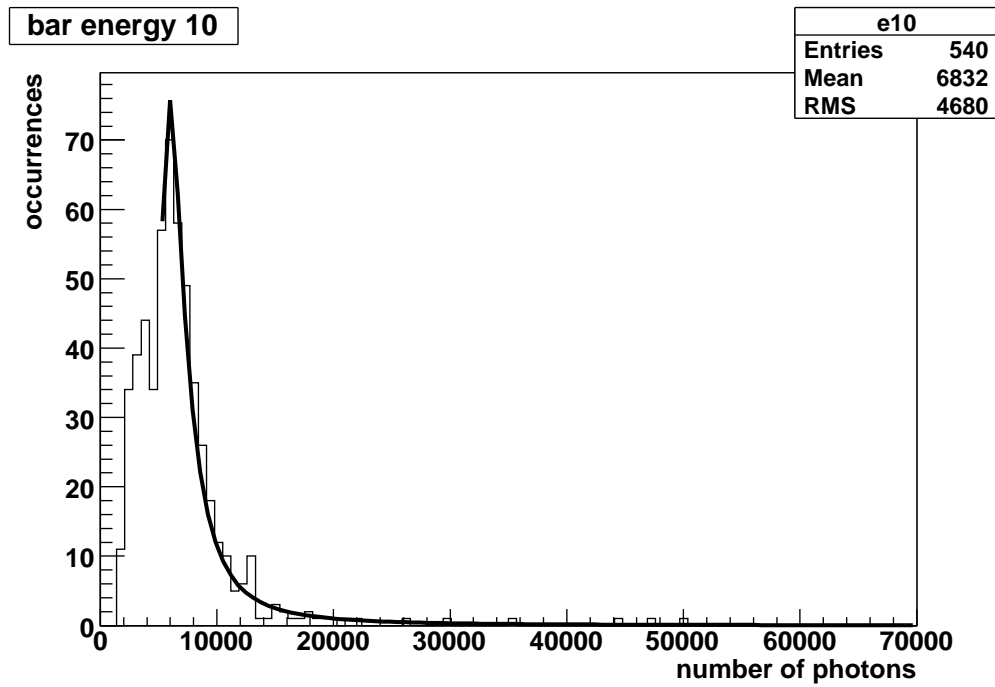
Figure 4.34: Energy deposit inside one bar in units of number of photons. Data are taken with a cosmic run. The Landau fit curve is superimposed.
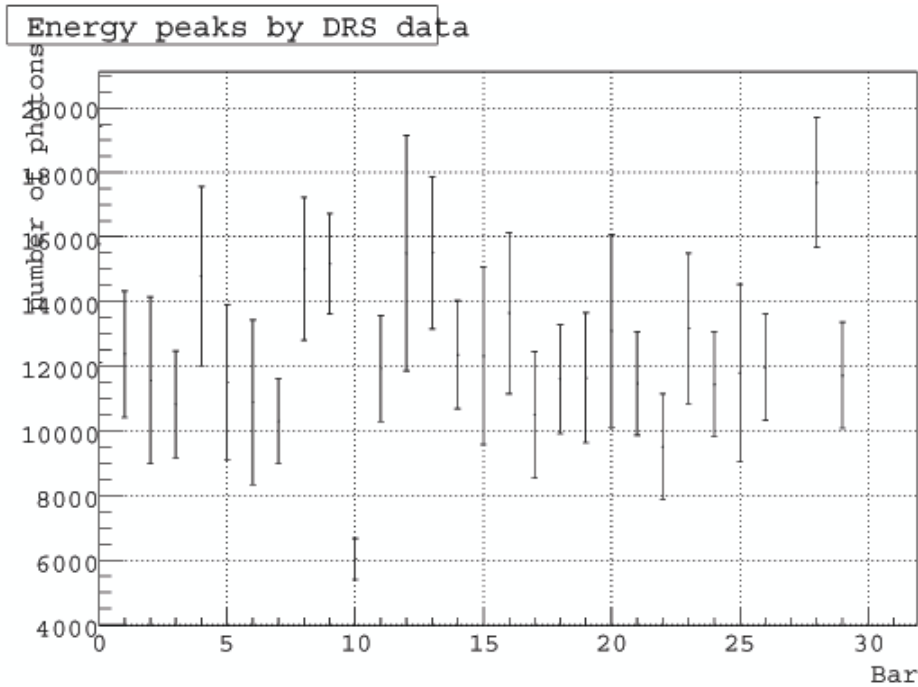
Figure 4.35: Summary plot of the Landau peaks for all the bars.

with these data we calibrated the energy scale for the LiF run and the Compton shoulder of the Fluorine photon is clearly visible at the right energy for each bar (see figure 4.36, where the cosmic background has been subtracted).

The distribution from monteCarlo follows the data as shown in figure 4.37 where is shown the Fluorine part of the spectrum.

4.3.2   Equalization of PMT

The data coming from both the runs with Michel positrons and the LiF have been used to check the equalization of PMTs couples of each bar [1]. Through a cut on time of arrival of signals we selected the center of the bar so to have a signal that is almost the same for both PMTs. If we take the $log(\frac{Q_{o}ut}{Q_{i}n})$ we expect a gaussian centered in zero in case of equalization and from the deviation from center we estimated the lack of equalization of the PMTs. In figure 4.38 are shown both a couple of equalized PMTs and not equalized ones.

Then from the values of the characteristic constants measured in laboratory PMT by PMT we deduced the correct Voltage value to apply to non equalized ones. If we indicate as $v_{d}iff$

---

[1]As equalization, as stated before, we indicate the condition of having the same signal from both the PMTs, wich means a different applied voltage both because of intrinsic differences and because of different value of B field they are in.
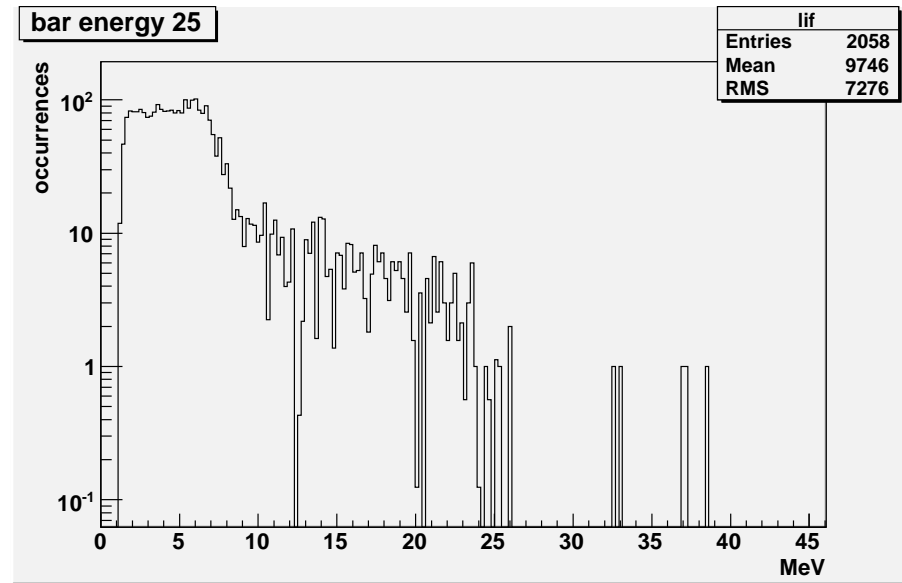
Figure 4.36: LiF Compton shoulder of the Flurine γ for one bar. The Energy scale is calibrated through the cosmic run and the cosmic background is suppressed.

the voltage adjust and with V_1 and V_2 the Voltages actually applied to the PMTs, with k_i and α_i $(i = 1, 2)$ the parameters of PMTs (coming from the equation $G = k \times V^\alpha$) which has been measured for each PMT and G_i the gain, we can easily obtain the equation giving the voltage correction as $v_d iff = (\frac{K_1 V_1^{\alpha_1}}{K_2})^{1/\alpha_2} - V_2$ in case of the first pmt signal higher than the second and the same with inverted indexes in the other case. In figure 4.39 is shown the summary plot of the data before the equalization that will be done during the next run stop.

4.3.3 Conclusions

The first data of MEG Timing Counter subdetector has been shown and analyzed. We show how data are partially in agreement with Monte Carlo simulations, even if the energy results are worse than expected. The experimental setup was not ideal because of the beam optimization happening during the 2006 data taking. This brought a poor understanding of the behavior of some PMTs. We also presented charge ratio studies which are a good way to determine the positron impact point on each TC bar in an independent way. A full characterization of the bars is needed for optimizing this method.

Through the analysis of the preliminary data taken during 2007 we shown how the equalization of PMTs is taking place and how the Litium Fluorine data have been useful to check the status of the detector.
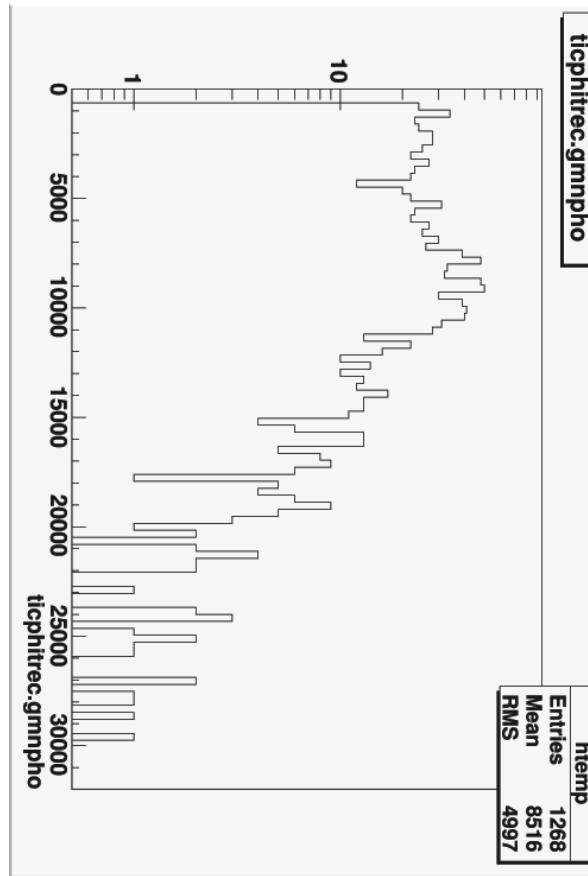
Figure 4.37: Montecarlo simulation of LiF Compton shoulder.
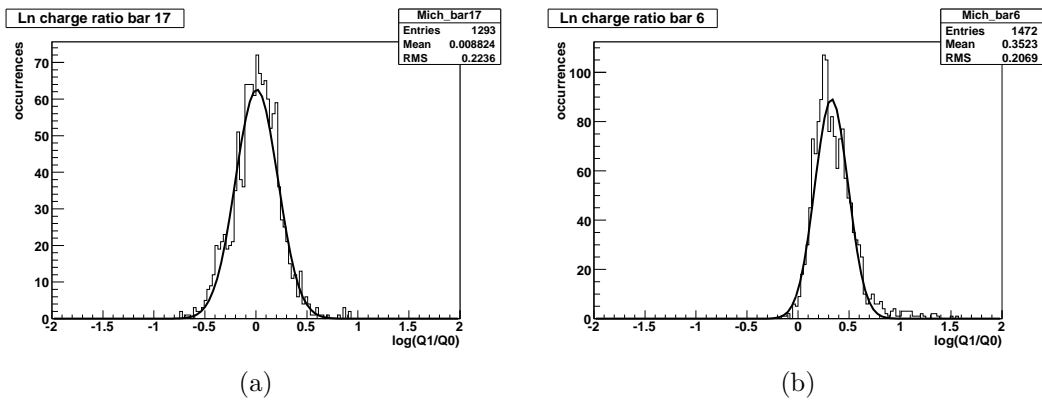
Figure 4.38: Equalized PMT couple (a). Non equalized PMT couple (b).
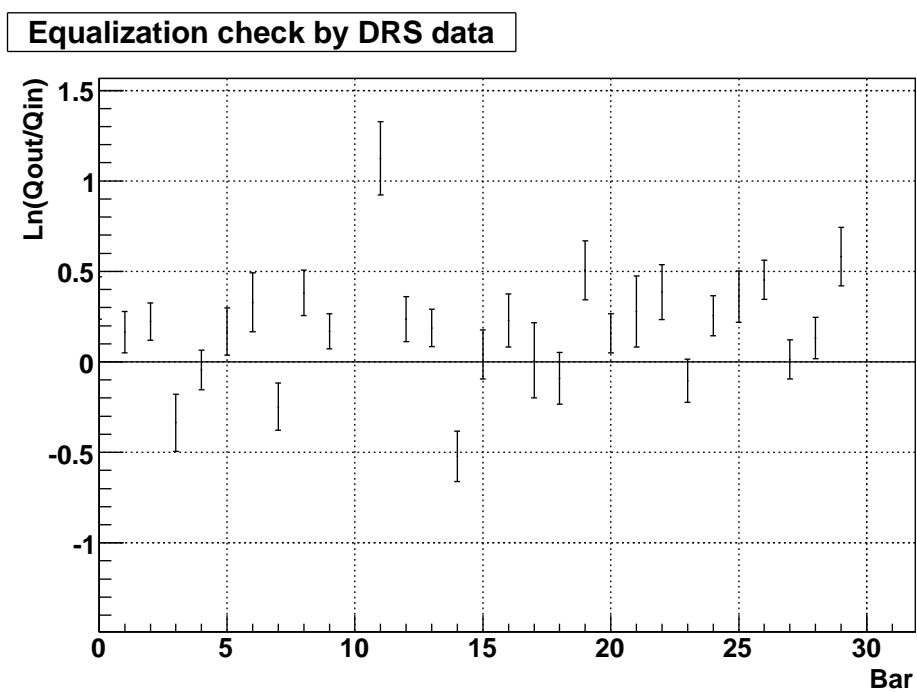
Figure 4.39: Equalization of PMT through Michel run datas.

Chapter 5

Calibration and Monitoring

In the following chapter we will discuss the requirements and the possible strategies for both calibration and monitoring, analyzing in particular the strategy choosen for the TC sub-detector. We will give an overview of the laser monitoring system that will be used and we will describe the possible improvements for the monitor of gain and non linearities of PMTs.

5.1   Preliminary considerations

We aim at measuring the time coincidence of two particles detected by two different sub-detectors. It is pretty difficult to check whether the "reference time" is the same for the whole apparatus, without shifts and delays. All the events are tagged in time with respect to the DAQ global clock, which has a period of 250 `ps`, so it is important to understand the time uncertainty arising from clock propagation delay and jitter.

In the Trigger system the coincidence window for particles to be observed is of the order of 20 `ns`.

The DC signal is too slow (~ 200 `ns`) to be useful at trigger level. The LXe calorimeter and the Timing Counter are the fast-response detectors whose signals are used by the trigger algorithm. The latter provides fast (~ 10`ns`) information about timing and positron direction (correlation of scintillator slices with the positron direction) and works as a filter for Michel positrons with p < 40 MeV/c or out of the acceptance angular range.

The signals coming from simultaneously emitted particles hitting these detectors must be into the Trigger time interval.

Beyond the detailed analysis of each detector system, data must be combined to ensure that the

photon measured in the LXe and the positron measured in the DC and TC come from the same
decay modes and are consistent with a neutrino-less two body decay.

We have to calculate the positron and photon angle and time at the decay vertex. Each of
these four quantities derives from measurements in one or more detectors and from corrections
from measured times and trajectories to transport them back to the target point. More in details:

- The impact time for the photon is obtained from the maximum charge PMT which is con-
  sidered to be the nearest to the conversion point. The decay point from positron trajectory
  and photon shower position is used to correct time at the shower back to the target.

- The photon angle is determined by the straight line connecting the photon conversion point
  and the vertex point.

- The positron time is measured through the TC photo-tubes times using the positron inter-
  section point in TC transverse sub-detector.
  The information on trajectory from DC and TC is used to take into account the particle
  propagation back to the target.

- The positron direction measurement uses the trajectory reconstructed in the DC and mea-
  sured magnetic field to determine the positron momentum vector at the target.

Let's consider the decay time t_0, from the measured response of the various detectors and from
Monte Carlo simulations, the time difference between the two fast detectors can be expressed as:

$$\Delta t = t_e - t_\gamma \tag{5.1}$$

in which the two quantities $t_{e/\gamma}$ are given for each detector by:

$$t_{e/\gamma} = t_{flight-e/\gamma} + t_{Det-e/\gamma} + t_{Elec-e/\gamma} \tag{5.2}$$

where the single contributions come respectively from the Time-of-Flight of each particle, the de-
tector material intrinsic time response and the contributions from electronic readout. This latter
shall be properly tuned so to have both signals within the required time-window. We can however
give a raw estimation range for the time differences, useful in preliminary settings.
Concerning the photon detector: we can take $R_{min}/c < t_{flight} < R_{max}/c$, where $R_{min/max}$ are the
minimum and maximum distance crossed by the photon before conversion occurs inside the LXe
calorimeter. The R values are respectively 65 `cm` and 112 `cm` and the time-of-flight limits for the
photon are consequently 2.1 and 3.8 `ns`.

The rise time of the scintillation light inside the liquid Xenon is of the order of $o(\mathtt{ns})$ and is
almost constant.
The fast strategy for the trigger takes into account the maximum charge PMT which is the nearest
to the conversion point.
From this one the propagation time of light inside the vessel is at most $t_{prop} = (R_{max} - R_{min})\frac{n_{Xe}}{2 \cdot c} =$

$47 \cdot 1.56/(6 \cdot 10^{10}) \sim 1.2$ `ns`.

The electronic timing t_{Elec} is harder to estimate due to the great number of components (PMTs, signal cables, splitter and analog electronics...). Its response adds a further delay. It is important to check that this delay remains constant from time to time not to degrade the timing resolution of the detector. This can be achieved with the laser system described in section 5.4.1.

We can apply almost the same considerations to the TC signal: positrons hit the TC after at least one turn inside the Drift Chambers; this gives a time-of-flight of 4÷6 `ns`. The efficiency limit results of about 80% with a cut on the positrons with two or more turns inside the DCs. If we keep these events in order to improve the efficiency, the time spread introduced increases to 4÷9 `ns` as can be seen from figure 5.1 coming from MC simulations.

The timing response of BC404 scintillator is as fast as 700 `ps` (rise time). The total propagation delay in a 80 `cm` bar, with a $v_{eff} = 15$ `cm/ns`, [1] gives less than 2.7 `ns` delay. The latter is the time in which the light reaches the photo-cathode and gives rise to a signal at the anode after the PMT's transit time: 9.5 `ns`. Additional delay comes from electronics and cables.

5.2 Calibration strategies

As stated above, the goal is to match the two delays in such a way that two simultaneously emitted particles give signals inside the trigger time acceptance. A first raw calibration could be obtained with a laser pulse illuminating both the LXe detector and the TC. In this way the electronic chain time differences are taken into account whereas the "physical" contributions to time differences, such as multiple scattering, are not.

For a more accurate calibration a physical source is needed as a first calibration step. The best calibration process would have a positron and a photon with suitable energy emitted. Obviously the emission point should be as close as possible to the final target position. With these requirements few choices are possible:

- Muon radiative decay (RD).

- two-photon decay of π^o;

- π^o decay with Dalitz pair emission;

MEGA [18] experiment, which set the last limit on the $\mu^+ \rightarrow e^+\gamma$ branching ratio, used RD as a calibration method. For the time being the Collaboration is still considering the three options. In the following section we present a brief discussion about the three methods.

- Radiative muon decay has a branching ratio of 1.4% (for a photon energy greater than 10 `MeV`). By softening the energy cut in the trigger algorithm, it is possible to start a calibration run.

---

[1] v_{eff} has been measured during test beams and is different bar by bar. Here is used a mean value.
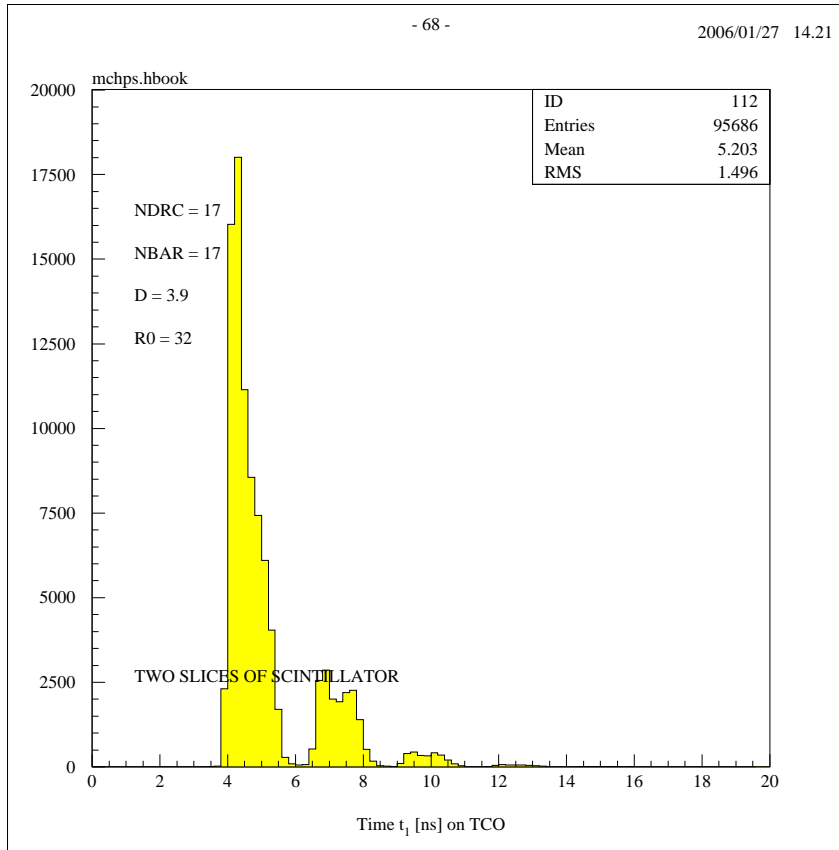
Figure 5.1: Time of impact of positrons on the TC. Notice the good separation between adjacent peaks. Each peak corresponds to a different number of orbits made by positrons before hitting the TC. FWHM of first peak is 1.2 `ns`, average value 4.4 `ns`.

Data taken in this conditions can be used even to test event analysis and reconstruction. In principle, through selecting one-turn positrons, it is possible to check the overall timing resolution to a level of about 1.2 `ns` FWHM, corresponding to the time spread of positron tracks reported in fig. 5.1, without need for positron track reconstruction algorithms: this procedure does not require track reconstruction with DC data. For a correct time synchronization of the detectors it's important to have no pile-up events in which more than one particle from different decaying muons reaches the detectors within the time-coincidence window. It should be useful to decrease the muon stopping rate on the target during the calibration runs to a level such that the probability of having "accidental background" from the calibration events is negligible (with a rate of 1×10^6 we would have an accidental background rate of the order of 8×10^{-16}).

In order to reduce the rate of possible candidates it is advisable to perform angular correlation on the observed particles. Neglecting multiple scattering effects an estimation of the

positron momentum can be given from the impact point on the TC, while for the photon momentum an indication with the same precision comes from the line connecting the target with the PMT which registers the highest signal (as stated before).

- A better determination without requiring the DC signal can be obtained with processes with intrinsic back-to-back emission of a photon and a positron or two photons, one of which could be converted into an electron-positron pair to be detected with the Timing Counter detector. This kind of events can be produced with the decay of neutral pions. Decaying releases two back-to-back photons with energies respectively 55 and 79 `MeV`. Two strategies are possible:

  - select the 55 `MeV`-γ with the LXe detector; the other photon can be converted in a e^-/e^+ pair. The resulting positron is guided by the magnetic field to the DC and the TC and is detected if its energy is in the acceptance range of the detector.

    A converter can be a thin slice of tungsten or other metal, with thickness $x \sim 10^{-2} X_o$ in order to have negligible multiple scattering of both electron and positron which keep original direction correlation with the photon. Photons from pion decays have already been used in preliminary test for the LXe energy resolution [155]. In addition it is quite simple to obtain a pion beam by tuning the beam line parameters. The conversion efficiency is low and multiple scattering is negligible for a conversion efficiency of about 2% [160]. The conversion could be achieved even with a small thickness detector such as a segmented Resistive Plate Chamber (RPC): in this case it is possible to check the conversion point and to have a reference time t_{cv} which can be used for further refining of the calibration measurements.

  - Dalitz-Pair production: in this decay channel the pair is produced directly by the pion decay, carrying (approximately) half of the available energy, together with a ~ 67 `MeV` γ. This produces intrinsically correlated particles with a 1.2 % branching ratio, comparable with the photon-conversion method.

Importance of these methods lies in the possibility to check sources of systematic errors. Difficulties arise from the need of a liquid Hydrogen target in order to convert charged pions from the beam line into neutral pions by means of charge-exchange process ($\pi^- p \to \pi^0 n$).

From this point of view the best calibration strategy is the RD one, since it uses simply the experimental apparatus without the need of time consuming and delicate procedure such as inserting a different target in place of the official one.

Uncertainties in the calibration processes could come from interactions of both photons and positrons with the materials inside the COBRA magnet, which can result in both production of high energy positrons from γ conversion and multiple scattering of positrons with lack of angular correlation.

It is clear that the number of background events entering the signal region can vary in case of time dependence of the detector resolutions, e.g. given by a time-dependent attenuation length for the scintillation light in xenon, or inside the BC404 in TC scintillator bars, or even a time-

dependent yield and quantum efficiency of the PMT both inside LXe and TC. It is therefore necessary to have a continuous and reliable monitoring system of all the experimental resolutions involved in the determination of the signal region. Once the calibration took place, it is needed to keep the detectors resolutions as stable as possible and however to monitor every change of the detectors parameters. The possibility of having different ways of calibration and monitoring, complementary to each other, is of extreme importance for the experiment.

For this reason some monitor systems of the sub-detectors have been realized as described below.

5.3   Calorimeter

LXe calorimeter needs time calibration and also energy calibration to insure the required [160, 161] resolution. Several possibilities are planned, which allow a survey of the detector in an energy range as large as possible:

- In the low energy region (5.5 MeV) α-source spots deposited on thin wires are used to measure the PMT quantum efficiencies and the liquid xenon attenuation length.

- In the intermediate energy region a small Cokcroft-Walton accelerator will be used to shoot 440 keV protons against a Lithium Fluoride target producing 17.6 MeV photons [157].

- In the high energy region measurements of photons from π_0 decays from charge exchange in a Liquid hydrogen target are planned at least twice a year.

5.4   Timing Counter

5.4.1   Laser monitoring

In order to insure that the reached performances of the TC are kept at the level required for the experiment, a laser monitoring is under development.

Checking the TC response with the signal provided by the laser system, it is possible to have a clear monitor on:

- the gain of each photo tube from both TC sections;

- the scintillation properties change of the BC404 of the bars;

- the time resolution due to photon statistic for each scintillator bar and intrinsic electronic limits;

- the lifetime of PMTs in order to have a prompt failure detection.

As we previously stated, for a particle crossing at a time t_0 a scintillator bar (equipped with two photo-multipliers i at the edges) at a distance x from its center, the time difference t_i, between the STOP from the PMT i and the START from the other, is given by:

$$t_i = t_0 + \frac{L/2 \pm x}{v_{eff}} - t_s + \delta_i \quad\quad i = 1, 2 \tag{5.3}$$

where L is the scintillator length, v_{eff} the effective light velocity in the scintillator bar (~ 15 cm/ns) and has been added δ_i which includes all delays (cables, PMT transit time ,...). The quantity $t_+ = \frac{t_1 + t_2}{2} = t_0 + \frac{L}{2 \cdot v_{eff}}$ is independent of the impact point x along the counter and allows to measure the time of flight, while the impact position x can be eventually deduced from $t_- = \frac{t_1 - t_2}{2} = \frac{x}{v_{eff}}$. The resolution of PMT i is given by $\sigma_i{}^2 = \sigma_{t_i}{}^2$, while the crossing time (t_0) resolution is given by $\sigma_0 = 1/2 \times \sqrt{\sigma_1{}^2 + \sigma_2{}^2}$ and is expected to be equivalent to the one calculated directly from the distribution of t_-. Drifts in delays are to be included in the calibration constants δ_i, that must be equalized at the beginning of the data taking period.

The intrinsic resolution of the scintillator counters of the TC has been preliminary evaluated to be around 100 `ps` (for details see chap 3) This puts severe constraints on the calibration system, especially on the laser monitoring system: time drifts have to be traced down at better than few tens of ps.

Accurate equalization of the time response of the different counters can be achieved with two methods: a physics calibrations, which could be repeated every 2-3 months and provide average values of the calibration constants, and a laser system, which allows for continuous monitoring of the evolution of the equalization constants, for instance on a daily basis.

5.4.2   Hardware structure of the laser monitoring system

A layout and a prototype of the laser calibration system almost ready for the TC is shown in figure 5.2

Given the requirement to spot out time drifts of the TC system at the level of l-2 TDC counts, i.e. down to 40 ps, all the elements of the system (laser source, optoelectronic fiber system, injection system into the single scintillator bars) had to be carefully chosen:

- power should be enough to illuminate with an adequate number of photons both the Timing Counter and the LXe calorimeter: at least 100 photons per PMT through optical fibers after leaks due to optical couplings laser-fibers-PM.

- pulse width should be small compared to the detector time resolution to allow the monitor of possible decrease of of the detector performances.

- the laser should work at a optical wavelength of `532nm` (corresponding to Geen) for the Timing Counter detector and to a Ultra Violet wavelength (`266nm`) for the LXe.

For the light source of the monitoring system we used a solid state pumped Nd:YVO$_4$ laser coupled with a electro-optical switch which allows the generation of ultra short pulses (oscillator
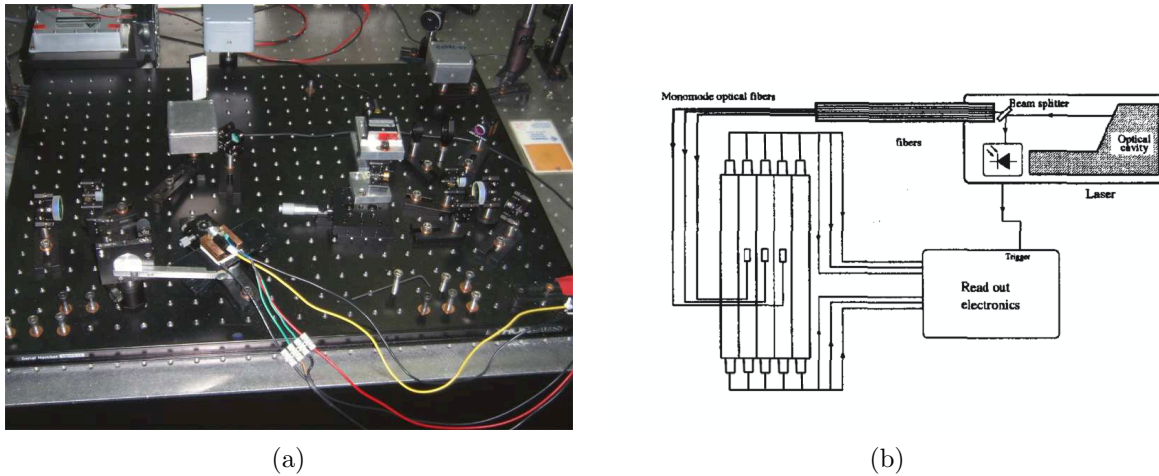
Figure 5.2: Layout of the laser calibration system for the Timing Counter. (a)Prototype under testing, (b)Scheme of the possible final layout, with also a reference counter.

is 50MHz and allows to have 1-1000 Hz repetition rate with a pulse duration of 10-12 ps FWHM see figure 5.3) and the release of a high energy ($\sim 1nJ/pulse$) pulse, which is amplified with solid state amplifiers diode pumped to a power of $\sim 100\mu J$ with an energy stability of 1% for 95% of the shots. The energy should be enough to illuminate both the TC and the LXe at the same time.

The infrared (IR) emission (at $\lambda = 1064$ nm) is converted into a second harmonic at 532 nm by a non linear crystal.

The laser pulse average energy of the prototype has been checked with a pyroelectric device, confirming the specifications (see figure 5.3). The pulse width (and as a consequence the sharpness of the leading edge) is an essential point for our system.

The PMTs of the TC are supposed to work with the BC404 emitted light which have emission spectrum centered at a wavelength of 420 nm. The 532 nm λ coming from the second harmonic is longer and suitable to avoid exiting the scintillation mechanism. With a different choice of the nonlinear crystal, it is possible to obtain even the fourth harmonic ($\lambda = 266$ nm) which can be fed to the LXe calorimeter to test its response. With this wavelength the Xenon fluorescence is not excited so it is possible to check the transmittance properties of the Liquid Xenon and conversely its purity. The power available for the second harmonic is half of the input one and approximatively 1/4 for the fourth harmonic.

In the calibration system the laser light could be beam split to a fast photo diode, providing a common time reference needed for QE $\times$ Gain check between different bars' PMTs.
The other light branch is addressed to a bundle of fibers that transmit the pulse to the different scintillator channels.

Due to the requirement to have the laser source out of the magnet platform to reduce vibrations during operations, relatively long fibers had to be used to inject the laser light into the single

(a)   (b)
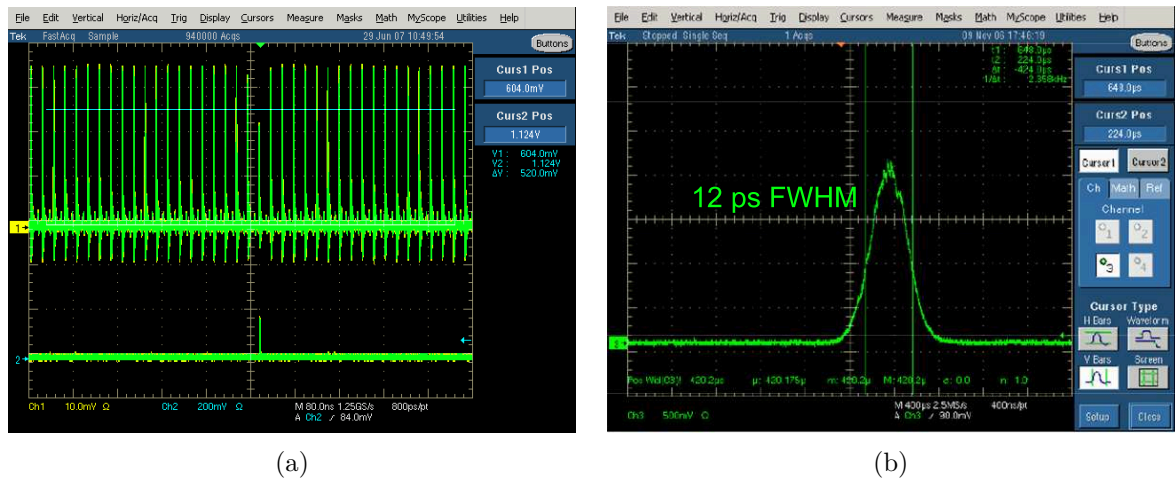
Figure 5.3: Laser system: (a) repetition rate, upper panel, before decimation, lower panel after decimation and (b) pulse width measurements on laser prototype.

Table 5.1: Optical fibers specifications

core diameter	8.2 pm
numerical aperture	0.14
zero dispersion wavelength (λ_0)	1312 nm
zero dispersion slope	0.090 ps/(nm x km)
dispersion D(λ)	$\frac{S_0}{4}(\lambda - \frac{\lambda_0{}^4}{\lambda^3})ps/nm \cdot km$ (1200 < λ <1600 nm)
refr. index difference	0.36%

scintillator counters of the TC.

The choice of the type of optical fiber in the bundle was a critical issue. Precise timing requires a minimum modification to the time characteristics of the fast injected laser pulse or more precisely that the leading edge of the pulse (on which discrimination is done) has a minimum jitter, therefore mono-mode fibers would be the optimal choice; however, light injection into the narrow core of such fibers is a quite delicate task. To reduce injection problems, we used larger core diameter IR mono-mode fibers, that for green light behave as a *limited number of modes* fiber. The choice of the fiber type was based on the measurement of the additional spread introduced on the shape of a laser pulse. Corning SMF-28 fibers (see table 5.1 for details) were chosen for the fiber bundle. The bundle consisted of 60 fibers cut at one edge, peeled and encapsulated in an optical cement matrix and then polished at the free surface. Before the injection in the fiber bundle, the laser beam spot could be enlarged (to about 5 mm diameter) by a system of lenses to reduce intensity dis-uniformities.

At the free end of each fiber the laser signal is injected into a small prism glued at the center of each scintillator bar (see figure 5.4).
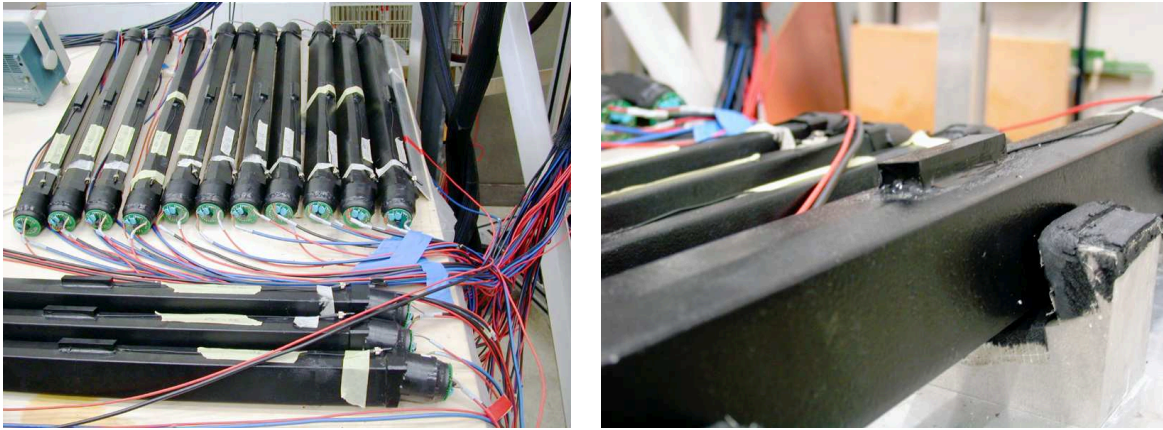
Figure 5.4: Position of insertion of the optical fiber inside each Timing Counterbar.
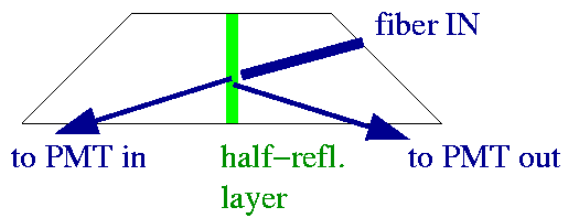
Figure 5.5: Scheme of the splitter prism for the laser calibration and a picture of the actual one before being glued to the bar and covered.

Calibration resolution
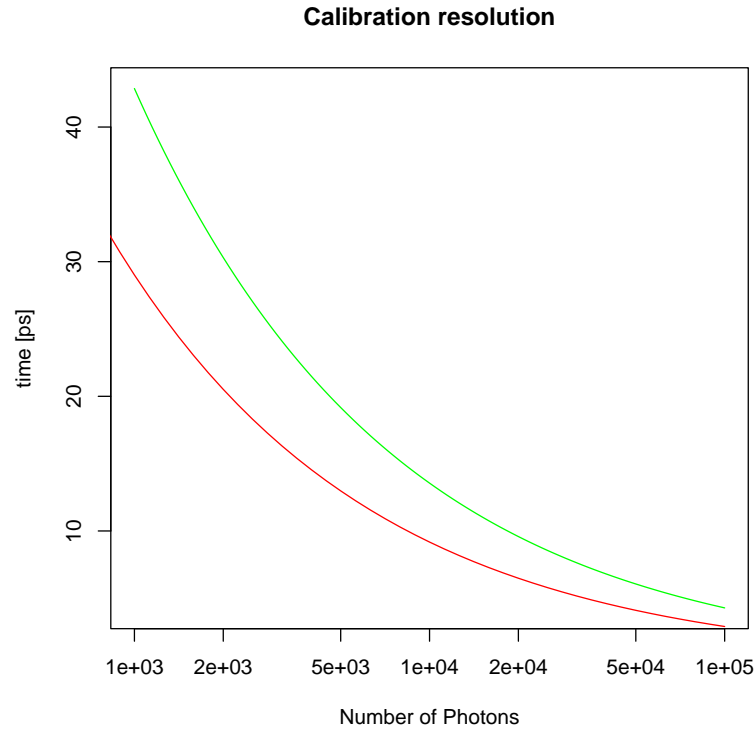
Figure 5.6: Calibration timing resolution versus number of injected photons estimated from a TTS of (red) 440 ps, (green) 650 ps and a QE of 23% not taking into account the saturation of the PMT.

With the optical power given by the laser pulse we can have $O(10^{14})$ *ph/pulse*. Assuming a factor 10^3 of attenuation because of not exact matching between fibers and laser, a further factor 10 due to fiber's *Numerical Aperture* and an efficiency for light incoming the bar to reach the photo-cathode of a PMT of order 10^{-4} we can drop some 10^6 *ph/pulse* on each PMT. In order to check effects on timing resolution of order $\sigma \approx 40$ `ps`, we need some $10^3 ph/pulse$ top reach a $\sigma_{PMT} \sim 30$ `ps` (see figure 5.6).

Thus we have some room left both for not accounted uncertainties and for splitting the pulse to send signals to the Liquid Xenon.

5.4.3   Time stability

The laser system is essential to monitor the TC stability even daily over all the data taking period. The time differences t_i (which will be measured at time t of the data taking period need to be studied for all PMT channels.)
A long term study is needed to understand the expected time drift of constants. Possible drifts in the calibration constants δ_i of the TC system due to temperature effects on a night-day timescale

should also be studied.

5.4.4   Ideas for gain and linearity monitoring

The main task of Gain monitoring (GM) is to monitor and rapidly diagnose the causes of any gain changes of the monitored detectors. Possible causes of a gain change are:

- high voltage (H.V.) instability,

- readout chain problem,

- PMT saturation.

In order to identify these causes effectively let's try to sketch a monitoring procedure.

Definition of relative gain

In general, the response R of a detector to N^γ incoming photons from the laser light is determined by the gain G. Using the subscript *det* to indicate a detector equipped with PMT, and *ref* to denote a reference detector, the gain relations are:

$$R_{det} = G_{det} \cdot N^\gamma{}_{det} \qquad R_{ref} = G_{ref} \cdot N^\gamma{}_{ref} \tag{5.4}$$

The absolute gains of the PMT detectors are determined using high-statistics calibration run. The GM is responsible for correcting these gains for fluctuations that may occur on a shorter time scale. To accomplish this, only the relative gains need to be measured. We define the relative gain G_{det} as follows:

$$g_{det} = R_{det}/R_{ref} = G_{det}/G_{ref} \cdot \beta_{det} \tag{5.5}$$

where $\beta_{det} = N^\gamma{}_{det}/N^\gamma{}_{ref}$ is the ratio of the number of incoming photons between the monitored detector and reference detector.

The main request for a reference detector is to be stable and reliable. PIN photo-diodes (S1190, Hamamatsu Corp.) can be used for this purpose because of the very small temperature dependence of their gain in the wavelength region of interest [139]. The light pulses can be transmitted to the reference detectors via optical fibers, in the same way as to the monitored detectors.

If the reference detector gain, G_{ref}, is constant with time, any change δ_{gdet} in the relative gain is proportional to the change δ_{Gdet} in the absolute gain, assuming β_{det} as a constant:

$$\delta_{gdet} = \delta G_{det}/G_{ref} \cdot \beta_{det} \tag{5.6}$$

In practice, the relative gain is evaluated by averaging the responses, R_{det}, R_{ref} over a sequence of GM events

$$g_{det} = \frac{\sum_i R^i{}_{det}}{\sum_i R^i{}_{ref}} \tag{5.7}$$

where the i index runs over all GM events recorded in the time interval of the measurement. The resolution of this averaged relative gain is roughly $\sigma/\sqrt{N}$, where σ is the intrinsic resolution in

relative gain of a single-event GM measurement and N is the total number of GM events used in the calculation.

It is possible that the laser power fluctuates because of *flash lamp* aging within the laser itself. When this occurs, the fluctuations in laser power can reach even 10%. The PMT and reference detectors see the same laser pulses which leaves g_{det} unaffected by any fluctuations of the laser intensity and β_{det} independent of time.

On-line monitor

An on-line monitoring system should provides a real-time diagnosis of detector problems, such as H.V. trips or readout chain failures. For this purpose, only a part of the full data stream can be taken (about 10 GM events for one gain measurement).
The relative gains for all monitored detectors are calculated with Eq.5.7.
These measurements are then compared to *initial* reference values which are reset every physic calibration run.
The deviation of the relative gains from their original values can be visualized with color on a display program providing a real-time monitor of the detector condition. Non linearity in the detector responses can be checked during an *offline* monitoring.
Non-linear behavior is revealed by the relative responses of the detectors to light pulses of different intensity. Any non-linear behavior affects the normalized gain change calculated by the GM system. The dependence of the gain on intensity can be used to distinguish between actual gain changes and changes in linearity. For the linearity check, some points from measurements of different intensities can be fit with a linear function $R_{det} = a \cdot R_{ref}$ and the relative gain is obtained from the slope: a, with a certain value of χ^2/ndf.
Under normal conditions, such a linear fit gives consistent results with Eq. 5.7, and shows a good linear response to the laser light. If the detector gain saturates, the fit result becomes worse. This is particularly evident in the points of highest intensity, which give the largest χ^2 contribution. As long as the detector keeps its linearity, χ^2 will not be affected and only the slope will change. In this manner, influences on the linearity and global gain of the PMT detectors can be distinguished. This would require a small improvement: a system able to change laser light intensity like the one described in the following subsection.

Light filter.

The light filtering system should be installed in front of the light source. This system consists of five reflective neutral density filters of different attenuation, a wheel, a DC motor, and LED/photo-transistor pairs (Fig. 5.7).

The light intensity is modified by the filters mounted on the motorized wheel. In order to identify which filter is in position at any given time, a series of small holes is drilled along the wheel radii (shown as (1) in Fig.5.7).
The holes are observed by fixed infrared-LED/photo-transistor pairs. The total photo-transistor
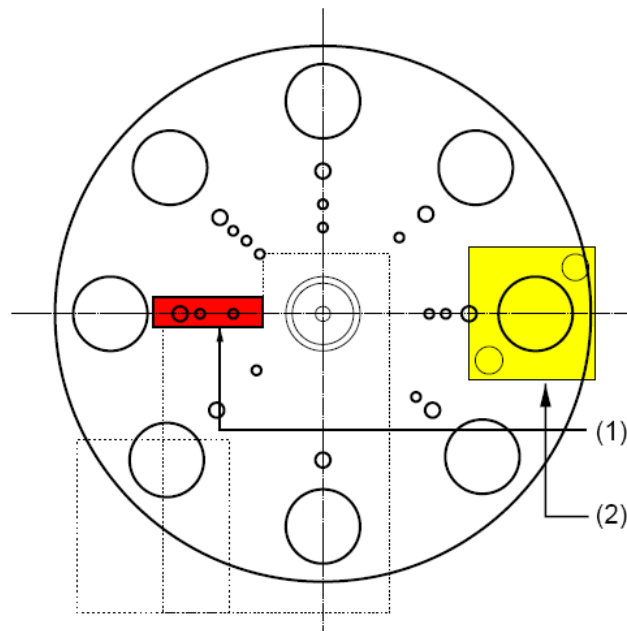
Figure 5.7: Cross-section of the light filtering system. The indicated holes are aligned along the radii of the motorized wheel. The attenuation filters are attached to the large, outermost holes. The small holes are coupled with fixed LED/photo-transistor pairs, (1), whose signals are used for filter identification and laser triggering. At (2) is an optical coupler to carry the filtered light to the main optical fiber.

signal takes one of 8 different values, depending on the pattern of the three innermost holes which is in position.

The outermost small holes of the series are used to verify that the filter wheel is aligned with the beam line of the laser. These holes are coupled with an LED/photo-transistor pair like the others.

5.4.5 Conclusions

A fast-laser based calibration system is under development for the time calibration and monitoring of the Timing Counter for the MEG experiment.
The intrinsic TC resolution of 100 ps has put severe requirements on the calibration system. Time drifts down to about 40ps can be monitored on a day by day timescale.
It is possible to extend the system to the LXe to achieve also a inter-detector calibration.
It has been illustrated how with a small improvement of the system it would be possible to monitor also gains variations and non linearities of the PMTs and to distinguish between them.

Conclusion

After the discovery of flavour violation in the neutrino sector it is very important to understand the root of this phenomenon.

A sizeable flavour violation could be explained by new physics beyond the SM. Supersymmetric GUT theories can naturally accomodate finite neutrino masses and also predict rather large branching ratios for lepton flavour violating decays.

Among the LFV processes, a special role was played along the years by the $\mu^+ \to e^+\gamma$ search. Each time it was repeated with improved sensitivity ($\sim$ a factor 100/decade). It has the chance, like the g-2 experiment, of providing important constraints to theories at critical moments of their development. The most recent upper limit on the Branching ratio was obtained in the 1999 by MEGA experiment: BR$< 1.2 \ 10^{-11}$ at 90% C.L..

MEG is supposed to reach a limit on BR of two orders of magnitude better.

A description of the MEG experiment, of its experimental apparatus and a full discussion of its sensitivity has been given in the first part of this work.

An accurate description of MEG Timing Counter sub-detector and how the proposed time resolution below 100ps for the positron time of flight have been achieved has been given in the second part .

The test of the prototype was of great importance because it brought to the understanding of problems concerning both scintillators and PMT, the PMT operation inside high B and how to overcome that.

Moreover a geometry optimization have been planned, realized and deployed during these tests which finally drive to what now is the MEG's Timing Counter sub-detector.

The preliminary run of 2006, with a reduced part of the final detector, and the ongoing engineering run of 2007 gave good results, as shown in the last part of this work. In a few weeks the entire apparatus will be validated in the final configuration and the experiment is foreseen to finish the engineering run at the end of 2007 and to start collecting data during next year.

Bibliography

[1] R. Barbieri, "The Standard Model of Electroweak Interactions", IFUP-TH06/95, and references therein.

[2] I.J.R. Aitchison, "Field Theory and the standard model", Lessons at European school of high energy physics (2001) Beatenberg

[3] A. Pich,"The Standard Model of Electroweak Interactions," arXiv:0705.4264 [hep-ph].

[4] S. Weinberg, "The Quantum Theory of Fields", Cambridge University Press (2000) Cambridge

[5] R. N. Mohapatra, "Unification and Supersymmetry", 2nd edition, Springer-Verlag, New York (1992)

[6] L. B. Okun, "Leptons and Quarks", North-Holland Publishing Company, Amsterdam (1982)

[7] B. T. Cleveland *et al.*, "Measurement Of The Solar Electron Neutrino Flux With The Homestake Chlorine Detector," Astrophys. J. **496**, 505 (1998).

[8] Y. Fukuda *et al.* [Super-Kamiokande Collaboration], "Measurement of the solar neutrino energy spectrum using neutrino electron scattering," Phys. Rev. Lett. **82**, 2430 (1999) [arXiv:hep-ex/9812011].

[9] Y. Suzuki [Super-Kamiokande Collaboration], "Solar Neutrino Results From Super-Kamiokande," Nucl. Phys. Proc. Suppl. **77**, 35 (1999).

[10] D. Kielczewska [SUPER-KAMIOKANDE Collaboration], "Neutrino Oscillations At Super-Kamiokande," Nucl. Phys. Proc. Suppl. **81**, 133 (2000).

[11] W. Hampel *et al.* [GALLEX Collaboration], "GALLEX solar neutrino observations: Results for GALLEX IV," Phys. Lett. B **447**, 127 (1999).

[12] J. N. Abdurashitov *et al.* [SAGE Collaboration], "Measurement of the solar neutrino capture rate with gallium metal," Phys. Rev. C **60**, 055801 (1999) [arXiv:astro-ph/9907113].

[13] M. Apollonio *et al.* [CHOOZ collaboration], "Search for neutrino oscillations on a long base-line at the CHOOZ nuclear power station" Eur. Phys. J. C**27**, (2003) 331 [arXiv:hep-ex/0301017]

[14] Q. R. Ahmad *et al.* [SNO Collaboration], "Measurement of the charged of current interactions produced by ^{8}B solar neutrinos at the Sudbury Neutrino Observatory," Phys. Rev. Lett. **87**, 071301 (2001) [arXiv:nucl-ex/0106015].

[15] M. Maltoni *et al.* "Status of global fits to neutrino oscillations", preprint `hep-ex/0405172`

P. Creminelli, G. Signorelli and A. Strumia, "Frequentist analyses of solar neutrino data," JHEP **0105**, 052 (2001) [arXiv:hep-ph/0102234].

[16] H. Georgi, in *Particles and Fields*, ed. C. E. Carlson, AIP (1975)

[17] Fritsch and Minkowski, Ann. Phys. **93** (1975) 193

[18] M. L. Brooks *et al.* [MEGA Collaboration], "New limit for the family-number non-conserving decay $\mu^+ \to e^+\gamma$", Phys. Rev. Lett. **83**, 1521 (1999) [arXiv:hep-ex/9905013].

[19] M. Ahmed *et al.*, "Search for the lepton-family-number nonconserving decay $\mu^+ \to e^+\gamma$," Phys. Rev. D **65** (2002) 112002 [arXiv:hep-ex/0111030].

[20] Bellgardt, U., *et al.*, 1988, Nucl. Phys. B **229**, 1.

[21] Wintz, P., 1998, in *Proceedings of the First International Symposium on Lepton and Baryon Number Violation*, edited by H.V. Klapdor-Kleingrothaus and I.V. Krivosheina (Institute of Physics Publishing, Bristol and Philadelphia), p.534.

[22] Willmann, L., *et al.*, 1999, Phys. Rev. Lett. **82**, 49.

[23] Edwards, K.W., *et al.* (CLEO Collaboration), 1997, Phys. Rev. B **55**, R3919.

[24] K. Abe *et al.* [Belle Collaboration] "Search for $\tau \to \mu\gamma$ decay at Belle," KEK PREPRINT-2001-79 (2001) *Prepared for the 20th International Symposium on Lepton and Photon Interactions at High Energies (LP 01) Rome, Italy, 23-28 Jul 2001*

[25] Bliss, D.W., *et al.*, 1998, Phys. Rev. D **57**, 5903.

[26] Krolak, P., *et al.*, 1994, Phys. Lett. B **320**, 407.

[27] Ambrose, D., *et al.* (BNL E871 Collaboration), 1998, Phys. Rev. Lett. **81** 5734.

[28] Lee, A.M., *et al.*, 1990, Phys. Rev. Lett. **64**, 165.

[29] L. Bellantoni *et al.* [KTeV collaboration], Proc. 36th Rencontres de Moriond (Les Arcs, France) 10-17 Mar 2001 [arXiv:hep-ex/0107045]

[30] Akers, R., *et al.* (OPAL Collaboration), 1995, Z. Phys. C **67**, 555.

[31] Abreu, P., *et al.* (DELPHI Collaboration), 1997, Z. Phys. C **73**, 243.

[32] L. J. Hall, V. A. Kostelecky and S. Raby, "New Flavor Violations In Supergravity Models", Nucl. Phys. B **267**, 415 (1986).

[33] R. Barbieri and L. J. Hall, "Signals for supersymmetric unification," Phys. Lett. B **338**, 212 (1994) [arXiv:hep-ph/9408406].

[34] R. Barbieri, L. J. Hall and A. Strumia, "Violations of lepton flavor and CP in supersymmetric unified theories," Nucl. Phys. B **445**, 219 (1995) [arXiv:hep-ph/9501334].

[35] Y. Kuno and Y. Okada, "Muon decay and physics beyond the standard model," Rev. Mod. Phys. **73**, 151 (2001) [arXiv:hep-ph/9909265].

[36] J. Hisano, T. Moroi, K. Tobe and M. Yamaguchi, "Exact event rates of lepton flavor violating processes in supersymmetric SU(5) model," Phys. Lett. B **391**, 341 (1997) [Erratum-ibid. B **397**, 357 (1997)] [arXiv:hep-ph/9605296].

[37] P. Ciafaloni, A. Romanino and A. Strumia, "Lepton flavor violations in SO(10) with large tan beta," Nucl. Phys. B **458** (1996) 3 [arXiv:hep-ph/9507379].

[38] J. Hisano and D. Nomura, "Solar and atmospheric neutrino oscillations and lepton flavor violation in supersymmetric models with the right-handed neutrinos," Phys. Rev. D **59**, 116005 (1999) [arXiv:hep-ph/9810479].

[39] K. Hagiwara *et al.* [Particle Data Group Collaboration], "Review of particle physics," Phys. Rev. **D 66**, 010001 (2002).

[40] H. N. Brown *et al.* [Muon g-2 Collaboration], "Precise measurement of the positive muon anomalous magnetic moment," Phys. Rev. Lett. **86**, 2227 (2001) [arXiv:hep-ex/0102017].

[41] J. Hisano and K. Tobe, "Neutrino masses, muon $g - 2$ and lepton-flavour violation in the super-symmetric see-saw model", Phys. Lett. B **510**, 197 (2001) [arXiv:hep-ph/0102315].

[42] S. H. Neddermeyer and C. D. Anderson, "Note On The Nature Of Cosmic Ray Particles," Phys. Rev. **51**, 884 (1937).

[43] H. Yukawa, Proc. Phys. Math. Soc. Jap. **17**, 48 (1935)

[44] D. Green, H. Haggerty, S. Hansen and M. Takasaki, "Accurate Two-Dimensional Drift Tube Readout Using Time Division and Vernier Pads," Nucl. Instrum. Meth. A **256** (1987) 305.

[45] M. Conversi, E. Pancini and O. Piccioni, "On The Disintegration Of Negative Mesons," Phys. Rev. **71**, 209 (1947).

[46] E. P. Hincks and B. Pontecorvo, "On The Absence Of Photons Among The Decay Products Of The 2.2-Microsecond Meson," Can. J. Res. **28A**, 29 (1950), reprinted in S. M. Bilenky *et al.* (editors) "Bruno Pontecorvo" Società Italiana di Fisica (1997)

[47] Lokonathan, S. and J. Steinberger, "Search for Improbable Muon Decays" Phys. Rev. **98**, 240 (1955).

[48] Feinberg, G., Phys. Rev. **116**, 1482 (1958)

[49] Danby, G., J.M. Gaillard, K. Goulianos, L.M. Lederman, N. Mistry, M. Schwartz, and J. Steinberger, Phys. Rev. Lett. **9**, 36 (1962)

[50] S. Ritt, Talks from Review Meetings, July 2004, http://meg.web.psi.ch/docs/

[51] A. Hitachi et al., Phys. Rev. B 27 (1983) 5279.

[52] A. Yamamoto et al., Nucl. Phys. B 78 (1999) 565.

[53] P. Depommier *et al.*, "A New Limit On The $\mu^+ \to e^+\gamma$ Decay," Phys. Rev. Lett. **39**, 1113 (1977).

[54] A. van der Schaaf, R. Engfer, H. P. Povel, W. Dey, H. K. Walter and C. Petitjean, "A Search For The Decay $\mu^+ \to e^+\gamma$", Nucl. Phys. A **340**, 249 (1980).

[55] W. W. Kinnison *et al.*, "A Search For $\mu^+ \to e^+\gamma$", Phys. Rev. D **25**, 2846 (1982).

[56] R. D. Bolton *et al.*, "Search For Rare Muon Decays With The Crystal Box Detector," Phys. Rev. D **38**, 2077 (1988).
R. D. Bolton *et al.*, "Search For The Decay $\mu^+ \to e^+\gamma$", Phys. Rev. Lett. **56**, 2461 (1986).

[57] Fronsdal, C., and H. Überall, Phys. Rev. **118**, (1959) 654.

[58] Eckstein, S.G., and R.H. Pratt, Ann. of Phys. **8**, (1959) 297.

[59] Y. Kuno and Y. Okada, "$\mu \to e\gamma$ Search with Polarized Muons," Phys. Rev. Lett. **77**, 434 (1996) [arXiv:hep-ph/9604296].

[60] S. Parker, H. L. Anderson and C. Ray, "Search for the decay $\mu^+ \to e^+\gamma$", Phys. Rev. **133** B768 (1964).

[61] S. Frankel *et al.*, "New Limit on the $e + \gamma$ Decay Mode of the Muon", Phys. Rev. Lett. **8** 123 (1962).

[62] H. P. Povel *et al.*, "A New Upper Limit For The Decay $\mu^+ \to e^+\gamma$" Phys. Lett. B **72**, 183 (1977).

[63] A.E. Pifer *et al* "A high stopping density μ^+ beam" NIM 135 (1976) 39

[64] H-W. Reist *et al.* "Development of a low-momentum "surface" muon beam for LAMPF", NIM 153 (1978) 61

[65] J. D. Bowman *et al.*, "Upper Limit For The Decay $\mu^+ \to e^+\gamma$", Phys. Rev. Lett. **42**, 556 (1979).

[66] A. Baldini, [MEG Collaboration], "The MEG experiment: search for the $\mu^+ \to e^+\gamma$ decay at PSI" at `http://meg.psi.ch/docs/prop_infn/nproposal.ps.gz`

[67] TRANSPORT - *A Computer Program for Designing Charged Particle Beam Transport Systems*, K.L. Brown *et al.* CERN Yellow Report 73-16, (1973);

[68] Decay TURTLE - *A Computer Program for Simulating Charged Particle Beam Transport Systems, including Decay Calculations* K.L. Brown and Ch. Iselin, CERN Yellow Report 74-2 (1974);
Graphics versions of both Programmes by U. Rohrer PSI-Report (1980).

[69] T. Mori *et al.*, Search for $\mu \rightarrow e + \gamma$ down to 10^{-14} branching ratio, proposal to PSI (1999) R-99.05.01

[70] MEG Collaboration, "Test measurements for the MEG drift chambers" in PSI Annual Report (2003), also at http://meg.pi.infn.it/docs/index.html

[71] G. Signorelli, "Towards a $\mu^+ \rightarrow e^+\gamma$ experiment", Pretesi per il passaggio al terzo anno di Perfezionamento della Scuola Normale Superiore (2002) unpublished.

[72] MEG Collaboration, "MUEGAMMA timing counter prototype test", PSI Annual Report (2001)

[73] F. Gatti, "Status of the MEG timing counter", February 2004, available at http://meg.psi.ch/docs

[74] F. Gatti, "Timing counter report", April 2007, available at http://meg.psi.ch/docs

[75] T. Doke and K. Masuda, "Present status of liquid rare gas scintillation detectors and their new application to gamma-ray calorimeters" Nucl. Instr. Meth. **A420** (1999) 62

[76] C. Rubbia, CERN EP Internal Report 77-8 (1977)

[77] E. Conti *et al.* [EXO Collaboration], "Correlated fluctuations between luminescence and ionization in liquid xenon," Phys. Rev. B **68** (2003) 054201. arXiv:hep-ex/0303008.

[78] P. K. Lebedev and V. I. Pryanichnikov, "Present and Future production of Xe and Kr in the former USSR", Nucl. Instrum. Meth. A **327** (1993) 222.

[79] P. Belli *et al.* "Liquid Xenon scintillators" Nucl. Instr. Meth. **A310** (1991) 150

[80] A. S. Schlüsser *et al.*, "Observation of excimer luminescence from electron-excited liquid Xenon", Appl. Phys. Lett. **77** (2000) 1

[81] E. Morikawa *et al.*, "Ar, Kr and Xe excimer luminescence: from the dilute gas to the condensed phase", J. Chem. Phys. **91** (1989) 1469

[82] J. Jortner *et al.*, "Localized excitations in condensed Ne, Ar, Kr and Xe", J. Chem. Phys. **42** (1965) 4250

[83] N. Schwenter, E.-E. Koch and J. Jortner, "Electronic Excitations in Condensed Rare Gases", Springer-Verlag, Berlin 1985

[84] N. J. Basov *et al.*, J. Luminescence 1/2 (1970) 834
N. J. Basov *et al.*, JETP Lett. **12** 329

[85] J. B. Gerardo and A. W. Johnson, "Photoattenuation in the extreme red wings of Xe and Kr resonant lines", Phys. Rev. **A 10** (1974) 1204

[86] L. D. Landau, E. M. Lifshitz, "Electrodynamique des milieux continus", 12 ed. MIR Moscow (1990)

[87] G. M. Seidel, R. E. Lanou and W. Yao, "Rayleigh scattering in rare-gas liquids" Nucl. Instrum. Meth. A **489** (2002) 189 [arXiv:hep-ex/0111054]

[88] A. Baldini *et al.*, "Liquid Xe scintillation calorimetry and Xe optical properties" arXiv:physics/0401072.

[89] L. M. Barkov *et al.* Nucl. Instr. Meth. **A379** (1996) 482

[90] J. D. Jackson, *Classical Electrodinamics*, 3rd ed. (1998) Wiley

H. Frohlich, *Theory of dielectrics*, Oxford University Press, New York (1957) 2nd edition.

[91] K. Watanabe E. Inn and M. Zelikoff, "Absorption coefficients of oxygen in the vacuum ultraviolet" J. Chem. Phys. **21** (1953) 1026

[92] The tabulated data are taken from the NASA web site http://uvisun.msfc.nasa.gov/GG/GG34-ECHAR/oldhome.html

[93] IUPAC Subcommittee on Gas Kinetc Data Evaluation - Data Sheet POx1, available at http://www.iupac-kinetic.ch.cam.ac.uk

[94] The tabulated data are taken from the Oregon Medical Laser Center, http://omlc.ogi.edu/spectra/water/ and references therein.

[95] IUPAC Subcommittee on Gas Kinetc Data Evaluation - Data Sheet PHOx1, available at http://www.iupac-kinetic.ch.cam.ac.uk

[96] K. Watanabe and M. Zelikoff, "Absorption coefficients of water vapor in the vacuum ultraviolet" J. Opt. Soc. Am. **43** (1953) 753

[97] The GEANT physics simulation reference manual, v. 3.21 (1994) CERN Library Long Writeup W5013

[98] S. Belforte *et al.*, *SVT Technical Design Report*, CDF note 3108 (1994); CERN EP report 81-12/ReV.

[99] T. Haruyama, "A pulse-tube refrigerator fo the PSI MUEGAMMA experiment", MUEGAMMA (2000) available at http://meg.pi.infn.it, and KEK-PREPRINT-2002-102

[100] MONO TORR PS15 Series, SAES Pure Gas, Inc. 4175 Santa Fe Road San Luis Obispo, California, 93401 USA.

[101] Oxisorb, Messer Griesheim GmbH, Dusseldorf, Germany.

[102] A. Beer G. Critin and G. Schuler, NIM A234 (1985) 294

[103] R. L. Carrington *et al.*, Nucl. Instr. Meth. **163** (1979) 203

[104] C. Bemporad *et al.*, Phys. Rev. **138** (1965) B1546

[105] F. R. Arutyunyan and V. A. Tumanian, Phys. Lett. **4** (1963) 176

[106] R. H. Milburn, Phys. Rev. Lett. **10** (1963) 75

[107] D. Babusci *et al.*, "Polarised and tagged gamma-ray Ladon beams", Riv. Nuovo Cim. **19** (1996) 1

[108] H. Ohgaki, H. Toyokawa, K. Kudo, N. Takeda, T. Yamazaki, "Generation and application of Laser-Compton gamma ray at ETL", NIM **A455**, 54-59 (2000)

[109] K. Ozone, University of Tokyo PhD thesis, in progress.
       MEG Collaboration, "Recent developments of the MEG liquid Xenon photon detector", PSI Annual Report (2003)

[110] A. S. Wightman, Phys. Rev. **77** (1950) 521

[111] E. Fermi and E. Teller, Phys. Rev. **72** (1947) 399

[112] W. K. H. Panofsky, R. L. Aamodt and J. Hadley, Phys. Rev. **81** (1951) 565

[113] J. F. Crawford *et al.*, Phys. Rev. D**43** (1991) 46

[114] J. Spuller *et al.*, "A remeasurement of the Panofsky Ratio", Phys. Lett. **67B** (1977) 479

[115] G. Signorelli, "PhD Thesis", (2004) unpublished

[116] Paul Scherrer Institut, PSI Accelerator Facilities Users' Guide, (1994) available from the PSI secretatiat. Information available also from the PSI web site `http://www.psi.ch`

[117] P-R. Kettle, private communication.

[118] B Rossi, "High energy particles", Prentice-Hall, New York (1952)
       M. G. Payne "Energy Straggling of Heavy Charged Particles in Thick Absorbers", Phys. Rev. **185** (1969) 611

[119] J. A. Bistirlich *et al.*, Phys. Rev. C **5** (1972) 1867.

[120] A. Papa, Tesi di Laurea Universitá di Pisa (2004), unpublished

[121] A. Bay *et al.*, "A Modular NaI(Tl) Detector for Intermediate Energy Photons", Nucl. Inst. Meth. **A271** (1988) 497

[122] E. Frlež, D. Počanić, S. Ritt, Nucl. Inst. Meth. **A463** (2001) 341 [arXiv:hep-ex/0009042]

[123] Birks, "Theory and practice of scintillation counting" New York (1964)
      Breitemberg, Progr. Nucl. Phys. **4** (1956) 56.

[124] M. Ambrosio *et al.* [MACRO collaboration] "The MACRO detector at Gran Sasso", Nucl. Instr. Meth. Phys. Res. A **486** (2002) 663

[125] The MIDAS Online and Analysis Framework, `http://midas.psi.ch`

[126] Y. Kubota et al., Nucl. Instr. and Meth. A 320 (1992) 66

[127] E.S. Smith et al., Nucl. Instr. and Meth A 432 (1999) 265

[128] B. Adeva et al., Nucl. Instr. and Meth A 491 (2002) 41

[129] B. Adeva et al., Nucl. Instr. and Meth A 491 (2002) 41

[130] G. Palla et al., Nucl. Instr. and Meth. A 451 (2000) 406

[131] V. Sum et al., Nucl. Instr. and Meth. A 326 (1993) 489

[132] M. Baldo Ceolin et al., Nuovo Cimento 105A (1992) 1679

[133] G.C. Bonazzola et al., Nucl. Instr. and Meth. A 356 (1995) 270

[134] S. Benerjee et al., Nucl. Instr. and Meth. A 269 (1988) 121

[135] J.S. Brown et al., Nucl. Instr. and Meth. 221 (1984) 503

[136] HAMAMATSU Photonics,http://sales.hamamatsu.com/assets/pdf/catsandguides/PMT_High_energy.pdf.

[137] HAMAMATSU Photonics,http://sales.hamamatsu.com/assets/pdf/catsandguides/PMT_High_energy.pdf.

[138] http://sales.hamamatsu.com/assets/pdf/catsandguides/PMT_Fine_Mesh.pdf.

[139] HAMAMATSU Photonics, product catalog (S1190 or S5821).

[140] R. Valle, PhD Thesis, Universitá di Genova, (2006) unpublished.

[141] S. Dussoni, PhD Thesis, Universitá di Genova, (2006) unpublished

[142] G. Gallucci, (2007) collaboration meeting presentation.

[143] F.Gatti private comunication

[144] http://www.detectors.saint-gobain.com/Data/Element/Product-/product.asp?ele_ch_id=P0000000000000001108

[145] W.R.Binns et al, NIM 216 (1983) 475.

[146] Table of isotopes, E.Browne et al., edited by C.M.Lederer and V.S.Shirley, 7th edition 1978

[147] http://www.photonis.com/briv/spec/pdf/XP2020.PDF

[148] W. B. Atwood, "Time of flight measurements" SLAC-PUB-2620 (1980)

[149] http://meg.web.psi.ch/docs/talks/review_july02/Alessandro/meg.pdf

[150] Yang, X. H.*et al.*, "Monte-Carlo studies of the performance of scintillator detectors for time-of-flight measurements" NIM **354**, 270 (1995)

[151] W. Braunschweig *et al.*, "A large area time-of-flight system with a resolution of 0.5 ns FWHM" NIM **134**, 261 (1976)

[152] http://meg.web.psi.ch/docs/talks/review_feb04/timing_counter/Meg TC feb04.ppt

[153] S–O Flyckt and C. Marmonier editors, "Photomultiplier Tubes: principles and applications", Photonis Brive, France, (2002)

[154] G. J. Feldman and R. D. Cousins, Phys. Rev. D **57** (1998) 3873;

[155] A.Baldini et al., IEEE, page(s): 337-340 (26 June-1 July 2005), Transparency of a 100 liter liquid xenon scintillation calorimeter prototype and measurement of its energy resolution for 55 MeV photons;

[156] A. Baldini *et al.*, MEG internal note TN032, A test on γ-ray Production by the reaction $^7_3Li(p,\gamma)^8_4Be$ and $^{11}B(p,\gamma)^{12}C$ at the Legnaro Laboratory, January 2006;

[157] ¡ R.L. Walker and B.D. McDaniel, **Phys Rev. 74**, 315 (1948); K. Spyrou *et al.*, **Eur. Phys. J A7**, 79(2000);

[158] F.E. Cecil *et al.*, **Nucl. Phys A539**, 75 (2002);

[159] L. Holland, Vacuum Deposition of Thin Films, Chapmann and Hall LtD (1961);

[160] A. Baldini *et al.*, MEG internal note TN027, Considerations on the Calibration and Monitoring of the MEG detector, May 2005;

[161] A. Baldini *et al.*, MEG internal note TN029, A Radioactive point-source lattice for calibrating and monitoring the MEG experiment Liquid Xenon Calorimeter, November 2005;

[162] http://meg.pi.infn.it/restricted/talks/lfvseminar_mar06/bill_photon_positron_correlation.ppt

Acknowledgments

Time has come to say *grazie*. First of all I would like to thank the MEG Rome group starting from the *Prof* who teached me a lot and lead me through these years with patience and his huge wisdom and culture, then I wish to thank Giancarlo who has been a great *first driver* leading me through all the obstacles in this last difficult period.

I wish to say thanks to Ceci and Luca for the always useful discussions both at PSI during the nights and in Rome during the days. Genova's group for the many answers they gave also to my stupid questions both in Frascati and during the Christmas time 2006 in PSI. Pavia's group for the many useful discussions both on hardware side and on software side and in particular Gianluigi for the answers he gave me also during summer time. I would like to thank also the whole of Pisa group and the guys of PSI.

It would not be possible to finish this work without the patience and help of the *GRIDders (griddaroli in Italian)* who gave me the possibility not only to participate to the experiment (they are the ones paying me), but always encoraged me in keep going.A very special thank goes to Enzo, my big boss, who is more a big father than a big boss who never stopped encoraging me, his own way :) obviously.

I wish to specially thank my ATLAS boss Lamberto who has been always present to make thing as smooth as possible.

And a very very special thank goes to *Sensei* who will always be my guru, it's impossible to *tar* in few lines how important has been his presence.

I really thank Daniela and all the guys working with me who has been a bit overloaded from my tension of the last period; a special thank goes also to Marco always there not only to help me but also to remember me to *breath. . .* it would not be the same without all of you.

I wish to say thank you to all the Uspid and ISPY guys I met really in hurry during the Pugwash conference in Bari while writing, since their nice discussions have been really a great pulse to go on, not only for this thesys but for life. I hope to have more time to join next ISPY meetings and to be useful now that this thesys is over.

I wish also to say a big thank you to SISSC guys I met the year before in Basel and then in Italy and in particular to Joe, I really believe you got the key of life. . . thanks for sharing it with us.

Friends' turn... e visto che mi dareste un sacco di *legnate* se scrivessi in inglese... cambio ! In cima alla lista una persona speciale, che pensavo di aver perso per sempre mentre il caso ha voluto che ci ritrovassimo e sono certo che non ci perderemo di vista molto facilmente ovunque saremo... mi sembra una vita, e forse lo è, da quando quella sera di inverno ci trovammo... tante cose diverse, tanto più grandi e diversi ora, ma sempre gli stessi e di nuovo insieme... Un pensiero va al mio adorato *Spin*... impossibile condensarne i motivi in poche righe... resti sempre il mio salvatore durante ogni scrittura di tesi... tanto ci unisce, tante parole ho riletto in questo periodo, tante altre scambiate a voce o per mail... tante ne verranno e alla fine come al solito riderai di me ricordandomi un altro integrale di $sin(x)/x$. Un ringraziamento di quelli speciali a Giovanna che, anche se non fisicamente, è sempre accanto a me quando sono di fronte ai miei *bivi* e che mi insegna sempre molto, con quel suo modo speciale...

il più dolce dei pensieri alla mia adorata Ludo che ho incontrato in quel posto così orribile... il tuo sorriso fa sempre sorgere il sole fuori e dentro di me, tanto ci ha unito in questo periodo... entrambi stressatissimi per la consegna. Al mio più caro Omonimo va un sorriso al pensiero di quella febbraccia presa durante una serata così lontana dalla fisica... ricordati che finita la casa te la riempio di quadri !!! ... un grazie a te Giulia, strana sconosciuta che mi hai capito e sei riuscita a esserci lievemente facendomi sentire forte un'amicizia nata per caso, adesso iniziamo a lavorare sul serio... Un abbraccio a Carletto, principe dei fotografi, che ringrazio per non avermi ucciso ogni volta che nell' ultimo periodo gli ho detto *ho da fare ho da fare ho da fare*... per essermi stato sempre accanto con la leggerezza di cui solo un amico è capace... a una Gnoma va il più allegro dei miei sorrisi... per la sua ipocondria che a volte mi fa sentire utile... lo so che ancora stai aspettando e che adesso non ho più scuse... a un Mostro va un abbraccio che ti possa accompagnare nella vita sicura e libera come ti ricordo... Per ultimo, come una ninnananna, mi piace ripensare alle parole sussurrate da te mia cara Romina, amica leggera dalla voce possente, nel pensiero delle tue forti mani in molti momenti di difficoltà ho trovato la forza, spero un giorno di poter davvero sentire la voce del tuo lago...

Ah quasi dimenticavo... :p bLuE quello che più d' ogni altro, forse, ho maltrattato in questi lunghi mesi e che a forza mi è stato accanto; grazie compagno di avventure e scusa se ho trascurato anche te.

A thought goes to *Mama*: your words go on echoing inside my ears, I remember you as the first time we met: your hands, your smile... your tatoos. I kept your postcard of the November '99 straight in front of my keyboard all the time...*The path that leads us through the most obstacles often provides the richest journey.* I hope one day I'll meet you again and you'll see how I grew strong and without loosing the power of smiling to the rainbow that will come whenever rain is falling.

Infine a te mia *Rossana* non posso che dedicare una riga vuota, un silenzio

...   ...

perché qualunque parola sarebbe toglierti qualcosa... Il tuo sorriso ogni giorno mi ha portato il sole, e lo stesso sorriso dolce ha accompagnato i miei sogni ogni notte ovunque io abbia posato il capo, mi ha nutrito il tuo respiro e le tue carezze hanno scacciato le mie fatiche... ogni girasole è

per te. . . tu sai. . . e presto tornerò a correre in quei campi. . . il rumore del mare a cullare le nostre danze. . .

Ringrazio la mia famiglia che mi è sempre stata accanto con pazienza e spesso con ignara ironia e vorrei scusarmi con loro per tutte le volte che ho disertato cene e festività . . . certo adesso non avrò più scuse, ma di certo inventerò qualcos'altro. Un grazie speciale al mio cuginetto Eros: so che il giorno prima della presentazione mi hai preso per matto . . . e forse avevi ragione. . .

So di essere stato un po' prolisso, ma le persone da ringraziare sono tante. . . e tante ne avrò dimenticate. . . perdonatemi, porto i vostri sorrisi sempre con me pronto a usarli al momento giusto. . .

L'ultimo pensiero. . . alla mia dolce cuginetta, l'unica che sia riuscita a distogliermi per un istante durante l'ultimo periodo di dura scrittura. . . al tuo sorriso bella Adele. . . e a quello, ancora più bello, della tua piccola Greta... che ora avrò tutto il tempo di viziare. . .